VOL 32 / SUPPL 1
OCTOBER 2019
Electronic only

ESMRMB
European Society for Magnetic Resonance in Medicine and Biology

MAGNETIC RESONANCE MATERIALS IN PHYSICS, BIOLOGY AND MEDICINE

MAGMA

Book of Abstracts
ESMRMB 2019
36th Annual Scientific Meeting
Rotterdam/NL, October 3-5, 2019

Official Journal of the European Society for Magnetic Resonance in Medicine and Biology

Springer

ESMRMB
European Society for Magnetic Resonance in Medicine and Biology

Table of Contents

ESMRMB

European Society for Magnetic Resonance in Medicine and Biology

ESMRMB 2019 Congress

October 3-5, Rotterdam/NL

Book of Abstracts

Thursday

DOI: 10.1007/s10334-019-00753-3

I01 Teaching Session

08:00–09:00 *Room 1 - Willem Burger Zaal*

ASL as an Alternative to Gadolinium

I01.01
Perfusion

I. Boscolo Galazzo
University of Verona, Department of Computer Science, Verona, ITALY

Learning Objectives: To learn the basic principles of Arterial Spin Labeling (ASL) MRI

- To understand the main ASL techniques and their feasibility.
- To understand how ASL images can be processed and quantified.
- To know how ASL can be applied in clinical practice for perfusion measurements

Body: Perfusion measurement is nowadays an important tool in the clinical routine, playing a key role to detect flow alterations in several pathologies including ischemic stroke, tumour, epilepsy, and neurodegenerative disorders. When focusing on the MRI field, dynamic susceptibility contrast (DSC) is still considered the optimal method to derive perfusion parameters (e.g., cerebral blood flow [CBF], volume [CBV], and time-to-peak [TTP]), although Arterial Spin Labeling (ASL) can represent a viable alternative, also compared to the more invasive techniques from nuclear medicine, as ^{15}O-water PET. ASL is indeed a completely non-invasive, quantitative, and easily repeatable technique that allows quantifying perfusion by exploiting magnetically labelled arterial blood water as an endogenous tracer [1]. In addition, when specific sequences as multi-time point ASL are employed, it can allow to estimate other perfusion-related parameters, such as arterial transit time (ATT) [2]. ASL acquisitions consist of label and control images, which are repeated over time to increase the SNR and whose subtraction generates a perfusion-weighted map, which can then be quantified to derive the different perfusion-related estimates. Despite its limited use in clinical settings, several studies have demonstrated its good reliability and stability, as well as its ability to produce accurate and reproducible CBF measurements, pointing towards its viability as robust imaging method [3, 4]. In particular, since the consensus paper in 2015, ASL has started to become a mainstream technique in the field and to achieve a greater consensus in the community thanks to the encouraging results, technical developments and recent clinical translation [5]. These have allowed ASL to gain its popularity and to shade lights on the several variants and specific parameters, which have historically created a great deal of confusion among the users willing to adopt ASL in their studies.
In this presentation, the key aspects of ASL techniques will be illustrated, from labelling and acquisition schemes to preprocessing and perfusion quantification. In addition, the recent technical developments will be introduced along with examples of clinical applications in the neurology field.

References

[1] Detre JA et al. (1992). Magn. Reson. Imaging 23, 37–45.
[2] Van Osch M et al. (2018). J Cereb Blood Flow Metab. 38, 1461-1480.
[3] Gevers S et al. (2011). J Cereb Blood Flow Metab. 31, 1706–1715.
[4] Mutsaerts H et al. (2015). Neuroimage 113, 143–152.
[5] Alsop DC et al. (2015). Magn. Reson. Imaging 73, 102–116.

I01.02
Angiography

Y. Suzuki
University of Oxford, Oxford, UNITED KINGDOM

Learning Objectives:
To notice that arterial spin labelling (ASL) is not only for perfusion imaging.
To get familiar what kind of information will be provided by ASL MR angiography (MRA).
To understand what kind of options can be (should be) considered for making an ASL-MRA sequence.
To be convinced that you would like to use ASL-MRA in your hospital.

Body: For many cerebrovascular diseases, visualization of blood flow through the large vasculature and quantitative microvascular information of downstream tissue perfusion are crucial for diagnosis and monitoring in follow-up examinations. The former is achieved by angiography and the latter is assessed by perfusion imaging, both which can be performed by using Arterial Spin Labeling (ASL) techniques.
Although it is less spread than ASL perfusion imaging, the use of ASL techniques for dynamic MR angiography (MRA) has been getting more attention due to its advantages over contrast-enhanced (CE) dynamic MRA in the brain. For example, not only its ability of visualizing arterial flow without relying on the contrast agent (please see Fig. 1), but also two more advantages can be considered.

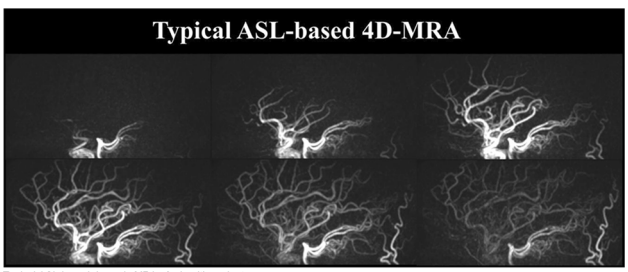

Typical ASL-based dynamic MRA of a healthy volunteer

Firstly, in the acquisition of CE dynamic MRA, it is desired to capture the first passage of the contrast agent bolus by means of a real-time dynamic acquisition. Due to very fast passage of the contrast agent through the vascular tree and the early appearance of venous signal,

each dynamic must be acquired very quickly, and therefore spatial resolution is often compromised. In ASL, on the other hand, the labeling of the arterial blood and following data acquisition can be repeated until sufficient data is acquired for both high spatial and temporal resolution, because it is not necessary to acquire all data during a single bolus passage. Therefore, it is easier to achieve fast time frame while keeping high spatial resolution as well. The second advantage is the ability to perform vessel specific visualization, in which the vascular tree arising from a selected artery can be exclusively visualized by means of spatially selective labeling. Figure 2 shows an example of vessel-selective dynamic-MRA visualizing internal and external carotid arteries (ICA and ECA) separately.

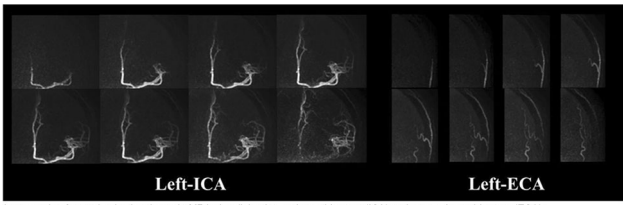

An example of vessel-selective dynamic-MRA visualizing internal carotid artery (ICA) and external carotid artery (ECA)

Such visualization could provide information e.g. how collateral flow or constructed bypass flow are working and allow for smoother examinations and treatments using X-ray digital subtraction angiography (DSA), or even could be a potential alternative of X-ray DSA examination for follow-up.

In this talk, the recent developments and implementation of ASL-based MRA will be presented including several clinical cases.

References:

References will be provided during the presentation.

I02 Teaching Session

08:00–09:00 *Room 2 - Van Weelde Zaal*

Introduction to Machine Learning

I02.01
Roadmap: From Clinical Need to Translatable Tool

T. Booth[1, 2]
[1]*King's College London, School of Biomedical Engineering and Imaging Sciences, London, UNITED KINGDOM,* [2]King's College Hospital, Neuroradiology, London, UNITED KINGDOM

Learning Objectives: To define biomarkers.
To determine the steps in a radiomics study.
To describe analytical and clinical validation

Body: This machine learning talk will be delivered through the lens of clinical radiology. The most relevant imaging biomarkers are diagnostic, prognostic, monitoring and predictive. Radiomics methodology allows imaging biomarkers to be derived. One step involves obtaining features from the image through explicit or implicit feature engineering. In addition to analytical validation, clinical validation is critical to ensure a biomarker is ready for clinical translation. Whilst some highly-defined machine learning classification tasks, such as lung cancer screening to diagnose whether a nodule is benign or malignant, using highly-selected data appear promising, few, if any techniques are ready to be incorporated into the clinic for routine use. Almost all machine learning studies, particularly where there is a combination of a relative scarcity of data and the clinical question is complex e.g. brain tumour treatment response, would benefit from improvements to their methodology. Examples include the use of using external validation datasets, comparison of the novel approach to simpler standard approaches and the use of larger datasets. Because the development and validation of machine learning models require large, well-annotated datasets, multidisciplinary and multi-centre collaborations are typically necessary. Given the challenges of translating machine learning models to the clinic, some groups have published roadmaps and scoring systems to improve study design: examples include the Imaging Biomaker Roadmap, the Image Biomarker Standardisation Initiative and the Radiomics Quality Score.

References

1. FDA-NIH Biomarker Working Group. In: BEST (Biomarkers, EndpointS, and other Tools) Resource. 1st ed. Food and Drug Administration (US), Silver Spring, USA: co-published by National Institutes of Health (US), Bethesda, 2016.
2. Zwanenburg A, Leger S, Vallieres M, Lock S. Image biomarker standardisation initiative. 28 Feb 2019 arXiv preprint arXiv:1612.07003.
3. Lambin P, Leijenaar RTH, Deist TM et al. Radiomics: the bridge between medical imaging and personalized medicine. Nat Rev Clin Oncol. 2017 Dec;14(12):749–762.
4. Booth T.C., Williams M, Luis A, Cardosa J, Keyoumars A, Shuaib H. Machine learning and neuro-oncology imaging biomarkers. Clin Radiol. In Press 2019.
5. Booth T.C. An update on machine learning in neuro-oncology diagnostics. In: BrainLes 2018, LNCS. A. Crimi et al. (Eds.): Springer Nature Switzerland AG. 11383, pp. 1–8, 2019. https://doi.org/10.1007/978-3-030-11723-8_4.

I02.02
Concepts and Lexicon of Machine Learning in Medical Imaging

G. Langs
Medical University of Vienna, Computational Imaging Research Lab, Vienna, AUSTRIA

Learning Objectives: Understand

- Concepts of machine learning such as supervised learning, weakly supervised learning, unsupervised learning, and the relationships of artificial intelligence, machine learning and deep learning.
- Different application domains of machine learning and AI: diagnosis, prediction, phenotyping, illustrated with examples.
- The range of state of the art machine learning methods, their capabilities, and limitations.

Body: This talk will give a primer on machine learning in medical imaging. We will discuss basic concepts such as supervised-, weakly supervised-, and unsupervised learning, and will illustrate them with examples, to make their purpose, requirements, and limitations clear. The examples should give participants a sense for matching method and problem specification in clinical application. We will then discuss different roles of machine learning in medical imaging and its use in clinical routine. They will range from diagnostic AI, where the primary purpose is to support diagnosis, by computationally detecting, measuring, or quantifying known markers, to predictive AI, that aims at predicting individual future disease course and treatment response. The latter opens up the possibility of revising our current diagnostic categories, expanding the vocabulary of markers and marker patterns we exploit, when informing individual treatment decisions. Finally, we will highlight current limitations, and next challenges in this rapidly evolving fields.

References

Langs, G., Röhrich, S., Hofmanninger, J., Prayer, F., Pan, J., Herold, C. and Prosch, H., 2018. Machine learning: from radiomics to discovery and routine. *Der Radiologe*, *58*(1), pp.1-6.
Vogl, W.D., Pinker, K., Helbich, T.H., Bickel, H., Grabner, G., Bogner, W., Gruber, S., Bago-Horvath, Z., Dubsky, P. and Langs, G., 2019. Automatic segmentation and classification of breast lesions through identification of informative multiparametric PET/MRI features. *European radiology experimental*, *3*(1), p.18.

I03 Teaching Session

08:00–09:00 *Room 3 - Ruys & van Rijckevorsel Zaal*

Practical Approaches to Efficient MRI

I03.01
Optimising Patient Management

J. Castillo[1, 2]
[1]*Mater Dei Hospital, San Gwann, MALTA,* [2]*Mater Dei Hospital, Medical Imaging, San Gwann, MALTA*

Learning Objectives: Learn about quality management system
Understand the parts of quality management system.
Introduce the radiographer's technical report as an assessment of image quality.
Establish quality criteria at each step of the pathway for audit purposes.

Body: A question commonly tackled by radiography managers is: how can a service be managed, controlled, measured, reviewed and improved through the collaboration of stakeholders? On way is through an optimised care pathway design as this is crucial for the attainment of effective and safe service. If care pathways can be used to deliver effective services, they can also be optimised to support a quality management system.

References:

Castillo J., Caruana C.J., Morgan P.S., Westbrook C & bMizza A (2016). MRI care pathway: Supportig a Quality Management System, HealthManagement, Volume 6 - Issue 1.

I03.02
Image Quality Versus Scan Time at 3T: Getting the Balance Right

M. Hayes
Sports Surgery Clinic, Diagnostic Imaging, Dublin, IRELAND

Learning Objectives:

1. To review the advantages and challenges associated with imaging at 3T based on key physical principles.
2. To discuss the importance of parameter selection for image optimisation.
3. To highlight image quality and scan time considerations in the context of efficient, and high quality, clinical MR service.

Body: Imaging at 3T, when compared to 1.5 T, provides better proton alignment and thus higher signal to noise ratio (SNR). Such SNR gains can facilitate higher resolution imaging, reduced scan time, or a combination of these advantages. Higher spatial resolution imaging may allow us to better evaluate anatomical and pathological details while improved temporal resolution provides opportunities to better evaluate contrast enhancement patterns.

However, 3T presents other challenges such as effecting tissue contrast and tissue relaxation times. The increased range and variety of artefacts also need to be considered. Specific absorption rate (SAR) may be a limiting factor for certain studies, which further complicates image optimisation. Pulse sequence and coil options are two further essential considerations. Thus careful parameter, sequence, and coil selection are key to making the most of 3T clinical MR.

To get the balance right at 3T, in terms of image quality and scan time optimisation, requires a team approach and knowledgeable and skilled MR radiographers who can rapidly adapt protocols and sequences to accommodate different patient presentations and clinical questions. A series of clinical images and cases as examples will be used to demonstrate practical image quality and scan time considerations for an efficient and high quality clinical MR service.

I04 Sir Peter Mansfield Lecture

09:30–10:15 *Room 1 - Willem Burger Zaal*

Sir Peter Mansfield Lecture

I04.01
Flow, Diffusion and Perfusion MRI: An Evolution Over 30 Years

F. Ståhlberg
Lund University, Lund, SWEDEN

Learning Objectives:
*To understand the historical background of the field.
*To follow the development from the early days until today.
*To see possible future trends in techniques and applications.

Body: A survey of techniques for *flow, diffusion and perfusion MRI* will be presented, including historical background, methodological development and future possibilities.

Regarding "macroscopic" *velocity and flow*, methods based on relations between phase and velocity for spins moving in a gradient field (1) have evolved into quantitative techniques, including dynamic versions where flow is encoded in three spatial dimensions ("4D flow"). In parallel, *MR angiography* (MRA) for vessel visualisation developed in the late 1980s and rapidly branched out into time-of-flight (TOF), phase contrast (PC) and contrast-enhanced (CE) MRA. Current progression includes modelling using computer fluid dynamics (CFD) and development of fast reconstruction techniques using compressed sensing and machine learning.

Diffusion MRI measurements are also based on the above-mentioned phase/velocity relation but utilize "microscopic" dephasing effects caused by molecular motion within the imaging voxel. Diffusion-weighted imaging (DWI) emerged in the mid-1980s and soon proved to be valuable in clinical applications such as acute ischemic stroke diagnosis. Diffusion encoding, in terms of intra-voxel incoherent motion (IVIM) imaging, was also introduced to probe the pseudo-random motion patterns of the microcirculation. DWI has developed into diffusion tensor imaging (DTI) and fibre tracking techniques, and many diffusion-related MRI parameters, e.g. anisotropy indices and kurtosis, can now be estimated.

Novel diffusion encoding strategies, utilizing the power and flexibility of state-of-the art gradient systems, can be used to reveal, for example, microscopic anisotropy.

Perfusion was first measured with MRI in the late 1980s, when dynamic susceptibility contrast (DSC) MRI was introduced. A few years later, the non-invasive arterial spin labelling (ASL) technique was presented. In parallel, the new research field of *neuronal activation studies* or *fMRI* emerged, opening the door to neurofunctional research. Perfusion techniques are developing towards assessment of complementary parameters such as oxygen metabolism and fMRI is frequently a part of a multimodal arsenal of techniques used in large-scale brain function studies. Combinations of resting-state fMRI and diffusion techniques also continue to develop towards investigations of brain networks and functional connectivity.

In summary, the development of flow, diffusion and perfusion techniques has been a prerequisite for MRI to become an important modality for functional studies in a broad sense, providing tools for visualization and quantification of important biophysical/physiological parameters used as biomarkers for disease.

References:
1. Moran PR. MRI 1982;1:197-203.

I05 Plenary Session

10:30–11:30 *Room 1 - Willem Burger Zaal*

Gadolinium-Free Imaging

I05.01
The Good, the Bad and the Ugly of Gadolinium

A. Radbruch
University of Essen, Radiology, Essen, GERMANY

Learning Objectives

- To understand the mechanism of gadolinium deposition.
- To understand the difference between temporary presence of the intact gadolinium chelate and dechelated gadolinium.
- To learn potential clinical correlates of gadolinium deposition.
- To understand why gadolinium in the glymphatic system can be used for diagnostic purposes (glymphatic imaging).

Body: Since Tomonori Kanda published in 2014 that serial injections of gadolinium based contrast agents cause hyperintensities in certain areas in the brain, multiple studies assessed the mechanism of gadolinium deposition as well as potential clinical correlates. The debate culminated in 2017 in different regulatory decisions of the FDA and the EMEA. While the EMEA decided in a precautionary approach to withdraw linear agents from the market, all agents (linear and macrocyclic) remain on the US market.

The talk will give an overview of the current scientific literature and focus on potential clinical correlates as well as on the mechanism of gadolinium deposition. It will be highlighted that one of the major flaws of the current debate is the often missing differentiation between chelated and dechelated gadolinium. It will be emphasized that the intact gadolinium chelate in the glymphatic system should not be mixed up with the release of the gadolinium from the chelate. Rather, temporary presence of the intact chelate in the glymphatic pathway might be used for diagnostic purposes. A fact that has been largely overlooked so far.

References:

- Kanda et al., High signal intensity in the dentate nucleus and globus pallidus on unenhanced T1-weighted MR images: relationship with increasing cumulative dose of a gadolinium-based contrast material, Radiology 2014.
_ Radbruch et al., Gadolinium retention in the dentate nucleus and globus pallidus is dependent on the class of contrast agent., Radiology 2015.
- Radbruch et al. Chelated or dechelated gadolinium deposition. Lancet Neurology 2017.
- Deike-Hofmann et al., Glymphatic Pathway of Gadolinium-Based Contrast Agents Through the Brain: Overlooked and Misinterpreted.

I06 Teaching Session

13:00–14:30 *Room 1 - Willem Burger Zaal*

Gadolinium-free Cardiac Imaging

I06.01
T1-rho as an Alternative to Late Gadolinium Enhancement

M. Froeling
University Medical Center Utrecht, Department of Radiology, Utrecht, NETHERLANDS

Learning Objectives:

1. Understanding the contrast mechanism of T1rho.
2. Understanding the advantages and disadvantages of T1rho compared to late gadolinium enhancement.
3. Clinical applications of T1rho in cardiac disease.

Body: In the heart the cardiomyocytes are surrounded by interstitial collagen. In cardiac disease there can be an increase of collagen due to the replacement of dead cardiomyocytes, i.e. replacement fibrosis, or an increase of collagen synthesis by myofibroblasts, i.e. reactive fibrosis. An increase of collagen formation can lead to heart failure by decreasing ventricular systolic function, induction of diastolic dysfunction and adverse cardiac remodeling. Adequate diagnosis and precise identification of the fibrotic region allows for better prediction of the prognosis and outcome after therapy. Invasive techniques such as endomyocardial biopsies can provide a qualitative and quantitative assessment of collagen. However, a biopsy only samples a small part of the myocardium. Therefore, on invasive techniques with full myocardial coverages are required. Cardiac infarct size can be assessed non- invasively with Cardiac Magnetic Resonance Imaging (MR). The most common MRI techniques use of exogenous gadolinium-based contrast agents to allows for indirect detection of fibrosis. The two most common methods are Late gadolinium enhancement for detecting replacement fibrosis and contrast enhanced T1 mapping (extra cellular volume mapping, or ECV) for detecting diffuse reactive fibrosis. As an alternative of using these two methods that used exogenous gadolinium contrast agents T1ρ has been proposed. T1ρ refers to the spin lattice relaxation time constant in the rotating magnetic field, and measures the transverse magnetization decay in the presence of a spin-lock radiofrequency (RF) field. Processes that give rise to T1 and T2 contrasts relate to molecular rotation in the Larmor time-scale, with frequencies on the order of megahertz. The T1ρ contrast mechanism is sensitive to a lower frequency in the kilohertz range, and picks up signal from lower energy interactions related to chemical exchange between extracellular water and complex macromolecules (1, 2).

The most clinically validated method is late gadolinium enhancement (LGE) for the evaluation of focal scar tissue (3–6). Data is typically acquired using an inversion recovery GE sequence which aims to null the signal from the myocardium. Around 10 min after contrast injection the contrast agent accumulates in the extra cellular space of fibrotic scars. Since the signal of the myocardium is nulled only the scar tissue give positive contrast. To measure scar size a region of interest is drawn in the healthy myocardium and a threshold is set at the mean signal intensity + 2 Standard deviations to select het fibrotic region. Another approach is to segment the hyperintense myocardium and determine the full width half max of this region and set the as a threshold to delineate the fibrotic regions (7). Although LGE allows to quantify the size of the hyperintense regions further quantitative evaluation is limited. Furthermore, in cases of diffuse fibrosis het signal intensity of the entire myocardium is enhance evenly. Since the myocardium is nulled using an inversion pulse this limits the use of LGE in the evaluation of diffuse fibrosis.

For the evaluation of diffuse fibrosis commonly ECV mapping is used. This is a quantitative method that aims to quantify the extra cellular volume fraction in the myocardium by comparing a pre and post contrast injection T1 map. For the acquisition of a T1 map of the heart modified look locker inversion recovery sequence (8) is commonly used but many other methods are available (9). The post contrast T1 map is acquired 15–20 min after contrast injection. Because in ECV mapping one measures the quantitative T1 relaxation time constants instead of using qualitative T1 contrast, it is possible to overcome the limitations of LGE in patients with diffuse myocardial fibrosis (10, 11). The ECV is defined as ECV = (1 − hematocrit) ($\Delta R1_{myocardium}/\Delta R1_{blood}$) where $\Delta R1_{myocardium}$ and $\Delta R1_{blood}$ are the differences of the longitudinal relaxation rates of the myocardium and blood before and after contrast injection. To obtain reliable ECV values the hematocrit value should be determined, which requires the withdrawal of blood before the MRI exam. This can be done by the intravenous line that is already in place for the gadolinium injection, but creates a time-consuming procedure in clinical workflow, as the blood sample needs to be analyzed, and the resulting ECV map can only be calculated afterward with the hematocrit value, pre- and post-T1 map combined, For reliable quantification of T1 maps the images at each inversion time should be aligned to compensate for cardiac motion. Furthermore, since the pre and post contrast T1 maps are acquired with a 15–20 min interval it is essential to align both scans to obtain reliable ECV maps. Tissue characterization with native T1 and ECV has been shown to have incremental diagnostic benefit even in very early disease stages (e.g. diffuse fibrosis not detectable by LGE).

Although both the methods describe above have made their way into clinical practice, they rely on the injection of exogenous contrast agents and require a 10–15 min waiting period after contrast injection. To overcome these limitations T1ρ has been proposed as an alternative. As mentioned T1ρ measures the spin lattice relaxation time constant in the rotating magnetic field. To generate T1ρ contrast a spin-lock pulse with a low amplitude radio-frequency (RF) is applied on-resonance with the precessing transverse magnetization. The relaxation rate constant of the transverse magnetization under influence of this spin-lock pulse is the T1r relaxation. The spin-lock technique used to generate T1rho contrast provides a mechanism to probe into macromolecular environment which conventional imaging methods cannot offer. Consequently, T1rho quantification has potential in many clinical applications.

It has been shown that in chronic myocardial infarction an increase of T1r relaxation time correlates with the infarcted area (12–18). As such T1ρ mapping allows for infarct detection, without the use of an exogenous contrast agent. Studies have shown that the scar size in chronic myocardial infraction measured using T1ρ is highly correlated with the measurements by LGE and the presence of fibrosis. However, the sensitivity of T1ρ mapping is lower than LGE imaging, there is room for improvements on the T1ρ mapping sequence that could provide a higher sensitivity and specificity. Since T1ρ mapping is a quantitative method that is related to the presence of fibrosis it also allows to detect and quantify diffuse fibrosis (19, 20). It has been shown that there is a significant positive correlation between the T1 ρ -relaxation time and the ECV-fraction. The benefit of T1ρ mapping over ECV mapping is that T1ρ only requires one acquisition and does not need contrast injection. However, the change in T1ρ in patients compared to heathy controls is small ($\sim 2 \times$ the standard deviation in healthy controls).

Native T1ρ-mapping for detection of infarct area or diffuse fibrosis require improvements on the T1ρ -mapping sequence to provide a

higher sensitivity and specificity. The endogenous method could be an alternative for LGE and ECV mapping imaging but there are limitations that have to be solved before wide adoption of the method. Similar to T1-mapping motion correction to compensate for cardiac motion during acquisition is required (21). Furthermore, the main limitation of T1ρ-mapping is that it is sensitive to inhomogeneities of both the B0 and B1 fields where the effective magnetic field with respect to the transverse plane is $\phi = \tan\text{-}1(|B0|/|B1|)$. When there is off-resonance, the effective magnetic field in the rotating frame during spin-lock is a combination of B1 RF and B0 field (22–24). A spin lock preparation pulse consists of a 90° excitation pulse followed by the spin lock pulse after which a 90-degree tip up pulse is applied to store the magnetization along the longitudinal axes. After this preparation pulse any readout can be applied. The effectiveness of the spin lock pulse is severely compromised in off resonance areas. To overcome the adversary effect from off-resonance during spin-lock a simple solution is to increase the amplitude of the spin-lock RF pulse. However high amplitude RF pulses with long duration will cause and increase of the special absorption rate. Additionally, common clinical RF-amplifiers are limited in their maximal RF amplitudes. A more effective way of compensating for off resonance is to introduce a 180-degree refocusing RF pulse in the middle of spin lock pulse. The 180-degree pulse compensates the accumulated off resonance effects during spin lock but can be sensitive to B1 inhomogeneities. To overcome the sensitivity to B1 inhomogeneities the phase of first and last 90° pulses needs to be alternated (22, 25). Static field heterogeneity should be reduced to less than 10% of the spin lock field amplitude to minimize T1rho quantification errors (24). When the B1 field greatly exceeds the resonance offset a composite spin lock pulse can be used. The direction of the spin lock pulse is along the + y direction for the first part of the pulse. Then after the 180-degree refocusing pulse the second part of the spin lock pulse is along the − y direction which corrects the accumulated phase during the spin lock period.

Although there are still improvements to be made to overcome limitations of T1ρ imaging in myocardial applications the methods show great promise. With better understanding of the correlation of the T1ρ contrast with fibrosis and more clinical validation the methods can complement current gadolinium-based methods for cardiac evaluation and potentially even replace these methods. In conclusion, the unique sensitivity of T1ρ to slow spin motions in tissue allows it to generate a unique contrast that shows great promise.

References:

1. Santyr GE, Henkelman RM, Bronskill MJ: Spin locking for magnetic resonance imaging with application to human breast. *Magn Reson Med* 1989; 12:25–37.

2. Gilani IA, Sepponen R: Quantitative rotating frame relaxometry methods in MRI. *NMR Biomed* 2016; 29:841–861.

3. Weng Z, Yao J, Chan RH, et al.: Prognostic Value of LGE-CMR in HCM. *JACC Cardiovasc Imaging* 2016; 9:1392–1402.

4. Becker MAJ, Cornel JH, van de Ven PM, van Rossum AC, Allaart CP, Germans T: The Prognostic Value of Late Gadolinium-Enhanced Cardiac Magnetic Resonance Imaging in Nonischemic Dilated Cardiomyopathy: A Review and Meta-Analysis. *JACC Cardiovasc Imaging* 2018; 11:1274–1284.

5. Kwong RY, Chan AK, Brown KA, et al.: Impact of unrecognized myocardial scar detected by cardiac magnetic resonance imaging on event-free survival in patients presenting with signs or symptoms of coronary artery disease. *Circulation* 2006; 113:2733–2743.

6. Karamitsos TD, Francis JM, Myerson S, Selvanayagam JB, Neubauer S: The Role of Cardiovascular Magnetic Resonance Imaging in Heart Failure. *J Am Coll Cardiol* 2009:1407–1424.

7. Flett AS, Hasleton J, Cook C, et al.: Evaluation of techniques for the quantification of myocardial scar of differing etiology using cardiac magnetic resonance. *JACC Cardiovasc Imaging* 2011; 4:150–156.

8. Messroghli DR, Radjenovic A, Kozerke S, Higgins DM, Sivananthan MU, Ridgway JP: Modified Look-Locker inversion recovery (MOLLI) for high-resolutionT1 mapping of the heart. *Magn Reson Med* 2004; 52:141–146.

9. Teixeira T, Hafyane T, Stikov N, Akdeniz C, Greiser A, Friedrich MG: Comparison of different cardiovascular magnetic resonance sequences for native myocardial T1 mapping at 3T. *J Cardiovasc Magn Reson* 2016; 18:65.

10. Sibley CT, Noureldin RA, Gai N, et al.: T1 Mapping in Cardiomyopathy at Cardiac MR: Comparison with Endomyocardial Biopsy. *Radiology* 2012; 265:724–732.

11. Haaf P, Garg P, Messroghli DR, Broadbent DA, Greenwood JP, Plein S: Cardiac T1 Mapping and Extracellular Volume (ECV) in clinical practice: a comprehensive review. *J Cardiovasc Magn Reson* 2017; 18:89.

12. Musthafa H-SN, Dragneva G, Lottonen L, et al.: Longitudinal rotating frame relaxation time measurements in infarcted mouse myocardium in vivo. *Magn Reson Med* 2013; 69:1389–1395.

13. Witschey WRT, Pilla JJ, Ferrari G, et al.: Rotating Frame Spin Lattice Relaxation in a Swine Model of Chronic, Left Ventricular Myocardial Infarction. *Magn Reson Med* 2010; 64:1454–1461.

14. van Oorschot JW, El Aidi H, Jansen of Lorkeers SJ, et al.: Endogenous assessment of chronic myocardial infarction with T(1ρ)-mapping in patients. *J Cardiovasc Magn Reson* 2014; 16:104.

15. Witschey WR, Zsido GA, Koomalsingh K, et al.: In vivo chronic myocardial infarction characterization by spin locked cardiovascular magnetic resonance. *J Cardiovasc Magn Reson* 2012; 14.

16. Madden M, Mohammed S, Contijoch F, et al.: Assessment of T1rho relaxation times after reperfused myocardial infarction. *J Cardiovasc Magn Reson* 2016; 18(Suppl 1):W13.

17. Stoffers RH, Madden M, Shahid M, et al.: Erratum to: Assessment of myocardial injury after reperfused infarction by T1ρ cardiovascular magnetic resonance. *J Cardiovasc Magn Reson* 2017:42.

18. Wang Y, Cai W, Wang L, Xia R: Evaluate the early changes of myocardial fibers in rhesus monkey during sub-acute stage of myocardial infarction using diffusion tensor magnetic resonance imaging. *Magn Reson Imaging* 2016; 34:391–396.

19. van Oorschot JWM, Güçlü F, de Jong S, et al.: Endogenous assessment of diffuse myocardial fibrosis in patients with T1ρ-mapping. *J Magn Reson Imaging* 2017; 45:132–138.

20. Wang L, Yuan J, Zhang S-J, et al.: Myocardial T 1 rho Mapping of Patients With End-Stage Renal Disease and Its Comparison With T 1 Mapping and T 2 Mapping: A Feasibility and Reproducibility Study. *J MAGN Reson IMAGING* 2016; 44:723–731.

21. Berisha S, Han J, Shahid M, Han Y, Witschey WRT: Measurement of Myocardial T1ρ with a Motion Corrected, Parametric Mapping Sequence in Humans. *PLoS One* 2016; 11:e0151144.

22. Chen W: Errors in quantitative T1rho imaging and the correction methods. *Quant Imaging Med Surg* 2015; 5:583–91.

23. Chen W: Artifacts correction for T1rho imaging with constant amplitude spin-lock. *J Magn Reson* 2017; 274:13–23.

24. Han Q, Han Y, Gorman RC, Witschey WR: The influence of static and RF field heterogeneity on T1rho cardiovascular MRI. *J Cardiovasc Magn Reson* 2014; 16:16–19.

25. Witschey WRT, Borthakur A, Elliott MA, et al.: Artifacts in T1ρ-weighted imaging: Compensation for B1 and B0 field imperfections. *J Magn Reson* 2007.

I06.02
T1 Mapping in Rest and Under Stress

V. Ferreira
University of Oxford, Division of Cardiovascular Medicine, Radcliffe Department of Medicine, Oxford, UNITED KINGDOM

Learning Objectives

(1) Principle of cardiac T1-mapping at rest and during vasodilatory stress
(2) Potential applications in the evaluation of ischemic heart disease

Body: Cardiac MRI T1-mapping has recently attained wide clinical validation of its potential utility. In this lecture, we address the basic principles of myocardial T1 mapping, with particular attention to stress T1-mapping using vasodilatory stress agents to interrogate the myocardial intravascular compartment and emerging applications in ischemic heart disease.

References:

Piechnik SK, Neubauer S, Ferreira VM. "State-of-the-Art Review: Stress T1-mapping - Technical considerations, Pitfalls and Emerging Clinical Applications ". Magnetic Resonance Materials in Physics, Biology and Medicine, 1-11, 2017.

I06.03
Cardiac Arterial Spin Labeling

F. Kober
Aix-Marseille Univ, CNRS, CRMBM, Marseille, FRANCE

Learning Objectives:

(1) To understand why we would want to measure perfusion without contrast agents in the heart.
(2) To learn why ASL in the heart is different.
(3) To get an overview over past and current method developments.
(4) To appreciate what these techniques can do now, what they may do better than contrast-based techniques in the future, and what they probably won't do.

Body: Beyond overcoming contrast-agent-related risks in patients with cardiovascular disease, non-contrast myocardial perfusion techniques might also open new ways of improving quantification accuracy due to their ease of use and due to their free repeatability within an MRI exam. These arguments have been motivating developments in cardiac ASL despite the technical challenges. This talk will give an overview over expectations, solutions, advantages and limitations related to measuring perfusion in the heart without contrast agents. I will discuss the major existing approaches to Arterial Spin Labeling (ASL) in the heart, but also recall coronary sinus flow measurements as an alternative. The reasons why myocardial ASL is challenging compared with other organs will be outlined. It should also become clear why cardiac ASL is a well-working and validated method in the rodent heart whereas human applications are still scarce.

Because the potential of ASL for quantifying myocardial perfusion is obvious, ongoing efforts by several groups aim at improving its efficiency and robustness. While the feasibility of cardiac ASL has been proven, it is not yet ready for replacing 1st pass techniques. Cardiac ASL remains an active area of research with many interesting solutions on the horizon.

References:

1. Poncelet BP, et al. Measurement of human myocardial perfusion by double-gated flow alternating inversion recovery EPI. Magn Reson Med 1999;41:510–9.
2. Wacker CM, et al. Quantitative assessment of myocardial perfusion with a spin-labeling technique: preliminary results in patients with coronary artery disease. J Magn Reson Imaging 2003;18:555–60.
3. Zun Z, et al. Assessment of myocardial blood flow (MBF) in humans using arterial spin labeling (ASL): feasibility and noise analysis. Magn Reson Med 2009;62:975–983.
4. Capron T, et al. Myocardial perfusion assessment in humans using steady-pulsed arterial spin labeling. Magn. Reson. Med. 2015;74:990–998.
5. Kober F, et al. Myocardial arterial spin labeling. J Cardiovasc. Magn. Reson. 2016;18:22.
6. Belle V, et al. In vivo quantitative mapping of cardiac perfusion in rats using a noninvasive MR spin-labeling method. J Magn Reson Imaging 1998;8:1240–5.
7. Kober F, et al. High-resolution myocardial perfusion mapping in small animals in vivo by spin-labeling gradient-echo imaging. Magn Reson Med 2004;51:62–67.

S01 Scientific Session

13:00–14:30 *Room 2 - Van Weelde Zaal*

Diffusion Imaging

S01.02

Separating intra- and extra-axonal susceptibility effects using a Diffusion-Filtered Asymmetric Spin Echo (D-FASE) sequence

E. Kleban[1], C. M. W. Tax[1], U. S. Rudrapatna[1], D. K. Jones[1], R. Bowtell[2]
[1]*Cardiff University, Cardiff University Brain Research Imaging Centre (CUBRIC), School of Psychology, Cardiff, UNITED KINGDOM,* [2]*University of Nottingham, Sir Peter Mansfield Imaging Centre (SPMIC), School of Physics & Astronomy, Nottingham, UNITED KINGDOM*

Purpose/Introduction: The quantification of brain white matter properties is a key area of application of MRI, with much effort focused on developing techniques to quantify tissue microstructure. Diffusion MRI probes the white matter microstructure by characterising the sensitivity of Brownian motion of water molecules to anisotropic structures, susceptibility-based techniques probe the tissue microstructure by observing interaction between the tissue and the magnetic field[1,2].

Here, we bring together these two complementary approaches using a novel Diffusion-Filtered Asymmetric Spin Echo (D-FASE) technique. Using D-FASE we can separately assess the evolution of the intra- and extra-axonal signals under the action of magnetic susceptibility effects arising from the myelin sheath.

Subjects and Methods: A diffusion-weighted spin echo (SE) sequence with EPI readout is a standard technique to probe white matter anisotropy. Differences in diffusive properties between intra- and extra-axonal water allow us to suppress the extra-axonal water signal by applying strong diffusion gradients perpendicular to the main fibre axis[3] (= *diffusion filter DF*). The SE sequence with EPI readout delayed by time Δt (= *asymmetric (A)SE*) is sensitive to magnetic field inhomogeneities.

The D-FASE sequence was produced by combining an ASE EPI acquisition with diffusion gradients yielding images that are sensitive to dephasing due to both diffusion and microscopic susceptibility effects. Data were collected from 4 healthy subjects on a Siemens Connectom 3T system[4,5] using 6 acquisition delay times Δt = [0, 10, 20, 30, 40, 50]ms and 4 *b*-values = [0, 1200, 2400, 4800] s/mm^2.

The data were corrected for misalignments due to subject motion and eddy currents[6,7] and Gibbs ringing[8]. Macroscopic R_2^* as a function of *b*-values was calculated for the corpus callosum (CC) and corticospinal (CST) WM tracts. 2-compartment model was used to fit the D-FASE signal as a function of Δt and *b*.

Results: D-FASE signal is a 2D function, **F1**. In all subjects we observed a decrease of the macroscopic R_2^* with increasing *b* in CC, but no clear change in CST, **F2**. The microscopic transverse relaxation rates of the intra-/extra-axonal signals overlap, but their diffusive properties are clearly separable. Thus, with added diffusion filtering ASE signals can be assigned to the intra- and extra-axonal compartments unambiguously, **F3**.

Discussion/Conclusion: The new approach is independently sensitive to diffusion and susceptibility effects in intra- and extra-axonal water signals. The source of the observed difference in susceptibility effects is the myelin sheath. Thus, this method is uniquely sensitive to WM structural anisotropy and to myelin sheath interaction with B_0 and can help to characterise WM microstructure.

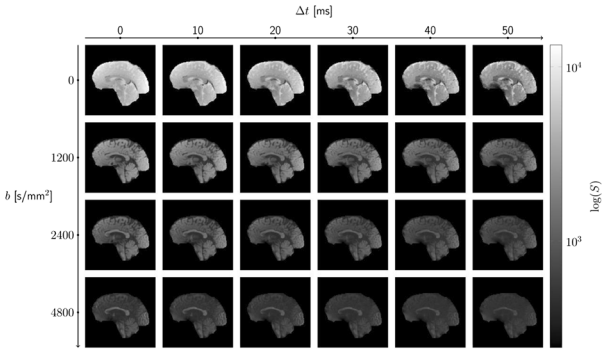

F1: The diffusion-filtered asymmetric spin-echo (D-FASE) signal (here, on a log-scale) was acquired by simultaneously varying the strength of the diffusion filtering, the b-values (rows), and by delaying the acquisition by the time Δt (columns).

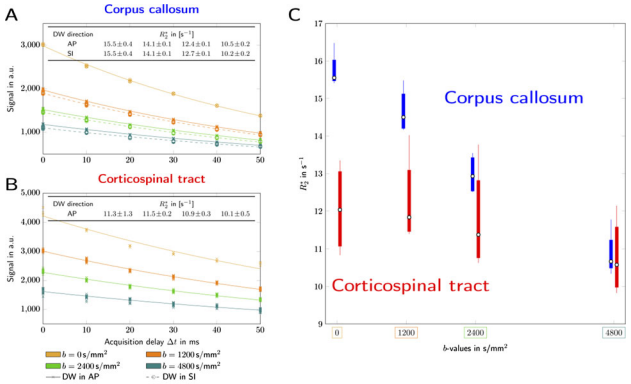

F2: At each DF level b, the macroscopic R2* was estimated from the D-FASE signal in the corpus callosum (A) and CST (B). The distribution of the mean macroscopic R2* as a function of b for each ROI are shown in C.

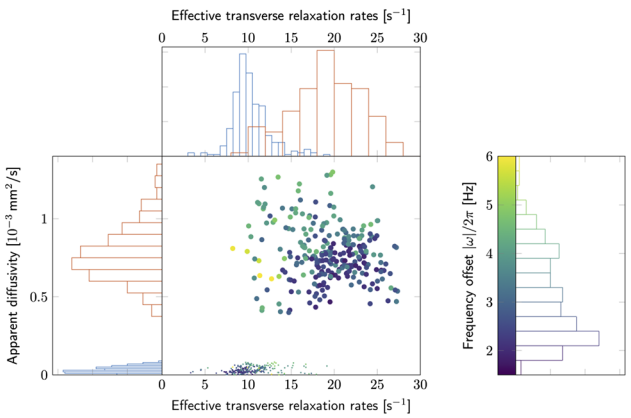

F3: The microscopic diffusivity and susceptibility properties of the intra-/extra-axonal water signals (blue/red histograms; small/large symbols) were extracted by analysing D-FASE signal from the CC with a 2-compartment model of parameters Δt and b.

References:
[1]Wharton et al. PNAS,2012.
[2]Sati et al. NI, 2013.
[3]Assaf et al. MRM, 2000.
[4]Setsompop et al. NI, 2013.
[5]Jones et al. NI, 2018.
[6]Stables et al. MRM, 1998.

[7]Nilsson et al. PLoS1, 2015.
[8]Klein et al. T-MI, 2010.

S01.03

On fiber orientation distribution peak selection for diffusion MRI fiber tractography

A. Zhylka[1], A. Leemans[2], J. Pluim[1], A. De Luca[2]
[1]*Eindhoven University of Technology, Biomedical Engineering, Eindhoven, NETHERLANDS,* [2]*University Medical Center Utrecht, Image Sciences Institute, Utrecht, NETHERLANDS*

Purpose/Introduction: With diffusion MRI (dMRI) based fiber tractography (FT), brain white matter fiber pathways can be reconstructed in vivo and noninvasively[2]. Recent work has shown that reliable and consistent computation of these fiber trajectories is challenging as there are various algorithms with different user-defined settings[4]. In particular, it is well known that probabilistic FT approaches can produce more false positive reconstructions than the deterministic ones. On the other hand, while deterministic FT approaches can sample dominant peak orientations from the fiber orientation distribution (FOD) in a robust way, they typically produce more false negative pathways (Fig. 1).
We developed a novel way to reconstruct pathways by considering a peak selection strategy that also integrates the orientations with a higher angular deviation. By incorporating prior knowledge of the location of seed and target regions of interest (ROI) while maintaining a deterministic view of FT, we can provide a more balanced tradeoff between true and false positive reconstructions.

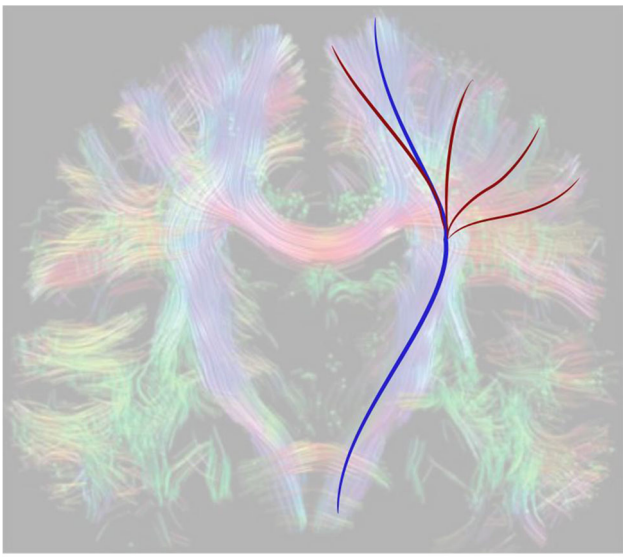

Current FT methods only use a part of the FOD peak information, reconstructing a subset of the pathways (blue). We aim to use the neglected information, to reconstruct the missing branches (red). Background image is from [5] (with permission).

Subjects and Methods: The peak selection strategy introduced in this work is implemented for the constrained spherical deconvolution (CSD) based FT method[1] and consists of the following steps. Firstly, conventional CSD FT is performed (with FOD threshold of 0.1 and angular deviation threshold of 45°). Secondly, every point of each pathway that has more than one FOD peak is considered as a new seed, but now with the other peak orientations as the initial directions for reconstructing new pathways. This procedure can be performed recursively with predefined convergence criteria. Finally, the resulting pathways are selected based on prior knowledge of the anatomical location of the ROI in combination with the topology of the fiber tracts.
The dMRI data used in this work were acquired with a 3T MRI system: 60 volumes at b = 3000 s/mm^2, 6 volumes at b = 0 s/mm^2; 2.5 mm isotropic voxel size. Visualizations are performed with *ExploreDTI*[3].
Results: In Fig. 2a, a conventional pathway is reconstructed with the seed point defined in the spine area (only one seed point is taken). Figure 2b shows the "unconstrained" result with the additional seed definition according to proposed strategy. Figure 2c shows the final result with target ROI selected. Fig. 3 shows the results in a more realistic scenario with more seeds.

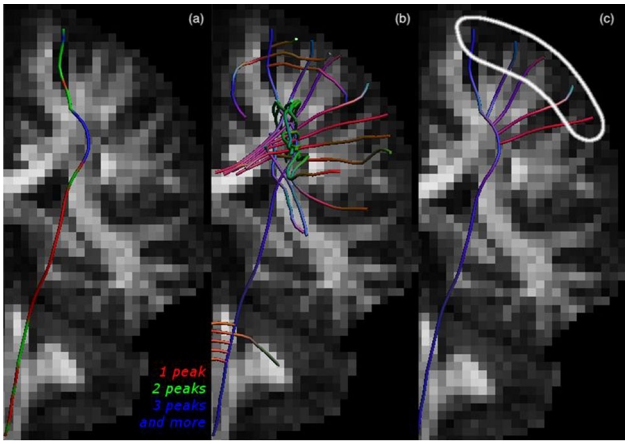

(a) Example pathway with color-encoding according to number of fiber peaks along its trajectory. (b) pathways crossing the original pathway in (a). (c) Final result showing the additional branches (see white target ROI).

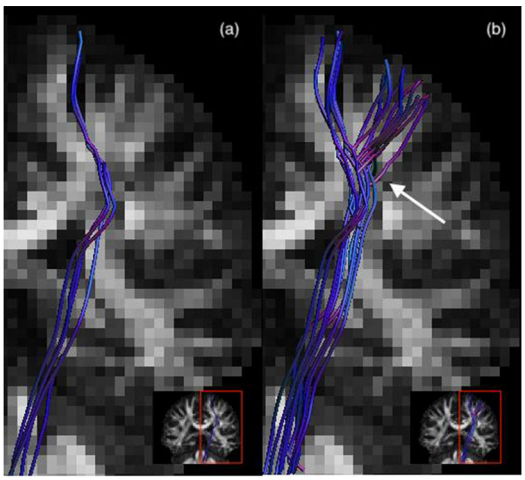

(a) Conventional FT result (similar as Fig. 2(a), but more seed points). (b) The final result after including our proposed peak selection strategy. Notice the increase of true positives (lateral tract branching as indicated by the white arrow).

Discussion/Conclusion: We developed a novel way to perform FT by considering a peak selection strategy that also integrates the orientations with a higher angular deviation and that incorporates prior knowledge of fiber tract anatomy. In doing so, we can obtain a more complete representation of brain pathways.
References:

1. Jeurissen B., et al. *Hum Brain Mapp* 2011;32(3):461-79.
2. Jeurissen B., et al. *NMR Biomed* 2019;32(4):e3785.
3. Leemans A., et al. *ISMRM* 2009;3537.
4. Maier-Hein K., et al. *Nat Commum* 2017;8(1):1349.
5. Tournier J.-D., et al. *MRM*2011;65(6):1532-56.

S01.04

Influence of diffusion pipeline on data analysis: UK Biobank example for age-diffusion dependences

I. I. Maximov, D. Alnaes, L. T. Westlye
University of Oslo, Oslo, NORWAY

Purpose/Introduction: Large brain data project[1] presents a great opportunity to understand different aspects of brain organisation. Combining obtained information from UK Biobank data into a common statistical framework benefits from universally adapted post-processing pipelines for harmonised data quality assessment and manipulation. Various post-processing steps have been suggested for diffusion MRI in order to correct common sources of noise[2], Gibbs ringing correction[3], susceptibility distortion correction[4], motion correction[4], correction of physiological noise and outliers[5], and the influence of eddy currents to the geometrical distortions of the images[6]. Several minimal post-processing steps have been recommended in order to prepare MRI data[7,8]. In order to assess how a chosen pipeline influences across-subject analysis we compared estimated age-curves of the diffusion metrics between pipelines using tract-based spatial statistic[9] and simple linear regression models using UK Biobank data.

Subjects and Methods: We used 218 subjects[1]. A general pipeline used in the present work is shown in Fig. 1 and includes following steps (S7): noise correction[2], Gibbs-ringing correction[3], field mapping and eddy-current, motion and susceptibility distortion corrections[4], bias field corrections[10], spatial data smoothing, and diffusion metric estimations[11]. In contrast, we used original UKB data processed with only field maps and corrected eddy-current, head motion artefacts and susceptibility distortions. Statistical analysis between S7 and UKB pipelines was performed using TBSS[9]. Linear regression analysis was implemented using the in-house Matlab scripts.

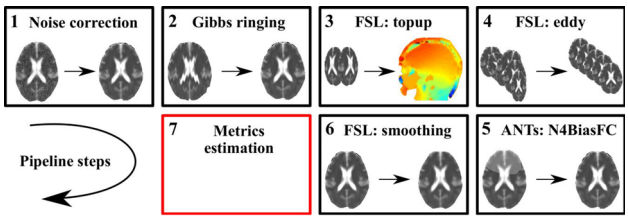

Figure 1. Scheme of diffusion pipeline.

Results: In Figure 2 we presented the estimated age-curves for a few diffusion metrics. Figure 3 shows the differences in the results obtained from general linear model testing linear age associations across the skeleton.

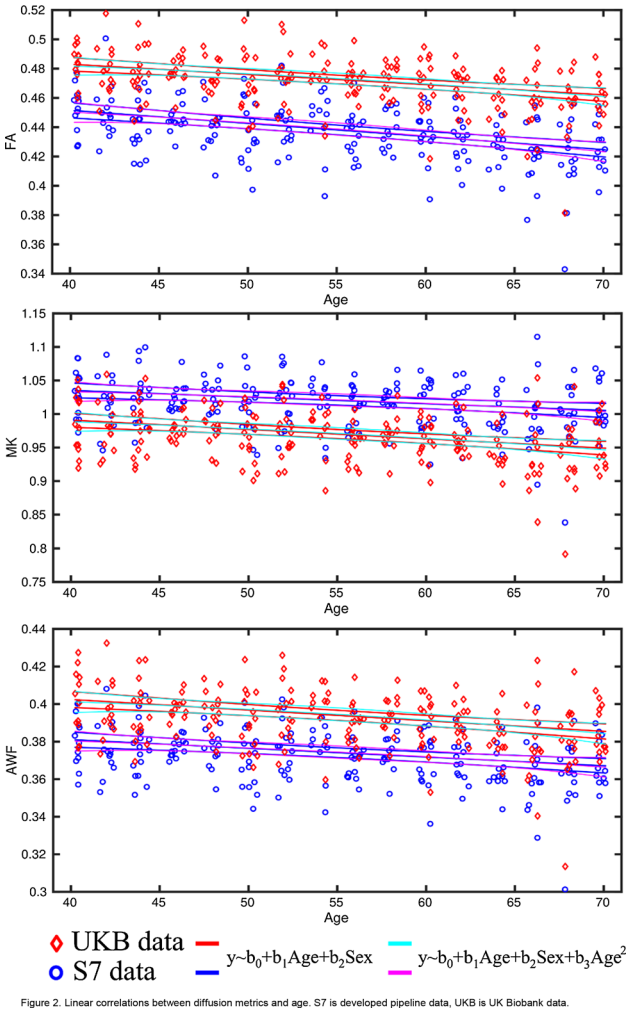

Figure 2. Linear correlations between diffusion metrics and age. S7 is developed pipeline data, UKB is UK Biobank data.

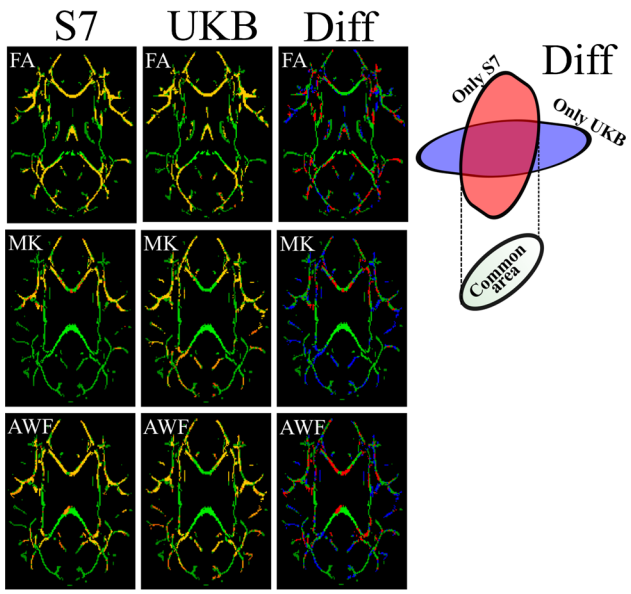

Figure 3. Results of linear age correlations between diffusion metrics and age across the TBSS produced skeleton. Column "Diff" emphasises the difference between results obtained for S7 and UKB pipelines.

Discussion/Conclusion: In conclusion, our analysis demonstrated that diffusion metric estimations benefit from the sequential advanced post-processing steps and present a general approach in diffusion data harmonisation applicable for different diffusion MRI studies. Based on these results we would like to encourage all neuroimaging scientists to follow up an idea of harmonisation of the diffusion data processing steps in order to avoid spurious or erroneous findings in the big datasets, in particular, for the complex diffusion models with many diffusion shells.

References:

[1]Miller et al., 2016. Nature Neurosci 19, 1523
[2]Veraart et al., 2016. NI 142, 394
[3]Kellner et al., 2016. MRM 76, 1574
[4]Andersson and Sotiropoulos, 2016. NI125, 1063
[5]Maximov et al., 2015. J Neuroim 25, 883
[6]Taylor et al., 2016. HBM 37, 4405
[7]Alfaro-Almagro et al., 2018. NI 166, 400
[8]Ades-Aron et al., 2018. NI 183, 532
[9]Smith et al., 2006. NI 31, 1487
[10]Tustison et al., 2010. IEEE TMI 29, 1310
[11]Veraart et al., 2013. NI 81, 335
[12]Roalf et al., 2016. NI 125, 903

S01.05

Generalized Stejskal-Tanner Equation. Practical meaning for MRI

A. Krzyżak[1], R. Obuchowicz[2]
[1]*AGH University of Science and Technology, Kraków, POLAND,*
[2]*Collegium Medicum of Jagiellonian University, Kraków, POLAND*

Purpose/Introduction: The problem of signal analysis and later MR imaging in the presence of heterogeneous magnetic field gradients is almost as old as NMR and MRI. This is particularly evident in the case of imaging using a natural contrast like diffusion and derivative techniques such as fiber-tracking. The presentation will focus on the significance of the recently derived Generalized Stejskal-Tanner (GS-T) equation [1] for the imaging in non-uniform magnetic field gradients. In other words, what we have in reality. A precursory solution assuming the spatiality of the distribution of magnetic field gradients was proposed by Bammer [2]. In that paper, the matrix *L(r)* which is a function of the position vector *r*, was called the "gradient coil tensor" and was introduced without derivation. The *L(r)* could be calculated on the basis of the specification provided by the manufacturer or indicated experimentally using formula (Fig. 1). In our approach, tensor *L(r)* is characteristic of the MRI sequence and is the gradient of the pattern function *p(r)* describing the space in which the gradient G is constant (see Fig. 2). It can be also regarded as the Jacobian matrix for the coordinates change from Cartesian to those curvilinear given by *p(r)*.

Figure 1. The formula proposed by Bammer [2] for calculation of tensor coil L(r):

$$\hat{L}(\vec{r}) = \frac{\frac{\partial\left(B_z(\vec{r})\right)_i}{\partial r_j}}{G_i}$$

B_z – magnetic field

G_i – gradient of magnetic field

r - position vector

Figure 2. Tensor $\hat{L}(\vec{r})$ is characteristic of the MRI sequence and is the gradient of the pattern function $\vec{p}(\vec{r})$ describing the space in which the gradient G is constant. It can be also regarded as the Jacobian matrix for the coordinates change from Cartesian to those curvilinear given by $\vec{p}(\vec{r})$.

$$\nabla \circ \vec{p}(\vec{r}) = \begin{bmatrix} \frac{\partial p_x}{\partial x} & \frac{\partial p_x}{\partial y} & \frac{\partial p_x}{\partial z} \\ \frac{\partial p_y}{\partial x} & \frac{\partial p_y}{\partial y} & \frac{\partial p_y}{\partial z} \\ \frac{\partial p_z}{\partial x} & \frac{\partial p_z}{\partial y} & \frac{\partial p_z}{\partial z} \end{bmatrix} \stackrel{\text{def}}{=} \hat{L}(\vec{r})$$

Figure 3. The Generalized Stejskal-Tanner equation [1]for non-homogeneous magnetic field gradients.

$$ln\left(\frac{A(b)}{A(0)}\right) = -\hat{b}(\vec{r}) : \hat{D}$$

A – amplitude of the signal with and without diffusion gradient.

b(r) – spatial distribution of the b-matrix

D – diffusion tensor

Subjects and Methods: Another embodiment is a BSD-DTI method proposed in 2008 [3], where spatial components of the b-matrix are determined by means of an anisotropic phantom with a well-defined structure, serving as diffusion tensor norm. The correction using the coil tensor was adapted by D. Malyarenko et al. [4], and E. Tan et al. [5]. In turn, the use of the BSD-DTI method was analyzed in several publications [6,7]. However, the above works using the S-T equation [8] were in contradiction with its main assumption about the constancy of gradients in space. This contradiction was removed by deriving the equation (Fig. 3), where the classic S-T equation is the specific solution of the GS-T equation for constant gradients.

Results: In phantom and human brain experiments using SE-EPI sequences on 1.5T and 3T systems, using BSD-DTI we determined the actual distributions of b-matrix and tensor L using the same sequences as for object research. The results before and after correction are shown in the Fig. 4.

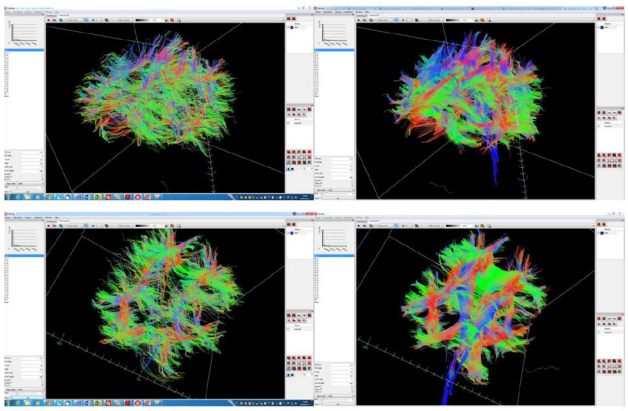

Figure 4. Example visualization of whole brain fiber tracts in coronal orientation registered with b=1000 s/mm2 and 6 directions of diffusion gradients. The calculation was performed using the same raw data and parameters for fiber tracking. The right image with BSD-DTI approach, the left image with standard approach.

Discussion/Conclusion: The generalized S-T equation shows the possibility of using the spatial (and thus consistent with reality) distribution of gradients in MRI. The use of techniques allowing the determination of the actual distribution of the matrix b (magnetic field gradients), in our case realized by means of the BSD-DTI method, allows for a significant improvement in the accuracy of determining the diffusion tensor components. What is visible is not only the improvement of the accuracy of the diffusion tensor components (a

lower standard deviation of the eigenvalues), but also a more accurate visualization of the tracts in fiber-tracking studies.

References: and **Acknowledgments**

1. Borkowski K, Krzyzak AT. J Magn Reson. 2018 Nov;296:23-28.
2. Bammer et al., Magn Reson Med, vol. 50, no. 3, pp. 560-569, Sep. 2003.
3. A. Krzyzak, Polish patent application no. P.385276, 26-May-2008 (granted patents in US, JP and EU)
4. D. I. Malyarenko and T. L. Chenevert. J. Magn. Reson. Imaging JMRI, vol. 40, no. 6, pp. 1487-1495, Dec. 2014.
5. ET. Tan, L. Marinelli, Z. W. Slavens, K. F. King, and C. J. Hardy. J. Magn. Reson. Imaging, vol. 38, no. 2, pp. 448-453, Nov. 2012
6. Krzyzak AT, OlejniczakZ, Magnetic Resonance Imaging 2015; 33:286-295
7. K. Klodowski and A. T. Krzyzak. Magn Reson Imaging, vol. 34, no. 4, pp. 404 409, May 2016.
8. Stejskal, The Journal of Chemical Physics, vol. 43, no. 10, pp. 3597-3603, Nov. 1965.

Acknowledgments

Dr. B. Figura for contribution to the development of mathematical formalism of the Generalized Stejskal -Tanner equation.

The work was partly financed by the National Centre of Research and Development, contract no. STRATEGMED2/265761 /10/NCBR/ 2015.

S01.06

Microscopic Diffusion Anisotropy Imaging As Potential Biomarker For The Pathogenesis Of Multiple Sclerosis Lesions

E. Martinez-Heras[1], M. Andorrà[1], E. Solana[1], J. Radua[2], E. López-Soley[1], C. Montejo[1], I. Pulido-Valdeolivas[1], A. Saiz[1], S. Llufriu[1]

[1]Hospital Clinic Barcelona, IDIBAPS and Universitat de Barcelona, Center of Neuroimmunology, Laboratory of Advanced Imaging in Neuroimmunological Diseases, Barcelona, SPAIN, [2]IDIBAPS and CIBERSAM, Department of Clinical Neuroscience, Karolinska Institutet, Stockholm, Sweden; Department of Psychosis Studies, Institute of Psychiatry, Psychology and Neuroscience, King's College London, London, UK, Barcelona, SPAIN

Purpose/Introduction: Tissue abnormalities in multiple sclerosis (MS) have been extensively investigated using fractional anisotropy (FA) and other diffusion tensor imaging indices as a measure of white matter (WM) integrity. Unfortunately, these indices are difficult to interpret and have limited ability to estimate changes in the underlying microanatomy due to confounding factors derived from fiber crossing or orientation dispersion [1]. Recently, multi-shell imaging methods have been proposed to provide a better characterization of microstructural properties of the brain [2]. The multi-compartment spherical mean technique has been specifically proposed to be more accurate detect changes in the underlying fiber microanatomy due to the lack of aforementioned confounding factors [3]. We aimed to assess whether an index derived from this technique, microscopic fractional anisotropy (μFA), discriminates more accurately between MS lesions and normal appearing WM (NAWM) than standard FA.

Subjects and Methods: A 3D-T1w, 3D FLAIR and multi-shell diffusion imaging (3 shells and 180 directions) scans were acquired on 3T Siemens Prisma scanner in 8 MS patients (33 ± 8 years, 4 male and 4 female). The tensor model approach and the microscopic diffusion tensor were computed using standard preprocessing techniques [4] [5]. Whole-brain tracking was performed with multi-tissue fiber orientation distribution function tractography with anatomical priors to improve the reliability of the reconstruction [6] [7]. FA and μFA values were extracted from WM tractography and lesion mask from each MS patient (Fig. 1). Finally, receiver operating characteristic (ROC) curves were generated to measure the ability of FA and μFA to discriminate MS lesions from NAWM.

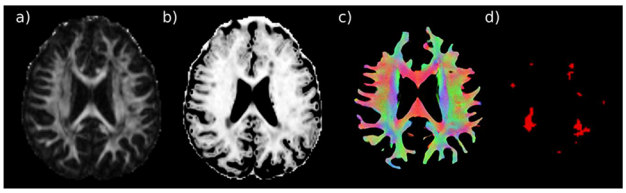

a) Fractional anisotropy, b) Microscopic fractional anisotropy, c) Whole-brain tracking and d) lesion mask

Results: Statistically significant differences ($p \leq 0.05$) between the areas under the ROC curve from FA and μFA were observed in all MS patients [8] (Fig. 2). Specifically, median value of the area under the curve was 0.63 for FA and 0.80 for μFA from all MS patients. The ROC analysis of μFA values demonstrated higher sensitivity and specificity at best Youden point, median values of 0.73 and 0.77 respectively, compared with FA indices, 0.55 and 0.72.

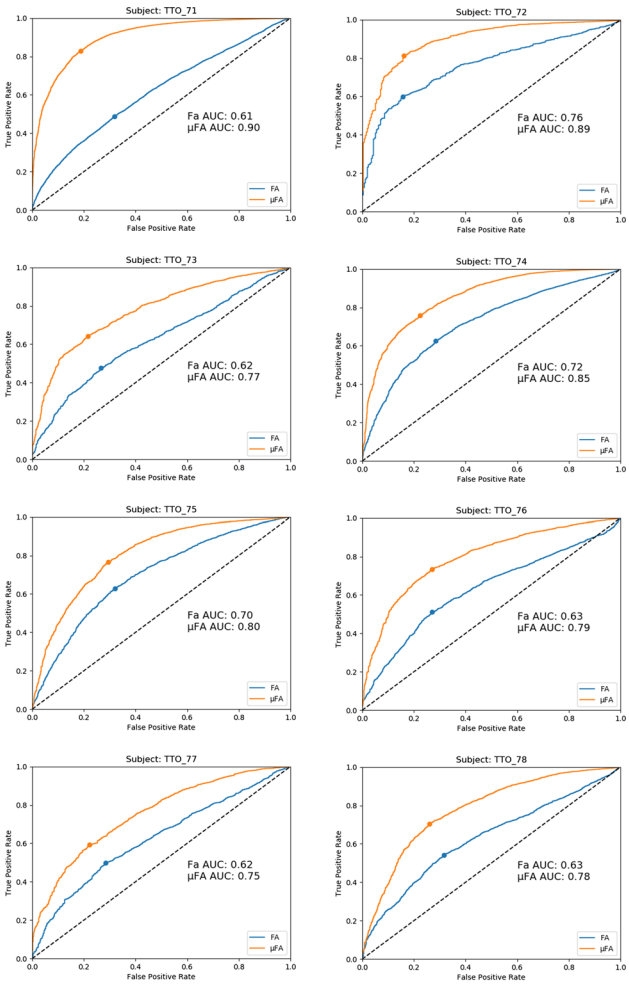

ROC curves and areas under the curves of each MS patient. The marker points indicated the best Youden's J statistic.

Discussion/Conclusion: μFA is substantially more sensitive and specific than standard FA to discriminate the presence of focal tissue damage. We suggest that microscopic diffusion index might be a more robust biomarker of microstructural abnormalities and open new insights to classify the different MS lesion types.

References
[1] Jones DK, Neuroimage 2013.
[2] Alexander DC, NMR Biomed 2019.
[3] Kaden E, Magn Reson Med 2016.
[4] Gelineau-Morel R, Hum Brain Mapp 2012.
[5] Tournier J-D, bioRxiv 2019.
[6] Jeurissen B, Neuroimage 2014.
[7] Martínez-Heras E, PLoS One 2015.
[8] Hanley JA, Radiology 1982.

S01.07

Watson vs. Bingham Distributions in NODDI Measures for 22q11.2 Copy Number Variants (CNVs) causing brain alterations

J. Villalon-Reina[1], T. Nir[1], N. Jahanshad[1], L. Kushan[2], C. E. Bearden[2], P. M. Thompson[1]
[1]*University of Southern California, Imaging Genetics Center, Los Angeles, UNITED STATES,* [2]*University of California Los Angeles, Semel Institute for Neuroscience and Human Behavior, Los Angeles, UNITED STATES*

Purpose/Introduction: Carriers of CNVs of the 22q11.2 locus show either increased risk for psychiatric diseases (chromosome 22q1.2 deletion - 22qDel) or protective phenotypes preventing psychiatric disease (22q11.2 duplication - 22qDup). 22qDel is linked to higher DTI fractional anisotropy (FA) in the white matter (WM)[1]. This counterintuitive finding poses challenges for interpreting developmental WM abnormalities. Neurite Orientation Dispersion and Density Imaging (NODDI), can differentiate between extracellular and Intracellular Volume Fractions (ICVF) and defines a neurite Orientation Dispersion Index (ODI). This may help understand the WM microstructure associated with 22q11 CNVs and aid in interpreting changes associated with their corresponding psychiatric outcomes. FA changes are rather nonspecific, but NODDI may disentangle contributions of ICVF and ODI to the abnormalities seen with DTI. Inittially, NODDI modeled ODI as a Watson distribution [2]. A newer NODDI version [3] uses a Bingham distribution, which may model bending and fanning fibers better. We compare NODDI-Watson and NODDI-Bingham in a sample of individuals with chromosome 22qDel and 22qDup and healthy controls (HC).
Subjects and Methods: Participants: 18 22q11Dup subjects (mean age: 21.4 ± 13.5 years), 13 HC (mean age: 21.6 ± 12.1 years), and 21 22q11Del subjects (mean age: 20.3 ± 8.7 years). Genetic tests were performed to confirm diagnosis. DMRI data were acquired (Siemens Prisma 3T, voxel size: 1.5 mm^3, TE: 0.08 ms, TR: 3.2 ms, 3 b = 200, 6 b = 500, 46 b = 1500, 46 b = 3000 s/mm^2, δ = 13.7 ms, Δ = 43.4 ms), and corrected for eddy and EPI distortions and normalized to the IIT WM atlas [4]. DTI, Watson and Bingham NODDI models were fit for all subjects. We performed linear regressions comparing FA, Watson-ICVF, Watson-ODI, Bingham-ICVF and Bingham-ODI across 17 IIT skeletonized WM regions between HC vs. 22q11Del and HC vs. 22q11Dup groups. We corrected for multiple comparisons.
Results: ODI did not show significant differences between the groups (HC vs 22qDel and 22qDup). Conversely, ICVF showed significant differences between groups for both models (NODDI-Watson and NODDI-Bingham), showing a high degree of correspondence. Regions with significant FA differences also showed significant ICVF changes in the same direction as FA in 22qDel and 22qDup. Significant ICVF differences were found in 10 out of 17 regions in 22qDel and 22qDup. See Figures:

Figure 1. Cohen's D effect sizes shown for each microstructural measure for 22q11.2 Deletion vs Healthy Control group comparisons. Stars indicate the significant regions (FDR q=0.05). Fmajor=forceps major, Fminor=forceps minor, Fornix, Lcing2=left cingulum hippocampal portion, Lcing=left cingulum, Lcst=left corticospinal tract, Lifo=left inferior-fronto-occipital fasciculus, Lilf=left inferior longitudinal fasciculus, Lslf=left superior longitudinal fasciculus, Lunc=left uncinate, Rcing2=right cingulum hippocampal portion, Rcing=right cingulum, Rcst=right corticospinal tract, Rifo=right inferior-fronto-occipital fasciculus, Rilf=right inferior longitudinal fasciculus, Rslf=right superior longitudinal fasciculus, Runc=right uncinate.

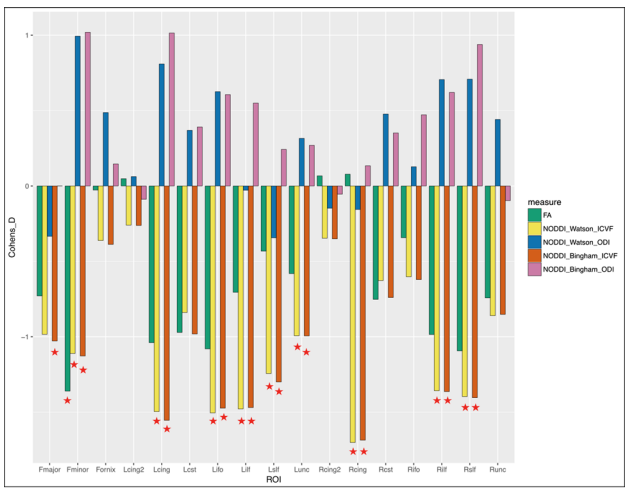

Figure 2. Cohen's D effect sizes shown for each microstructural measure for the 22q11.2 Duplication vs Healthy Control group comparison. Stars indicate the significant regions (FDR q=0.05).

Discussion/Conclusion: There does not seem to be an advantage of Bingham vs. Watson ODI modeling. ICVF seems to be more sensitive than ODI and FA. Changes seen with FA may be primarily caused by changes in ICVF rather than ODI. Opposite effects of ICVF and FA in the WM may depend on gene dosage (22qDel vs 22qDup).
References:
1. Jalbrzikowski, M., et al. Front Behav Neurosci, 8 (2014)
2. Zhang, H., et al. Neuroimage, 61.4 (2012): 1000-1016
3. Tariq, M., et al. NeuroImage, 133 (2016): 207-223
4. Zhang, S. et al. Neuroimage, 172 (2018): 40-50

S01.08

Comparison of clinically feasible DWI techniques for the microstructural characterization of neurodegenerative and demyelinating diseases. A simulation study

S. Oliviero[1], **C. Del Gratta**[2]
[1]*Università degli Studi di Chieti Pescara G. D'Annunzio, Neuroscience, Imaging, and Clinical Sciences; ITAB, Chieti, ITALY,*
[2]*Università degli Studi di Chieti Pescara G.D'Annunzio, Neuroscience, Imaging, and Clinical Sciences; ITAB, Chieti, ITALY*

Purpose/Introduction: The purpose of this study is to quantify the sensitivity and the specificity of ordinary clinically feasible DWI techniques to demyelination and axonal loss to identify a possible biomarker for demyelinating diseases

Subjects and Methods: A novel synthetic model of damaged WM has been developed, using three permeable compartments (intra-axonal, intra-myelin and extra-cellular space), each of them being characterized by its own wall permeability, diffusivity, and T2 relaxion [1-6]. The ability to reveal the presence of axonal loss and demyelination and to distinguish one from the other, has been tested by evaluating the changes in the metrics of three diffusion models (i.e. DTI, DKI, NODDI) with different degrees of damage induced in the synthetic tissue. The results have been then quantified in terms of sensitivity and specificity indices. The impact of the acquisition protocol on these performances has been also evaluated.

Results: All models are sensitive to both demyelination and axonal loss, but sensitivity and specificity of the metrics are very different and, in some cases, strongly depends on the acquisition protocol, the impact of which is found to be different than assumed in the literature. In any case, NODDI-derived metrics related to the intra-axonal volume fraction (over the whole voxel)-fia-and isotropic volume fraction-fiso-show the best performances in terms of sensitivity with respect to both demyelination and axonal loss, especially when the optimized acquisition protocols are used [Figs. 1, 2, Table 1].

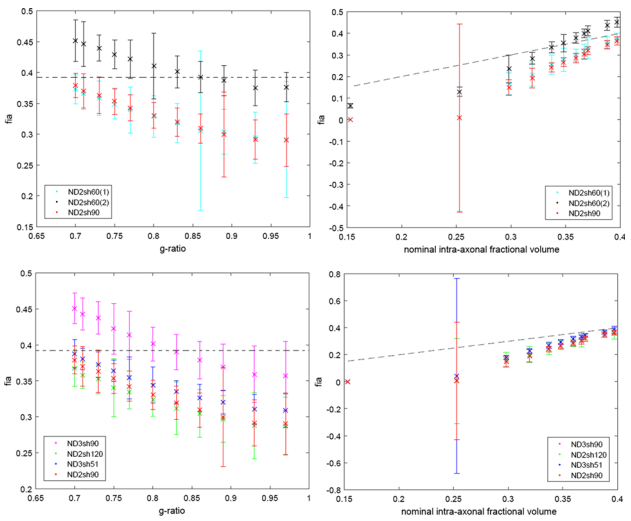

Changes in fia induced by reduced g-ratios (demyelination)-LEFT- and reduced intra-axonal vol. fractions (axonal loss) -RIGHT,for various acquisition protocols(Tab.1),considering Rician noise with SNR=20.Dotted lines mark the expected values of fia.

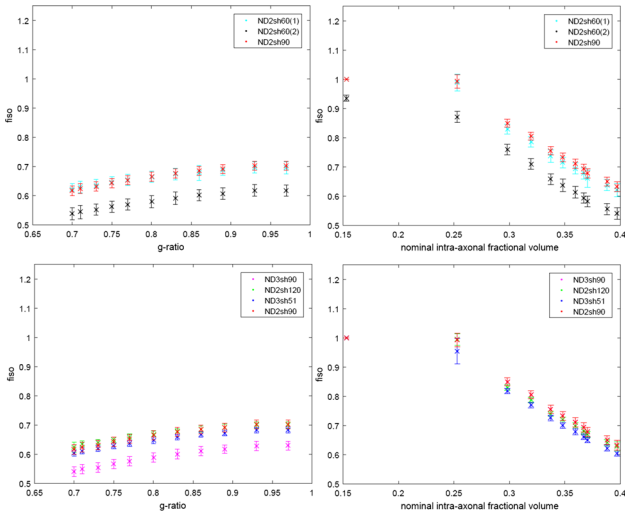

Changes in fiso induced by reduced g-ratios (demyelination) - LEFT- and reduced intra-axonal vol. fractions (axonal loss) - RIGHT, for various acquisition protocols (Tab.1), considering Rician noise with SNR=20.

	N dir.	b-value (s/(mm^2))	G (T/m)	Δ (s)	δ (s)	TE (s)
NODDI3sh51	6 / 15 / 30	300.2 / 712.9 / 1997.8	0.0207 / 0.0319 / 0.0534	0.0387	0.0175	0.0780
NODDI2sh60 (1)	30 / 30	1000 / 2000	0.0378 / 0.0534	0.0387	0.0175	0.0780
NODDI2sh60 (2)	30 / 30	711 / 2855	0.0318 / 0.0638	0.0387	0.0175	0.0780
NODDI2sh90	30 / 60	711 / 2855	0.0318 / 0.0638	0.0387	0.0175	0.0780
NODDI2sh120	60 / 60	711 / 2855	0.0318 / 0.0638	0.0387	0.0175	0.0780
NODDI3sh90	30 / 30 / 30	1000 / 2000 / 2855	0.0378 / 0.0534 / 0.0638	0.0387	0.0175	0.0780

NODDI Acquisition Protocols

Simulation results also confirm the recent experimental observations demonstrating that NODDI-derived fia parameter provides the unique opportunity to directly estimate with a good accuracy, the true intra-axonal volume fraction by using a non-invasive and clinically feasible DWI technique.

Discussion/Conclusion: It is indeed possible to extract information on brain microstructure by using a non-invasive imaging method, but it is not possible to distinguish between demyelination and early axonal loss (if they are both present in the tissue) with ordinary clinical acquisition protocols (magnetic field gradient strengths obtainable with a standard 3T scanner and acquisition times lower than 30 min). NODDI-derived intra-axonal fractional volume is the best candidate to become a potential biomarker in demyelinating diseases. Special care is recommended in selecting the acquisition protocol: it has a non-negligible impact on the sensitivity and specificity of the metrics.

References:

1. Hall et al. 2009. https://doi.org/10.1109/tmi.2009.2015756.
2. Aboitiz et al. 1992. https://doi.org/10.1016/0006-8993(92)90178-C.
3. Stanisz et al. 2006. https://doi.org/10.1002/mrm.1910370115.
4. Trevor et al. 2006. https://doi.org/10.1002/mrm.20945.
5. Menon et al. 1991. https://doi.org/10.1002/mrm.1910200205.
6. Menon et al. 1992. https://doi.org/10.1002/mrm.1910280208.

S01.09

Optimized b-value distributions for triexponential liver IVIM

A. Riexinger, F. Laun
University Hospital Erlangen, Friedrich-Alexander-University (FAU), Radiology, Erlangen, GERMANY

Purpose/Introduction: Recent paper[1,2] used a triexponential intravoxel incoherent motion (IVIM) model to address the strong signal decay at small b-values ($b < 5$ s/mm^2). Since a fit of the triexponential signal decay is challenging, the choice of b-values is essential for reducing fit uncertainties and measuring time. The purpose of this study was to optimize six different sets of b-values, depending on the available acquisition time for triexponential IVIM liver imaging.

Subjects and Methods: Six b-value distributions with a fixed number of b-values (6, 11, 16, 25, 45, 68) were optimized assuming a signal-to-noise ratio (SNR) of 30. To reduce computation time, only a certain number of b-values (minimal value: step size: maximum value; 0:0.1:2; 2.5:0.5:5; 6:1:10; 15:5:100; 150:50:800) in s/mm^2 were considered. To further speed up the computation not all considered b-values were used for single optimization steps. The range of tested b-values is defined by the total fit error of the last two optimization iterations. If the total fit error decreased, all considered b-values between the adjacent b-values of the current distribution were tested, otherwise the full set of considered b-values was tested.

Based on the results of Riexinger et al.[2] we varied the reported IVIM parameter to generate 27 different sets of IVIM parameter (see Fig. 1). For each parameter set a signal was generated using the triexponential IVIM model. Beginning with an distribution evenly spaced between 0 and 800 s/mm^2 each b-value was optimized separately. The selected b-value was stepwise replaced by each of the tested b-values and fitted to N = 20, 40, 100, 200 Gaussian noise added signals for each set of IVIM parameter. The tested b-value with the lowest overall fit-error was considered as optimal b-value and replaced the old one. After each b-value was optimized once, the resulting b-value distribution was saved and optimized again (80 iterations in total). More detailed information is illustrated in Fig. 1.

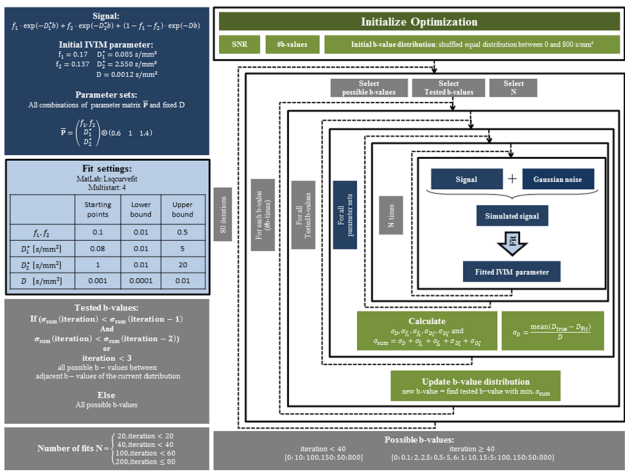

Optimization scheme

Afterwards, the resulted optimized b-value distributions were compared to distributions reported in literature[1,3] by fitting simulated signals based on the 27 IVIM parameter sets.

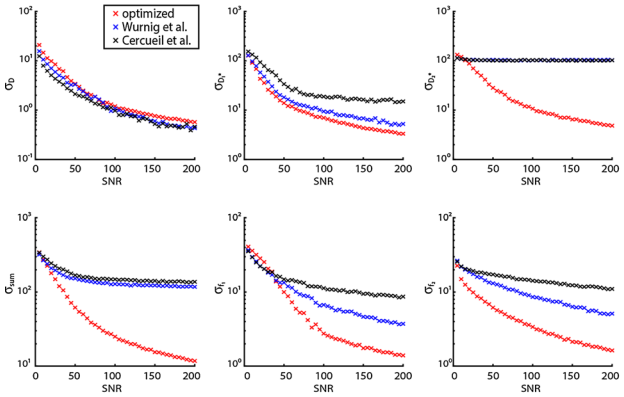

Relativ fit error of IVIM parameter as a function of SNR. Comparison of sigma using the optimized b-value distribution for 16 b-values (0, 0.1, 0.1, 0.9, 1.5, 2, 2, 7, 8, 10, 35, 40, 65, 90, 100, 700) with distributions reported in literature.

Results: The performed optimization resulted in b-value distributions that can be applied depending on the available time. All distributions followed the same scheme, independent of the number of b-values. There are only few high ($b > 600$ s/mm^2) and medium-sized ($50 < b < 600$ s/mm^2) b-values. The most frequent ones are in the range of low ($1 < b < 50$ s/mm^2) and very low ($b < 1$ s/mm^2) b-values.

Discussion/Conclusion: In triexponential IVIM measurements only few b-values should be chosen in the range of $b > 50$ s/mm^2 to determine the tissue diffusivity. The largest amount of the acquisition time should be invested in low and very low b-values to detect the strong initial signal decay.

References:

Cercueil J.P., EurRadiol, 2015, p.10.
Riexinger AJ, jMRI, 2019, p.10.
Wurnig, MagnResonMed, 2015, p.9.

S02 Scientific Session

13:00–14:30 *Room 3 - Ruys & van Rijckevorsel Zaal*

MR Signals & Artefacts

S02.02

Simulation frame work for predicting flip angles in echo-train sequences

M. Blaimer[1], F. Breuer[1], D. Weber[1], S. Malik[2], V. Herold[3]
[1]*Fraunhofer Institute for Integrated Circuits (IIS), Magnetic Resonance and X-Ray Imaging, Würzburg, GERMANY,* [2]*King's College, Biomedical Engineering Department, London, UNITED KINGDOM,* [3]*University of Würzburg, Experimental Physics 5, Würzburg, GERMANY*

Purpose/Introduction: Fast spin echo (FSE) sequences are very robust and provide images with clinically relevant contrasts and high signal-to-noise ratio (SNR). However, especially at higher field strength their application is often limited by the high specific-absorption-rate (SAR) due to the 180° radio-frequency (RF) pulses. We present a simulation frame work for automatically identifying lower flip angles for SAR reduced FSE imaging with minimized losses in the desired image contrast. Compared to previous approaches such as transitions between pseudo steady states (TRAPS) (1) our framework considers multiple tissue types and the sampling properties of a FSE sequence. Initial results for SAR reduced FSE exams are presented.
Subjects and Methods: The method aims to find a SAR-reduced FSE image with minimum deviation from a target image (e.g. 100% SAR). To that end, FSE images are simulated using the extended phase graph approach (2) and information from a digital brain phantom (http://brainweb.bic.mni.mcgill.ca/brainweb/) (3). A constrained optimization algorithm is used to identify optimal flip angles by minimizing the root-mean-squared-error (RMSE) between reconstructed (i.e. SAR-reduced) and target image (Fig. 1). The relative SAR level is the only constraint and flip angles are bound between 15° and 180°. Simulation results were validated by in vivo experiments on a healthy volunteer using a 3T clinical MRI system. Sequence parameters were: echo train length = 17, echo spacing = 10 ms, TE = 90 ms, TR = 5000 ms. The TE of the SAR reduced image was prolonged to TE = 120 ms.

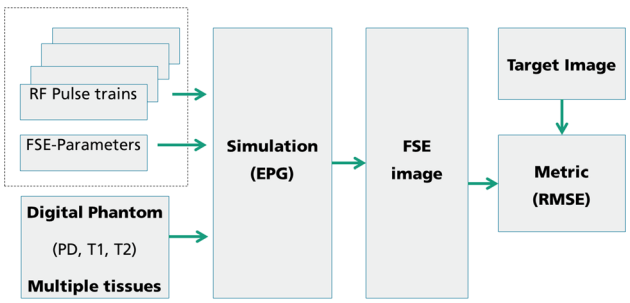

Fig. 1: Schematic of simulation framework for finding flip angles in SAR reduced FSE imaging

Results: Figure 2 shows predicted flip angles for an exemplary test case with 70% SAR reduction (Fig. 2, bottom). As expected, the shape of the flip angle train exhibits similarities to TRAPS. The contrast of the SAR reduced image (top row, middle) is very close to that of the full SAR image (top row, left).

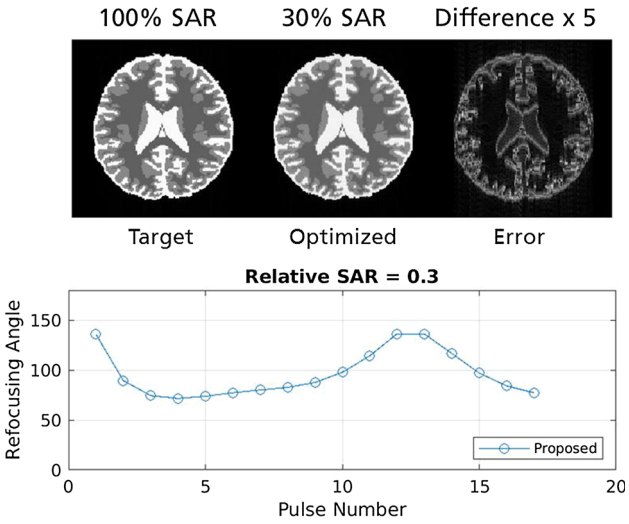

Fig. 2: Predicted flip angles for an exemplary test case with 70% SAR reduction

Figure 3 shows measured images with 100% SAR and 30% SAR using predicted flip angles.

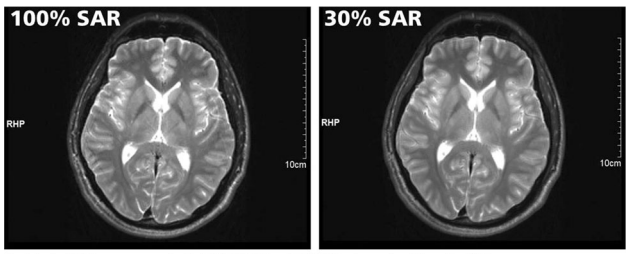

Fig. 3: In vivo FSE images measured with 100% SAR (left) and 30% SAR using predicted flip angles (right)

Discussion/Conclusion: The presented simulation frame work provides a flexible basis for predicting flip angles of an echo-train sequence. Multiple tissue types and sampling schemes are considered. For future applications, our simulations will be extended to include system imperfections (e.g. transmit inhomogeneities) or complex tissue models (e.g. magnetization transfer or chemical exchange) (4).
Acknowledgements: We thank Brian Hargreaves and Matthias Weigel for providing simulation code. Funding by EU (H2020-EU.1.2.1.-737180) and Bavarian Ministry of Economic Affairs, Regional Development and Energy.
References:
1. Hennig J, et al. Magn Reson Med. 2003; 49(3):527-35.
2. Weigel M. J Magn Reson Imaging. 2015;41(2):266-95.
3. Cocosco CA, et al. NeuroImage. 1997; 5(4), part 2/4: 425.
4. Malik SJ, et al. Magn Reson Med. 2018;80(2):767-779.

S02.03

In-vitro validation of clinically relevant PC MRI methods using the SYNC SPI method as a gold standard

M. Bruschewski, K. John, S. Grundmann
University of Rostock, Institute of Fluid Mechanics, Rostock, GERMANY

Purpose/Introduction: Phase-contrast (PC) MRI is a promising method for flow quantification in medical flows. For many cardiovascular diseases, the decision to undergo surgery is often based on the assessment with PC MRI. Since most clinical PC MRI techniques are based on frequency encoding, the encoding process is not instantaneous which can lead to motion-related errors known as misregistration and displacement. Incorrect estimation of either jet velocity or blood vessel area is a direct result of these errors [1]. A gold-standard PC-MRI method is proposed to assess the severity of the motion-related errors in clinically relevant PC-MRI methods.

Subjects and Methods: The proposed gold-standard PC MRI method was specifically developed for highly accurate velocity measurements for in vitro flow experiments [2]. The imaging technique is based on single-point imaging (SPI) with synchronized (SYNC) encoding. All spatial coordinates and velocity components are encoded simultaneously to reduce motion-related errors effectively. After a thorough validation of the imaging accuracy, the proposed SYNC SPI method was compared against a conventional PC MRI technique. First experiments were conducted in vitro on a 3T Siemens Magnetom Trio. The investigated flow system was a pipe with a concentric contraction to simulate stenosis. The setup of the flow system and a 2D slice of the measured 3D velocity field are shown in Fig. 1.

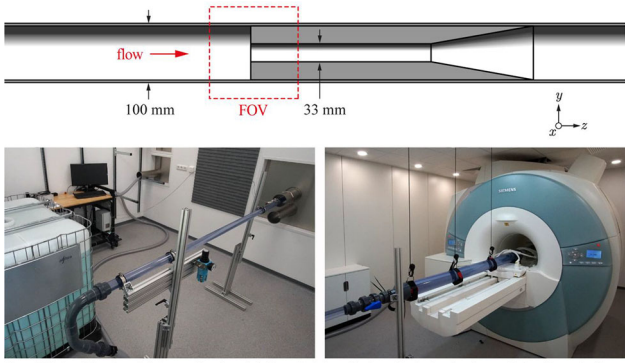

Figure 1: Setup of the stenosis test case. The stenosis test case includes a 3 m long pipe for flow development before the contraction.

Results: Compared to the results of the SYNC SPI method displayed in Fig. 2, the velocity field obtained from the conventional PC MRI method exhibits notable displacement errors in the geometry and the flow field. Figure 3 shows the deviation in the velocity data more clearly. It can be seen that the local error is up to 100% in the data of the conventional PC MRI method.

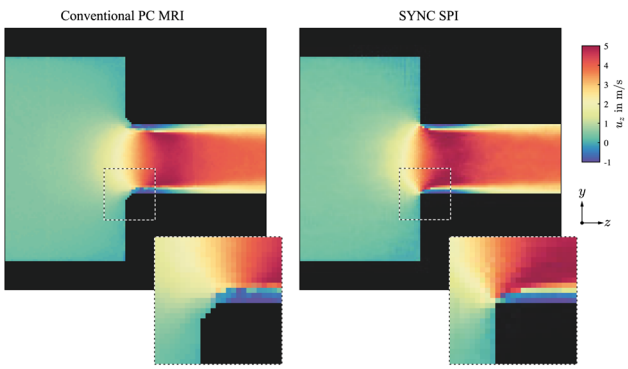

Figure 2: Axial velocity field in the stenosis test case measured with a conventional Cartesian PC MRI method and with SYNC SPI. A slice of the three-dimensional acquisition is shown.

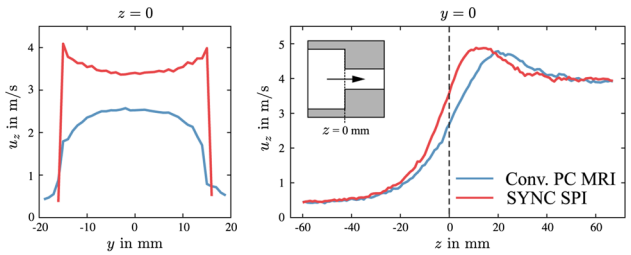

Figure 3: Quantitative comparison of the velocity fields shown in Fig. 2.

Discussion/Conclusion: Using the proposed SYNC MRI method as a gold standard, measurement errors in other PC MRI techniques can be directly assessed. Clinically relevant PC MRI techniques can be validated in vitro with this technique before being applied in vivo. It is planned to extend the study to various other commercial PC MRI techniques that are commonly used for the diagnosis of cardiovascular diseases.

References:

[1] O'Brien KR, Cowan BR, Jain M, Stewart RA, Kerr AJ, Young AA. MRI phase contrast velocity and flow errors in turbulent stenotic jets. J Magn Reson Imaging 2008; 28(1):210-218.

[2] Bruschewski, M, Kolkmannn, H, John, K, & Grundmann, S. Phase-contrast single-point imaging with synchronized encoding: a more reliable technique for in vitro flow quantification. Magn Reson Med; 2019; 81(5):2937-2946.

S02.04

Myelin water imaging using the transient phase of an inversion-recovery balanced steady-state-free-precession (IR-bSSFP) measurement

M. Blaimer[1], D. Zehe[2], J. Pfister[1], A. Bartsch[3], F. Breuer[1], P. Jakob[2]
[1]Fraunhofer Institute for Integrated Circuits (IIS), Magnetic Resonance and X-Ray Imaging, Würzburg, GERMANY, [2]University of Würzburg, Experimental Physics 5, Würzburg, GERMANY, [3]Heidelberg University Hospital, Department of Neuroradiology, Heidelberg, GERMANY

Purpose/Introduction: Myelin water imaging (MWI) has the potential for providing important information on myelin sheaths surrounding axons. However, MWI is challenging because the low myelin water signal is fast-relaxing and has to be separated from multiple water components. We demonstrate that myelin water maps can be generated from inversion-recovery (IR) balanced SSFP signals. To this end, a multi-component analysis of the transient phase (i.e. approach of steady-state) is performed and information on short relaxing components including myelin water is extracted from the resulting relaxation time spectra.

Subjects and Methods: IR-bSSFP has been shown to provide simultaneous quantitative information on T_1, T_2 and proton density using a mono-exponential model (1). However, the signal is more accurately described by a multi-exponential process due to multiple water components. It has been shown that relaxation time spectra can be computed allowing the identification of several tissue components in a voxel (2,3). Here, we use a multi-shot Cartesian IR-bSSFP sequence to acquire transient phase signals with high temporal resolution. The signal starts at $-S_0$ and approaches the steady-state S_{stst} with the time constant T_1* (Fig. 1, top, right) which depends on T_1, T_2 and the flip angle. Typically, 2000 echoes with TR = 4 ms are acquired per shot. The k-t-space is randomly sampled and an iterative PCA based algorithm (3) is used to generate 400 images per slice. T_1* spectra are computed for each voxel using a non-negative least

squares (NNLS) algorithm (Fig. 1, bottom, right). Myelin water can be identified as a peak around $T_{1,Myelin}$* = 150 ms. To generate myelin water maps, a spectral window is applied to filter the myelin signal followed by integration along the T_1* dimension (Fig. 1, bottom). For proof-of-concept, two healthy volunteers were examined on a clinical 3,0T scanner.

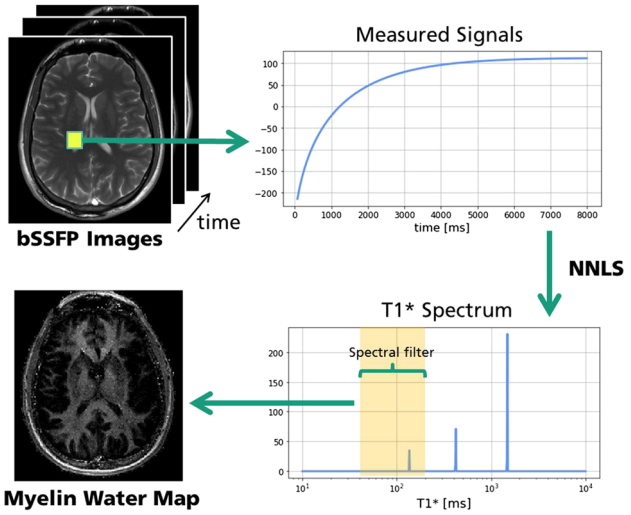

Figure 1: Schematic of myelin water mapping procedure

Results: Initial results illustrate short-relaxing components including myelin water in the brain and subcutaneous fat in the scalp (Fig. 2).

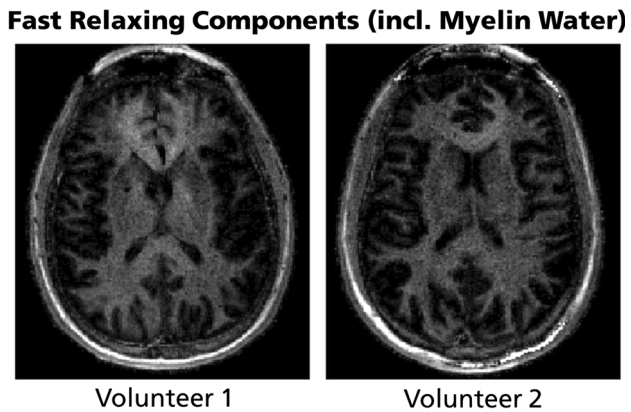

Figure 2: Myelin water maps from two healthy volunteers

Myelin water fraction (MWF) can be estimated without extra scans from the myelin signal, the initial signal $S_{0,total}$ of all water components and a correction factor taking into account steady-state effects (Fig. 3).

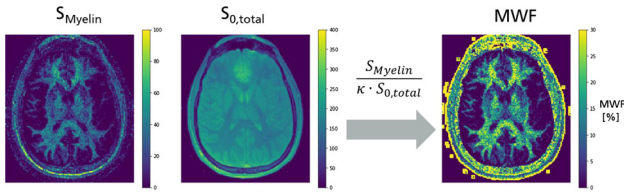

Figure 3: Schematic for estimating water-myelin-fraction (MWF)

Discussion/Conclusion: Initial experiments reveal the potential of IR-bSSFP for MWI. Compared to approaches based on T_2 measurements, IR-bSSFP has the advantages of shorter echo-spacing and longer apparent relaxation constants T_1* (2). Further improvements will focus on scan time reduction and extension to 3D imaging.

Acknowledgements: Funded by the EU (H2020-EU.1.2.1.-737180) and the Bavarian Ministry of Economic Affairs, Regional Development and Energy.

References:

1. Schmitt P, et al. Magn Reson Med. 2004;51(4):661-7.
2. Hargreaves BA, Nishimura DG. Proc 11th ISMRM, Toronto, Canada, 2003:1100.
3. Pfister J, et al. Magn Reson Med. 2019;81(6):3488-3502.

S02.05

Fat deblurring in golden angle radial stack-of-stars water-fat imaging for navigator-gated abdominal fat quantification

C. Zöllner[1], S. Kronthaler[1], C. Böhm[1], S. Ruschke[1], M. Diefenbach[1], D. Franz[1], G. M. Beck[2], J. M. Peeters[2], D. C. Karampinos[3]
[1]Technical University of Munich, Department of Diagnostic and Interventional Radiology, School of Medicine, München, GERMANY, [2]Philips Healthcare, Best, NETHERLANDS, [3]Technical University of Munich, Department of Diagnostic and Interventional Radiology, School of Medicine, Munich, GERMANY

Purpose/Introduction: Respiratory motion limits the spatial resolution of abdominal chemical shift encoding-based water-fat imaging. Besides performing the measurement during breath-holds (BH), golden angle stack-of-stars (SoS) k-space trajectories provide higher resolution while enabling free breathing[1]. One major challenge of using radial k-space acquisition schemes is the chemical shift induced blurring, compromising fat-separation and PDFF mapping[1-3]. Therefore, this work uses a k-space based water-fat separation method in combination with a navigator-gated pseudo golden angle SoS acquisition for in vivo liver water-fat imaging.

Subjects and Methods: A time-interleaved multi-echo gradient-echo sequence[4] (Fig. 1) with pseudo-golden angle ordering and SoS was used to acquire abdominal scans of three volunteers on a Philips 3T Elition X. A 1D-navigator between the liver and the lung was used to reduce breathing motion artefacts. Two scans were acquired for each subject with a large (1632.7 Hz/Px) and a low (326.5 Hz/Px) bandwidth.

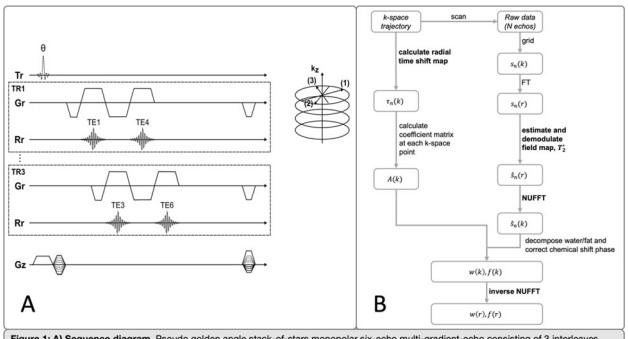

Figure 1: A) Sequence diagram. Pseudo golden angle stack-of-stars monopolar six-echo multi-gradient-echo consisting of 3 interleaves with 2 echoes each.
B) Chemical-shift induced phase errors are removed simultaneously while performing the water fat separation in radial k-space. The fieldmap and T2* values are calculated based on the reconstructed image and demodulated before generating radial k-space profiles. Based on the knowledge of the trajectory a sampling time shift map is computed which allows to correct for the phase shift of off-resonant fat peaks at each k-space point.

After correcting for B0-inhomogeneities and T_2 decay, the signal can be expressed in k-space[2]:

$$S_n(\tau_{k,n}, k) = \Sigma\rho_m(k) \sum r_{m,p} \exp(i2\pi\Delta f_{m,p}(t_n + \tau_{k,n}))$$

τ models the frequency shift of the fat peaks due to the finite read out time.

Prior to the water-fat separation a novel single-min-cut graph-cut with variable layer graph construction was used to estimate the fieldmap and an IDEAL based chemical shift separation method to calculate the R_2^* values. After the demodulation, the non-uniform fast Fourier transform[5] was used to generate radial k-space data. The water–fat separation was performed directly in radial k-space (**Fig. 1**). Water and time shift corrected fat maps of the k-space based water–fat separation were compared to the cartesian water–fat separation.

Results: The corrected fat-images are significantly deblurred for the low bandwidth acquisitions enabling an improved delineation of subcutaneous fat (Fig. 2). The deblurred navigator-gated PDFF maps are of significantly higher resolution than the corresponding BH PDFF maps (Fig. 3).

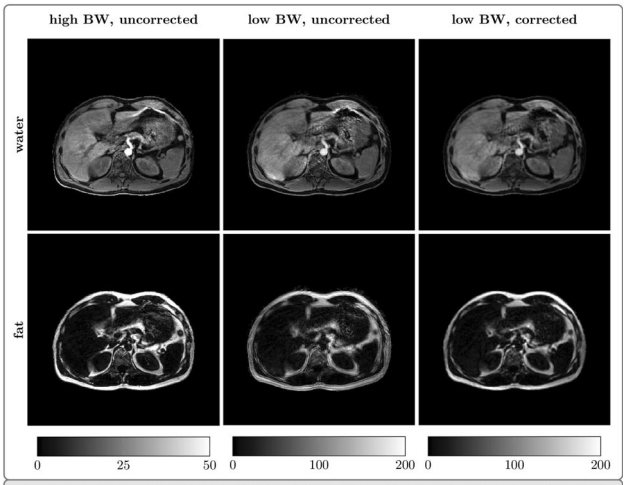

Figure 2: Water-fat separation results. Left: Water and fat images from a high BW scan with minimal water-fat shift, obtained by the cartesian image space-based water-fat separation already used to estimate the fieldmap and $T2^*$ (see **Fig1**). Center: A low BW results in a visible blurring of the fat signal when using the cartesian image space-based water-fat separation. Right: The k-space based time shift correction method is able to deblur the low BW fat image to a degree that visceral fat streaks become visible.

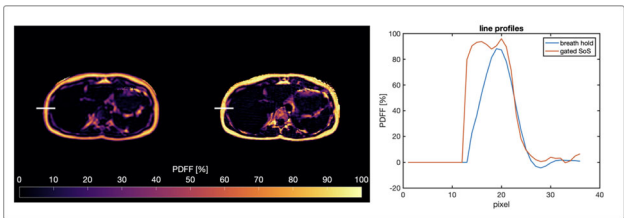

Figure 3: PDFF comparison. Left: The PDFF of a cartesian single breath hold acquisition, PDFF was calculated by the vendor implementation. Center: low bandwidth navigated SoS acquisition, the PDFF was calculated based on the radial k-space based water–fat separation. Right: Line profiles through subcutaneous fat along the white lines. The SoS PDFF has a higher resolution than the breath hold PDFF confounded by partial volume effects.

Discussion/Conclusion: The present work proposes a reconstruction pipeline building upon the k-space-based water-fat separation methodology previously proposed in [2,3] for the needs of deblurring the chemical shift effect of fat in navigator-gated SoS quantitative water–fat imaging. Adipose tissue PDFF mapping has been recently gaining interest in metabolic research[6]. The proposed reconstruction pipeline would be useful for maintaining adequate SNR when limiting the slice FOV and increasing the spatial resolution of PDFF mapping in thin subcutaneous, visceral and pancreatic fat. Further work is needed to fully characterize the quantitative fidelity of the corrected PDFF maps in regions with low PDFF and to address blurring effects induced by B0 field inhomogeneity effects.

References:

1. Sodickson, MRM, 2016
2. Reeder, MRM, 2008
3. Wang, JMRI, 2010
4. Ruschke, MRM, 2016
5. Fessler, JMRI, 2007
6. Franz, IJO, 2018

S02.06

Pre-emphasis of Twisting Radial Lines (TWIRL) using the Gradient System Transfer Function (GSTF) at 7T

P. Eirich[1], T. Wech[1], M. Stich[1], T. Reiter[2], L. M. Schreiber[3], H. Köstler[1]

[1]University Hospital Würzburg, Department of Diagnostic and Interventional Radiology, Würzburg, GERMANY, [2]University Hospital Würzburg, Department of Internal Medicine I, Würzburg, GERMANY, [3]University Hospital Würzburg, Chair of Cellular and Molecular Imaging, Würzburg, GERMANY

Purpose/Introduction: The Gradient System Transfer Function (GSTF) characterizes the impulse response of a linear and time-invariant system and can be exploited to compensate for imperfections of the magnetic field gradient dynamics, which result in k-space inaccuracies and image artifacts when using varying magnetic field gradients. Recently a prototype GSTF pre-emphasis was proposed [1]. The purpose of the present work was to modify the prototype towards an automated GSTF pre-emphasis that enables double-oblique MR imaging for arbitrary k-space trajectories at 7T. Therefore, an extended GSTF pre-emphasis was implemented in a 2D FLASH sequence using a Twisting Radial Lines (TWIRL) k-space trajectory [2] and subsequently tested in a human cardiac cine study.

Subjects and Methods: The GSTF self-terms of all three axes of a 7T MR scanner (MAGNETOM Terra, Siemens Healthcare GmbH, Erlangen, Germany) were determined by playing out 12 triangular input gradients and measuring the phase evolutions in two parallel slices of a spherical phantom equidistantly from the scanner isocenter [1,3]. The automated pre-emphasis was realized through projection of any gradient waveform input onto the physical x-,y- and z-axis, followed by multiplication with the respective inverse GSTF in the frequency domain.

The technique was applied to an in vivo cardiac cine study using a 2D FLASH sequence with an optimized TWIRL trajectory. Within a breath-hold of a healthy volunteer 2500 consecutive TWIRL readouts with a double golden angle increment were acquired and then sorted into 20 heart-phases by means of self-gating (TR = 3.0 ms). The datasets were reconstructed using GRAPPA Operator Gridding (GROG) [4] and the compressed sensing technique presented in [5]. For comparison, the sequence was repeated without pre-emphasis.

Results: The magnitude and phase of the GSTF self-terms are depicted in Fig. 1a, b, respectively. The magnitude demonstrates low-pass behavior, as well as scanner-specific resonances. In general, the transfer characteristics of the z-axis differ from that of the x- and y-axis.

Figure 2 shows the results of the cardiac cine study. Both datasets were reconstructed with the nominal trajectory, resulting in high image quality when the pre-emphasis was applied, whereas typical artifacts caused by trajectory errors are present without pre-emphasis.

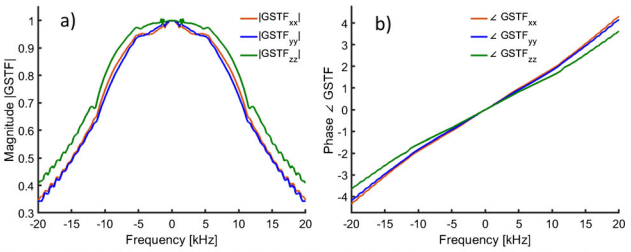

Fig. 1: Magnitude (a) and phase (b) of the Gradient System Transfer Function (GSTF) self-terms, measured at the 7T Terra system.

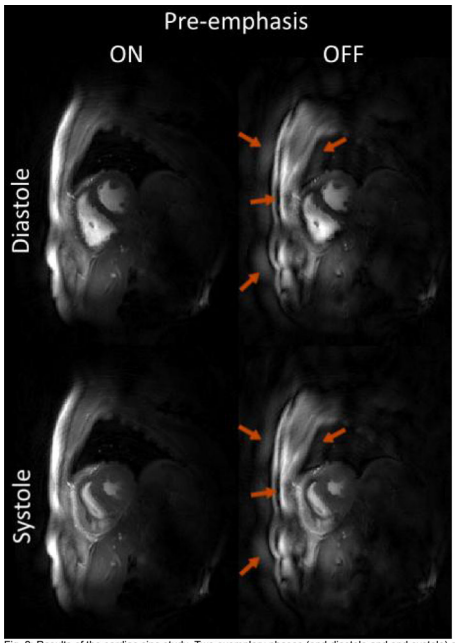

Fig. 2: Results of the cardiac cine study. Two exemplary phases (end-diastole and end-systole) are shown in pre-emphasis mode ON and OFF. Artifacts caused by imperfect magnetic gradient waveforms are highlighted by orange arrows.

Discussion/Conclusion: In summary, the presented pre-emphasis demonstrates the substantial benefit of considering the GSTF-based correction of gradient inaccuracies already within the pulse sequence code. The possibility to image double-oblique slice orientations with generally arbitrary k-space trajectories especially facilitates cardiac applications.

References:

[1] Stich M et al., MRM, 80(4):1521-1532 (2018).
[2] Jackson JI et al., MRM, 25:128-139 (1992).
[3] Campbell-Washburn AE et al., MRM, 75(6):2278-2285 (2016).
[4] Seiberlich N et al., MRM, 58:1257-1265 (2007).
[5] Otazo M et al., MRM, 73(3):1125-1136 (2015).

S02.07

Impact of head motion on SMS-accelerated fMRI: GRAPPA *versus* no GRAPPA

A. Fouto[1], R. G. Nunes[1], N. A. Silva[2], A. Ruiz-Tagle[3], P. Figueiredo[1]
[1]ISR-Lisboa/LARSyS and Department of Bioengineering, Instituto Superior Técnico, Universidade de Lisboa, Lisbon, PORTUGAL, [2]Hospital da Luz Learning Health, Lisbon, PORTUGAL, [3]1ISR-Lisboa/LARSyS and Department of Bioengineering, Instituto Superior Técnico, Universidade de Lisboa, Lisbon, PORTUGAL

Purpose/Introduction: The simultaneous multi-slice (SMS) acceleration of 2D EPI is increasingly used in fMRI studies [1]. One question that arises is whether to combine SMS with parallel imaging using GRAPPA to also reduce B0-induced geometric distortions, exploiting the growing availability of multi-channel receiver coil arrays. In fact, the heterogeneous sensitivity of these arrays may render GRAPPA image reconstructions sensitive to head motion [2]. Here, we aimed to evaluate the impact of head motion on the sensitivity and specificity of fMRI activation, when using SMS combined with GRAPPA vs. no GRAPPA.

Subjects and Methods: 4 healthy volunteers were imaged on a Siemens Vida at 3T with a 64-channel head coil while performing a visual task (20 s checkerboard alternated with 20 s fixation). BOLD-fMRI data were collected using 2DEPI (TR/TE = 1690/37 ms, 2.2 mm isotropic), accelerated with an SMS factor of 3, with or without GRAPPA in-plane acceleration (R = 2). 6 fMRI runs were performed in each of 3 conditions, both with and without GRAPPA: 1) no motion; 2) rotation in x (pitch) and 3) rotation in z (roll) - for 2) and 3) the subjects were instructed to move at 10 s of each stimulation block. Data analysis was performed in FSL. After fieldmap distortion correction, and standard preprocessing, activation maps were obtained for each fMRI run using general linear modeling including extended motion parameters ($Z > 2.3$, $p < 0.05$). The visual and motor cortex areas were extracted from the Juelich atlas and transformed into the functional space. The number of activated voxels and the maximum Z-score were obtained in each area, and the Dice coefficient was computed between each individual fMRI activation map and the visual and motor areas.

Results: The effects of fieldmap distortion correction are illustrated in Fig. 1. As expected, GRAPPA acquisitions produced less distortion, which was however corrected for to a level similar to that of no-GRAPPA acquisitions by fieldmap unwrapping. An illustrative example of the fMRI activation maps obtained with and without GRAPPA, and with or without motion is shown in Fig. 2. Boxplots of the Dice coefficients, number of voxels (true positives, TP) and maximum Z in visual cortex are shown in Fig. 3, for both no motion and motion, All parameters indicate that visual activation is poorer with motion, and relatively poorer with GRAPPA.

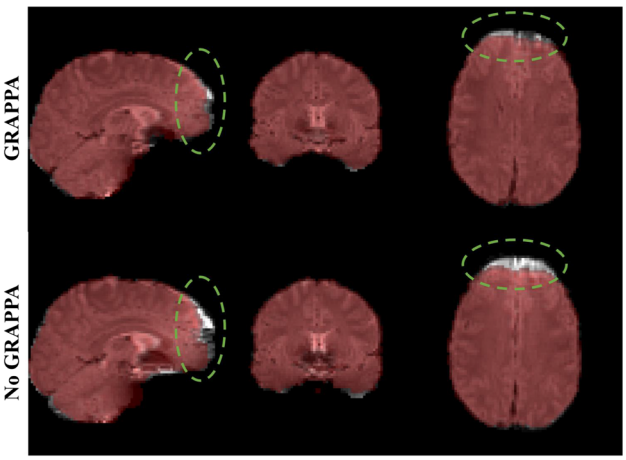

Illustrative example of B0-induced distortions in the fMRI data before (red) and after (gray) fieldmap correction. Distortions were greater for no GRAPPA (bottom) compared to GRAPPA (top) as highlighted by the dashed circles (green).

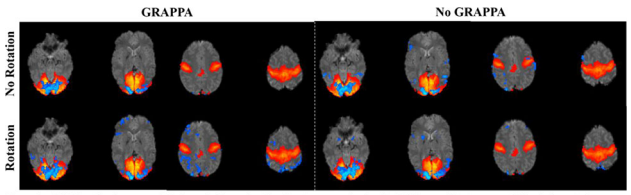

Example of fMRI activation maps (blue) overlaid on visual and motor areas (red-yellow). When subjects were still (top) almost all activations were true positives, when instructed to move (bottom) there were activations outside the red-yellow areas.

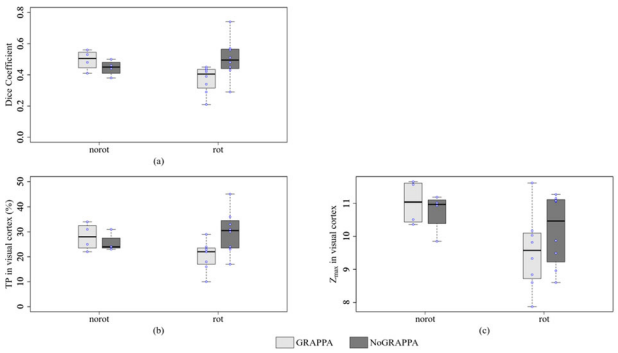

fMRI sensitivity analysis: GRAPPA vs No GRAPPA for no motion (norot) and both types of motion (rot). Boxplots across subjects of Dice coefficients, number of voxels (true positives, TP) and maximum Z in visual cortex area.

Discussion/Conclusion: We showed that combining GRAPPA with SMS-accelerated fMRI yielded brain activation results that were more sensitive to head motion compared to no GRAPPA. Although B0-induced distortions are reduced, in-plane acceleration with GRAPPA should be considered with caution in this case.

Acknowledgements: Portuguese Science Foundation grants LISBOA-01-0145-FEDER-029675 and UID/EEA/50009/2019.

References:

1. Feinberg et al., J Magn Reson. 2013 Apr;229:90-100.
2. Faraji-Dana et al., J Neurosci Methods. 2016 Sep 1;270:46-60.

S02.08
MOCO-MAP using a TWIRL trajectory

J. Portmann, T. Wech, P. Eirich, H. Köstler
University Hospital of Würzburg, Department of Diagnostic and Interventional Radiology, Würzburg, GERMANY

Purpose/Introduction: Cardiac delayed enhancement imaging is time-consuming and requires many breath holds of the patient. Additionally, the procedure demands for TI scouting to yield optimal contrast [1]. As an alternative, MOCO-MAP (Motion Corrected - Model-based Acceleration of Parameter mapping) provides an image reconstruction from a single FLASH acquisition [2]. Beyond that, it allows adjusting the TI dependent contrast in post-processing.

So far, the k-space trajectories were limited to radial sampling patterns, which inefficiently cover the outer parts of the k-space [3]. Hence, the objective was to implement a more elaborate acquisition trajectory and to test the sequence in vivo.

Subjects and Methods: An inversion recovery (IR) prepared MR sequence with twisting of the radial trajectory (TWIRL), and thus with adjustable k-space sampling density, was implemented ([3], TR = 3.14 ms, resolution = 1.3 × 1.3 × 8.0 mm^3). A pre-emphasis, based on the gradient system transfer function (GSTF), was used to compensate for imperfections of the gradient system [4].

The GSTF correction was first tested using a phantom study without IR preparation. Both an image with and without pre-emphasis were acquired for this purpose.

Subsequently, the new sequence was tested on a healthy volunteer. A mid-ventricular short-axis slice was chosen and the subject was asked to hold breath for 10 s. The MOCO-MAP reconstruction algorithm was adjusted to cope with TWIRL trajectories and was then applied for a reconstruction of the accelerated acquisition.

Results: The results of the phantom study (Fig. 1) prove that the trajectory errors caused by gradient system imperfections clearly require the application of a GSTF correction when using TWIRL.

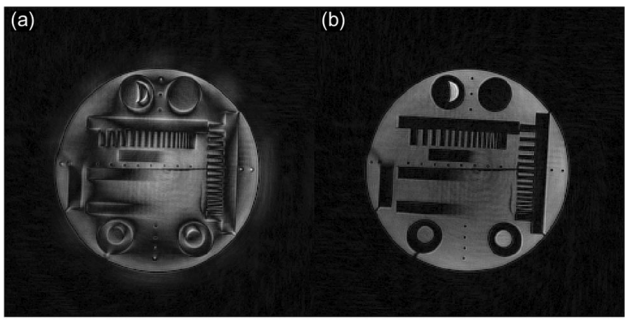

1) Phantom measurement using the TWIRL trajectory with (a) pre-emphasis switched off and (b) pre-emphasis switched on.

Figure 2 illustrates the change in contrast over time in the motion corrected image series after 8 iterations of the MOCO-MAP reconstruction. At this stage, undersampling artifacts are successfully suppressed and blurring caused by cardiac motion is not noticeable.

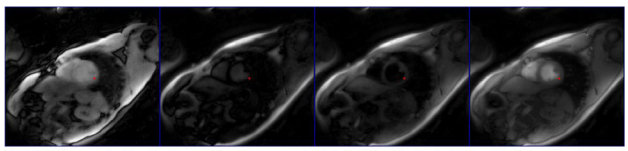

2) MOCO-MAP reconstruction of in-vivo acquisition. Frames from left to right: TI (inversion time) = 12.8 ms, TI = 756 ms, TI = 1.13 s and TI = 9.65 s.

Figure 3 shows the temporal course of one pixel of the in vivo acquisition, which is marked in Fig. 2. The oscillation caused by the cardiac motion (a) can be reduced by the motion correction such that an exponential model can be applied (b: red line).

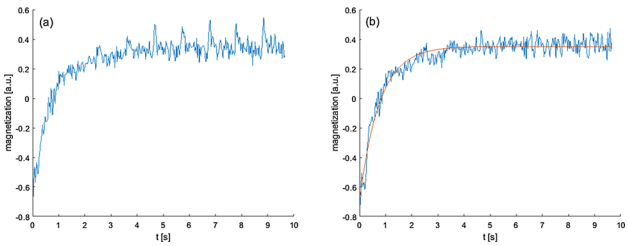

3) Development of one pixel marked in Fig. 2: (a) before applying MOCO-MAP, (b) with motion correction applied (blue) and fitted using the exponential model (red).

Discussion/Conclusion: In the presented study, we enhanced the MOCO-MAP technique by introducing TWIRL-readouts based on pre-emphasized gradient waveforms. MOCO-MAP can substantially improve the procedure of delayed enhancement imaging in terms of acquisition time and image contrast. A possible focus for future applications could be the generation of quantitative T1 maps, which is a byproduct of the MOCO-MAP technique.

References:

[1] Kim et al., J Card Magn Reson 2003;5:505-14.
[2] Wech et al., Magn Reson Imaging 2018;47:48–53.
[3] Jackson et al., Magn Reson Med, 1992;25:128-39.

[4] Stich et al., Magn Reson Med, 2018;80:1521-32.

S02.09

Strategies for gradient duty cycle reduction in high resolution gradient echo imaging

J. Leupold[1], L. Hesse[2], M. Weigel[3], M. Wapler[4], S. Bär[1]
[1]University Medical Center Freiburg, Radiology - Medical Physics, Freiburg, GERMANY, [2]Botanischer Garten der Universität Freiburg, Plant Biomechanics Group, Freiburg, GERMANY, [3]University Hospital Basel, Department of Radiology, Division of Radiological Physics, Basel, SWITZERLAND, [4]University of Freiburg, Department for Microsystems Engineering, Freiburg, GERMANY

Purpose/Introduction: Reducing gradient duty cycle (GDC) while keeping all imaging parameters unchanged can make MRI more efficient in terms of energy consumption, acoustic noise or strain of the gradient coils and amplifiers. Particularly in micro MR, too high GDC (resulting from too high spatial resolution) can block a given imaging protocol due to heat production. Here, we propose methods to reduce GDC in 3D gradient echo imaging (GRE), while maintaining all imaging parameters.

Subjects and Methods: The GDC reduction is accomplished by omitting all spoiler gradients in RF-spoiled GRE, such that only the uncompensated part of the readout gradient leads to a spoiling moment of π (0.5 cycles) per voxel. Without further means, this is in general insufficient and leads to ghost artefacts. However, two approaches are here proposed leading to sufficient spoiling.

(A) In high resolution GRE imaging (with or w/o RF-spoiling) the imaging gradients alone (i.e. w/o spoilers) can lead to ideal spoiling if the diffusion coefficient of the sample is high enough (e.g. free water), and if imaging parameters lead to a high b-value of the readout gradient (high resolution, low readout bandwidth, long TR).

(B) In high resolution imaging, averaging of several acquisitions is often performed to enhance SNR. With RF-spoiling, the adapted k-spaces averaging method [1] can be employed for artefact-free images with reduced GDC, while maintaining the SNR gain. Averaging of k-space lines is performed that lie *N* cycles apart with *N mod P = P/Av*, with number of averages *Av* and the number of cycles *P* after which the RF-spoiling pseudo-steady state [2] repeats (e.g. P = 40 for the common spoil increment of 117°).

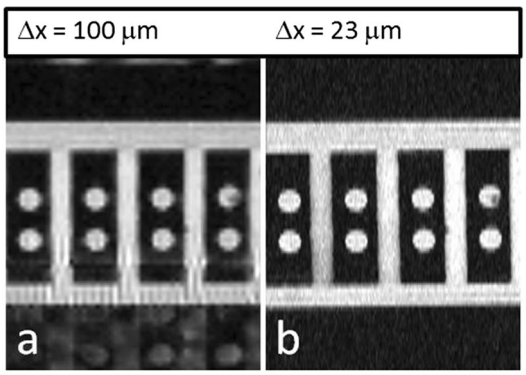

Fig. 1: RF-spoiled 3D GRE of a PMMA phantom in water in a 5 mm NMR tube with TR = 60 ms, readout bandwidth of 20 kHz, of 20° and resolution Δx in readout direction. Ghost artefacts vanish in b.

Results: Omission of spoiler gradients is shown in Fig. 1. The applied readout gradient in 1b leads to a b value of ∼ 360 s/mm^2, such that diffusion leads to ideal spoiling. The influence that diffusion in general has on GRE signals is illustrated in Fig. 2, where the signal of non-RF-spoiled GRE collapses to the ideal spoiling case due to diffusion.

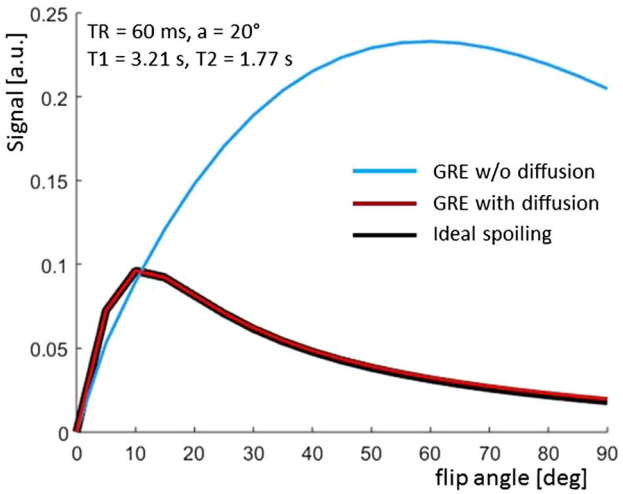

Fig. 2: Simulation of non RF-spoiled GRE Signal without additional spoilers but high b-value of the readout gradient. With diffusion, ideal spoiling is established. Parameters as used for Fig. 1b.

Figure 3 shows omission of spoiler gradients in combination with the adapted averaging method (3c,d). Ghost are reliably suppressed and SNR is enhanced. GDC of the readout gradient is reduced by 30% in comparison to the full spoiling in Fig. 3b.

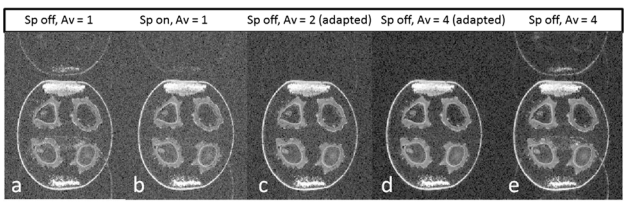

Fig. 3: RF-spoiled 3D GRE of an ilex aquifolium fruit, with spoiler (Sp) on (RO gradients spoil 1 cycle per voxel) or off (RO spoils 0.5

Discussion/Conclusion: In high resolution GRE imaging, GDC can get reduced by omission of spoiler gradients, if diffusion in combination with suitable imaging parameters lead to ideal spoiling. However, a more robust strategy is to perform averaging of k-space lines that is often anyway necessary in high resolution MRI or MR microscopy; and to perform it as adapted averaging according to [1]. Then, ghost artefacts are robustly suppressed and imaging is performed with higher gradient efficiency or can just be made possible at all since omission of spoiler gradients leads to a feasible GDC level.

References:

[1] Leupold,Hennig.MRM66:1123-28(2011).
[2] Denolin et al.MRM54:937-54(2005).

S03 Scientific Session

13:00–14:30 *Room 4 - Plate & Van der Vorm Zaal*

Cancer Imaging

S03.02

MR-based treatment planning for proton beam therapy of ocular tumors

J.-W. Beenakker[1], E. Fleury[2], M. Hassan[3], M. Jaarsma-Coes[1], B. Stoel[3], A. Webb[3], M. Hoogeman[2], P. Trnková[2]
[1]Leiden University Medical Center, Departments of Radiology and Ophthalmology, Leiden, NETHERLANDS, [2]Erasmus Medical Center & Holland Proton Therapy Center, Radiation Oncology, Rotterdam, NETHERLANDS, [3]Leiden University Medical Center, Department of Radiology, Leiden, NETHERLANDS

Purpose/Introduction: Uveal Melanoma (UM) is the most common primary ocular tumor. OcularProton therapy (OPT) for UM is often the therapy of choice for medium to large size tumors. Conventionally the therapy is planned on 2D ultrasound, which does not accurately describe the 3D shape of the tumor and relies on a population-based model of the location of the organs-at-risk (OAR) such as the optic nerve and other surrounding tissues. The aim of this study is to overcome these limitations by developing a high-resolution MRI-based treatment planning approach for treating UM in proton therapy, which in addition determines the optimal gaze angle for treatment to limit the dose for organs-at-risk (OAR) such as the optic nerve.
Subjects and Methods: Ten patients diagnosed with UM were scanned on a 7 Tesla Philips MRI using a dedicated eye coil. A cued blinking protocol was used to mitigate eye-motion artifacts.[1] The eye, tumor and OAR, including optic nerve and lens, were subsequently automatically segmented based on isotropic T1- and T2-weighted images (T1: TI/TR/TE/FA: 1280 ms/5.4 ms/2.4 ms/7; resolution: $(0.6\ \text{mm})^3$ T2: TR/TE:2500 ms/194 ms with SPIR; resolution: $(0.6\ \text{mm})^3$). A treatment planning approach was developed in-house using a proton dose algorithm and the MR-based eye-model.

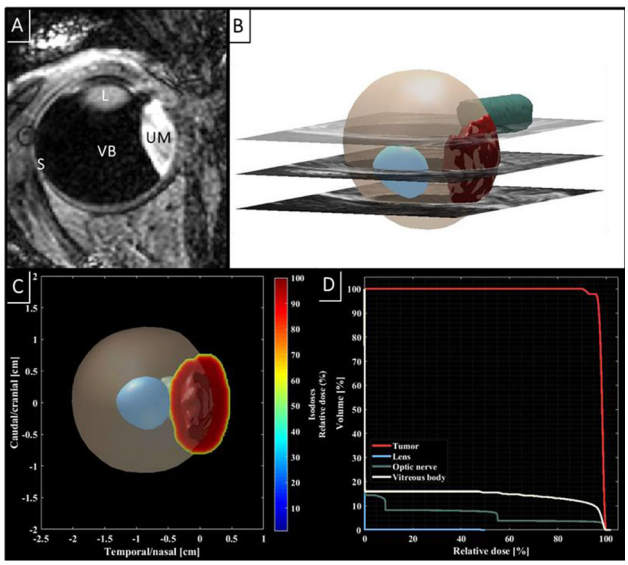

MRI-based treatment planning. A) A T1-weighted image showing the tumour and OAR (L:Lens; VB:Vitreous body; S:Sclera). B) 3D-MR-based eye reconstruction. C) 3D-dose distribution within the patient's eye. D) Generated plan with dose volume histogram.

To minimize proton doses to OARs, a weighted-sum objective function was computed for each gaze angle, which also included an objective to penalize extreme gaze angles: weights could be adjusted to prioritize sparing of specific OARs.
Results: On the MR-images the different anatomical structures could clearly be differentiated and automatic segmentation succeeded in all cases, although the segmentation would benefit from manual corrections for all patients. These 3D models of the eye were subsequently loaded into the developed MR-based treatment planning, which calculated the dose for the organs and automatically determined the optimal gaze direction. Tumor coverage was reached for all cases ($D_{95\ \%} > 95\%$).

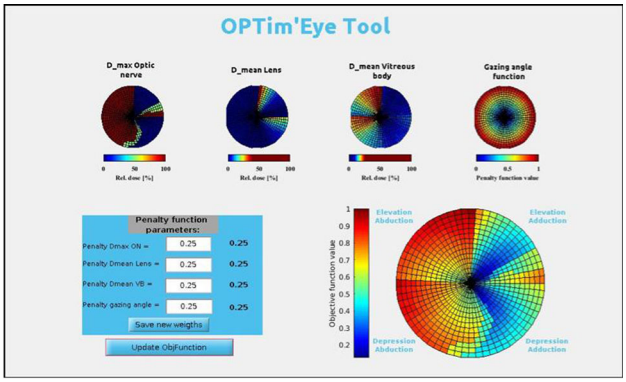

Retina maps of the weighted-sum objective function values showing an iso-weighting scenario for the patient of Fig.1. Clinical gaze angles between -30 to 30 degrees, both for abduction/adduction and elevation/depression, with increments of 2 degrees.

The figure shows an example of the weighted-sum objective function for one patient in the range of clinically feasible gaze angles. In this example, the chosen weights penalized four parameters equally: mean dose to the lens, maximum dose to the optic nerve, mean dose to the vitreous body and size of the gaze angle.
Discussion/Conclusion: An MR-based treatment planning method for OPT was developed which allows planning therapy on a 3D instead of the conventional 2D model. MRI also enables incorporation of the accurate (gaze dependent) location of the OAR, which reduces the side-effects after treatment.
References:
1. Beenakker, et al. NMR Biomed (2013)

S03.03

Early assessment of external beam radiotherapy response in an animal model of small-intestine neuroendocrine tumour (GOT1) using VERDICT modelling of diffusion MR data

L. Lundholm, M. Montelius, O. Jalnefjord, E. Shubbar, J. Swanpalmer, E. Forssell-Aronsson, M. Ljungberg
Institute of Clinical Sciences, Sahlgrenska Cancer Center at Sahlgrenska Academy, University of Gothenburg, Department of Radiation Physics, Gothenburg, SWEDEN

Purpose/Introduction: Methods to non-invasively characterize tumour tissue would facilitate therapy response prediction and assessment and enable personalized treatment. One promising technique for such purposes is the Vascular, Extracellular, and Restricted Diffusion for Cytometry in Tumours (VERDICT) model based on diffusion MRI (dMRI)[1]. VERDICT aims to provide estimates of microstructural parameters, such as cell size, and volume fractions of intracellular (fIC), extracellular (fEES) and vascular (fVASC) space. Previous studies using VERDICT have focused on validating and

optimizing the method[2,3]. To our knowledge, no studies using VERDICT for longitudinal evaluation of therapy response in small-intestine neuroendocrine tumour (SI-NET) have been presented.

The aim was to study if VERDICT modelling can be used to study treatment response to external beam radiotherapy in an animal model of SI-NET.

Subjects and Methods: Balb/C nude mice (n = 5) with subcutaneous GOT1 SI-NET xenografts were irradiated externally with an absorbed dose of 8 Gy to the tumour on day 0, using a 6 MV photon beam (Varian Medical Systems). The in vivo dMRI experiments were conducted on days -1, 2, 3, 7, and 15 using a 7T preclinical MR system (Bruker, Biospec), table 1. The VERDICT model BallSphereAstrosticks was fitted to data using the AMICO framework[4] with fixed compartment diffusivities based on a previous study[5] (dEES = dIC = 0.7×10^{-9} m^2/s, dVASC = 40×10^{-9} m^2/s). Tumour volumes were measured on days – 4, – 1, 0, 2, 3, 7, and 15 using callipers.

The Gothenburg Ethical Committee on Animal Research approved this study.

δ [ms]	Δ [ms]	|G| [mT/m]	b-values [s/mm²]	TE [ms]
4	9	53	20	19
4	9	100	70	19
4	9	131	120	19
4	9	213	320	19
4	9	338	800	19
3	30	120	225	39
3	30	280	1223	39
3	30	360	2021	39
3	40	120	304	49
3	40	280	1656	49
3	40	360	2738	49
10	30	40	283	46
10	30	120	2550	46
10	40	40	393	56
10	40	120	3535	56

Scantime:	50 min
Number of averages:	20
TR:	3000 ms
In-plane resolution:	400 × 400 μm²
Slice thickness:	500 μm
Number of directions:	3 (orthogonal)

Table 1. Scan parameters used in the VERDICT diffusion MRI protocol

Results: A significant therapeutic effect was observed based on tumour volume reduction, as well as decreased fIC days 2-7 after treatment (Fig. 1). Reduced fIC may indicate reduced cell density due to radiotherapy. After day 7 fIC tended to increase, possibly indicating renewed tumour progression, which is also coincident with the reduced tumour volume regression (Fig. 1). Figure 2 shows fIC parameter maps for all dMRI experiment time points of an example mouse, revealing the progression of tumour heterogeneity after treatment.

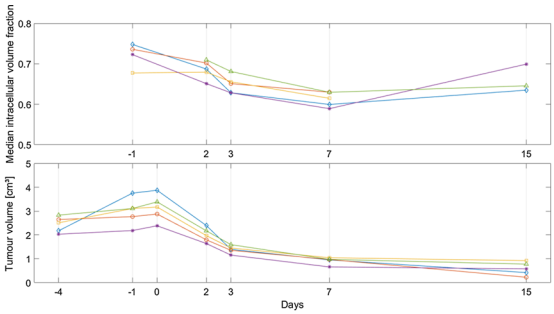

Figure 1. Median values of intracellular volume fraction within the tumour as estimated by VERDICT (upper), and tumour volumes (lower), for all included time points and mice. Individual mice are indicated by color and marker symbols

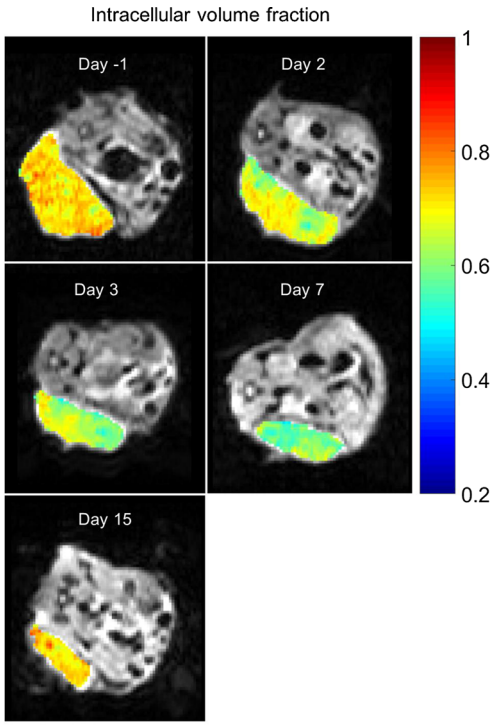

Figure 2. VERDICT parameter maps of absolute intracellular volume fraction in an animal model of small-intestine neuroendocrine tumour prior to (day -1), and following (days 2, 3, 7 and 15), external beam radiotherapy

Discussion/Conclusion: Our findings show that there is potential in using VERDICT to study the early microstructural effects in tumours after radiotherapy. Future work should focus on optimization and verification of the VERDICT model for the studied tumour type and treatment setting.

References:

1. Panagiotaki et al., *NMR in Biomed*. 2014.
2. Panagiotaki et al., *Invest Radiol*. 2015.
3. Bailey et al., *NMR Biomed*. 2019.
4. Bonet-Carne et al., *NMR Biomed*. 2018.
5. Jalnefjord, *ISMRM,* 2019.

S03.04

Cluster-based evaluation of T2* for early and longitudinal tumor radiotherapy response assessment in a small-intestine neuroendocrine tumor model

M. Montelius[1], L. Lundholm[1], O. Jalnefjord[2], E. Shubbar[1], J. Swanpalmer[1], E. Forssell-Aronsson[1], M. Ljungberg[1]
[1]*University of Gothenburg, Institute of Clinical Sciences, Department of Radiation Physics, Gothenburg, SWEDEN,* [2]*Sahlgrenska University Hospital, Medical Physics and Biomedical Engineering, Gothenburg, SWEDEN*

Purpose/Introduction: Tumor hypoxia is associated with radioresistance, metastasis and poor prognosis, but remains difficult to measure accurately in vivo. MRI enables quantification of tissue T2* relaxation, which is reduced by deoxyhemoglobin, and may thus provide a non-invasive surrogate marker for hypoxia with high spatial and temporal resolution[1]. Maps showing hypoxic tumor sub-regions could, e.g., enable more aggressive localized treatment using modern radiotherapy. However, accurate identification of clinically relevant hypoxic tumor sub-regions and monitoring of changes induced by therapy based on T2* maps have proven difficult and prone to subjectivity due to, e.g., limited knowledge on clinical significant T2* levels for specific tumor types and gross morphological changes induced by therapy or growth[2].
Our aim was to correlate radiotherapy response in a small-intestine neuroendocrine tumor model with objectively classified T2* data by applying a Gaussian mixture model approach.
Subjects and Methods: Balb/C mice (n = 12) bearing human neuroendocrine tumor (GOT1) received 8 Gy absorbed dose to tumor from external radiotherapy (6MV photons, Varian Medical Systems). Tumor volume assessment using calipers and T2*-weighted MRI (MGE, TR/TE [ms]: 2500/3, 7, 12, 16, 20, 24, 28 and 32, NSA: 3, Pixel/slice dim [mm]: 0.2 × 0.2/1.0) was performed within 24 h before treatment (day 0), and on days 2, 3, 7 and 15 (7T Bruker BioSpec, 30-mm tr/tx resonator, Rapid). T2*-maps were constructed pixel-wise using mono-exponential model fitting, and clustering was based on a 2-component Gaussian mixture model using pooled T2* data from all tumors images and time points.
The Gothenburg Ethical Committee on Animal Research approved this study.
Results: Two clusters were identified (mean T2* [ms]: 16.8 and 9.4, Fig. 1) and mapped back to each tumor and time point for the 8 animals that survived to day 15. Both tumor volumes and tumor area assigned to the high-T2* cluster significantly decreased after treatment (Fig. 2), and there was a strong correlation between relative tumor area in the high-T2* cluster before treatment and relative volume day 15 (Fig. 3).

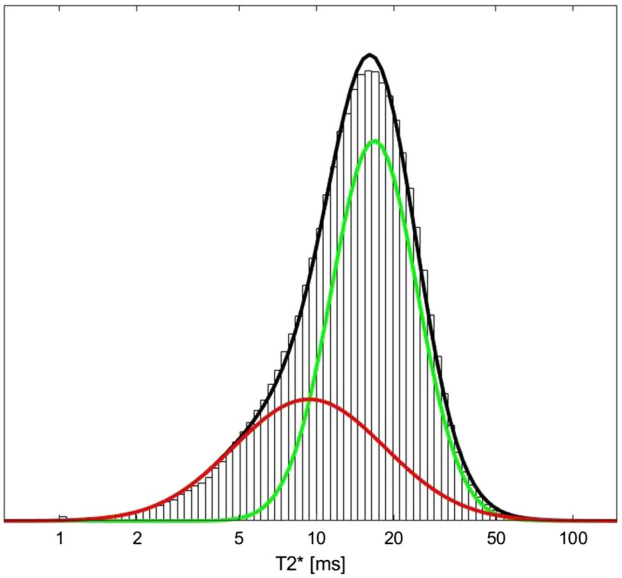

Figure 1. Histogram of T2* data (log-scale) from all tumors and time points, where low (red) and high (green) T2* clusters, identified by Gaussian mixture modelling, are superimposed. The sum of both clusters (black) shows histogram agreement

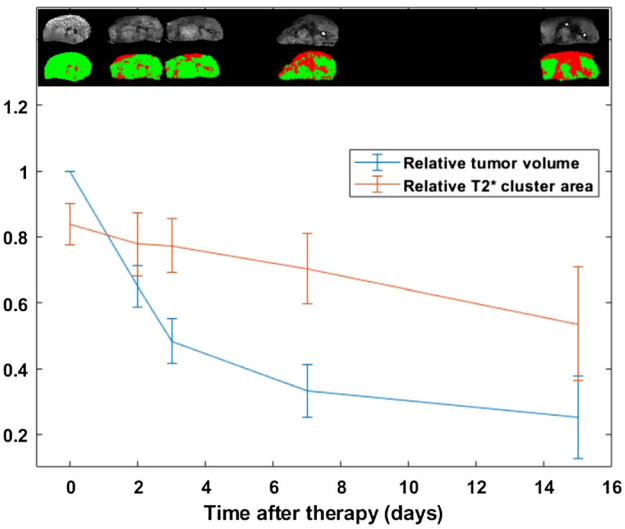

Figure 2. Relative tumor volume and High-T2* cluster area (mean±sd) vs. time after treatment for n=8 tumors, with an example tumor T2*-and cluster map shown for corresponding days

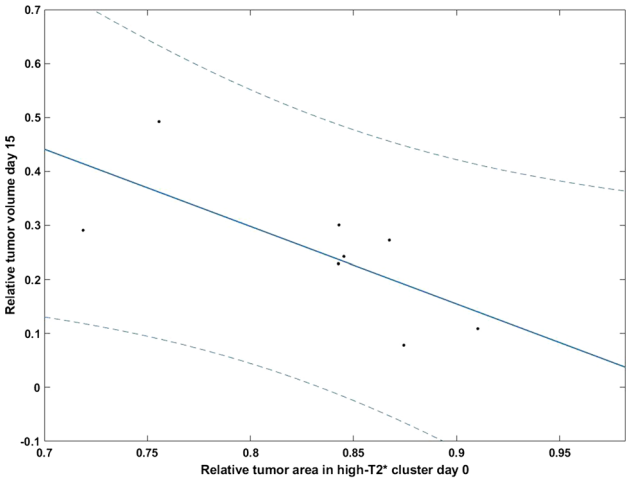

Figure 3. Linear regression for high-T2* cluster relative area day 0 and relative tumor volume day 15. Slope: -0.36 (95%-confidence bounds: -0.71 – 0.01), R2: 0.51

Discussion/Conclusion: In this study, we demonstrate the feasibility to objectively predict and assess radiotherapy response using T2*-quantification in our tumor model. A high proportion of tumor voxels assigned to the high-T2* cluster before radiotherapy was predictive of a greater loss of relative tumor volume 2 weeks later, which agrees with the assumption that adequate supply of oxygen (low deoxyhemoglobin concentration and less reduction of T2*) implies less radioresistance. The cluster-based methodology reduces subjectivity in the response evaluation, and should be considered for similar assessment of a wider range of tumor types and therapeutic interventions.

References:

1. Horsman et al. *Nrclinonc*., 2019.
2. Vaupel et al., *Cancer Metastasis Rev.,* 2007.

S03.05

Differentiation of Benign and Malignant Ovarian Tumors by Dynamic Contrast-enhanced Magnetic Resonance Imaging

B. Olimov[1], M. Lapteva[1], M. Beregov[1], F. Kossov[1], I. Panichenko[2], V. Panov[1], I. Tyurin[1]
[1]*Russia National Oncology Center, radiology, Moscow, RUSSIAN FEDERATION,* [2]*Russia National Oncology Center, Radiosurgery, Moscow, RUSSIAN FEDERATION*

Purpose/Introduction: Preoperative diagnostic of ovarian tumors (OT) is crucial to avoid unnecessary surgery of ovarian benign tumors (BOT) and women believed to have malignant ovarian tumors (MOT) require additional cytoreductive surgery followed by different type of chemotherapy with interval debulking surgery. Women with BOT may be either treated conservatively or undergo simple resection by a general gynecologist [1]. Dynamic Contrast-enhanced Magnetic Resonance Imaging(DCE MRI) could be used not only to assess the microcirculatory perfusion and vascular permeability in OT noninvasively, but provides a more comprehensive discrimination of OT according to the time-intensity curves (TIC) and some semi-quantitative parameters (SQP) [2]. The aim of our study is to evaluate the diagnostic efficacy of DCE-MRI with SQP analysis in BOT and MOT differentiating.

Subjects and Methods: This study included 66 patients (age range, 23–83 years; mean, 55 years): 16 patients with BOT, 34—with MOT and 16 patients without any diagnosed ovarian pathology. All images (T1WI, T2WI and DCE-MRI) were obtained on Magnetom Espree®1.5T Siemens-Germany. All tumors were histologically verified.

On DCE images, ROI, including ROI1 (OT) and ROI2 (myometrium), were selected. TIC were fitted to a logistic function with 4 SQP calculation: enhancement amplitude (EA), maximal slope (MS), time of half rising (THR), and initial area under curve at 60 s (IAUC60). Ratios of EA, THR, MS, and IAUC60 to same myometrial parameters were determined (EAr, THRr, MSr, and IAUC60r) and were compared in with BOT and MOT and with normal ovaries groups by the Mann–Whitney test with the Holm-Bonferroni correction for multiple testing.

Results: Significant difference in all 4 analyzed parameters was found between groups of BOT & normal ovaries and the MOT group as well as in BOT&MOT comparison ($p < 0,05$ for (EAr, THRr, MSr, and IAUC60r) (Image01). Difference in BOT group and women with normal ovaries wasn't statistically significant for all parameters. The mean value of EAr in BOT and MOT groups and "normal ovaries" group were 0.47, 0.76, 0.50, respectively. According to the ROC analysis, IAUC60r was the most relevant factor of BOT/MOT differentiation among TIC SQP (sensitivity 82%; specificity 91%) (Image02).

DCE MRI Parameters	MOT	BOT	normal ovaries	p-value between MOT & BOT	p-value between BOT & normal ovaries	p-value between MOT&BOT+normal ovaries
Enhancement amplitude ratio (EAr)	0,76	0,47	0,50	0,0068	0,37	0,001
Time of half rising ratio (THRr)	0,84	1,45	1,61	0,001	0,25	0,001
Maximal slope ratio (MSr)	0,96	0,23	0,20	0,006	0,41	0,002
$IAUC_{60}$ ratio	0,91	0,30	0,31	0,0003	0,477	0,001

Comparison of DCE MRI Parameters Between BOT, BOT and Normal Ovaries

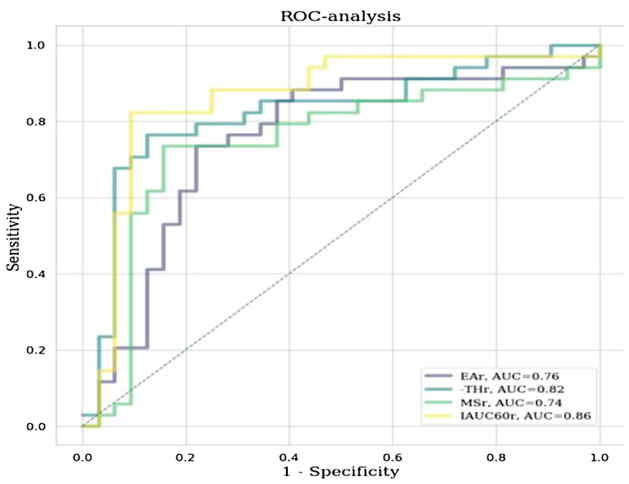

ROC curve for EA, MS, THR and IAUC60 ratios for discrimination of benign from malignant ovarian tumors.

Discussion/Conclusion: DCE-MRI is useful for differential diagnosis between BOT and MOT. TIC type III was specific for MOT and type I - for BOT. IAUC60r was the most accurate SQP of TIC for distinguishing BOT and MOT.

References:

1. Anthoulakisa C et al. 2014: MRI as the gold standard in the subsequent evaluation of ultrasound-indeterminate OT. Systematic review gynecologic oncology, 132(3):661-668.

2. Bernardin L, et al. (2012): Effectiveness of semi-quantitative multiphase dynamic contrast-enhanced MRI as a predictor of malignancy in complex adnexal masses: radiological and pathological correlation. Eur Radiol., 22:880-890.

S03.06

Quantitative dynamic contrast enhancement in uveal melanoma

M. Jaarsma-Coes[1], P. van Houdt[2], U. van der Heide[2], J.-W. Beenakker[1]
[1]Leiden University Medical Center, Radiology & Ophthalmology, Leiden, NETHERLANDS, [2]the Netherlands Cancer Institute, Department of Radiation Oncology, Amsterdam, NETHERLANDS

Purpose/Introduction: Uveal Melanoma (UM) is the most common primary ocular tumor. MRI is increasingly used in the diagnosis and follow-up of these patients[1], but quantitative techniques, such as dynamic contrast enhancement (qDCE), are hardly used although they might aid in diagnosis and prediction of metastatic disease[2,3]. Eye-motion, absence of large blood vessels and, B1 inhomogeneities makes qDCE of the eye challenging. The close proximity to air results in an inhomogeneous B1, even at 3T. In this abstract we present the steps taken to overcome these challenges to enable qDCE of UM.
Subjects and Methods: 6 patients diagnosed with UM were scanned on a 3T Philips MRI using a 47 mm surface coil. The variable flip angle method (FA: 2°, 5°, 9° & 15°) was used to obtain T1 maps from a linear fit of the Ernst Equation. All FA ware corrected using the obtained B1 map (DREAM). The DCE images were acquired using a steady-state gradient echo sequence (TR/TE/FA: 4.5 ms/2.3 ms/5; resolution:1.5 × 1.5 × 1.5 mm^3) with a contrast injection delay of 6 s. TWIST was implemented to increase the temporal resolution to 2 s/dynamic. Masked registration was performed in Elastix, since the eye can rotate within the FOV. Signal intensities were conversed to concentration (Ct) using formulas as used by Tofts.[4] A population-based AIF, an average of 10 AIFs in the carotid arteries, was used as input for the Tofts model.
Results: The B1 maps showed a median value of 87% in the tumours (5^{th} percentile: 73 and 95^{th} percentile: 103). Figures 1 and 2 illustrate the effect of B1 correction and registration on the T1 map, concentration and pharmacokinetic quantification. DCE quantification showed median K_{trans} values in the tumour between 0.1 and 0.5 min^{-1} and k_{ep} values between 0.9 and 2.6 min^{-1} (Fig. 3).

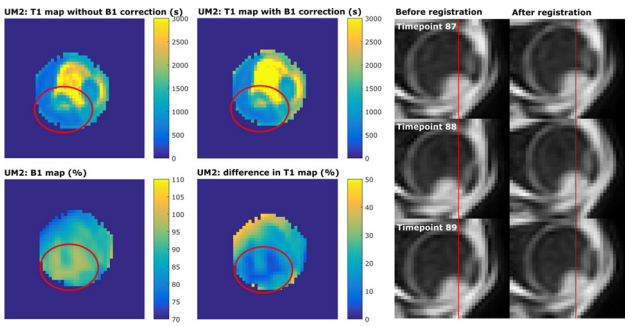

Figure 1: The effect of B1 inhomogeneities on T1 map and the effect of registration. In UM2 differences in tumour T1 ranged from 0-20%. Some other patients were even more affected. On the right an example of eye motion and minimized by registration.

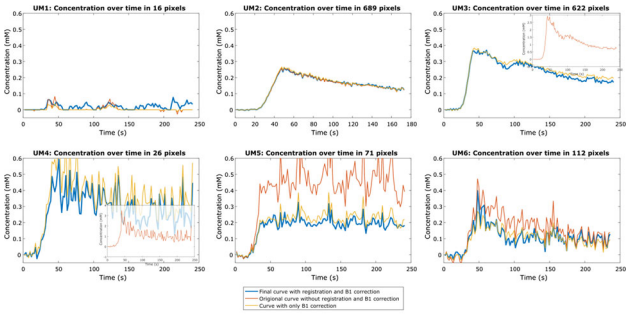

Figure 2: The influence of B1 correction and registration Ct. B1 inhomogeneities severely change the calculated T1 values thereby influencing the calculated Ct clearly visible in UM patient 3-5. More noise is observed in small tumours (UM1, 4-6).

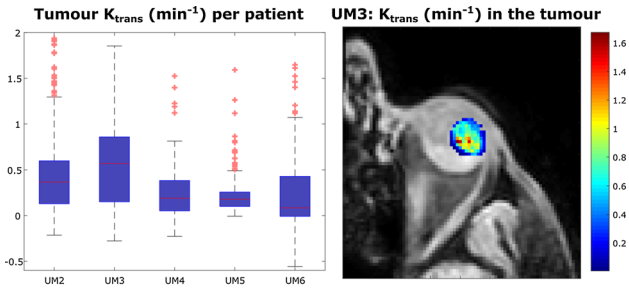

Figure 3: K_trans of the five larger tumours. The five tumours show quite inhomogeneous K_trans values. The median K_trans value is higher in UM 2 and 3 (0.4 & 0.6) compared to UM 4-6 (0.1 - 0.2).

Discussion/Conclusion: In this study we showed the feasibility of qDCE in the eyes, and the importance of correcting for B1 and eye motion. Due to the symmetry of the eye, small motion in the order of the voxel-size remained. The tumour of the first patient was very thin and caused problems in registration and quantification. In some voxels a negative K_{trans} was found, which could be caused by a mismatch in the registration or fitting errors. The obtained quantitative parameters of the five analyzed patients are slightly higher than the only other qDCE study performed in UM who found a K_{trans} between 0.0 and 0.2[2]. This might be explained by the absence of B1-correction and possibly by the difference in AIF. This method will be applied on the rest of the cohort of patients to investigate the possible role of qDCE in the diagnosis and follow-up of UM.
Acknowledgements: We would like to thank Kilany Hassan and Denis Shamonin for the help with the registration. This work is funded by NWO (146654).
References:
1. Ferreira, et al. *Cancers* 2019.
2. Wei, et al. *Journal of computer assisted tomograp hy* 2017.
3. Kamrava, et al. *Neuroradiology* 2015.
4. Tofts, *signal* 2010.

S03.07

Assessing histology structures by ex vivo MR microscopy texture analysis in peritoneal carcinomatosis implants

M. Tardieu[1], L. Khellaf[2], M. Cardoso[3], O. Sgarbura[2], P.-E. Colombo[2], C. Goze-Bac[3], S. Nougaret[1]
[1]Montpellier Cancer Research institute (IRCM), INSERM U1194, University of Montpellier, Montpellier, FRANCE, [2]Montpellier Cancer Institute (ICM), Montpellier, FRANCE, [3]L2C, UMR 5221,

BioNanoNMRI group, CNRS, University of Montpellier, Montpellier, FRANCE

Purpose/Introduction: Radiomics consists in the extraction, analysis, and interpretation of medical image characteristics based on shape, intensity or volume to derive so-called 'texture features'[1]. These features can be correlated with tumor diagnosis, genomics and/or prognosis[2]. To our knowledge, MR texture analysis (TA) have never been evaluated at a microscopic scale. In this proof of concept study, resected peritoneal implants were analyzed with MR microscopy, and TA maps were compared to histology.

Subjects and Methods: Peritoneal carcinomatosis implants from 8 patients were excised peroperatively and fixed in formalin solution. Fixed specimens were immersed in saline with 1% Gd-BOPTA during 1 h, then in fluorinert solution for imaging. MR acquisitions were performed on a 9.4T-MR scanner (Agilent Technologies) using a dedicated coil[3]. MRI experiments included high-resolution images and $90 \times 90 \times 180$ µm^3 resolution images for TA, using fat-suppressed T1w and T2w scans, with acquisition parameters presented on Table1. Images for TA were preprocessed following IBSI guidelines[4], TA maps were then extracted. After experiments, implants were cut into 3 mm sections according to MRI slice plane for H&E-stained histological analysis.

	High-resolution		Texture analysis acquisition	
Sequence	T1w GE MS	T2w SE MS	T1w GE MS	T2w SE MS
TR/TE (ms)	2000/9.14	2000/14.76	2000/9.14	2000/11.96
Flip angle	60°	-	60°	-
Scan time	34 min 12 s	25 min 40 s	17 min 8 s	25 min 40s
Averages	4	3	4	3
FOV	26×13 mm^2		46×23 mm^2	
Matrix	512×256		512×256	
Resolution	$51 \times 51 \times 300$ μm^3		$90 \times 90 \times 180$ μm^3	
Slices	30		40	

Table.1 Sequence parameters for high-resolution and texture analysis acquisitions, at 9.4 T. Both acquisitions were performed with fat-suppressed T1- and T2 weighted sequences

Results: For all 8 patients, ex vivo MR microscopy texture analysis was matched with histological images. Signal loss on MR images (as in Fig. 1, area #1 and #2) resulted on non cellular fibrous stroma on pathology whereas intermediate tissue signal was associated with cellular tissue. High density of tumor cells on histology was linked on TA maps to an increase homogeneity and uniformity scores and a decrease contrast score compare to stroma area or adipose tissue, as in Fig. 2 (area #2) (energy: 0.25 ± 0.12 vs 0.13 ± 0.10 (48%), homogeneity: 0.72 ± 0.09 vs 0.59 ± 0.12 (18%), contrast: 1.28 ± 2.21 *vs* 3.39 ± 3.10 (– 62%)). Normal tissue (such as liver, spleen or colon) adjacent to the peritoneal implants showed higher uniformity (energy) and homogeneity scores than the tumor, with lower contrast score. Hence, in Fig. 1, two parts are clearly visible: a liver section (upper part) and the tumor (bottom part) [energy: 0.23 ± 0.10 vs 0.18 ± 0.10 (22%), homogeneity: 0.70 ± 0.12 vs 0.65 ± 0.12 (7%), contrast: 0.79 ± 0.12 vs 2.18 ± 2.50 (− 64%)].

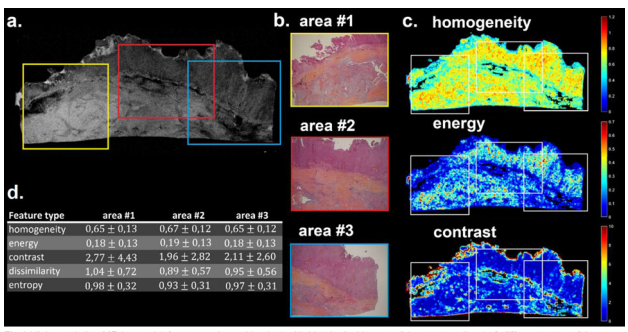

Fig.1 High-resolution MR image (a) for one peritoneal implant with histological images (b) corresponding to 3 different areas of the implant: yellow, red and blue squares on (a). TA maps of the implant (c) and TA mean values for each area (d)

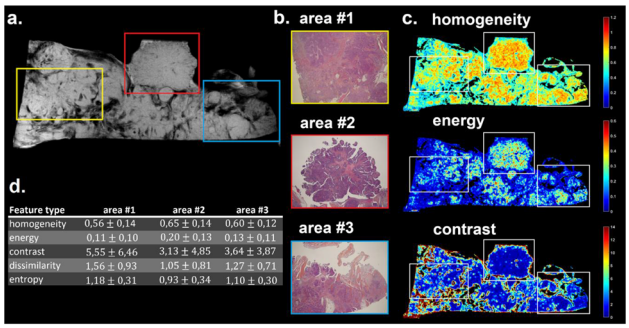

Fig.2 High-resolution MR image (a) for one peritoneal implant with histological images (b) corresponding to 3 different areas of the implant: yellow, red and blue squares on (a). TA maps of the implant (c) and TA mean values for each area (d).

Discussion/Conclusion: In this preliminary study, we showed the feasibility of imaging histological structures on resected implants, by combining high-resolution MR images and TA. For all 8 patients, ex vivo MR microscopy texture analysis was able to differentiate the different tissue content on histological images (tumor cells, stroma, adipose tissue…).

References:

[1]Haralick et al. IEEE 1973;6:610-621.
[2]Aerts. JAMA oncology, 2016;2(12):1636-1642.
[3]Coillot et al. JSSS 2016;5:137-145.
[4]Zwanenburg et al. IBSI. 2016.

S03.08

Daily IVIM and weekly DCE time trends in prostate cancer patients during radiation treatment

E. Kooreman[1], P. van Houdt[1], M. Nowee[1], V. van Pelt[1], A. Tree[2], W. Hall[3], U. van der Heide[1]
[1]The Netherlands Cancer Institute, Department of Radiation Oncology, Amsterdam, NETHERLANDS, [2]The Institute of Cancer Research and the Royal Marsden NHS Foundation Trust, Joint Department of Physics, London, UNITED KINGDOM, [3]Medical College of Wisconsin, Department of Radiation Oncology, Milwaukee, UNITED STATES

Purpose/Introduction: MR-linear accelerators (MR-linacs) are hybrid systems that can be used to deliver radiation treatment while simultaneously acquiring MR images. This creates the opportunity for daily treatment response monitoring. A candidate for measuring treatment response is tumor perfusion, which is typically measured using dynamic contrast-enhanced (DCE) MRI. However, due to the injection of contrast agent this is not feasible daily. A potential alternative for perfusion imaging is intravoxel incoherent motion (IVIM), which is a non-invasive method that gives information about the tumor microenvironment. Measuring these parameters daily and following their trends during treatment could lead to new insights. The aim of this study is to show feasibility of daily IVIM of patients during radiation treatment on an MR-linac, and to find if changes in IVIM parameters correlate to changes in DCE tracer kinetic analysis (TKA) parameters.

Subjects and Methods: Four prostate cancer patients were imaged daily during their treatment (20×3 Gy). Starting on the first fraction, a T2-weighted and DWI (IVIM) scan were acquired daily, and a DCE scan was acquired weekly on the Unity MR-linac. Scan are presented in Table 1. The extended Tofts model was used to derive tracer kinetic analysis (TKA) parameters K^{trans}, k_{ep}, v_e, and v_p. The bi-exponential IVIM model was fit to the DWI in a segmented fashion: the slow diffusion (D) and perfusion fraction (f) were derived from the high b-value (150 and 500) images, and then used to

determine the fast diffusion (D*) from the low b-value (0 and 30) images. The prostate was delineated on the T2-weighted image and propagated to the parameter maps. The mean value of these propagated delineations was used for further analysis.Linear trend analysis was performed, where Holm adjusted p-values were used to determine significance ($\alpha < 0.05$). Additionally, Pearson r was calculated for the time series of the different parameters using the five time points where both DCE and DWI were available.

	T2-weighted (3D TSE)	DWI IVIM (EPI)	DCE (3D FFE)
Field of view [mm]	400 x 448 x 250	430 x 430 x 60	220 x 251 x 60
Acquired voxel size [mm]	1.2 x 1.2 x 1.2	4 x 4 x 4	2.6 x 2.7 x 7
Reconstructed voxel size [mm]	0.5 x 0.5 x 1.2	1.9 x 1.9 x 4	1.6 x 1.6 x 3.5
Repetition time [ms]	1300	2960	4
Echo time [ms]	129	82	1.9
b-values [s/mm2] (averages)	-	0 (8), 30 (8), 150 (8), 500 (16)	-
Acquisition time [m:ss]	6:25 (NSA = 2)	5:11	5:05 (2.8 s p/dynamic)

MRI acquisition parameters.

Results: The change of the TKA and IVIM parameters over the course of radiation treatment is shown in Fig. 1. All TKA parameters show an increasing trend over the course of treatment. Linear trend analysis indicated a significant increase for the perfusion fraction f. Figure 2 shows the Pearson correlations between the parameters. Interestingly, the IVIM perfusion fraction f correlates strongly and significantly (non-adjusted $p < 0.05$) to k_{ep} and K^{trans}, and the IVIM diffusion D correlates to K^{trans}.

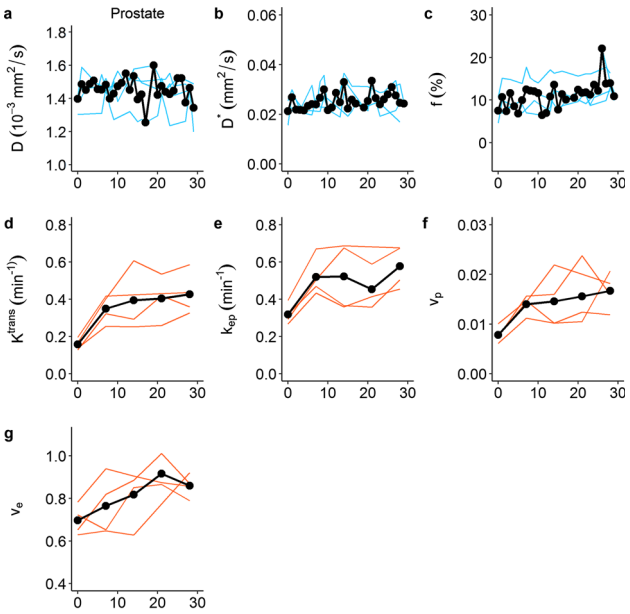

The change of TKA and IVIM parameters over the course of radiation treatment. The x-axis indicates days, starting at 0 on the first fraction. a, b, and c show parameters derived from the IVIM model, and d, e, f, and g parameters derived from TKA.

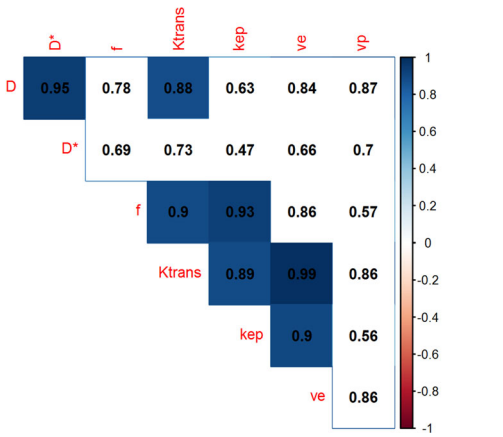

Correlation matrix of all parameters. The values and colors indicate Pearson r. Non-significant squares are white, significant (non-adjusted p < 0.05) squares are colored.

Discussion/Conclusion: This study demonstrates the feasibility of daily DWI on an MR-linac. Time trends are appearing, which is promising for treatment response monitoring. More patients are needed to determine if the trends will be significant. The strong correlations between some IVIM and TKA parameters suggest that IVIM has potential as an alternative method for perfusion imaging.

References: -

S03.09

Direct comparison of different methods proposed for enhanced conspicuity and discriminability of prostate cancer on diffusion-weighted imaging (DWI)

A. M. Sprinkart, C. Marx, W. Block, D. Thomas, G. Kukuk, P. Mürtz

University of Bonn, Dept. of Radiology, Bonn, GERMANY

Purpose/Introduction: To evaluate different post-processing methods of diffusion-weighted imaging (DWI) for the detection of prostate cancer (PCa): the calculation of exponential apparent diffusion coefficient (eADC)[1], computed high b-value (c_DWI)[2] maps, and a combination of both.

Subjects and Methods: 3T clinical routine DWI data with acquired b-values of 0, 50, 800 s/mm^2 of 104 consecutive patients with subsequent MR-guided prostate biopsy were included in this retrospective study. In addition to conventional ADC maps, standard eADC maps, cDWI maps, and additionally eADC maps for computed b-values of 2000 and 3000 s/mm^2 (c_eADC) were computed:

$$cDWI_b = S_0 * \exp(-ADC * b)$$

with b = 2000 and 3000 s/mm^2, and S_0 = signal intensity at b = 0 s/mm^2.

To obtain exponential ADC maps, the signal intensity at b = 800 s/mm^2 was normalized to S_0:

$$eADC = S_{800}/S_0.$$

In analogy to the standard eADC of the original DWI data, the cDWI images were also normalized to the signal intensity at b = 0, yielding the computed eADC:

$$c\_eADC_b = cDWI_b/S_0.$$

For each of 123 lesions, the contrast (CR) and contrast-to-noise ratio (CNR) were determined:

$$CR = (S_{lesion} - S_{normal}) / (S_{lesion} + S_{normal})$$

and

$$CNR = (S_{lesion} - S_{normal}) / SD_{normal}.$$

Differences in the CR and CNR of malignant lesions (n = 83) between the different image types and group differences between benign (n = 40), low-risk (Gleason score 6 and 7a, n = 53) and high-risk (Gleason 7b, 8, 9, n = 30) lesions were assessed by repeated measures ANOVA and one-way ANOVA with post hoc tests. The ability to differentiate between benign and malignant and between low-risk and high-risk lesions was assessed by receiver operating characteristic (ROC) curve analyses.

Results: Figure 1 shows the results for a 72-year-old patient with PCa in segment 6p.

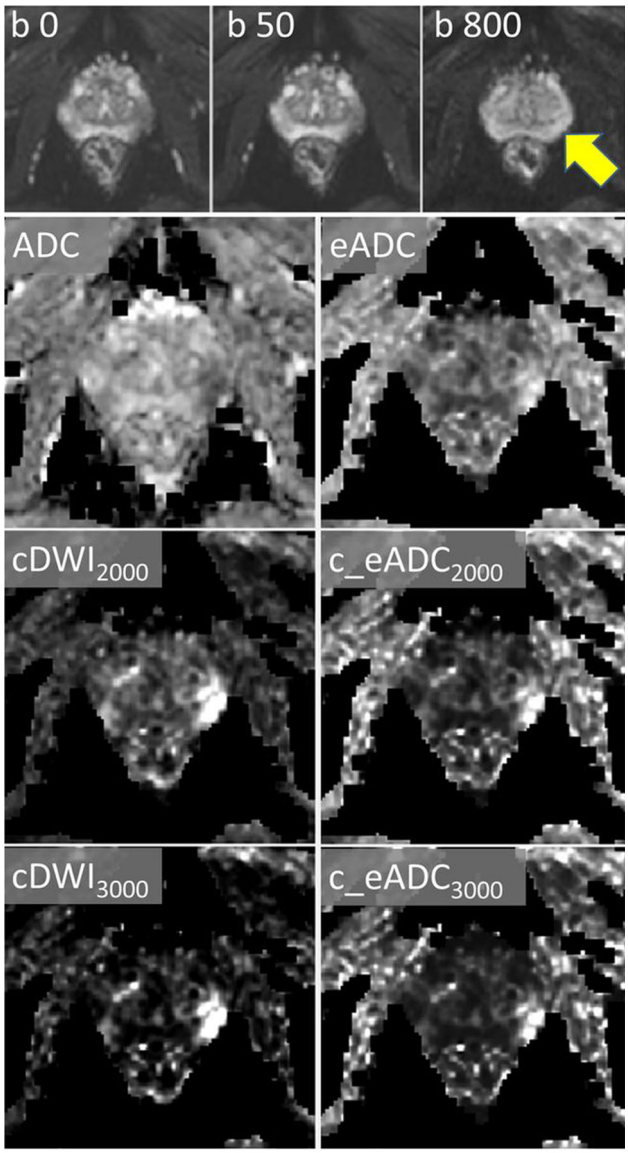

PCa appears inconspicuous on original DWI b800 image due to inverse T2-shine-through (yellow arrow). Computed DWI images at b = 2000–3000 s/mm² clearly yield highest lesion-to-normal-tissue contrast. Automated background suppression was applied.

The CR and CNR were higher for computed DWI and related c_eADC at b = 3000 s/mm^2 and 2000 s/mm^2 compared to original DWI, conventional ADC and standard eADC.

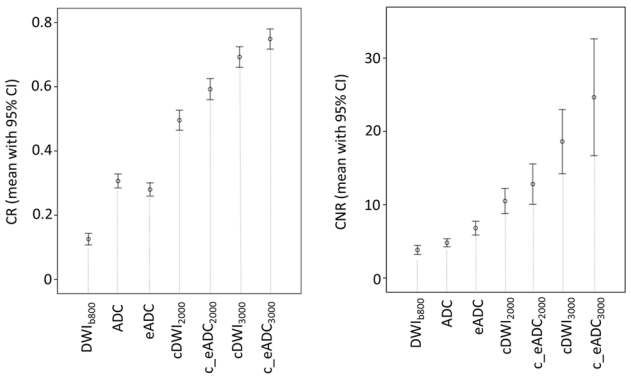

Overall results for contrast ratio (CR) and contrast-to-noise ratio (CNR) for the different image types

The highest AUC value for differentiation of benign and malignant lesions was obtained for conventional ADC (0.868, $p < 0.001$). For discrimination of low-risk from high-risk lesions, the CR of c_eADC_{3000} had the highest AUC (0.711, $p < 0.001$)

Discussion/Conclusion: Computed DWI and eADC at b-values between 2000 and 3000 s/mm^2 were superior to the original DWI b800, conventional ADC and standard eADC in the detection of prostate cancer. Standard eADC maps did not show any benefit over conventional ADC maps. Conventional ADC was best suited for discrimination between benign and malignant lesions, while computed eADC maps at high b-values may be helpful for discrimination between low-risk and high-risk lesions.

References:

1 Park et al., Br J Radiol 2016.
2 Maas et al., Investigative Radiology 2013.

L01 Lightning Talks

13:00–14:00 *The Stage*

Molecular Imaging, Spectroscopy & Animal Models

L01.01

Non-invasive imaging of vascular inflammtion during the onset and progression of angiotensin-II induced formation of abdominal aortic aneurysm in apoE deficient mice by $^{1}H/^{19}F$ MRI

S. Temme[1], M. Yakoub[2], P. Bouvain[1], C. Jacoby[1], J. Schrader[3], J. Stegbauer[2], U. Flögel[1]
[1]University of Düsseldorf, Molecular Cardiology/Experimental Cardiovascular Imaging, Düsseldorf, GERMANY, [2]University of Düsseldorf, Experimental Nephrology, Düsseldorf, GERMANY, [3]University of Düsseldorf, Molecular Cardiology, Düsseldorf, GERMANY

Purpose/Introduction: Abdominal aortic aneurysms (AAA) are a common disease associated with high mortality but reasons for the formation/progression of AAAs are still elusive. There is evidence that the renin-angiotensin system and inflammation are of crucial importance. Several modalities can be used to visualize the formation of AAAs, however detection of the inflammatory component of AAAs is still difficult. Our group has recently utilized perfluorocarbon nanoemulsions (PFC) which are preferentially taken up by monocytes and macrophages for detection of inflammation by combined $^{1}H/^{19}F$ MRI [1]. In the present study we aimed to apply this approach to monitor vascular inflammation and AAA-formation in angiotensin II-treated apoE deficient mice.
Subjects and Methods: $ApoE^{-/-}$ mice were treated with angiotensin II (1000 ng/kg/min) via osmotic minipumps and monitored longitudinally by $^{1}H/^{19}F$ MRI. Acquisition of anatomical ^{1}H reference images and MR angiography was performed using a flow compensated 2D flash sequence. PFCE-PFCs (10% PFCE) were injected immediately and on day 2 and 4 after minipump implantation. $^{1}H/^{19}F$ MRI datasets were acquired on day 2, 4, 7, and on day 10 using a ^{19}F RARE sequence. Flow cytometry and high resolution $^{1}H/^{19}F$ MRI of excised abdominal aortae was performed.
Results: ^{1}H MRI revealed that angiotensin II treatment led to the formation of AAAs in about 40% of the mice on day 10. The formation of AAAs could be detected by analysis of the outer vascular diameter rather than blood flow which was due to aortic dissection and subsequent thrombus formation. Moreover, we observed that AAAs developed at early (day 0-2), intermediate (days 2-7) and late (days 7-10) time points. To monitor vascular inflammation, we intravenously injected PFCs and subjected mice to $^{1}H/^{19}F$ MRI. As expected, we found strong ^{19}F signals in the area of the aneurysm but in some cases ^{19}F signals were also found in areas distant of the AAAs indicating widespread vascular inflammation. The amount of ^{19}F signal was also related to the time point of AAA-formation with the strongest signals in early AAAs. The localization of ^{19}F signals was verified by high resolution ex vivo $^{1}H/^{19}F$ MRI of isolated aortae. Histological analysis confirmed the presence of macrophages in this area and flow cytometry revealed higher numbers of immune cells in isolated aortae of AAA mice.

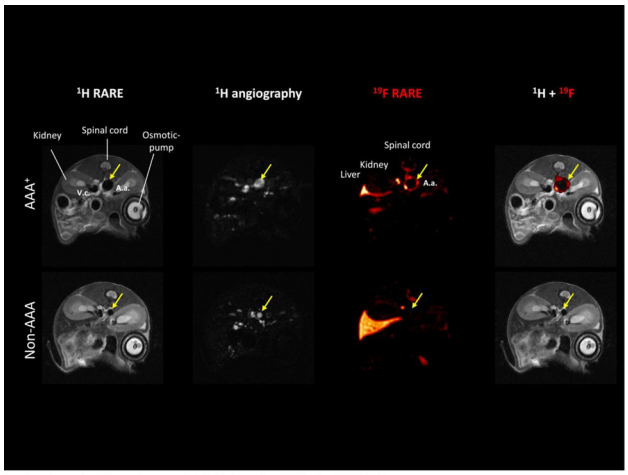

Imaging of vascular inflammation associated with formation of AAAs by 1H/19F MRI

Discussion/Conclusion: Here, we show that i.v. injected PFCs in combination with $^{1}H/^{19}F$ MRI is suitable to visualize vascular inflammation associated with AAA-formation. This may help to further elucidate the role of inflammation in AAA-formation and to monitor the impact novel therapeutics on AAA-formation and progression.
References:
Temme S, Bönner F, Schrader J, Flögel U. 19F magnetic resonance imaging of endogenous macrophages in inflammation. Wiley Interdiscip Rev Nanomed Nanobiotechnol. 2012 (3):329-43.

L01.02

Addressing long-term fate of iron oxide nanoparticles(ION) and specific MRI cell tracking by combining MRI and mass spectrometry with ^{57}Fe-ION

M. Masthoff[1], A. Beuker[1], R. Buchholz[2], U. Karst[2], W. Heindel[1], M. Wildgruber[1], **C. Faber**[1]
[1]University Hospital Muenster, Institute of Clinical Radiology, Muenster, GERMANY, [2]University of Muenster, Institute for Inorganic and Analytical Chemistry, Muenster, GERMANY

Purpose/Introduction: Iron oxide nanoparticles (ION) are common contrast agents for (pre-)clinical MRI, but signal is influenced by endogenous iron, hampering quantification of administered ION. We combine non-radioactive ^{57}Fe-ION MRI with laser-ablation-mass-spectrometry (LA-ICP-MS) for differentiation between endogenous iron (^{56}Fe) and applied ION.
We aim to assess distribution and long-term fate of ION, to correlate ION concentration to T2-relaxivity and to apply ^{57}Fe-ION for cell tracking.
Subjects and Methods: Healthy C57BL/6 mice were injected with custom engineered ^{57}Fe-ION (760 µmol Fe/kg body weight, Nano-PET, Berlin). For ION distribution T2-mapping of liver, spleen, kidney and brain was performed on a 9.4T small-animal MRI after 2 h, 1d, 3 day, 7 days, 30 days and 90 days (n = 5 each). For iron

amount/T2 correlation mice were injected with increasing ION dosage (51–760 µmol Fe/kg body weight). Mice were sacrificed and organs extracted for LA-ICP-MS to quantify ^{57}Fe and the ^{56}Fe/^{57}Fe isotope ratio.

To evaluate ^{57}Fe-ION for cell tracking mice were injected s.c. with a polyacrylamide-gel (pellet) to induce local inflammation. After 24 h first baseline MRI with T2-mapping of the pellet was performed, followed by i.v. injection of either ^{57}Fe-ION or PBS as control (n = 3 each). 24 h later MRI was repeated followed by histology and LA-ICP-MS.

Results: ^{57}Fe-ION MRI in combination with LA-ICP-MS enabled to specifically resolve local distribution and long-term fate of ION. ^{57}Fe of ION was first found in cells of the reticulo-endothelial-system (RES), but relocated to endogenous iron stores especially in spleen, blood and brain parenchyma after 90d (exemplarily for the spleen in Fig. 1).

A non-linear dependence of T2-relaxivity on increasing ION dosage was observed in the liver, likely resulting from ION packing and state during metabolic processing (Fig. 2). T2-relaxivity in the cell tracking model was mainly influenced by applied ^{57}Fe-ION, which were located in adjacent inflammatory tissue representing invaded labelled cells, and not by endogenous iron sources (Fig.. 3).

Figure 1

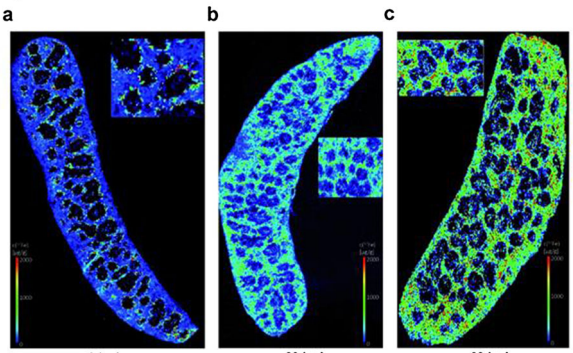

Exemplary quantitative 57Fe LA-ICP-MS distribution maps of the spleen at a) 3d, b) 30d, c) 90d after 57Fe-ION i.v. injection shows redistribution of 57Fe from the marginal zone, where RES cells are located, to endogenous iron sources in the red pulp.

Figure 2

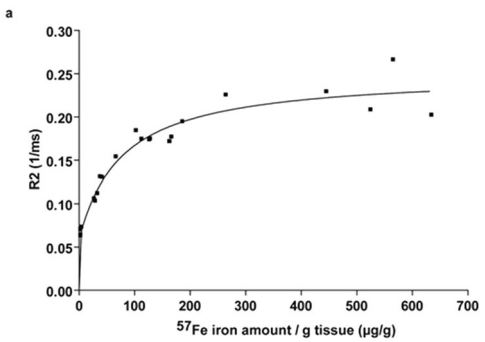

a) R2 (1/ms) over 57Fe (µg/g tissue) in liver as analysed by MRI UTE sequence and mass spectrometry (3d p.i.) with increasing i.v dose of 57Fe-ION. The graph doesn't show a linear dependence but rather a saturation curve of R2 on iron concentration.

Figure 3

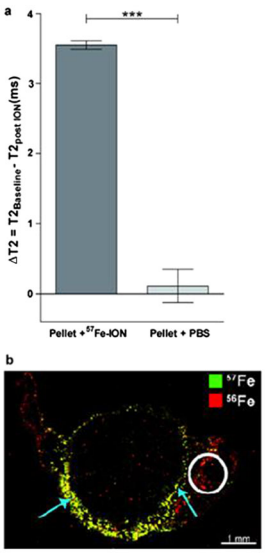

a) ΔT2 at the pellet boundaries was significantly higher for mice with 57Fe-ION as with control (***p<0.001). b) Exemplary LA-ICP-MS 57Fe and 56Fe overlay map of a pellet shows 57Fe from 57Fe-ION labelled cells at the pellet boundaries (blue arrows).

Discussion/Conclusion: Combining ^{57}Fe-ION MRI and LA-ICP-MS enables to study ION distribution and long-term fate, MRI iron quantification and validation of ION-based cell tracking in a specific, non-radioactive and quantitative manner.

References:

No references.

L01.03

Strategies to avoid isoflurane chemical shift artefacts in high sensitivity *in vivo* ^{19}F MRI

X. Staal[1], A. Veltien[2], N. K. van Riessen[1], A. Heerschap[1], M. Srinivas[1]

[1]*Radboudumc, Tumor Immunology Lab, Nijmegen, NETHERLANDS,* [2]*Radboudumc, Department of Radiology, Nijmegen, NETHERLANDS*

Purpose/Introduction: ^{19}F MRI is an increasingly popular imaging technique exploiting the benefits of background free imaging with the stable ^{19}F isotope in imaging agents mainly consisting of inert perfluorocarbons [1]. Isoflurane (ISO) is the anaesthetic of choice for preclinical imaging studies, however, as this compound contains ^{19}F, it can be a complicating factor, and may result in chemical shift artefacts (CSA). Currently, ISO artefacts are avoided by short imaging times, injection anaesthesia or chemical shirt imaging. Here, we show three distinct, easy to implement, strategies for avoiding ISO artefacts.

Subjects and Methods: A phantom consisting of 50% PFCE and 50% ISO was imaged as a proof of concept. For *in vivo*imaging, mice were injected with 20 mg PFCE containing nanoparticles [2] and imaged after 2 days. MRI was performed on an 11.7T BioSpec. A RARE sequence was used with 4 different parameter sets. (1) standard: TE = 15.2 ms, TR = 5000 ms[2]) out of plane shift with an extremely small bandwidth (3) suppression pulse (4) 3D selective excitation. *In vivo* imaging time was 12:48 min. For *in vivo*^{1}H reference scans a respiratory-gated FLASH was used.

Results: *In vitro* NMR spectra of the phantom show ISO and PFCE peaks (Fig. 1a), *in vivo*NMR spectra show two broad ISO peaks and one sharp PFCE peak (Fig. 1b)

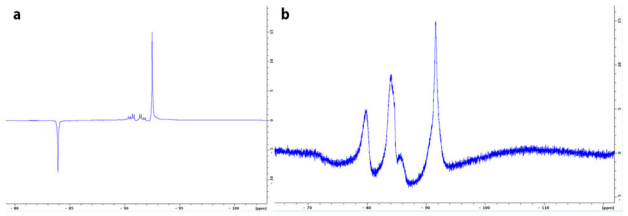

19F-spectra, a: in vitro, ISO F3 with negative phase at -84ppm, fragmented ISO F2 at -91ppm, PFCE at -92.5ppm. b, in vivo spectrum with the 2 broad ISO peaks and one sharp PFCE peak.

In vitro ^{19}F MRI shows the CSA when using a standard sequence(-Fig. 2a), a very narrow acquisition bandwidth shifts it out of plane(Fig. 2b). Figure 2c shows the ISO and PFCE signal a fair distance apart, either signal can be suppressed using a frequency selective 90° pulse before the excitation pulse.

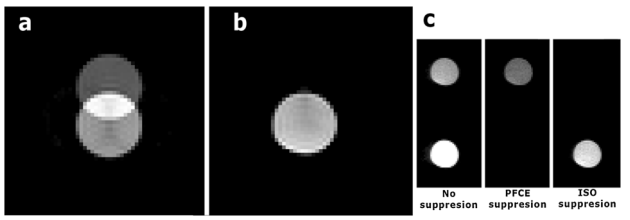

Figure2: in vitro imaging, a. standard imaging, b. shift ISO out of plane c. frequency specific suppression pulse. Note: in all images only one phantom is present

In vivo^{19}F MRI with a standard sequence shows the ISO problem; ISO CSA ghosts confound image interpretation and quantification (Fig. 3a). Shifting these signals out of plane is feasible in vivo, but results in susceptibility artefacts (Fig. 3b). An ISO suppression pulse results in effective in vivo suppression of ISO signals (Fig. 3c). Selective 3D slab excitation with a narrow excitation bandwidth results in artefact free images (Fig. 3d).

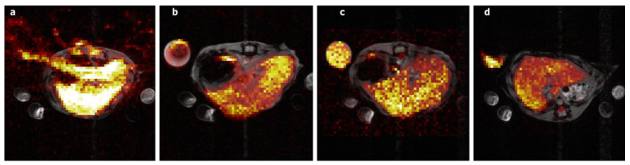

in vivo imaging 1H reference image 19F image in red hot. a. standard imaging with ISO ghosts, b. ISO artefact is shifted out of plane, clear 19F susceptibility artefacts, c. ISO suppression pulse d. selective excitation both without ISO artefacts.

Discussion/Conclusion: Preclinical ^{19}F MRI scan times are limed by isoflurane chemical shift artefacts, complicating imaging analysis and quantification. Here we show three strategies to avoid these chemical shift artefacts while maintaining a high signal to noise ratio. Having 3 different approaches allows for flexibility in sequence design.

References:

1. M. Srinivas, 2010; 28(7): 363-70.
2. E. Swider, RSC Adv. 2018; 8: 6460-6470.

L01.04
^{19}F-MR probe with tunable biodegradability

D. Jirak[1], N. Ziolkowska[1], A. Galisova[1], K. Kolouchova[2], O. Sedlacek[2], M. Hruby[2], M. Hajek[1]
[1]*Institute for Clinical and Experimental Medicine, Prague, CZECH REPUBLIC,* [2]*Institute of Macromolecular Chemistry, Prague, CZECH REPUBLIC*

Purpose/Introduction: Fluorine (^{19}F) magnetic resonance (MR) represents a promising diagnostic tool due to its high specificity allowing 'hot-spot' imaging. Based on our previous work with novel class of multiresponsive injectable fluorinated polymers with slow biodegradation [1], we present a modified probe with a tunable biodegradation rate of the implants while keeping their high content of fluorine. The goal was to confirm sufficient sensitivity of MR method for the implants imaging, to assess biocompatibility and to monitor biodegrability of implants using ^{19}F MRI in a long term in vivo study.

Subjects and Methods: Copolymers *P(DFEAM-ImPAM-HEAM) FIH1-5* were prepared by reversible addition-fragmentation chain transfer RAFT polymerization with *4-cyano-4-(dodecylsulfanylthiocarbonyl)sulfanyl]pentanoic acid* as chain transfer agent. A tunable biodegradation rate was achieved by introducing of a hydrophilic monomer unit, 2-hydroxyethyl acrylamide, what changed implants' hydrophilicity. Moreover, the increased polymer water-solubility facilitates the in vivo administration of these implants. Four different terpolymers were prepared and applied to rats into muscle and subcutaneously (males, Lewis, n = 16, 4 animals in each group, 200 µl to each site).

Long-term ^{19}F MR spectroscopy and imaging were carried out on a 4.7 T experimental MR scanner (MRS: single pulse, repetition time TR: 3000 ms, acquisition time TA: 1 min; MRI: turbo spinecho, TR: 1000 ms, echo time TE: 7 ms, turbo factor TF: 16, TA: 17 min, resolution: 1 × 1 × 13 mm^3) for 8 months. To check the feasibility of the probe for possible transition into human medicine, we performed in vivo measurements of one animal from group C (1 day after contrast administration) also at clinical scanners 3T, as a proof of principle.

Results: The ^{19}F MR signal was detected at the both injection sites in all animals and continuously decreased with different rate (Fig. 1). Probe with the slowest biodegradation was detected up to 8 months, ^{19}F MR signal of the second polymer was detected up to 6 months. Two remaining polymers possessed the fastest biodegradation; the signal reached the range of background within 14 days. Data are summarized in Table 1. Regular blood testing confirmed non-toxicity of the probes. A strong 19F MR signal was detected also at a clinical 3T MR scanner.

	Day 1	Day 3	Day 7	Day 14	2 months	6 months
Polymer 1	62%	50%	52%	50%	40%	11%
Polymer 2	22%	17%	14%	10%	7%	2%
Polymer 3	11%	9%	7%	4%	4%	no signal
Polymer 1	21%	11%	9%	10%	4%	no signal

The mean integral of the 19F spectra for a different animal group in different time points detected on 4.7T. The area was calculated within the ±3.5ppm from the maximum of 19F signal peak.

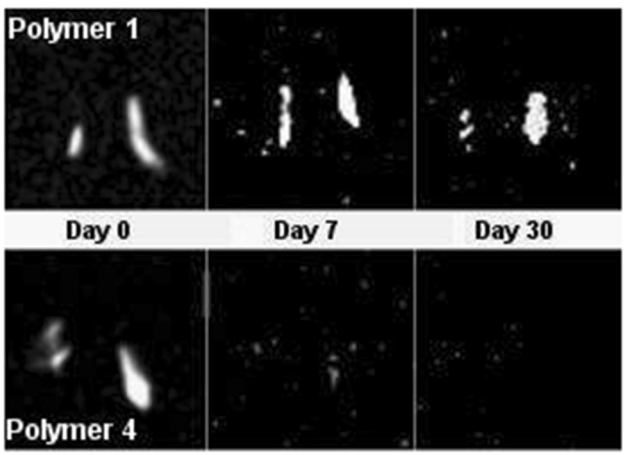

19F MR imaging of polymers with different biodegradability.

Discussion/Conclusion: MR imaging confirmed the presence of the injected probes which formed depots at the muscle and the subcutaneous area. The probes were non-toxic and had different biodegrability rate ranging from 1 week to 8 months. Sufficient MR sensitivity of the probe even at a clinical scanner and its tunable biodegradability suggest potential for its theranostic use.

Acknowledgement: MH CZ-DRO (Institute for Clinical and Experimental Medicine–IKEM, IN00023001).

References:

1. Sedlacek et al. Chemistry of Materials 2018; 30(15), 4892-4896.

L01.05

New class of biodegradable responsive phosphorus-containing contrast agent for $^{1}H/^{31}P$ MR

N. Ziółkowska[1, 2], D. Jirák[2], M. Hrubý[3], M. Vít[2], Z. Pechrová[3]
[1]Charles University, First Faculty of Medicine, Institute of Biophysics and Informatics, Prague, CZECH REPUBLIC, [2]Institute for Clinical and Experimental Medicine, Department of Computed Tomography, Magnetic Resonance and Clinical Experimental Spectroscopy, Prague, CZECH REPUBLIC, [3]Institute of Macromolecular Chemistry, Czech Academy of Sciences, Supramolecular polymer systems department, Prague, CZECH REPUBLIC

Purpose/Introduction: The aim of this project is to develop and to test a new class of biodegradable responsive phosphorus-containing contrast agent for $^{1}H/^{31}P$ MR. Presented probe is based on phytate crosslinked with Ca^{2+} ions doped with different concentrations of Fe^{3+} ions. Paramagnetic Fe^{3+} ions broaden the ^{31}P signal, making it invisible on ^{31}P MRI and could act as a probe for ^{1}H MR only. When the link is broken and Fe^{3+} is cleaved out the ^{31}P signal appears due to narrowing of its signal in the spectrum. This detachment is a response to physiological changes (lower pH in cancer tissue [1] etc.). Here we present pilot in vitro study focusing on the effect of iron on ^{31}P MR signal.

Subjects and Methods: Six samples with the same phosphorus concentration (1 mM) and different iron concentrations (Fe^{3+} replacing Ca^{2+} in the probe: 0.717071 μM, 25.4295 μM, 35.5867 μM, 92.7846 μM, 212.582 μM, 431.557 μM) were prepared. Fe^{3+} release from the probe was performed with deferoxamine, a compound possessing high affinity to Fe^{3+} ions. MR measurements were performed at 4.7T magnet with ^{1}H MR (RARE, TR/TE = 129/3.7 ms, 4 averages) for probes positioning. Probes properties were than assessed by ^{31}P MRS (Single pulse, repetition time TR = 1800, scan time ST = 30 min, 600 acquisitions), and ^{31}P MRI (CSI, TR = 1000, ST = 1h30 min, 30 acquisitions, resolution $2.1 \times 2.1 \times 5.8$ mm^3)

Results: MRS showed dependence of ^{31}P signal on iron concentration and confirmed its influence on ^{31}P signal widening: the highest ^{31}P signal was observed for 0.717071 μM of iron (Fig. 1). ^{1}H MRI of phantoms containing high amount of iron appear darker on T_2-weighted images (Fig. 2).

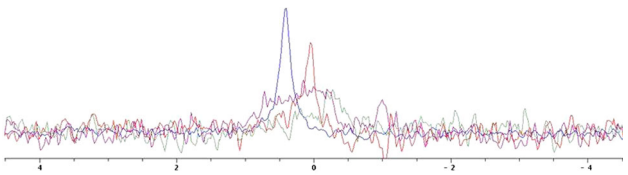

Fig. 1 31P MRS of calcium (II) phytate doped with different iron concentration: 0.717071 μM (blue), 25.4295 μM (red), 35.5867 μM (green) and 212.582 μM (purple) of iron; TR=1800.

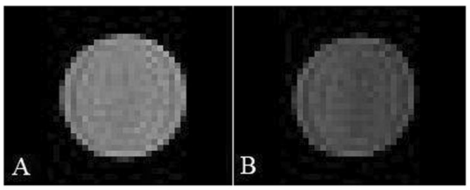

Fig. 2 T2-weighted 1H MR image of calcium (II) phytate doped with (A) 0.717071 μM and (B) 431.557 μM of iron.

Discussion/Conclusion: This bimodal responsive probes reflecting physiologic activity of environment [2] is extremely challenging. The advantages are that both ^{1}H and ^{31}P MRI represent two imaging modalities offering complementary information and can be easily combined at the same experiment. Our data confirmed the effect of iron on ^{31}P signal, so this approach could be used as a smart contrast agent changing its properties in presence and absence of the linked agent as a response to external stimulus.

References:

1. Kato, Y., et al. (2013). Acidic extracellular microenvironment and cancer. Cancer Cell Int., 13 (89).
2. Yoo, B. and Pagel, M.D. (2008). An overview of responsive MRI contrast agents for molecular imaging. Front. Biosci., 13, 1733-1752.

Acknowledgement: The study was supported by the Charles University, GA UK No 358119; Institute for Clinical and Experimental Medicine IKEM, IN00023001; Charles University, First Faculty of Medicine.

L01.06

Free radical mapping in the lung by OMRI using an accelerated 3D FSE sequence

A. Rivot, P. Massot, T. T. V. Pham, P. Mellet, E. Parzy, E. Thiaudière
Magnetic Resonance Center, UMR5536, CNRS, University of Bordeaux, Bordeaux, FRANCE

Purpose/Introduction: Free radicals are interesting contrast agents, which enhance NMR signal by polarization transfer from electron to surrounding protons (Overhauser effect) [1]. In living small animal, Overhauser-enhanced MRI (OMRI) with specific nitroxide probes can be used to reveal proteolysis[2]. In the case of lung inflammation, OMRI of the associated proteolysis needs further developments because of poor field homogeneity and low proton density. The purpose of this study was to evaluate 3D fast spin-echo(FSE) imaging for mapping free radicals in mouse lungs by OMRI.

Subjects and Methods: The instrumental OMRI setup includes a 0.194T MRI system (Cirrus Open, MRI-Tech, Canada) and an Electron Paramagnetic Resonance (EPR) cavity (Bruker, Wissembourg, France). The FSE sequence parameters were: TR/TE = 9 ms/600 ms; FOV : $64 \times 32 \times 32$ mm^3. To decrease the acquisition time in OMRI experiments, partial k-space was acquired with a keyhole scheme[3]. The full k-space matrix was $64 \times 64 \times 64$, acquisition time: 10 min. The undersampled matrix was $64 \times 32 \times 32$ acquisition time: 38 s.

This sequence was used to image lung and to determine Overhauser enhancement after intra tracheal instillation of 50μL of 3 carboxyproxyl nitroxide at 100 mM in female mice (CB57/CRL, n = 6 Charles River, France).

Results: Keyhole OMRI acquisition allowed fast 3D FSE imaging of nitroxide distribution in mouse lungs. Control images displayed SNR of 7.8 ± 1.4 in lungs. Overhauser effect was observed 3 min after nitroxide instillation. Overhauser enhancements of 3 could be generated in the lung (Fig. 1). In various areas signal decreased with a

phase inversion, denoting the presence of low-concentrated nitroxides.

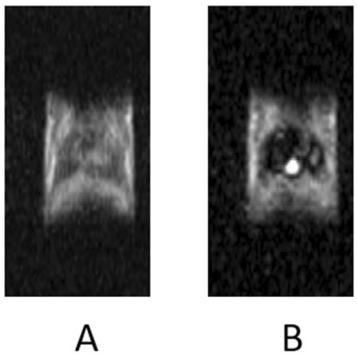

Figure 1 : OMRI of nitroxyde in mouse lung. A : Control image without EPR. B : Image with EPR (Overhauser effect)

Discussion/Conclusion: The keyhole approach allowed a marked reduction in acquisition time, making 3D-FSE-OMRI possible without adverse heating. No significant flaw in image quality was observed upon keyhole reconstruction. The use of specific nitroxide probes should permit detection of abnormal proteolysis through OMRI in the case of lung inflammation.

References:

1. Overhauser, A.W., *Phys Rev* 92, 411-415 (1953).
2. Koonjoo, N. et al. *Contr Media & Mol Imag* 9, 363–371 (2014).
3. Vaals, Joop J. Van et al. *Journal of Magnetic Resonance Imaging* 3(4): 671-75.

L01.07

Reliability and reproducibility of ^{1}H-MR Spectroscopy for measurement of cerebral glutathione

A. Anton[1], R. A. Edden[2], I. D. Wilkinson[1]
[1]*University of Sheffield, Academic Radiology, Sheffield, UNITED KINGDOM,* [2]*The Johns Hopkins University School of Medicine, Baltimore, MD, UNITED STATES*

Purpose/Introduction: Glutathione (GSH) is an important antioxidant in the human brain, and marker of oxidative stress, implicated in aging and various psychiatric and neurodegenerative conditions[1]. However, it is difficult to estimate using standard, one-dimensional, non-editing MRS, such as PRESS, due to low concentrations (< 4 mM) and resonances that overlap with other metabolites[1]. Editing sequences such as MEGA-PRESS were developed to alleviate this uncertainty and confer more confidence and reliability in quantifying GSH[2]. Moreover, it has been shown that at 3T, physiological GSH concentrations cannot be reliably measured from PRESS spectra, whilst MEGA-PRESS acquisitions allow accurate quantification of GSH[3]. Only one very recent study reported test–retest reproducibility of GSH quantification from GSH-edited MEGA-PRESS spectra (N = 10 young HVs scanned twice 15 min apart, CV = 13.5%)[4].

The aim of the current study was to assess the reproducibility of GSH quantification from MEGA-PRESS spectra intra-day, as well as 1 month apart.

Subjects and Methods: A 3T MR system with a 32 channel radiofrequency head coil (*Ingenia,* Philips, NL) were used to scan 6 healthy volunteers (2F 4 M, 32-66 years, mean ± SD: 51 ± 12.5 years) three times on two visits (V1 and V2): one scan performed at V1 and two consecutive scans at V2, 1 month after V1. MEGA-PRESS spectra were acquired from two cubic 27 cm^3 voxels placed (Fig. 1) in motor and occipital cortex (TE/TR = 120[5]/2000 ms, 256 dynamics, NSA1, acquisition time: 8.5 min. + 16 s unsuppressed H_2O spectra – internal reference). GSH concentrations were estimated in AMARES[6], jMRUI[7].

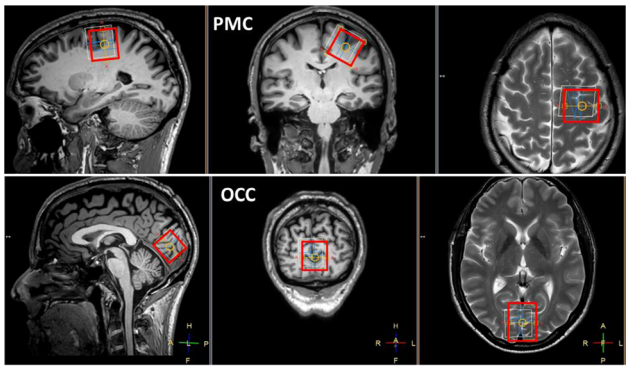

Fig. 1. 3x3x3 cm3 MRS voxels positioning in PMC (up) and OCC (bottom).

Results: The mean ± SD GSH concentrations were 2.25 ± 0.43 mM in motor cortex (PMC) and 2.57 ± 0.89 mM in occipital cortex (OCC). All calculated coefficients of variation (CV) between any two repeated GSH measures were below 7%. For the intra-day-repeat (between scans at V2), the mean CV was 2.2% in PMC and 1.8% in OCC. The mean CV for monthly repeat was 3.9% in PMC and 2.8% in OCC.

Discussion/Conclusion: All GSH concentrations were in the expected range. The CVs compare favourably to literature CVs[4] and show high precision for GSH estimation, due to data quality and AMARES fitting (Fig. 2), adaptable to spectra particularities.

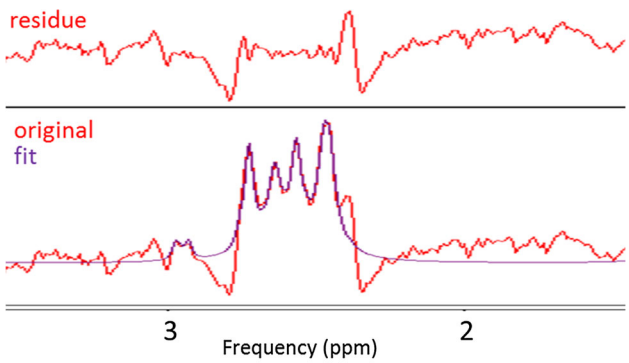

Fig. 2. Example of an "original" GSH-edited spectrum (bottom, red), the corresponding fit (bottom, purple) and the residue (up, red, residue = original - fit).

In agreement with previously reported data[3], our findings suggest that appropriate acquisition and analysis techniques used herein yield repeatable, accurate and precise human GSH measurement, applicable for longitudinal human studies and clinical trials.

References:

[1] C.D.Rae and S.Williams, Analytical Biochemistry,2017;529:127-143.
[2] M.Terpstra et al., Magn.Reson.Med.,2003;50(1):19–23.
[3] F.Sanaei Nezhad, A.Anton, et al., Magn.Reson.Med.,2017;78(4): 1257-1266.
[4] S.A.Wijtenburg et al.,J. Magn.Reson.Imaging,2019;49(1):176-183.
[5] K.L.Chan et al., Magn.Reson.Med.,2017;77:498–504.
[6] L.Vanhamme et al.,J.Magn.Reson.,1997;129:35–43.
[7] D.Stefan et al.,Meas.Sci.Technol.,2009;20(10):104035.

L01.08

Estimation of T_2 Relaxation Times and Absolute Quantification of Metabolites in the Human Brain at 9.4 T

S. Murali-Manohar[1], T. Borbath[1], A. Henning[2]
[1]*Max Planck Institute for Biological Cybernetics, MRZ, Tuebingen, GERMANY,* [2]*UT Southwestern Medical Center, Advanced Imaging Research Center, Dallas, Texas, UNITED STATES*

Purpose/Introduction: For the absolute quantification[1] of metabolites, appropriate T_2 relaxation times must be used in the calculation. T_2 relaxation times are usually specific to the sequence, tissue type, and region of interest in the human brain. Deelchand et al.[2], reported T_2 relaxation times of singlets at 9.4 T. In this work, T_2 relaxation times of both singlets and J-coupled metabolites are reported for a GM rich voxel in the occipital region in the human brain at 9.4 T for the first time. The absolute concentrations mmolal (mmol/kg) of the metabolite peaks are also calculated.

Subjects and Methods: A TE series of metabolite-cycled semi-LASER[3] spectra were acquired on 11 healthy volunteers (TE:24, 32, 40, 52, 60 ms; TR: 6000 ms; NEX:96) with the transmit reference frequency set at 7.0 ppm and another spectra (TE/TR: 24/6000 ms, NEX:32) was acquired with the transmit reference frequency set at 2.4 ppm for absolute quantification. Tissue volume fractions were obtained from MP2RAGE image segmentation. Also, water reference spectra (NEX: 16) were acquired using semi-LASER sequence in order to avoid any influence of MC pulses.

The raw data were pre-processed and were fit using LCModel-v6.3-1L[4]. The concentrations were fit to a mono-exponential decay across the TE series in order to estimate the T_2 relaxation times of the metabolite peaks. The concentrations of the metabolites were absolutely quantified using the formula given by Gasparovic et al.[1] including correction factors. T_1 and T_2 relaxation times of water at 9.4 T were taken from Hagberg et al.[5]. T_1 relaxation times of metabolites were considered from Wright et al.[6], and T_2 relaxation times calculated from this work were taken.

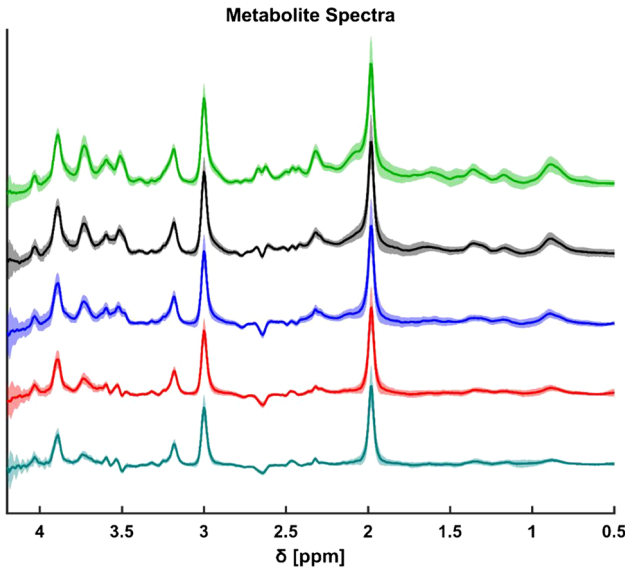

Fig. 1: Echo time series of metabolite spectra with inlay of voxel position

Results: TE series of metabolite spectra is shown in Fig. 1.

	T_2 Summed [ms]	T_2 ± Std [ms]	R^2 ± Std
Asp	72.01	73.12 ± 38.59	0.61 ± 0.20
tCr(CH_3)	95.24	100.21 ± 15.97	0.90 ± 0.10
tCr(CH_2)	95.39	81.82 ± 10.80	0.83 ± 0.08
Glu	76.79	87.00 ± 23.29	0.73 ± 0.10
Gln	65.9	50.27 ± 10.78	0.75 ± 0.16
GSH	70.65	74.04 ± 32.34	0.71 ± 0.12
Glyc	58.2	62.27 ± 10.87	0.48 ± 0.11
mI	84.52	90.05 ± 18.02	0.70 ± 0.09
NAA(CH_2)	90.36	102.17 ± 23.76	0.92 ± 0.12
NAA(CH_3)	104.86	110.49 ± 27.74	0.93 ± 0.12
NAAG	37.68	43.48 ± 16.30	0.83 ± 0.15
tCho+	80.42	90.11 ± 23.53	0.92 ± 0.11
tNAA+	93.22	100.57 ± 21.84	0.93 ± 0.11
mI+Glyc	77.81	84.44 ± 16.79	0.77 ± 0.12
Glx	72.83	75.92 ± 15.68	0.73 ± 0.12

Table 1: T2 relaxation times from summed and individual spectra with standard deviation

The calculated T_2 relaxation times for the summed spectra from 11 healthy volunteers and the mean from T_2 values for individual spectra with standard deviations are reported in Table 1, which are overall in a good agreement. All reported T_2 relaxation times show the expected negative correlation with increasing the field strength[7,8].

	Absolute Conc. with T_2 correction	Absolute Conc. without T_2 correction
Alanine	-	-
Asp	4.52 ± 0.79	3.25 ± 0.57
Asc	-	-
Cr	5.99 ± 0.94	4.60 ± 0.72
PCr	4.68 ± 0.96	3.60 ± 0.74
GABA	0.93 ± 0.63	0.70 ± 0.47
Glucose	-	-
Gln	6.83 ± 1.08	4.24 ± 0.67
Glu	10.53 ± 0.74	7.99 ± 0.56
Glyc	1.47 ± 0.23	1.00 ± 0.16
GSH	2.29 ± 0.28	1.65 ± 0.20
Lac	-	-
mI	5.57 ± 0.71	4.27 ± 0.54
NAA	12.14 ± 0.86	9.69 ± 0.69
NAAG	1.26 ± 0.29	0.72 ± 0.17
tCho	1.20 ± 0.13	0.92 ± 0.10
PE	1.83 ± 1.03	1.40 ± 0.79
Scyllo	0.23 ± 0.08	0.17 ± 0.06 [c]
Tau	2.17 ± 0.48	1.63 ± 0.36
NAA+NAAG	12.91 ± 0.72	10.31 ± 0.57
mI+Glyc	7.03 ± 0.80	5.29 ± 0.60
Cr+PCr	10.64 ± 0.36	8.17 ± 0.27
Glu+Gln	16.81 ± 1.52	12.26 ± 1.11

Table 2: Absolute concentrations in mmolal for metabolite peaks

Absolute concentrations in mmolal with and without T_2 correction are shown in Table 2 for a fair comparison between this work and other studies[2,9] which do not include T_2 correction. The values with T_2 correction also agree with Marjanska et al.,[8] except for minor discrepancies which could be from small deviations in the calculation of T_2 values.

Discussion/Conclusion: T_2 relaxation times of most of the metabolite peaks at 9.4 T in the human brain are reported in this work for the first time. Also, the absolute concentrations of the metabolites are reported in mmolal units.

References:

1. Gasparovic et al., MRM 2006.
2. Deelchand et al., J Magn Reson 2010.
3. Giapitzakis et al., MRM 2017.
4. Provencher et al., 2005.
5. Hagberg et al., NeuroImage 2017.
6. Wright et al., ISMRM, 2019.
7. Wyss et al., MRM 2018.
8. Marjanska et al., NMR Biomed 2012.
9. Mekle et al., MRM 2009.

L01.09

Hepatic water T_2 is longer in the morning vs. evening in healthy lean subjects

J. Mevenkamp[1], P. Veeraiah[1], K. H. M. Roumans[2], J. E. Wildberger[1], P. Schrauwen[2], V. B. Schrauwen-Hinderling[1], L. Lindeboom[1]

[1]Maastricht University Medical Center, Departments of Radiology and Nuclear Medicine, Maastricht, NETHERLANDS, [2]Maastricht University, Nutrition and Movement Sciences, Maastricht, NETHERLANDS

Purpose/Introduction: Water is commonly used as an internal reference for absolute quantification of metabolites in proton magnetic resonance spectroscopy (^{1}H-MRS). A reference is required to be stable, but the MR relaxation processes of water may be influenced by macromolecules. We hypothesize that changes in liver glycogen concentrations will affect T_2 relaxation of water. Therefore, we measured the T_2 of water in the postprandial and twelve hours fasted state.

Subjects and Methods: All experiments were performed on a 3T MR system (Philips Achieva 3T-X, Philips Healthcare, The Netherlands). Phantoms with different concentrations (15, 30, 45 and 60 g/l; 500 ml; 0.9% NaCl) of corn starch as glycogen substitute were used to determine changes in water T_2. These concentrations were assumed to cover the physiological range of liver glycogen concentrations [1]. Water T_2 relaxation time in phantoms was determined by using STEAM with varying TE (Voxel: 30 × 30x30 mm; TE: 29, 44, 59, 74, 89 and 200 ms; TR: 4000 ms) and by fitting an exponential function to the water intensities. The in vivo hepatic water T_2 was determined in five lean healthy subjects, three hours after a carbohydrate rich dinner (postprandial) and after an overnight fast of twelve hours (fasted). Again, STEAM with varying TE (Voxel: 30 × 30 × 30 mm; TE: 10, 20, 30, 40, 50, 60, 70 and 80 ms; TR 4000 ms) was used to determine water T_2. Additionally, in three of the subjects, liver glycogen levels were measured by acquiring non-localized ^{13}C NMR spectra (FID; TR: 280 ms; NSA: 4096) with a 21 × 24 cm ^{13}C quadrature detection surface coil (RAPID Biomedical GmbH, Germany), no decoupling was applied. Data analysis was performed with an in-house developed Matlab script.

Results: Water T_2 increased in lean subjects from postprandial to fasted state by an average of 7.2 ± 2.8 ms (Fig. 1, N = 5). Liver glycogen levels decreased in the same period by 16.2 ± 4.3% (Fig. 2, N = 3). Phantoms with increasing corn starch concentrations show decreasing water T_2 relaxation times (Fig. 3).

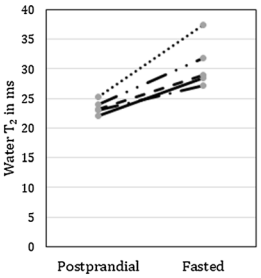

Figure 1: Water T2 three hours after meal (postprandial) and after an overnight fast of at least 12 hours (fasted). An average increase in water T2 of 7.24 ±2.75ms (N=5) from postprandial to fasted state was observed

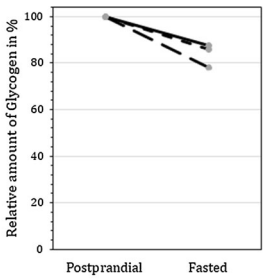

Figure 2: Changes in liver glycogen between three hours after dinner (postprandial) and subsequent overnight fast (fasted), determined by 13C MRS (N=3). Postprandial glycogen scaled to 100%, fasted glycogen level relative to postprandial

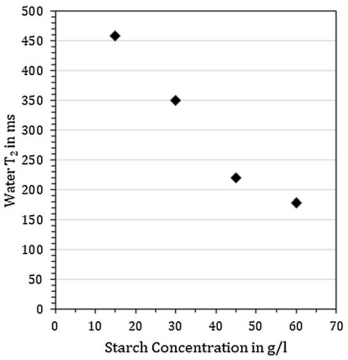

Figure 3: Water T2 dependence on corn starch concentrations measured in phantoms. Increasing the starch concentration results in decreased water T2 values

Discussion/Conclusion: The in vivo water T_2 in the liver appears to decrease in the postprandial state, when compared to the fasted state in healthy lean subjects, concomitant with increased glycogen levels. Similarly, we found in phantoms that a higher macromolecular concentration decreased the water T_2. These findings are important when designing intervention studies or when comparing liver metabolite concentrations over the day. Furthermore, it is very interesting to note that the T_2 of water seems to be an indicator of glycogen status. Therefore, these results might give a lead towards an indirect measurement of liver glycogen.

References:

[1] J. Jensen et. al. 2011.

L01.10
Protein unfolding affects the sodium triple-quantum signal

D. Kleimaier, R. Hu, L. R. Schad
Heidelberg University, Computer Assisted Clinical Medicine, Mannheim, GERMANY

Purpose/Introduction: Sodium triple-quantum (TQ) techniques have received attention due to the higher intracellular sensitivity compared with single-quantum (SQ) techniques[1,2]. A TQ signal arises in the interaction of sodium ions with negatively charged e.g. carboxyl groups of proteins[3]. The protein and sodium concentration affect the TQ signal strength while protein conformational changes, occurring in e.g. cancer, have not been considered yet[2,4]. We hypothesize that protein conformational changes affect the total number of accessible, negatively charged groups, therefore altering the TQ signal strength. We used a TQ spectroscopic sequence (TQTPPI) for the simultaneous measurement of the TQ and SQ signal[3]. Nonlinear fitting of the TQTPPI FID allows to entangle the contribution of the transversal relaxation times and of the TQ amplitude to the TQ signal[3].
The hypothesis was investigated by urea unfolding of the protein bovine serum albumin(BSA). The TQ signal changes were correlated to fluorescence measurements (gold standard).
Subjects and Methods: Data was acquired on a 9.4T preclinical MRI(Bruker, Germany) equipped with a $^{1}H/^{23}Na$ volume coil. T_1 was measured by an inversion recovery to determine $T_R = 5T_1$ for the TQTPPI sequence (Fig. 1). The TQTPPI FID was nonlinearly fitted[3] to obtain the SQ and TQ amplitude(A_{SQ} and A_{TQ} respectively), and the transversal relaxation times.
Two sets of phantoms (pH = 7) were used:

1. Unfolding measurement: 154 mM NaCl and 5%w/v BSA with [0,1,2,3,4,5,5.5,6,7,8] M urea
2. Control: 154 mM NaCl with [0,5.5,10]M urea

Fluorescence spectra(Tecan, Switzerland) were excited at 295 nm and acquired between 320-400 nm. Pearson correlation coefficient(PCC) was calculated between the integrated fluorescence spectra and the A_{TQ}/A_{SQ} ratio.

a)

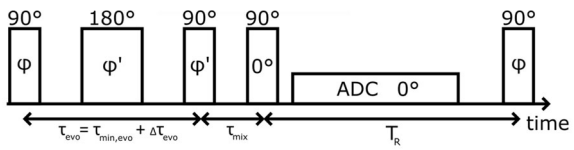

b)

Sequence	Sequence parameters
TQTPPI	$T_R = 5T_1$, 7 Repetitions, 3 Averages, 1024 points, $\Delta\tau = 25\,\mu s$, $\Delta\tau_{evo} = 200\,\mu s$, 8 phase steps, 100 phase cycles
Inversion Recovery	$T_R = 5T_1$, 3 Repetitions, 8 Averages, 1024 points, $\Delta\tau = 25\,\mu s$, 125 inversion times

c)

Urea [M]	T_1 [ms]	T_2 [ms]
0	53.5 ± 0.1	50.6 ± 0.1
5.5	35.4 ± 0.1	34.7 ± 0.1
8	26.1 ± 0.1	25.2 ± 0.1

Fig.1:a) The TQTPPI sequence is shown. b) The sequence parameter for the TQTPPI sequence as well as the inversion recovery sequence are listed. c) Addition of urea to 154mM NaCl solution resulted in a reduction of both relaxation times.

Results: Control measurements resulted in a nonsignificant TQ signal(SNR < 2) compared to a significant TQ signal(SNR > 25) for the unfolding measurements (Fig. 2). Therefore, the addition of urea resulted in no TQ signal but shortened the relaxation times (Fig. 1).

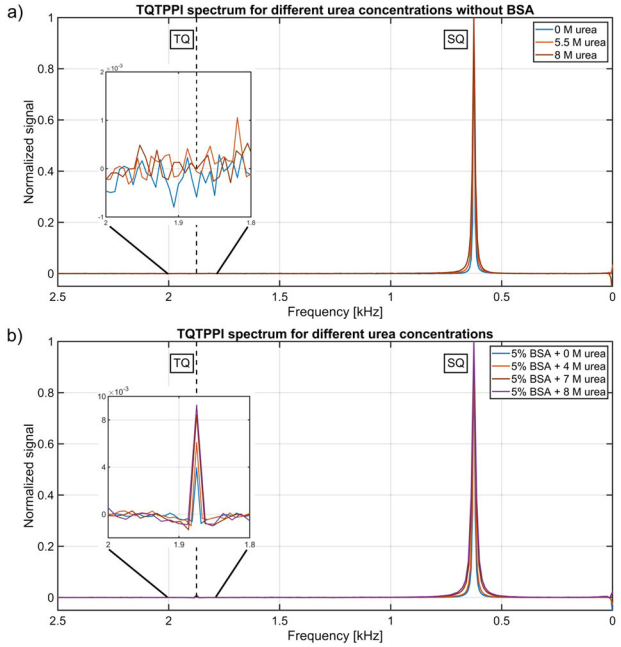

Fig.2:a)Addition of different urea concentrations to 154mM NaCl resulted in a nonsignificant TQ signal. b)While addition of different urea concentrations to 5%BSA altered the TQ signal caused by changes in the relaxation times and the TQ amplitude.

The relative change of A_{TQ}/A_{SQ} ratio showed the characteristic sigmoid shape during the transition of native to unfolded BSA (Fig. 3). The PCC = − 0.99 ($p < 0.01$) implies a negative linear correlation as the A_{TQ}/A_{SQ} ratio increased during the unfolding contrary to the reduction of the fluorescence signal.

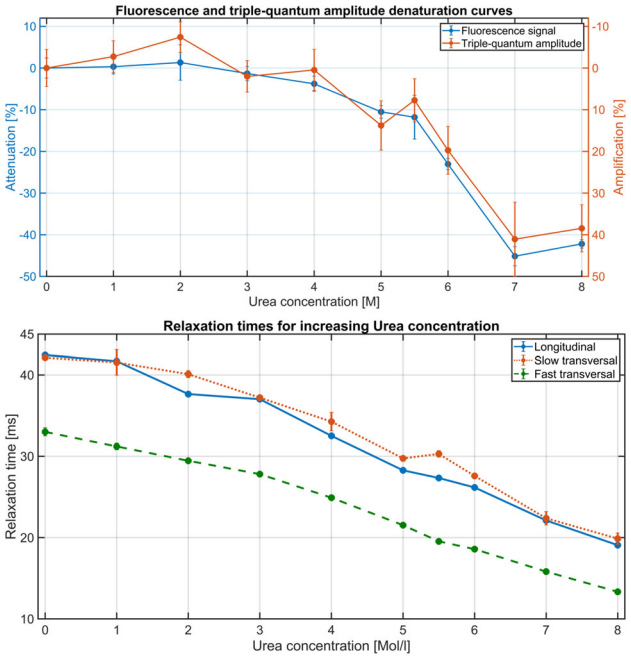

Fig.3:a)Fluorescence signal as well as the ATQ/ASQ ratio show the same characteristic sigmoid shape with a high negative linear correlation to each other(PCC=−0.99). b)Shortening of the relaxation times is primarily caused by the addition of urea.

Discussion/Conclusion: The shortening of all relaxation times arose primarily from the addition of urea while the A_{TQ}/A_{SQ} ratio increase was caused by the unfolding of BSA due to a higher number of accessible, negatively charged groups.
The excellent correlation of the TQ signal with the fluorescence signal during the unfolding of BSA indicates a TQ signal dependency on the

protein conformation. This should be considered when the TQ signal is applied as an intracellular sensitive parameter in diseases associated with protein conformational changes.

References:
[1]Fiege MRM 2013.
[2]Schepkin MRM 1998.
[3]Schepkin JMR 2017.
[4]Torres MRC 2005.

L01.11

An in vivo proton magnetic resonance spectroscopy study with multi-echo-time technique for concurrent quantification and T2 measurement targeting glutamate

C.-H. Yoo[1], H.-M. Baek[2], D.-C. Woo[3], B.-Y. Choe[1]
[1]The Catholic University of Korea, Seoul, SOUTH KOREA, [2]Gachon University, Department of Health Sciences and Technology, Incheon, SOUTH KOREA, [3]Asan Medical Center, Asan Institute for Life Sciences, Seoul, SOUTH KOREA

Purpose/Introduction: As a tool for investigating brain metabolism, the value of in vivo proton magnetic resonance spectroscopy (^{1}H MRS) has been increasing with application of high-field and short-echo-time (TE) MRS. These synergistic advantages can be applied to optimize quantification of glutamate (Glu). Recently, in vivo ^{1}H MRS has been extendedly applied for investigation of the brain microenvironment by measuring the T2 relaxation time of the metabolites. In this study, we propose the concept of a multiple-TE (mTE) in vivo ^{1}H MRS for the concurrent measurement of concentration and T2 relaxation time of Glu.

Subjects and Methods: All the MRI/MRS scans of five Sprague–Dawley rats were performed using a Bruker PharmaScan® 7T MRI system. An MRS voxel of 22.5 μL was located in the prefrontal cortex, and automatically shimmed with the FASTMAP. *In vivo* ^{1}H MRS scans were performed using a point-resolved spectroscopy sequence with the following methods: (1) the typical short-TE MRS for quantification (Quant), (2) typical T2 measurement (T2-measurement), and mTE. The acquisition of the mTE was spread into eight TE points, which was selected and validated by spectral simulation and analyses by investigating the effects of J-modulation in the pseudo-triplet of the Glu-C4. All schemes of MRI/MRS scans were addressed in Table 1. Quantifications were performed using the LCModel software with simulated basis-sets using the VeSPA software. The mono-exponential curve-fitting was used to estimate T2 of the metabolites, and the CRLB and R^2 value was used as a reference. To verify the feasibility of the mTE, the concentration and CRLB value of the metabolites obtained by the Quant and mTE, and the T2 of the metabolites and R^2 value of the T2-measurement and mTE were compared.

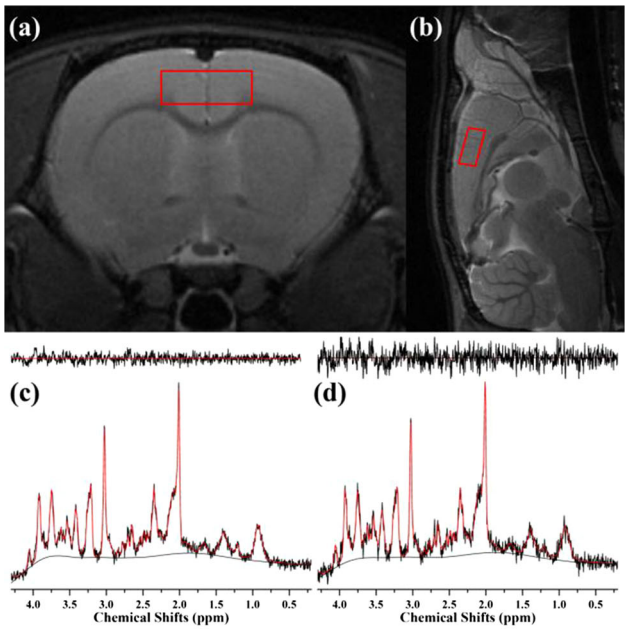

Figure 1. Representative multislice (a) axial and (b) sagittal T2-weighted MRI scans of rat brains obtained with the TurboRARE sequence with the following: TR, 4,000 ms; TE, 11 ms; effective TE, 1 ms; RARE factor, 8; averages, 2; FOV, 30 × 30 mm2; matrix size, 256 × 256; slice thicknesses, 1.5 mm (axial) and 1 mm (sagittal). (c) The T2-weigthed images (axial/sagittal) are shown with the voxel of in vivo 1H MRS (red box). Magnetic resonance imaging, MRI; rapid acquisition with relaxation enhancement, RARE; repetition time, TR; echo time, TE; field of view, FOV; proton magnetic resonance spectroscopy, 1H MRS.

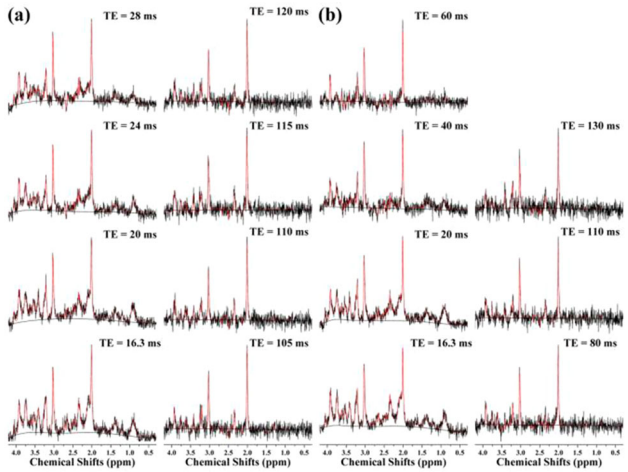

Figure 2. Representative in vivo 1H MRS spectra of (a) the Quant and (b) mTE method demonstrating the original spectra (black), LCModel-fitted spectra (red), baseline, and residual errors (topside) obtained in the rat brain using a PRESS sequence and the following scan parameters: TR, 5000 ms; TE, 8.7944 + 7.507 ms (TE1+TE2); number of averages, 192/48 × 2 (Quant/mTE); complex data points, 2,048; spectral bandwidth, 5,000 Hz. Linear Combination of Model, LCModel; point-resolved spectroscopy, PRESS, repetition time, TR; echo time, TE.

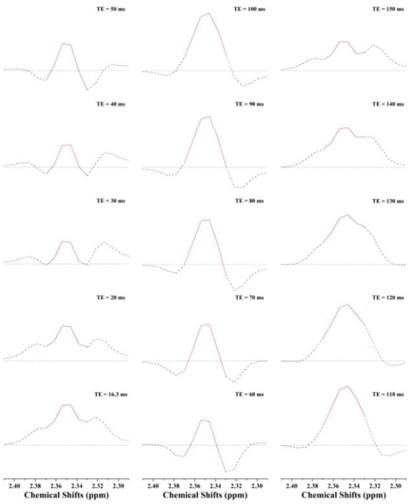

Figure 3. Visual illustration of the pseudo-triplet structures of the C4 resonances of Glu (2.29–2.41 ppm), simulated by the VeSPA software using software-imbedded PRESS-ideal sequence with the fifteen TE points. For spectral analysis, the spectra were divided into the central peak (red line), down-field (black dash) and up-field outer-wings (blue dash), and illustrated with the baseline (black dot). glutamate, Glu; versatile simulation, pulses and analysis, VeSPA; point-resolved spectroscopy, PRESS; echo time, TE.

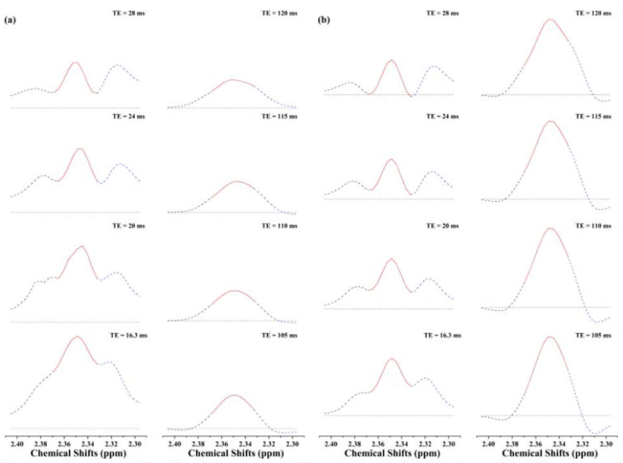

Figure 4. Representative visual illustration of the pseudo-triplet structures of the C4 resonances of Glu (2.29–2.41 ppm), extracted from (a) the simulation and (b) mTE with the eight TE points. For spectral analysis, the spectra were divided into the central peak (red line), down-field (black dash) and up-field outer-wings (blue dash), and illustrated with the baseline (black dot). glutamate, Glu.

Table 1. Acquisition schemes of the MRI/MRS scans

	MRI		*In vivo* ^{1}H MRS		
	T2WI (AX/SAG)		Quant	T2-measure	mTE
Pulse sequence	TurboRARE		PRESS		
TR/TE_{eff} (ms)	4,000/1 ms	TR/TEs	5,000/16.3 ms	5,000/(16.3, 20, 40, 60, 80, 110, 130, 150, 170, 200, 300) ms	5,000/(16.3, 20, 24, 28, 105, 110, 115, 120) ms
FOV/ matrix size	30 × 30 mm²/ 256 × 256	Voxel size	22.5 μL; 5 × 3 × 1.5 mm³		
Slice thickness (AX/SAG)	1.5/1 mm	Spectral bandwidth	5,000 Hz		
Averages	1	Averages	192	36 × 2	48 × 2
RARE factor	8	Data points		2,048	

Table 2. The mean concentrations and CRLB values of the major metabolites measured using *in vivo* ^{1}H MRS with (a) the Quant and (b) mTE (TE = 16.3 ms).

	Metabolites										
	GABA	Gln	Glu	mIns	Tau	Glc	GSH	tCho	tNAA	tCr	Glx
	Quant										
Conc. (μmol/g)	0.47 ± 0.064	3.08 ± 0.21	12.10 ± 1.027	4.18 ± 0.60	7.08 ± 0.54	1.70 ± 0.25	1.65 ± 0.17	1.45 ± 0.12	12.67 ± 0.70	8.04 ± 0.18	15.89 ± 1.07
CRLB (%)	13.20 ± 2.86	3.78 ± 0.21	3.00 ± 0	5.80 ± 1.10	4.00 ± 0	13.00 ± 2.55	9.80 ± 0.45	4.40 ± 0.55	6.00 ± 0.71	2.60 ± 0.55	3.40 ± 0.55
	mTE										
Conc. (μmol/g)	0.43 ± 0.086	3.97 ± 0.64	11.10 ± 1.20	3.91 ± 0.77	6.57 ± 0.34	1.97 ± 0.50	1.59 ± 0.26	1.39 ± 0.11	12.90 ± 0.83	7.91 ± 0.43	15.07 ± 1.21
CRLB (%)	17.60 ± 3.21	3.97 ± 0.64	3.80 ± 0.45	7.60 ± 1.52	4.80 ± 0.45	13.60 ± 3.44	12.80 ± 2.95	5.60 ± 0.55	6.80 ± 0.84	3.20 ± 0.45	4.00 ± 0

Table 3. The mean T2 relaxation time and R2 value of the major metabolites measured using in vivo 1H MRS with (a) the mTE and (b) T2-measurement.

		Metabolites						
		Glu	mIns	Tau	tCho	tNAA	tCr	Glx
mTE	T2 (ms)	68.54	148.41	89.21	91.41	191.83	145.50	66.09
	R^2	0.9710	0.9422	0.9943	0.9334	0.9579	0.9966	0.9673
T2-measure	T2 (ms)	71.58	173.70	127.54	118.95	195.31	148.39	68.49
	R^2	0.8353	0.7819	0.7620	0.9333	0.9337	0.9885	0.8579

Table 4. The relative area ratio of the upfield (a/b) and downfield outer-wings (c/b) to the central peak of the pseudo-triplet of the Glu-C4 obtained using the spectral simulation and mTE.

	a/b		c/b	
TE (ms)	Simulation	mTE	Simulation	mTE
16.3	0.31	0.33 ± 0.05	0.65	0.73 ± 0.06
20	0.44	0.42 ± 0.06	0.65	0.77 ± 0.08
24	0.55	0.49 ± 0.04	0.81	0.90 ± 0.05
28	0.48	0.48 ± 0.03	1.11	1.17 ± 0.03
105	0.10	0.13 ± 0.02	0.32	0.29 ± 0.03
110	0.11	0.14 ± 0.03	0.32	0.31 ± 0.05
115	0.12	0.15 ± 0.03	0.33	0.34 ± 0.07
120	0.14	0.20 ± 0.04	0.35	0.34 ± 0.02

Results: Significant differences in the concentrations of the metabolites between the Quant and mTE were not observed ($p > 0.050$), suggesting that the mTE can measure brain metabolites with comparable quantification reliability. In addition, the estimated T2 relaxation time of glutamate (68.54 ms) by the mTE was similar to that of the T2-measurement (71.58 ms), with an enhanced signal-to-noise ratio and estimation reliability, suggesting the mTE as a reliable method for T2 estimation of glutamate.

Discussion/Conclusion: The quantification reliability of the mTE was comparable with that of typically used high-field and short-TE MRS. Although some discrepancies, the mTE might be used for the reliable T2 estimation of tNAA, tCr, and Glu, and thus can be used to investigate microenvironmental changes in localized brain tissues. Thus, high-field in vivo ^{1}H MRS MRS with the mTE can be used for effective measurement of concentration and T2 of Glu to investigate the physiology of brain metabolism and microenvironment and its disease-related changes.

References:

Xin L, et al. (2008) Proton T2 relaxation time of J-coupled cerebral metabolites in rat brain at 9.4 T. NMR Biomed.

L01.12

Reduction of Ghost Artifacts in ^{31}P EPSI Using a Gradient Impulse Response Model

H. N. Dang, M. E. Ladd, P. Bachert, A. Korzowski
German Cancer Research Center (DKFZ), Division of Medical Physics in Radiology, Heidelberg, GERMANY

Purpose/Introduction: Accelerated magnetic resonance spectroscopic imaging (MRSI) sequences like echo-planar spectroscopic imaging (EPSI) place high demands on the MR gradient system. Imperfections in gradient trajectories lead to ghost artifacts in conventionally reconstructed MRSI data due to phase inconsistencies between individual gradient echoes. The separate phase-corrected reconstruction of odd and even echo trains avoids these ghosts; however, this approach limits the spectral bandwidth, which is a disadvantage for ^{31}P MRSI at B_0 = 7T.
Characterization of the gradient system by a gradient impulse response function (GIRF) can be used to describe distortions in the gradient waveform. In this work, a method is presented to reduce ghost artifacts in in vivo ^{31}P EPSI data by employing the GIRF.
Subjects and Methods: A GIRF characterization [1] was performed on a MAGNETOM 7T (Siemens Healthineers) using gradient waveform measurements [2] of a series of triangular waveforms (12 triangles; slew rate = 71 mT/m/s; triangle gradient amplitude = 7.8–25 mT/m; triangle length = 110–320 ms).
For MRSI reconstruction, a self-written MATLAB routine (MathWorks) was used. The actual k-space trajectory was calculated using the acquired GIRF to predict the waveform distortion of the EPSI gradient train (Fig. 1). The accordingly non-uniformly sampled k-space data of the actual EPSI measurement were reconstructed with a conjugate phase reconstruction algorithm. Each interleave was reconstructed separately.
In vivo ^{31}P MRSI was performed on the calf muscle of a healthy volunteer using an interleaved ^{31}P-EPSI sequence [3] (4 interleaves, spectral BW = 6250 Hz, voxel size (15 × 15 × 20)mm^3, matrix (16 × 16 × 16)).

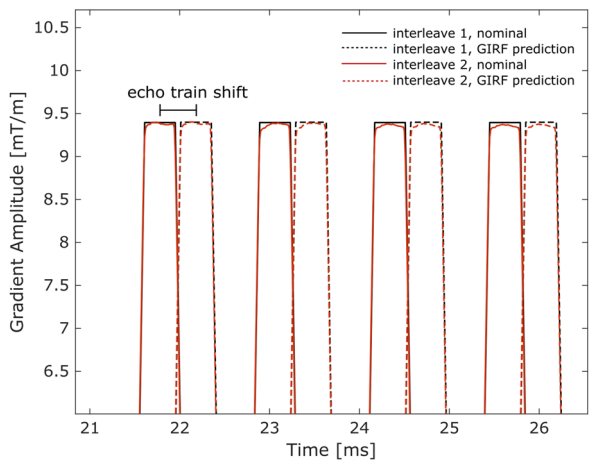

Figure 1: Excerpt of a gradient train of a 31P EPSI sequence (τ=1.28 ms between two odd echoes, Δf=781.25 Hz) with two representative interleaves. Waveform distortions (red) are predicted by applying GIRF correction to the nominal gradient (black).

Results: The proposed correction method was verified in simulations and in ^{31}P EPSI measurements on model solutions. Figure 2 shows a conventionally and GIRF-corrected reconstruction of an in vivo ^{31}P EPSI dataset. The uncorrected spectrum is heavily superimposed by ghosting artifacts of the dominant PCr resonance, whereas in the GIRF-corrected spectrum the ghosting artifacts are below the noise level and the peaks of all metabolites are clearly visible.

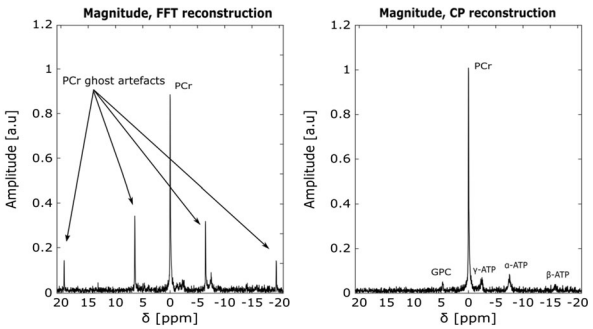

Figure 2: Representative 31P spectra acquired in a central voxel of human calf muscle using an interleaved EPSI-sequence, uncorrected (left) and GIRF-corrected (right).

Discussion/Conclusion: The presented method enables ^{31}P EPSI sequences without the need for reference scans or separated reconstruction of odd and even echoes to suppress ghosting artifacts, which increases the acquired bandwidth without a penalty in acceleration. Over a period of 3 months, no deviations in the acquired GIRF were observed, making a quarter-year maintenance measurement of the GIRF reasonable.
References:
1. Vannesjo SJ, et al. (2014), Field camera measurements of gradient and shim impulse responses using frequency sweeps. Magn. Reson. Med., 72: 570-583.
2. Zhang Y, et al. (1998), A novel k-space trajectory measurement technique. Magn. Reson. Med., 39: 999-1004.
3. Korzowski A and Bachert P (2018), High-resolution 31P echo-planar spectroscopic imaging in vivo at 7T. Magn. Reson. Med, 79: 1251-1259.

L01.13

An MRS Phantom Design with Multiple Compartments for Mimicking IDH Mutant and IDH Wild-Type Brain Tumors

A. Gursan[1], H. Sahin[1], B. Altun[1], A. T. Talas[1], **G. H. Hatay**[1], O. Kocaturk[1], B. Garipcan[1], A. Dincer[2], E. Ozturk-Isik[1]
[1]Bogazici University, Institute of Biomedical Engineering, Istanbul, TURKEY, [2]Acıbadem Mehmet Ali Aydınlar University, Department of Radiology, Istanbul, TURKEY

Purpose/Introduction: MR spectroscopy (MRS) sequences are first validated on phantoms before in vivo studies. Previous studies employed 3D printers to produce MR phantoms for other MRI modalities or generic use [1,2]. In this study, we designed and 3D printed a human head sized multi-compartment MRS phantom, which includes a compartment with solution mimicking an isocitrate dehydrogenase wild-type (IDH-wt) glioma, and another compartment with solution mimicking an IDH mutant (IDH-mut) glioma.
Subjects and Methods: A half sphere with a diameter of 17 cm and thickness of 1 cm was designed in Solid Edge (Siemens PLM Software, Plano, Texas). Three compartments with volumes of 35 ml each were placed inside the phantom at least 1 cm away from each other (Fig. 1).

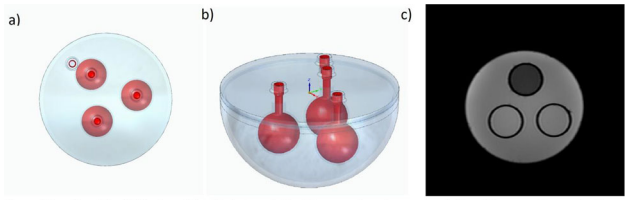

Figure 1. Top (a) and frontal (b) views of the 3D phantom design. The compartments were placed at least 1 cm away from each other and also from the outer shell to avoid susceptibility issues. (c) MR image of the phantom.

Acrylonitrile butadiene styrene (ABS) was used as the 3D printing material. Two of the compartments were filled with solutions mimicking IDH-mut and IDH-wt gliomas with concentration ratios taken from previous studies [3] (Table 1).

Metabolite	IDH-Mut	IDH-WT	Normal Brain
NAA	7.50	6.32	12.50
Myo-Inositol	4.50	3.80	7.50
Creatine	6.32	6.32	10.00
Choline	4.50	5.00	3.58
Lactate	5.25	6.00	0.00
Glutamate	5.75	5.75	12.50
GABA	3.00	3.00	3.00
2HG	5.20	0.00	0.00

Table 1: Metabolite concentrations in milimolar for each solution. Glutamine was not added to the phantom solutions, because it's instable.

Last compartment was filled with a solution mimicking cerebrospinal fluid (CSF). Rest of the volume was filled with a solution mimicking normal brain white matter. Metabolites were added to the solutions one by one, and pH of the solutions were fixed to 7.2 by titration of sodium hydroxide (NaOH) and potassium monophosphate (KH_2PO_4) buffer solutions. Gadolinium and NaN_3 were added to the solutions for shortening T1 and preventing bacterial growth, respectively.

The phantom was scanned on a Siemens Prisma 3T scanner using a 32 channel head coil. A Mescher-Garwood Localization by Adiabatic Refocusing (MEGA-LASER) sequence (ref4) was used for detecting 2-HG and other metabolites (TR = 2000 ms, TE = 68 ms, Resolution = 16x16, voxel size = 0.5 ml). LCModel[5] was used for quantification of metabolites, and a CRLB threshold of 25% was employed. Metabolite maps were generated in MATLAB R2018a (MathWorks Inc., Natwick, MA).

Results: MRSI acquisition grid on top of the reference MR image, two spectra of respective tumor compartments, and the main metabolite maps are given in Fig. 2.

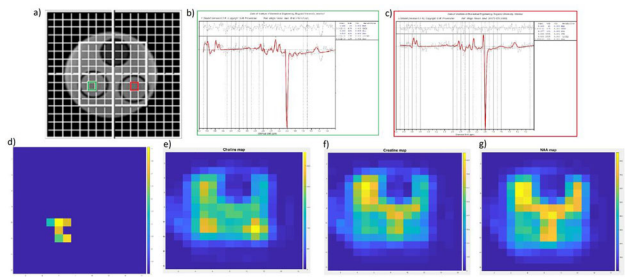

Figure 2: a)Acquisition grid on phantom image. Difference spectra from tumor compartments (b,c). d)2HG detected only at IDH-mut compartment voxels. Metabolite maps generated from LCModel results of off-spectrum for choline(e), creatine(f) and NAA(g).

LCModel is optimized for in vivo data quantification, so the quantification was less accurate for metabolites having overlapping peaks, such as glutamine, glutamate, and 2HG in the phantom even with phantom settings.

Discussion/Conclusion: In this study, a 3D printed multi-compartment head MRS phantom was successfully produced, which would aid MRS sequence development studies for brain tumors.

References: Acknowledgement: The authors gratefully acknowledge Dr. Ovidiu Andronesi for MIT C2P support. This research was supported by TUBİTAK 1003 grant 216S432.

1. Kasten, J.A., et al. MRM, 2016. **75**(1):287-94.
2.Gopalan, K., et al. *ISMRM2017*. 3733
3.Ozturk-Isik, E. et al. *ISMRM-ESMRMB*. 2018. 955.
4. Hnilicova, P. et al. NMRBiomed. 2016. **29**(11):1656-1665
5. Provencher, S.W. MRM 1993. **30**(6):672-679.

L01.14
Gray and white matter cerebral aspartate concentrations measured with J-edited MRS

P. Menshchikov[1, 2], A. Manzhurtsev[3], M. Ublinskiy[1], T. Akhadov[1], N. Semenova[2]
[1]*Clinical and Research Institute of Emergency Pediatric Surgery and Traumatology, Radiology, Moscow, RUSSIAN FEDERATION,*
[2]*Semenov Institute of Chemical Physics of RAS, Biophysics, Moscow, RUSSIAN FEDERATION,* [3]*Emanuel Institute of Biochemical Physics of RAS, Moscow, RUSSIAN FEDERATION*

Purpose/Introduction: Recent studies [1,2] revealed detection of strong non-overlapped Asp signal with MEGA-PRESS editing (Asp edited MEGA-PRESS), using four TE (90, 115, 140 and 150 ms). This theoretically makes it possible to measure T_2 of Asp from Asp edited MEGA-PRESS and consequently is an important step in making this editing method quantitative.

Subjects and Methods: Phantom T_2 values of Asp and Cr were obtained from phantom (Asp – 6 mM; Cr – 20 mM) from PRESS spectra (TE = 35, 70, 90, 100, 120, 140 ms, TR = 10 s) using quantification with prior data. In vivo T_2 was measured from Asp edited MEGA-PRESS (TE = 90, 115, 140 and 150 ms, TR = 2 s) spectra. TE-dependence of the Asp signal in Diff spectrum were expressed from appropriate phantom Asp edited MEGA-PRESS spectra (Fig. 1).

$$ln\left[\frac{S_{Asp}^{in\ vivo}\cdot\exp\left(-\frac{TE}{T_{2\,tCr}^{in\ vivo}}\right)}{S_{tCr_2}^{in\ vivo}\cdot\exp\left(-\frac{TE}{T_{2\,tCr}^{phant}}\right)}\right]=ln\left[\frac{Asp_{phant}}{Asp_{in\ vivo}}\right]=ln\left[\frac{[Asp]^{phant}}{[tCr]^{phant}}\cdot\frac{S_{0\,Asp}^{in\ vivo}}{S_{0\,tCr}^{in\ vivo}}\right]+\left(\frac{1}{T_{2\,Asp}^{phant}}-\frac{1}{T_{2\,Asp}^{in\ vivo}}\right)\cdot TE$$

$[Asp]^{phant}$ $[tCr]^{phant}$ - initial concentrations of Asp and Cr in phantom

$S_{Asp}^{in\ vivo}$ $S_{tCr_2}^{in\ vivo}$ - average integral intensities of Asp and Cr, quantified from *in vivo* Asp edited MEGA-PRESS spectra for TE = 90, 115, 140 and 150 ms.

S_{Asp}^{phant} $S_{tCr_2}^{phant}$ - integral intensities, quantified from *phantom* Asp edited MEGA-PRESS spectra for TE = 90, 115, 140 and 150 ms.

Formula, which takes into consideration TE-dependence of Asp signal in DIFF spectra

The following spectra were acquired from both the phantom (Asp – 6 mM; Cr – 20 mM) and in vivo (16 healthy volunteers, 8 spectra for each TE point, VOI in size of 50 × 25 × 25 mm, ACC) (Fig. 2a).

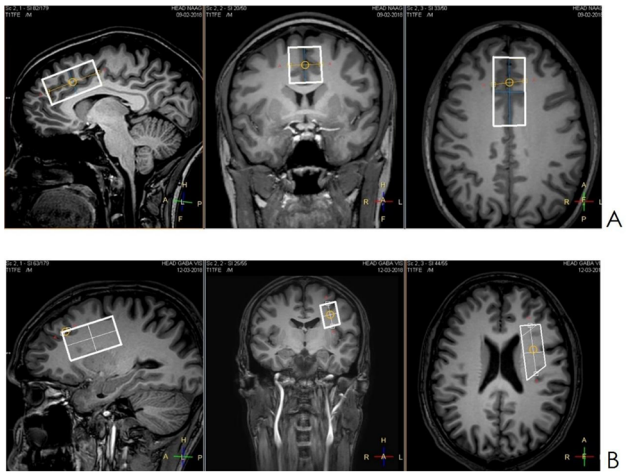

Typical VOI location in GM-rich (A) and WM-rich (B) brain region

Spectra were quantified using AMARES routine.

Asp concentrations with were quantified from gray- (ACC 50 × 25 × 25 mm, Fig. 2a) and white-matter (left centrum semiovale (LCS) 50 × 19 × 27 mm, Fig. 2.B) dominant regions using Asp edited MEGA-PRESS (TE = 90, 115, TR = 2 s). The spectra were fitting using Amares. Totally, there were 29 healthy volunteers enrolled in the concentration estimation.

Results: T_2 values of aspartate and Creatine were quantified as follows: 303 ± 35 and 327 ± 27 ms. According to expression (Fig. 1) significant linear regression (R2 = 0.97, $p < .01$) were found (Fig. 3.). Where, in vivo T_2 of Asp were quantified as 169 ± 33 ms.Asp concentrations in gray matter (GM)- and white matter (WM)-dominant brain regions were measured as 2.78 ± 0.21 mM and 1.04 ± 0.16 mM, respectively.

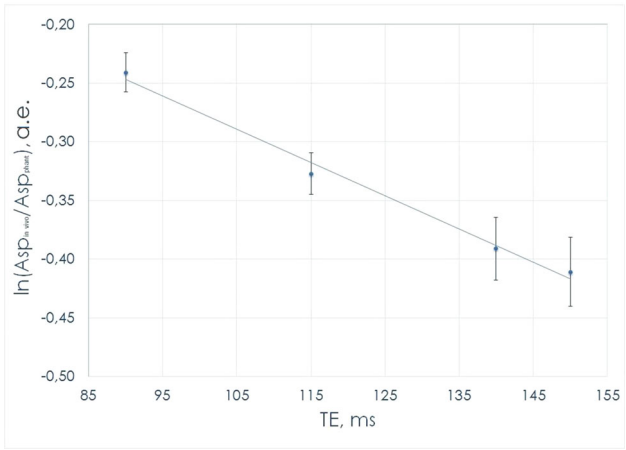

Mono-exponential fit of the quantified from Asp-edited MEGA-PRESS (Asp in vivo)/(Asp phantom) ratio versus TE

Discussion/Conclusion: For the first time, the T_2 value for the Asp – CH_2 resonance (δ = 2.71 ppm) was measured at 3 T in the present study and found to be 161 ± 33 ms. The cortical GM Asp concentration coincides with the cerebral concentration measured in the rat cortex4 with short-TE STEAM at 9.4T (2.72 ± 0.19 vs 2.43 ± 0.14). The value for the CS is in good agreement with those measured with HERMES [2], for which T_2 was set as 270 ms (1.05 ± 0.15 vs 0.88 ± 0.17 mM). it is likely that Asp levels are higher in GM than in WM because GM contains more neuronal cell bodies and thus contains more mitochondria. In conclusion it is nessesary to say that estimation of the absolute Asp concentrations with Asp editing MEGA-PRESS has potential in many research applications, such as studying the processes underlying the reduction of N-acetyl aspartate as well as studying some mithohondrial diseases.

References: This work was supported by RFBR Grant 17-04-01149

[1] P. Menshchikov, T. Akhadov, N. Semenova. Magn Reson Mater Phy 2017; 27:5499.

[2] K. Chan, M. Saleh et al. NeuroImage 2017;155: 587–593.

L01.15
Keyhole reconstruction of multiparametric ^{31}P MRSI

S. Neumann, J. Breitling, M. E. Ladd, P. Bachert, A. Korzowski
German Cancer Research Center, Heidelberg, GERMANY

Purpose/Introduction: One of the main challenges of using phosphorous magnetic resonance spectroscopic imaging (^{31}P MRSI) in vivo is a low signal-to-noise ratio, which leads to long measurement times. Acquiring multiple datasets with different contrasts, therefore, exceeds feasible time limits. A suitable approach to shorten measurement time for multiple scans is keyhole imaging.[1] The purpose of this study was to demonstrate the feasibility of this concept for use in ^{31}P MRSI.

Subjects and Methods: In this study, ^{31}P MRSI was performed on a calf muscle of a healthy volunteer on a MAGNETOM 7T (Siemens Healthineers) using a double-resonant ^{31}P/^{1}H volume coil (Rapid Biomedical) and elliptical 3D CSI readout (voxel size (15 × 15 × 30) mm^3, 16 × 16 × 8 matrix, Δf = 5000 Hz) for 5 different contrasts (TR = (0.24, 0.4, 0.6, 1.0, 2.0) s, T_{meas} = 10-20 min). Reconstruction and data evaluation were performed with a homebuilt MATLAB routine (MathWorks).

The keyhole approach uses a reference data set, for which the entirety of k-space is acquired and a keyhole data set, for which only the center of k-space data is acquired. The keyhole data are then substituted into the reference data set after correcting for contrast differences. Scaling was obtained using the ratio of each spectral point in the k-space centers of both datasets after smoothing with a weighted moving mean.

For evaluation, each contrast was used as both reference and keyhole data to enable 20 different reconstructions. The size of the keyhole data used for reconstruction was varied between 5% and 50% of full-resolution k-space data. The mean relative deviations between metabolite amplitudes, quantified by the AMARES algorithm[2], of the reconstructed and original data were calculated in the volume of interest in three central slices.

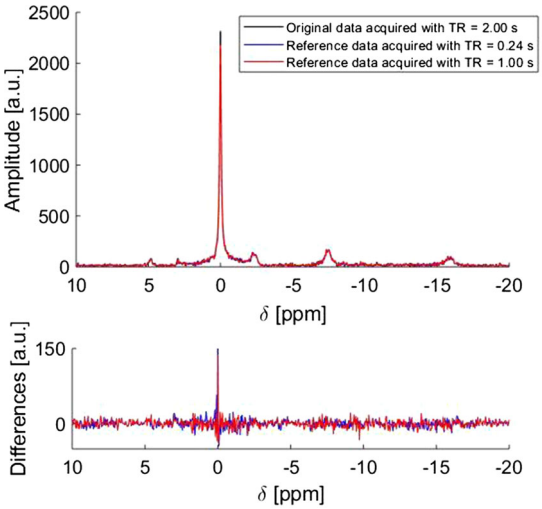

Figure 1: Representative 31P Spectra acquired in a central voxel of the human calf muscle at TR = 2 s. The original data (black) is compared to keyhole reconstructions with keyhole size of 30%. Reference data: TR = 0.24 s (blue) and TR = 1 s (red).

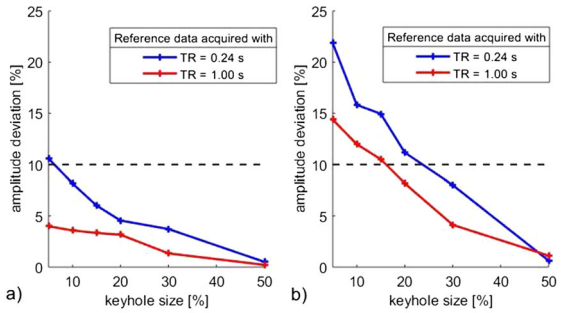

Figure 2: Amplitude deviation between reconstructed and original data for a) PCr and b) γ-ATP at different keyhole sizes (TR = 2 s). Reference data: TR = 0.24 s (blue), TR = 1 s (red). The dashed line represents a threshold for deviations at 10%.

Results: In all in vivo ^{31}P spectra only small deviations between the original data and the keyhole reconstructions were observed (Fig. 1). Figure 2 illustrates the expected decrease in deviation between reconstructed and original data of PCr and γ-ATP as the keyhole size is increased. Furthermore, the smaller the difference in contrast (TR), the smaller the deviations. To reach amplitude deviations below 10% for PCr and γ-ATP, 30% and 10% of the full-resolution data have to be acquired, respectively.

Discussion/Conclusion: The presented data demonstrate the feasibility of keyhole imaging for multiparametric ^{31}P MRSI measurements. 50% of the full-resolution data has to be acquired to reach amplitude deviations below 10% for all metabolites. However, the extent to which noise differences contribute to these deviations must be investigated further.

References:

1. Jones RA, et al. K-space Substitution: A Novel Dynamic Imaging Technique. Magn. Reson. Med. 1993;29(6):830-4.

2. Vanhamme L, et al. Improved Method for Accurate and Efficient Quantification of MRS Data with Use of Prior Knowledge. J. Magn. Reson. 1997;129(1):35-43.

L01.16

One week high-fat diet alters MTR, T2 and ADC values in the mouse hypothalamus and reward centers

B. W. Campillo, S. Cerdan, P. Lopez-Larrubia, **B. Lizarbe**
Instituto de Investigaciones Biomédicas "Alberto Sols" CSIC, Madrid, SPAIN

Purpose/Introduction: Obesity development is linked to inflammation in the hypothalamus, the brain structure responsible for appetite regulation and energy homeostasis. Furthermore, appetite has in mammals a hedonic component, controlled by the reward centers, affected during inflammation[1]. In rodents, inflammation has been characterized, at a histological level, by the emergence of microgliosis and astrogliosis, events that can be detected before gain in body weight. Studies using Magnetic Resonance Imaging (MRI) have identified a rise in the transverse relaxation time (T2) –a surrogate marker of astrocytosis- in the hypothalamus of long-term high-fat diet (HFD) mice and in obese patients[2]. Nevertheless, no MRI hypothalamic inflammatory markers of the initial stages of obesity have yet been investigated, and the role of the reward centers remains to be determined. Therefore, the aim of this study was to assess the onset of obesity development in mice in vivo using MRI. We evaluated the longitudinal changes of T2, magnetization transfer ratios (MTR) and apparent diffusion coefficients (ADC) in mice during the initial stages of high-fat or standard diet consumption.

Subjects and Methods: Two animal groups, fed with either standard food chow (n = 7) or with a 60% high-fat (butter-based) diet (n = 8) were investigated before diet diversification (T = 0) and on days 1, 7 and 14. Body weight and blood glucose levels were controlled at every time point. MRI were performed in a 7T magnet (Bruker Biospect). Briefly, the hypothalamus (Hyp), nucleus accumbens (ACB) and infralimbic area (ILA) were localized in a T2-image using an anatomical atlas[3], and T2 (50 images, TE: 12–600 ms,TR = 5000 ms), MTR (MT pulse on/off, TE/TR = 9.8/2500 ms) maps and DWI (9 b:200-2000 s·mm^{-2}) were acquired (5 slices, 1.25 mm thickness, 0.16 × 0.16 mm^2). Longitudinal changes of the fitted parameters were assessed statistically using SPSS and a generalized estimated equations model

Results: Body weight and blood glucose levels increased significantly on HFD mice from days 1 and 7, respectively, and control animals increased only body weight after 14 days (Figure 1).

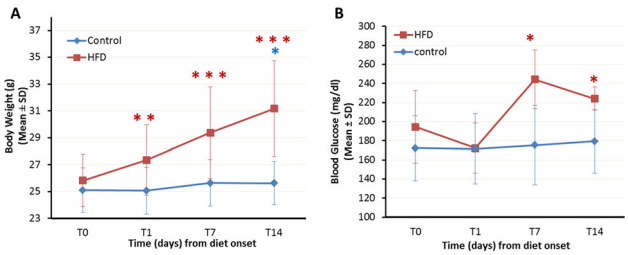

Figure 1. Mean (± SD) values of body weight (A) and blood glucose values (B) of the control and HFD groups at each time point. Statistical significance refers to comparisions to baseline values (*p<0.05, **p<0.005,***p<0.001).

MTR remained constant over time in control animals, but increased significantly on HFD mice in the three zones from day 7 (Figure 2).

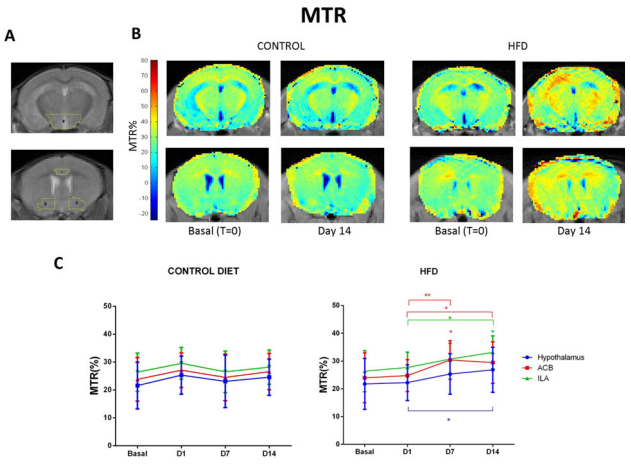

A) MT images and ROIs: Hyp (top), ILA, ACB right and left (bottom). B) Representative MTR maps. C) Mean (± SD) MTR values of control and HFD groups. Significance refers to comparisons to basal values, except otherwise indicated (*p<0.05,**p<0.001)

T2 values decreased significantly on both animal cohorts reward centers', and showed a HFD-specific significant increase on the hypothalamus between days 7 and 14 (Figure 3).

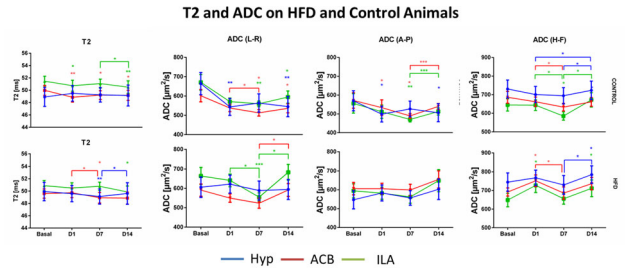

T2 and ADC mean (±SEM) values for control (top) and HFD (bottom) animals, area (Hyp, ACB or ILA) and time point. Statistical significance refers to comparisions to basal values, except otherwise indicated (*p<0.05,**p<0.005,***P<0.001).

ADC values tend to decrease on controls in all directions and areas (Figure 3), and values on the HFD cohort where either more constant or increased significantly (Figure 3).

Discussion/Conclusion: One week of high-fat diet is sufficient to trigger a robust increase in MTR in the mouse hypothalamus and reward centres, on agreement with inflammation, which is additionally supported by the partial T2 and ADC increases.

References:

[1]Miller, AA et al., *Brain Behav Immun*(2014).
[2]Lee D. et al.*Am J Physiol Endocrinol Metab*(2013).

L01.17

Free diffusion increases coinciding with enhanced glymphatic clearance during initial tau burden loading in a mouse model of tauopathy determined using NODDI and contrast enhanced MRI

N. Colgan[1], I. Harrison[2], A. Machhada[2], O. Ismail[3], J. Wells[2], J. O'Callaghan[2], H. Zhang[4], B. Siow[2], M. Lythgoe[2]
[1]*National University of Ireland Galway, Physics, Galway, IRELAND,* [2]*University College London, Centre for Advanced Biomedical Imaging, London, UNITED KINGDOM,* [3]*University College London, London, UNITED KINGDOM,* [4]*University College London, Centre for Medical Image Computing, London, UNITED KINGDOM*

Purpose/Introduction: In the rTg4510 Alzheimer disease model pathology starts in the cortex and spreads over time in a prion like manner to connected regions of the hippocampus and frontal/temporal cortices, and finally to the striatum and thalamus but the cerebellum is spared. The tangles are observed in the cortex by 4 months of age, the hippocampus by 5.5 months (1) with cortical cell loss occurring at 8.5 months (2). In this process glial cells lose some homeostatic function acquiring a proinflammatory phenotype believed to precede neurodegeneration (3). In this study we demonstrate increased CSF ICF exchange in the presence of the proposed neuroinflammation marker of free/isotropic diffusion (4) at the initial onset of tau loading in the striatum and thalamus at 8.5 months

Subjects and Methods: MRI A 9.4TAgilent scanner with 205/120HD gradient, RF via 72-mm coil and 4 channel reciever.

NODDI Imaging parameters were: FoV 20 × 20 mm^2, resolution 200 × 200 μm, 16 × 500 μm, TR = 2 s, TE = 24 ms. To enable the NODDI analysis, the diffusion MRI protocol consisted of two shells, which were:

1. Shell one:30 directions,four b = 0 and b = 2000 s/mm^2 with parameters:G = 0.349T/m, Δ = 9.3 ms,δ = 5.5 ms,TR = 2000 ms.
2. Shell two: 20 directions,three b = 0 and b = 1000 s/mm^2 with parameters:G = 0.250T/m, Δ = 9.3 ms,δ = 5.5 ms,TR = 2000 ms.

Glymphatics An intrathecal catheter was advanced 1 mm into the cisternal space via a durotomy and sealed in place and 30 μL of magnavist contrast was delivered intrathecally at an infusion rate of 0.6 μL per minute. 3D GRE MRI acquisitions continued over 2 h.

Results: In the cortex we see a normal glymphatic clearance with an increase in gadolinium in the cortex via the glymphatic pathway and no penetration in the rTg4510. We also see no significant difference in the free diffusion compartment. However, in the thalamus and striatum regions which are in the process of forming NFT's we see a statistically significant increase in the gadolinium entering the structure when compared with the wild type which coincides with a statistically significant increase in the isotropic diffusion.

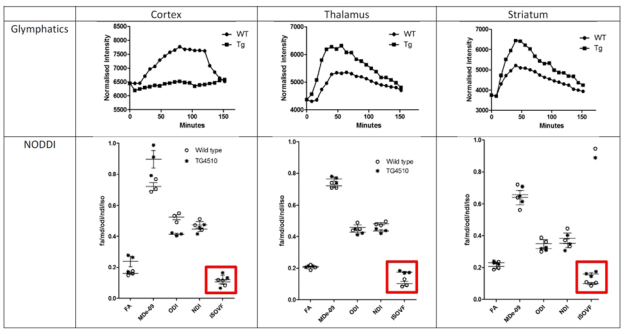

Average time series of glymphatic images of the three wt and three rTg4510 mouse brain under infusion of gadolinium (top) and the single time point free diffusion NODDI measurements (bottom) of the same animals.

Discussion/Conclusion: Neuroinflammatory reactive gliosis is considered a key abnormality in AD where glial cells lose some of their homeostatic functions and acquire a proinflammatory phenotype with neuroinflammation preceding neurodegeneration. Neuroinflammation in AD reflects a vicious cycle of microglial activation, release of proinflammatory factors, and neuronal damage. There is a hypothesis that the neuroinflammatory response aims to aid the glymphatic mechanism and our findings of increased isotropic diffusion aiding the glymphatic CSF ISF exchange at the onset of tau burden in the thalamus and striatum may reflect this mechanism.

References:

(1) K. Santacruz, et al.,Science 309, 476-481 (2005).
(2) Ramsden,et al.,J Neurosci 25,10637-10647 (2005).
(3) Calsolaro&Edison,Alzheimer's & Dementia 12, 719-732 (2016).
(4) Pasternak, et al.,Schizophrenia research 161, 113-118 (2015).

L01.18

Imaging Changes in Blood Brain Barrier Permeability in a Human African Trypanosomiasis Mouse Model using Diffusion Weighted Multiple Boli Arterial Spin Labelling

S. Paterson[1], A. Vallatos[2], J. Rodgers[3], L. Gallagher[1], L. Carberry[1], W. Holmes[1]
[1]University of Glasgow, Institute of Neuroscience and Psychology, Glasgow, UNITED KINGDOM, [2]University of Edinburgh, Edinburgh, UNITED KINGDOM, [3]University of Glasgow, Glasgow, UNITED KINGDOM

Purpose/Introduction: Human African Trypanosomiasis (HAT) commonly known as Sleeping Sickness is a parasitic disease transmitted by the Tsetse fly. The parasite trypanosoma triggers a breakdown in the blood brain barrier (BBB) with the disease being fatal if left untreated[1]. Being able to image the BBB to look for permeability changes is crucial in HAT. The standard for imaging changes in the BBB is to use a contrast agent but these aren't sensitive for imaging subtle changes in the BBB and are invasive. We propose using the newly developed multiple boli arterial spin labelling[2] (mbASL), a high SNR ASL sequence, accompanied with bipolar diffusion gradients to explore changes in the BBB throughout the disease. mbASL is a high SNR sequence that can be used to non-invasively image perfusion changes in the brain along with acquiring cerebral blood flow (CBF) values.

Subjects and Methods: Groups of female CD1 mice (n = 6) were imaged at multiple disease points post infection: Day = 0, 7, 14, 21, 28. Experiments were performed on a Bruker PharmaScan 7T MRI system using a mouse surface head coil. DW-mbASL images were acquired at b = 0,25,50,75,100,200,300 s/mm^2, with CI = 5000 ms, TI = 50 ms. T1 maps and CE-MRI using a T1 weighted sequence were also acquired. After scanning, the mice were killed, and brains taken for histological purposes. Data was exported in DICOM format and analysed using in-house MATLAB code.

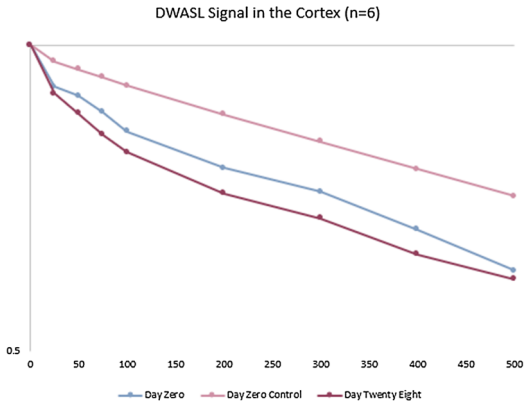

Figure 1: Signal comparison from the DWASL sequence at days 0 and 28 post infection in the HAT infected mouse.

Results: Figure 1 shows a comparison of DWASL signal obtained at days 0 and 28 post infection. Changes in the ratio of intravascular signal (capillaries) and extravascular signal (tissue) is seen between the two time points. This shows there is changes in water exchange rate in the HAT mouse. This suggests that although in the later stages of the disease when a contrast agent can cross the BBB[2], the rate of exchange of water may have decreased. Further analysis is on-going, but this data has shown that changes in the brain of HAT infected mice can be examined using DWASL.

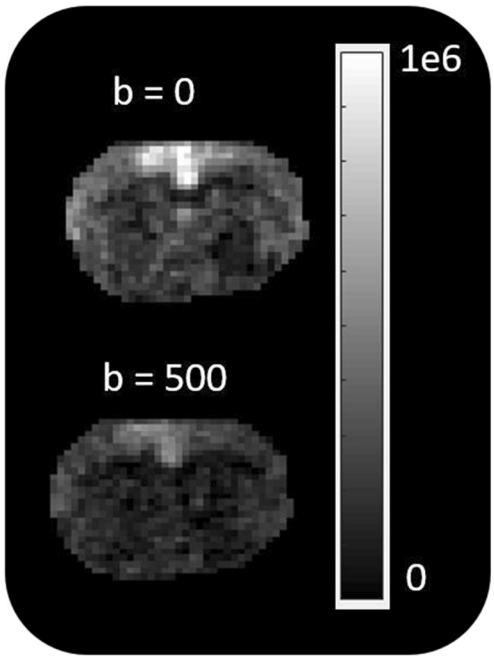

Figure 2: High SNR DWASL images produced using a diffusion weighted multiple boli arterial spin labelling sequence.

Figure 2 demonstrates the high SNR DW-mbASL images in a non-infected mouse at multiple b values. This data can be fitted to the mbASL kinetic model and produce quantitative cerebral blood flow maps (analysis on going).

Discussion/Conclusion: We have produced a high SNR diffusion weighted ASL sequence that is being used to image subtle changes in blood brain barrier permeability. By using DW-mbASL to image the brain during various stages of the disease, we have managed to explore new details about permeability and CBF that weren't known previously in HAT.

References:

[1]Rodgers, J et al. (2017).
[2]Vallatos, A et al. (2017).

L01.19

Magnetic resonance imaging approaches to follow-up the outcome of a glioblastoma rat model with anti-inflammatory -NSAIDs and SAIDS- treatments

I. Cabete[1], A. De Galdo[2], M. J. Guillén Gómez[2], **N. Arias-Ramos**[2], P. López-Larrubia[2]
[1]University of Coimbra, Coimbra, PORTUGAL, [2]Instituto de Investigaciones Biomédicas, CSIC/UAM, Madrid, SPAIN

Purpose/Introduction: Glioblastoma (GBM) is the most aggressive human brain tumor, with poor prognosis and survival[1]. Agents with anti-inflammatory (AI) properties have been studied as anti-tumoral drugs[2] and tested in GBM models with promising results[3]. We have worked with GBM murine models, identifying MRI parameters to be used as biomarkers of the pathology[3]. In this work we aimed to assess the overall survival (OS) and the tumor features evolution of GBM-bearing rats treated with either non-steroidal AI (NSAID) or steroidal AI drugs (SAID).

Subjects and Methods: GBM was induced in Wistar rats by stereotaxic injection of C6 cells[4]. When tumors were visible by MRI, animals were randomized in 3 groups: 5 rats were injected s.c.

(3 days) with a NSAID (meloxicam, 1 mg/kg), 5 rats with a SAID (methylprednisolone, 1 mg/kg) and 3 with saline (controls).
MRI evaluations were carried out in a 7T system until day 45 post-cell injection (or until end-point criteria). Tumor volume was followed-up with Gd contrast-enhanced T1 W images at different times after C6 injection. Besides, diffusion-weighted and magnetization transfer (MT) images were acquired before and 1 week after starting the treatment. Parametric maps were generated with home-made software.
Therapy success was evaluated by calculating the relative tumor volume at the end of the study (RTVf) compared with the pre-therapy size and the OS of the different groups.
Results: Higher OS was observed in animals treated with AI drugs (32.2 ± 12.6 days for rats treated with NSAID and 28.2 ± 10.0 for rats treated with SAID), than control rats (20.0 ± 2.0 days). RTVf reached higher volume in the control group than in the treated groups with NSAID and SAID.
Moreover, the glioma volume of 2 rats treated with meloxicam and 1 rat with methylprednisolone progressively decreased until a complete regression. Fig. 1 shows three examples of tumor evolution of a control rat and 2 treated that showed a total regression, and Fig. 2 the T1 W images of these animals.

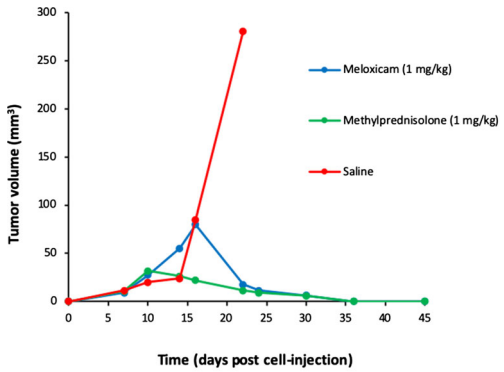

Figure 1. Tumor volume evolution with time. A control rat injected with saline (red), one treated with meloxicam (blue) and one with methylprednisolone (green) are presented as examples. The two treated animals showed a regression of the tumor.

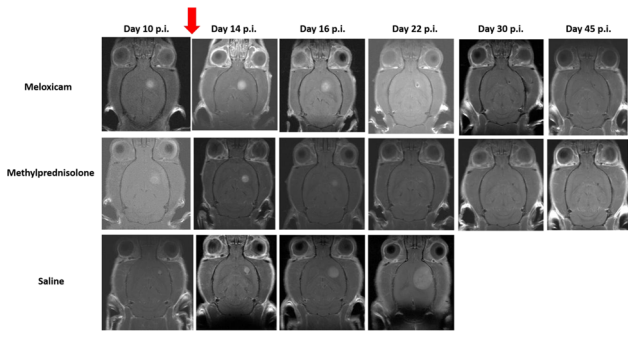

Figure 2. Coronal CE-T1W studies. Images show the tumor evolution along days post C6 cell-injection (p.i.) of the rats presented in fig. 1. Red arrow points the beginning of the therapy.

Mean diffusivity (MD) and MT maps of control and treated rats - 1 week after starting the treatment- are shown in Fig. 3. MD values were higher in the tumor area of the rat treated with SAID compared with treated with NSAID and control, while MT values were lower.

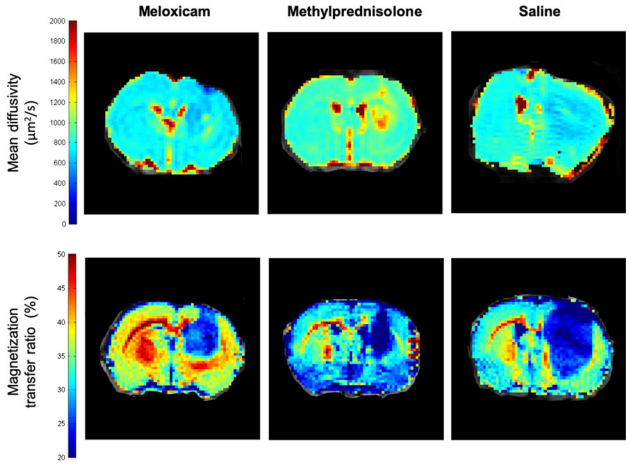

Figure 3. Parametric images 1 week after starting the therapy. Tumors in rats treated with meloxicam presented lower MD (up) and higher MTR (bottom) values than those observed in animals treated with methylprednisolone and saline.

Discussion/Conclusion: These preliminary results point meloxicam (NSAID) and methylprednisolone (SAID) as potential candidate therapies against GBM. Differences in the studied MRI parameters (MD and MT) indicate that the distinct AI effect is translated in a different behavior of the functional MRI biomarkers. This can potentially give useful information about the therapy effect and improve the therapy follow-up.
References:
1. Buckner et al. Semin Oncol. (2003)30:10–14.
2. Rayburn et al. Mol Cell Pharmacol. (2009)1:29–43.
3. De Souza et al. J Magn Reson. (2015)42:1582–1591.
4. Pérez-Carro et al. EJNMMI Res. (2014)4:44.

L01.20

In vivo MRI assessment of the pharmacological opening of the blood brain barrier by intraperitoneal mannitol injection in mice

A. Tessier, M. Bernard, A. Viola, **T.-A. Perles-Barbacaru**
Aix-Marseille University, CRMBM UMR CNRS 7339, Marseille, FRANCE

Purpose/Introduction: Hyperosmolar mannitol administration is used in the clinical and preclinical setting to deliver therapeutic agents across the Blood Brain Barrier (BBB). In most rodent studies, invasive intracarotid mannitol administration is performed. Here, we use dynamic Rapid Steady State (RSS)-MRI[1] with the low-molecular weight contrast agent Gd-DOTA and a long observation interval to assess BBB opening upon intraperitoneal (ip) injection of mannitol.
Subjects and Methods: Acquisitions were performed at 7T with a 72 mm volume resonator for emission and a 2 × 2 elements phased array surface cryoprobe. Female Swiss mice (n = 5) underwent dynamic T_1-weighted RSS-MRI[1] over 2 h, with ip Gd-DOTA injection (10 mmol/kg) at 5 min and ip mannitol injection (2.5 g/kg, 20%) at 20 min. RSS MRI was performed with a 3D inversion recovery prepared fast gradient echo sequence ($TR/TI/TR_{echo}/TE/\alpha$ = 750/295/5/1.5 ms/10°, 300 repetitions, matrix 64x64x33, resolution 230x230x500 mm^3). Time parameters are optimized to null the signal from brain parenchyma and blood ($T_1 > 1$ s). Heuristic parameters such as delay and initial slope of signal increase were determined in key brain regions to study the effects of mannitol.
Results: The vascular signal reaches thermal equilibrium within 5 min post Gd-DOTA injection (blood $T_1 < 60$ ms indicating a

vascular Gd-DOTA concentration > 4.6 mM) while interstitial signal remains nulled ($T_1 > 1$ s). The brain tissue signal therefore reflects the blood volume fraction (average murine BVf: 0.01–0.02) and remains constant (RSS) until mannitol results in interstitial Gd-DOTA accumulation. Regionally varying brain signal increase is noticeable when interstitial T_1 drops below 1 s, which happens for an interstitial Gd-DOTA concentration of 60 μM. In our study, the brain signal continued to increase over 100 min even when the vascular signal was gradually decreasing. Earliest and steepest signal increase was detectable in ventricles and olfactory bulb. Cortical regions showed signal increase delayed by up to 30 min. In muscle tissue, the Gd-DOTA extravasation rate increases within seconds upon mannitol administration.

Discussion/Conclusion: This minimally invasive MRI protocol is suited for direct detection of BVf changes or disruption of the BBB, without monitoring the arterial input function. Ip injection of Gd-DOTA ensures a vascular steady state signal while the BBB is intact. Modulation of BVf or BBB permeability can be performed over tenth of minutes. Continuous MRI signal increase in our study indicates that Gd-DOTA influx into the interstitial compartment is greater than backflux into the blood at 1.5 h after 2.5 g/kg mannitol (< 1/10 of reported doses[2]). This is important information on the available time window for brain delivery of small hydrophilic agents.

References:

1. Perles-Barbacaru et al. Magn Reson Med 2013;69(5):1451-6.
2 Sun et al. J Neurosci Methods 2012;203(1):122-9.

L01.21

Gadolinium Deposition in the Brain in a Large Animal Model: Comparison of Linear and Macrocyclic Gadolinium Based Contrast Agents

A. Jeibmann[1], H. Richter[2], S. Fingerhut[3], A. Radbruch[4], M. Sperling[5], U. Karst[5]
[1]University hospital Münster, Institute of Neuropathology, Münster, GERMANY, [2]Clinic for Diagostic Imaging, Vetsuisse faculty, Diagnostic Imaging Research Unit, ZÜrich, SWITZERLAND, [3]University Münster, Münster, GERMANY, [4]University Clinic Essen, Essen, GERMANY, [5]University Münster, Institute of Inorganic and Analytical Chemistry, Münster, GERMANY

Purpose/Introduction: Recent studies reported a signal intensity increase in the deep cerebellar nuclei (DCN) on MRI images caused by gadolinium deposition following the injection of gadolinium based contrast agents (GBCAs). There is an ongoing debate if the propensity of a GBCA to deposit gadolinium is primarily determined by its class as either linear or macrocyclic. In the current study, we aimed to compare the amount and the distribution of retained gadolinium of linear and macrocyclic GBCAs in the DCN after a single injection at a dose comparable to a human patient´s in a large animal model.

Subjects and Methods: Eighteen sheep were randomly assigned in six groups of three animals which received a single injection of 0.1 mmol/kg bodyweight of either the macrocyclic GBCAs gadobutrol, gadoteridol or gadoterate meglumine, the linear GBCAs gadobenate dimeglumine or gadodiamide, or saline. Animals were sacrificed ten weeks after injection. Local distribution and concentration of gadolinium and co-localization to other metals (iron, zinc, copper) in the DCN was assessed by laser ablation-inductively coupled plasma-mass spectrometry (LA-ICP-MS).

Results: Average gadolinium concentration for the macrocyclic GBCAs and the saline group was below the limit of quantification (5.7 ng/g tissue). In contrast, 14 (for gadobenate) and 27 (for gadodiamide) times more gadolinium than the limit of quantification was found for the linear GBCAs gadobenate (mean 83 ng/g) or gadodiamide (mean 155 ng/g brain tissue). Gadolinium distribution co-localized with other metals for linear GBCAs and a specific accumulation in the DCN was found.

Discussion/Conclusion: The current study supports the hypothesis that the amount of gadolinium deposited in the brain is primarily determined by its class as either macrocyclic or linear. The accumulation of gadolinium in the DCN for linear GBCAs explains the hyperintensities in the DCN found in previous studies for linear GBCAs and co-localization of gadolinium with other metals supports the hypothesis of a partial transmetalation of gadolinium from linear GBCAs as the cause for the accumulation in metal rich areas such as the DCN.

References: Gadolinium retention in the dentate nucleus and globus pallidus is dependent on the class of contrast agent.

Radbruch A, Weberling LD, Kieslich PJ, Eidel O, Burth S, Kickingereder P, Heiland S, Wick W, Schlemmer HP, Bendszus M. Radiology. 2015 Jun;275(3):783-91.

L01.22

Transgenerational neuroprotection of polyphenol supplementation in neonatal hypoxia–ischemia

U. Dumont[1], S. Sanchez[1], M.-C. Beauvieux[1], L. Pellerin[1], D. Deffieux[2], S. Quideau[2], J.-F. Chateil[1], **A.-K. Bouzier-Sore**[1], H. Roumes[1]
de Résonance Magnétique des Systèmes Biologiques UMR 5536 CNRS Université de Bordeaux, BORDEAUX, FRANCE, [2]Univ. Bordeaux, ISM (CNRS-UMR 5255), TALENCE, FRANCE

Purpose/Introduction: Introduction and purpose: Therapeutic strategy in neonatal hypoxia–ischemia (HI), a major cause of perinatal death and chronic disability, is limited to hypothermia. As many newborns do not respond to it, new treatments are needed. Intraperitoneal injection of resveratrol (RSV, polyphenol present in grapes) has shown neuroprotective properties in HI-pups. Our aim was to study the effects of maternal supplementation with piceatannol (PIC, hydroxyl homologue of RSV with higher bioavailability) in a context of neonatal HI.

Subjects and Methods: Materials and methods: HI (left carotid artery ligation + hypoxia (8% O_2, 92% N_2, 2 h) was induced in Wistar P7 rats (7 days post natal). Maternal drinking water was supplemented with PIC (0.15 mg/day/kg) during the first week of lactation (picL group, n = 8) or during the last week of gestation and the first week of lactation (picGL group, n = 11) or not supplemented (sham group, n = 15 and Ct group, n = 18). Brain lesion volumes (BLV) were measured in vivo, 3 h (P7), 48 h (P9) and 23d (P30) after HI, using diffusion-weighted MRI (4.7T Bruker, TE = 24 ms, TR = 2 s, 30 directions, 20 sections, 1 mm thick) and expressed as % of total brain volume. The severity of edema was assessed by measuring the apparent diffusion coefficient (ADC). Neuronal fiber integrity was estimated by measuring the fractional anisotropy (FA) at P30. Finally, motor and cognitive abilities were evaluated by behavioral tests.

Results: HI induced brain lesions in 100% of the Ct group (BLV, at P7: 40.78 ± 2.90%), 75% of the picL group (BLV, at P7: 20.78 ± 5.61%) and 55% of the picGL group (BLV, at P7: 15.90 ± 5.76%). Cytotoxic edema was significantly lower in the picL and picGL groups (higher ADC values compared to the Ct group, $p < 0.001$). At P30, 67% of the Ct group still had cerebral lesions compared to only 37% in the picL group and 29% in the picGL group (BLV at P30: 24.70 ± 7.65% vs 3.00 ± 1.70% and 2.41 ± 2.24%, for the groups HIC, picL and picGL, respectively, $p < 0.01$). At P30, FA was higher for picL and picGL groups than for the Ct group. For

behavioral tests, only PIC groups recovered motor and cognitive abilities.

Discussion/Conclusion: Conclusion: This study shows for the first time a neuroprotective role of PIC maternal supplementation in the context of a neonatal HI. A nutritionally realistic daily amount (corresponding to one passion fruit) was sufficient to avoid brain damage in some pups and to recover cognitive and motor functions.

References: -

L01.23

Exploring the potential of magnetic susceptibility-based MRI for identifying microstructural degradation in arterial vessels

A. J. Stone[1], B. Tornifoglio[1], R. D. Johnston[1], C. Kerskens[2], C. Lally[1]

[1]*Trinity College Dublin, Trinity Centre for Bioengineering & Department of Mechanical and Manufacturing Engineering, Dublin, IRELAND,* [2]*Trinity College Dublin, Trinity College Institute of Neuroscience, Dublin, IRELAND*

Purpose/Introduction: In diseased arterial tissue, key components of the tissue microstructure, such as collagen fibres, smooth muscle cells and elastic lamina become disrupted, impairing vessel function[1]. As such, assessment of vessel microstructure can provide improved indicators of function and disease.

Magnetic susceptibility-based MRI has provided insights into cartilage microstructure, demonstrating sensitivity to microstructural arrangement[2] and degradation[3]. Here, we investigate the link between arterial microstructure and magnetic susceptibility by applying a Quantitative Susceptibility Mapping (QSM) approach in artificially degraded ex vivo vessels. Following this, the magnetic susceptibility anisotropy of arterial microstructure is investigated.

Subjects and Methods: Models of tissue degradation were generated using ex vivo porcine carotid arteries (PCaA, n = 4) subjected to selective digestion of microstructural components: collagen degraded (collagen), elastin degraded (elastin) and decellularized (decell). An untreated (native) sample served as a control. Magnetic susceptibility anisotropy of vessel microstructure was investigated using native PCaA cut in half and placed in a custom holder to orient segments perpendicularly (Fig. 2a).

Samples were scanned using a 7T Bruker BioSpec system. Data was acquired using a 3D multi-echo GRE. Preprocessing of multi-echo phase data was performed using the MEDI toolbox[4]. Susceptibility maps were calculated from local field maps using truncated k-space division[5].

Results: Tissue masks were generated and voxel values of susceptibility extracted and referenced to background water. Voxel distributions of susceptibility differed between native and selectivley degraded tissues (Fig. 1).

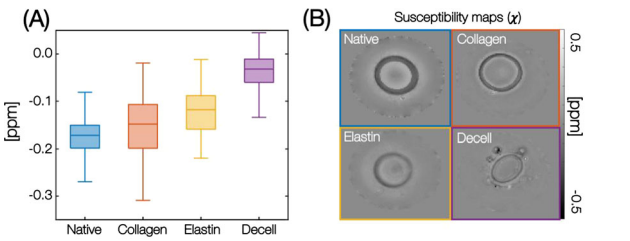

Fig1: (A) Susceptibility distributions measured in native and collagen degraded (collagen), elastin degraded (elastin) and decellularized (decell) PCaA. (B) Representative slices from susceptibility maps of native and selectively degraded vessels

Similarly, susceptibility distributions were extracted for each vessel segment in the perpendicularly oriented set-up. The vessel axis oriented parallel to B_0 demonstrated a unimodal distribution compared to the bimodal distribution of the perpendicularly oriented vessel axis (Fig. 2b). A masked line profile of the susceptibility map demonstrates differences in measured susceptibility dependent on vessel orientation (Fig. 2c).

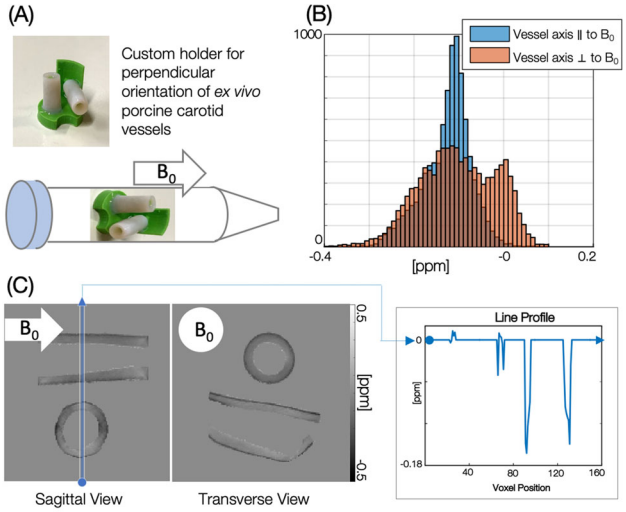

Fig2: (A) Schematic of vessel orientation (B) Distributions are unimodal when circumferentially arranged microstructure is perpendicular to B0 (blue) and bimodal when orientation to B0 is variable (red) (C) Line profile through oriented vessels

Discussion/Conclusion: Susceptibility mapping demonstrated sensitivity to induced microstructural degradation, suggesting it as a potential marker of microstructure damage in arterial vessels. Vessel microstructure showed susceptibility anisotropy indicating sensitivity to the circumferentially arranged microstructure. Future work will focus on scanning increased sample numbers and investigating the influence of orientation on degradation models to ascertain the susceptibility contribution of individual microstructural components, before applying this technique to diseased or degenerated human vascular tissues.

References:

[1]Humphrey et al. J. Biomech.2009;42(1).
[2]Wei et al. MRM.2017;78(5).
[3]Nykänen et al. MRM.2018;80(6).
[4]http://weill.cornelledu/mri/pages/qsm.html.
[5]Shmueli et al. MRM.2009;62(6).

L01.24

Renal functional and metabolic sex differences in rats – assessed with hyperpolarized [1-^{13}C]pyruvate MR

H. Qi, Y. Wen, C. Ø. Mariager, P. M. Nielsen, L. B. Bertelsen, H. Stødkilde-Jørgensen, C. Laustsen

Aarhus University, The MR Research Centre, Department of Clinical Medicine, Århus N, DENMARK

Purpose/Introduction: Metabolic sex differences have recently been demonstrated to be particularly important in tailoring treatment strategies. Sex has a major effect on fat turnover rates and plasma lipid delivery in the body [1]. However, whether renal sex differences exist is largely unknown. In this study, we investigated the gender specific renal metabolic and functional status in healthy Wistar rats.

Subjects and Methods: Sixteen eight week-old male (n = 8) Wistar rats and female (n = 8) Wistar rats were included in this study. All

MR examinations were performed in a 9.4 T pre-clinical MR system (Agilent, UK) using a dual tuned $^{13}C/^{1}H$ volume rat coil (Doety Scientific, US). Hyperpolarize [1-^{13}C]pyruvate scanning was used to assess the metabolic difference and was started at the beginning of injection. A balanced steady-state free precession (BSSFP) imaging sequence was interleaved with a standard slice selective free induction decay (FID) acquisition to acquire spectra, both sequences using the same slice selection parameters. BOLD and DCE scanning were used to assess the functional hemodynamic differences between male and female rats. After MR scanning, samples of arterial blood, urine and kidney tissue was harvested for further laboratory experiments. Unpaired two-tailed Student's test was used to compare the difference between male and female. $p < 0.05$ was considered statistically significant.

Results: A 50.6% higher lactate production and 58.5% higher fractional perfusion of lactate was found in male rats compared to female rats (Fig. 1),

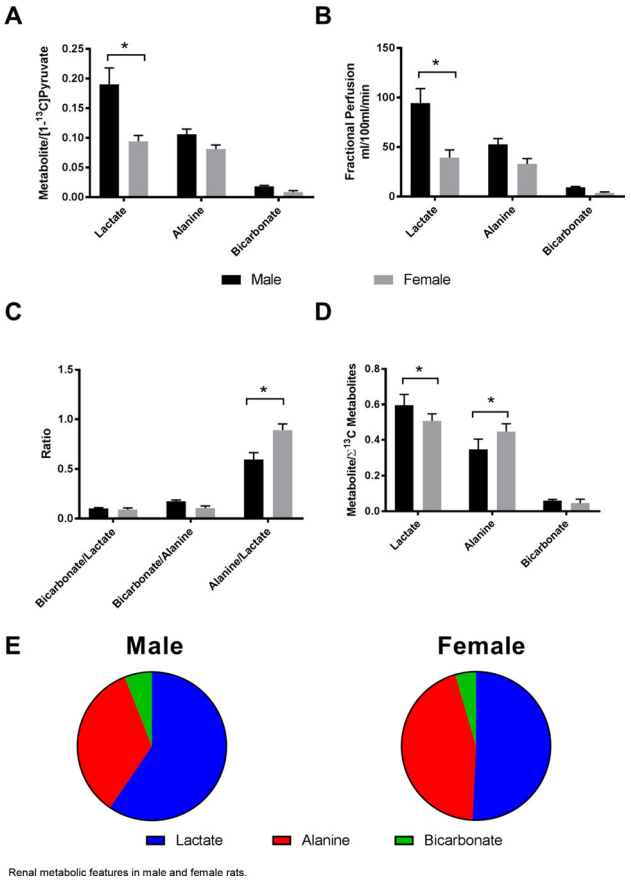

Renal metabolic features in male and female rats.

concomitant with altered hemodynamic parameters (Fig. 2)

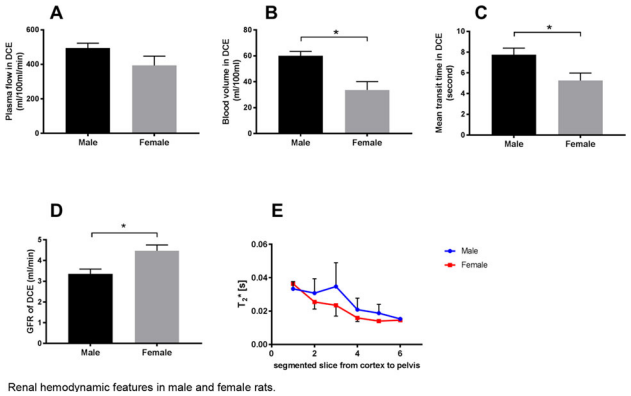

Renal hemodynamic features in male and female rats.

Discussion/Conclusion: This study demonstrates that there exists a metabolic shift between the male and female sex rats and as such this could explain, why female diabetes patients are more at risk of developing renal disease.

References:

1. Franck Mauvais-Jarvis. Sex differences in metabolic homeostasis, diabetes, and obesity. Biol Sex Differ. 2015 Sep 3;6:14.

L01.25

In vivo and ex vivo quantification of hepatic fatty acid in mice fed with CDAA-diet using magnetic resonance spectroscopy at 9.4 T

A. Xavier[1], F. Zacconi[2], T. Eykyn[3], B. Plaza[3], A. Phinikaridou[3], M. Andia[1]

[1]Pontificia Universidad Catolica de Chile, Biomedical Imaging Center, Santiago, CHILE, [2]Pontificia Universidad Catolica de Chile, Faculty of Chemistry, Santiago, CHILE, [3]King's College London, School of biomedical engineering and imaging sciences, London, UNITED KINGDOM

Purpose/Introduction: Nonalcoholic fatty liver disease (NAFLD) covers a group of liver disorders starting with steatosis and progressing to steatohepatitis, fibrosis and cirrhosis. The gold-standard to confirm the stage of NAFLD is the biopsy, but it is risky for the patients[1].

The aim of define a classifier using MRS emerges due to the need of replace biopsy with a non-invasive method that could classify NAFLD based on the chemical structure of fatty acids (FA) in the liver.

The purpose of this study is to compare the liver FA composition in a NAFLD mice model using CDAA diet during the time they have steatohepatitis (NASH). Mice fed with CDAA diet develop liver inflammation from week 3[2].

Subjects and Methods: The study of the liver was performed using in vivo and ex vivo MRS acquisition. For the ex vivo study, we fed a group of 6 mice (C57BL/6) with CDAA diet for 4 weeks and 10 weeks and for the in vivo study we fed 4 mice for 10 weeks. We also fed a control group. In the ex vivo study, a portion of the liver was used for histology and the remaining liver was used to analyse their fatty acids methyl esters (FAME) using a 9.4T MRS and gas chromatography with mass spectrometer (GC–MS). The diagram of the study is shown in Figure 1.

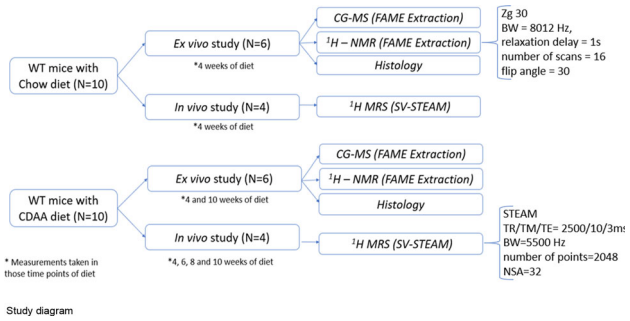

Study diagram

Results: ***Ex vivo*** **results**: The amount of fat acids stored in the hepatocytes during the diet intervention increased from 2.5 ± 0.8% (chow-diet) to 17.0 ± 4.1% (10 weeks-diet), $p < 0.05$. From the MRS results, we found 7 peaks correspondent to lipids, 3 of them are similar in all FA (0.9 ppm; 1.6 ppm; 2.2 ppm), therefore they present no significant differences. The other peaks showed significant differences between control group and 4 weeks of diet but no significant differences between 4 and 10 weeks of diet. The results from GC–MS are in according to the results obtained with MRS (Fig. 2). ***In vivo*** **results**: The fat fraction increased from 1.1 ± 0.2%(chow-diet) to 35.0 ± 4.3% (8 weeks-diet), $p < 0.05$ and it remained the same in 10 weeks-diet 34.0 ± 4.8, $p > 0.05$. Four peaks showed a small, but significant, difference between 4 and 10 weeks-diet. In the in vivo MR image it's possible to observe the heterogenous distribution of fat in the liver (Fig. 3).

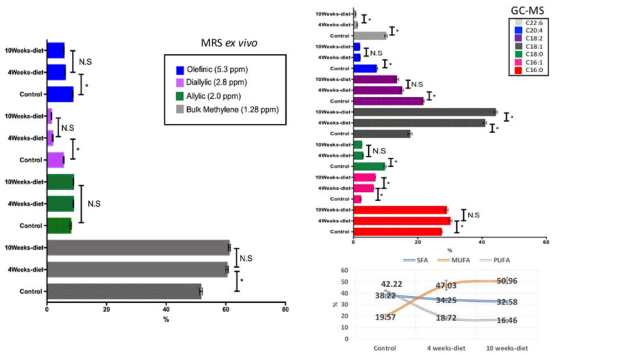

Ex vivo results form 1H-NMR and gas chromatography. Statistical analysis with Mann-Whitney test was performed from the results ex-vivo. N.S means no significant difference. (*) means significant difference (p<0.05).

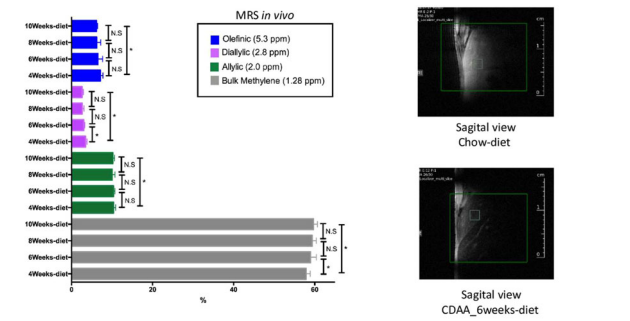

In vivo results form 1H-MRS. Statistical analysis with Mann-Whitney test was performed from the results in-vivo. N.S means no significant difference. (*) means significant difference (p<0.05)

Discussion/Conclusion: Some previous work showed a decrease in polyunsaturated FA (PUFA) with the progression of the disease in the steatosis stage[3]. In the present work the mice developed NASH and it seems that the PUFA remain constant in the progression of the disease in NASH stages. This study aims to help in the FA' characterization of different NAFLD models, which seems to have a clinical potential to monitoring the progression of this disease.

References:

[1]Williams et al.ISBN: 9781118912034(2016).
[2]Matsumoto, M. et al. (2013) Int. J. Exp. Pathol. 94. [3]Xavier, A. et al. ISMRM (2019):5380.

This publication has received funding from Millenium Science Initiative of the Ministry of Economy, Development and Tourism, grant Nucleus for Cardiovascular Magnetic Resonance.

L01.26

Mouse model of kit-induced cancer: initial results of MRI-based monitoring of disease progression

M. Kraiger[1], B. Rathkolb[2], H. Fuchs[1], J. Calzada-Wack[1], T. Klein-Rodewald[1], E. Wolf[2], V. Gailus-Durner[1], M. Hrabě de Angelis[1]
[1]Helmholtz Zentrum München/Institute of Experimental Genetics, German Mouse Clinic, Munich, GERMANY, [2]Ludwig-Maximilians-University München/Institute of Molecular Animal Breeding and Biotechnology, Gene Center, Munich, GERMANY

Purpose/Introduction: In the Munich ENU Mouse Mutagenesis Project we established a mutant mouse line Kit^{mvd013} carrying an activating c-Kit mutation homolog to the Imatinib®-resistant N822 K mutation found in human patients [1]. The heterozygous mutant animals of this model develop erythrocytosis and gastrointestinal stromal tumor (GIST). In addition, based on preliminary histological findings we hypothesize that malignancy of c-kit induced tumor is influenced by unknown inherent genetic characteristics [2]. Here we report on initial results of an ongoing MRI follow up study monitoring age-related disease progression in c-kit mutant mice compared to age-matched wild-type littermates.

Subjects and Methods: The design of the longitudinal study comprises MRI experiments every other month over a period of one year. The MRI experiments were performed on a 9.4 T Biospec 94/20 small animal system equipped with a 675 mT/m gradient system (Bruker, Germany). A quadrature transmit/receive coil with an inner diameter of 35 mm was used (M2 M imaging corporation, USA). The protocol comprises: **relaxometry** of bone marrow and spleen, T1 IR-FISP [3] parameters: TR/TE 10500/2.65 ms, TI(1)/ΔTI 57/480 ms, FA 180°/10°, 7 inverison times, nex = 4, T2 MSME parameters: TR/TE/ΔTE 2000/6/6 ms, FA 90°/180°, nex = 1, 14 echos; **morphometry** of gastrointestinal (GI) organs, 2D FS RARE parameters: TR/TE = 2665/12.6 ms, rare = 4, FA = 90°/180°, nex = 4, 3D FISP parameters: TR/TE = 5/2.4 ms, FA = 15°, nex = 4; and **dynamic imaging** capturing GI motion, trueFISP parameters: TR/TE = 3/1.5 ms, FA = 30°, frame duration 289 ms, 300 frames.

Results: T1 relaxation times of lumbar vertebra of mutant mice (n = 8) are in the range of 1619 ± 95 ms, of the wild-type (n = 8) T1 times ranging 1587 ± 109 ms. For the mutant and the wild-type cohort mean splenic T2 times of 10.78 ± 1.75 ms and 10.37 ± 1.72 were obtained. Exemplary results of the segmental motion and morphological analysis are given in Figure (1).

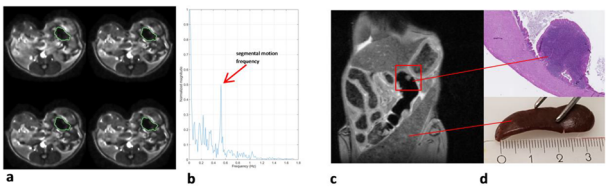

Fig1: Example of the analysis. a: tracing of the caecum b: frequency plot of temporal changes of caecum's cross section. c: RARE image showing enlarged spleen and prominent Peyer´s patch. d: histopathology of enlarged Peyer's patch, enlarged spleen.

Results of the motion analysis were in good agreement with segmental motion derived from previous studies [4], with a frequency range of 0.1–0.5 Hz ± 0.12 Hz for the segmental motion of the caecum of the sixteen animals.

Discussion/Conclusion: At a high field strength of 9.4 T non-invasive study of gut motility is feasible. The interpretation of the difference in the estimated T1 times and the obtained T2 times of similar range is expected to be clarified by additional histological analysis. In conclusion, preclinical MRI facilitates the monitoring of disease progression in KIT mutant mice in terms of high-resolution, quantitative relaxometry and functional gut motility analysis.

References:

[1] Baek JO, Kang HK, Na SY, et al. Dermatol 2012; 166:1370-3.
[2] Micklich K, doctoral dissertation. http://nbn-resolving.de/urn:nbn:de:bvb:19-150198.
[3] Deichmann R and Haase A, JMR 1997; 96:608-612.
[4] Ailiani AC, Neuberger T, Brasseur JG, et al. MRM 2009; 62:116-126.

L01.27

Functional MRS of GABA + , GABA- and macromolecules in human visual cortex at 3 Tesla

A. Yakovlev[1], A. Manzhurtsev[2], P. Menshchikov[3], M. Ublinskii[4], T. Akhadov[4], N. Semenova[2]
[1]Lomonosov Moscow State University, Physics, Moscow, RUSSIAN FEDERATION, [2]Emanuel Institute of Biochemical Physics of the Russian Academy of Sciences, Moscow, RUSSIAN FEDERATION, [3]Semenov Institute of Chemical Physics of the Russian Academy of Sciences, Moscow, RUSSIAN FEDERATION, [4]Clinical and Research Institute of Emergency Pediatric Surgery and Trauma, Moscow, RUSSIAN FEDERATION

Purpose/Introduction: The glutamate/GABA relation is an important indicator of CNS functioning. MEGA-PRESS pulse sequence is widely used for the measurement of GABA and glutamate + glutamine (Glx) at 3T [1]. However, the presence of the macromolecular (MM) signal in MEGA-PRESS GABA + spectra at 3 ppm may affect the small changes in [GABA] caused by any reason, for example, by mTBI [2] or neuronal activation. The aim of this study is to reveal changes in GABA + , GABA- and pure MM signal intensities in activated visual cortex. This would allow to assess the influence of MM on the accuracy of GABA measurements.

Subjects and Methods: Forty subjects (age 24 ± 3) participated in the study. InVivo SensaVue was used for stimulus transmission. The activated region was defined by the preliminary fMRI study. The spectroscopy voxel was positioned in the activated visual cortex. At first, spectra in rest were accumulated, after that – spectra during continuous 8 Hz flashing checkerboard stimulation (9 min 36 s each). GABA + spectra were obtained in 8 subjects, GABA- in 16 subjects. For parameters see Table 1.

Pulse sequence	Duration of editing pulses, ms	δ-on, ppm	δ-off, ppm	TE, ms	TR, ms	NSA
MEGA-PRESS GABA+	14	1.9	7.5	68	2000	288
MEGA-PRESS GABA-	20	1.9	1.5	80	2000	288

Table 1. Parameters the MEGA-PRESS pulse sequences for GABA+ and GABA- spectral acquisition used in the study. The editing pulse at δOff=1.5 ppm suppresses the MM signal.

The MM levels during stimulation were measured in 16 subjects. In order to obtain the MM signal, MEGA-PRESS GABA + sequence was modified by an additional inversion pulse before the base sequence. Inversion delay = 530 ms (BW = 50 Hz, δ = 3 ppm).

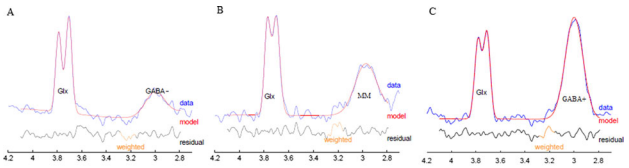

Figure 1. Spectral processing in Gannet. A – GABA- spectrum, B – macromolecular spectrum, C – GABA+ spectrum.

All spectra were processed in Gannet. The GABA/Cr and Glx/Cr (both from GABA + and GABA- spectra) and MM signal intenstites were obtained. The relative values of these parameters (stimulation/rest) were calculated and tested against the value = 1 using Mann–Whitney criterion.

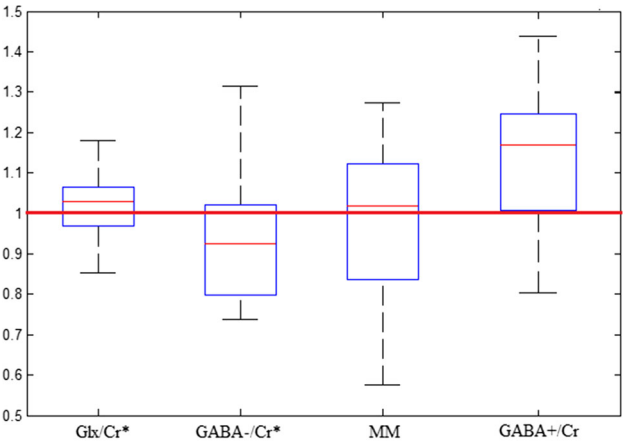

Figure 2. Relative changes (stimulation/rest) in the parameters obtained in the study. * - p<0,05 by Mann-Whitney criterion.

Results: The statistically significant reduction in GABA-/Cr and GABA-/Glx, as well as the increase in Glx/Cr were revealed. The MM intensity and GABA +/Cr were unchanged under activation.

Discussion/Conclusion: We revealed the decrease in GABA level only when GABA signal was collected with MM suppression (GABA-). This result is in agreement with the MM-suppressed data obtained at 7 T [3]. On the contrary, GABA + measurements did not allow to reveal this reduction of GABA. The increase in Glx/Cr also complies with the literature data [4]. The results obtained say for the predominance of the glutamatergic neurons role in the neuroactivation process.

To our knowledge, the fMRS of macromolecules at 3 T was performed for the first time. The MM levels are not affected by continuous visual stimulation. However, here we demonstrate that the presence of the MM resonance in GABA + spectra at 3 ppm may

mask the effect of stimulation on GABA levels. The results obtained demonstrate the importance of the MEGA-PRESS GABA- usage, otherwise the effect of any impact on [GABA] may be missed.

References:
1. Mullins P.G. et al. https://doi.org/10.1016/j.neuroimage.2012.12.004.
2. Menshchikov P.E. et al. https://doi.org/10.1134/s0006350917060161.
3. Chen C. et al. https://doi.org/10.1016/j.neuroimage.2017.05.044.
4. Stanley J.A. et al. https://doi.org/10.3389/fpsyt.2018.00076.

L01.28

Lesion volume and metabolic changes in focal brain ischemia in rats treated with human induced pluripotent stem cell-derived neural precursors

N. Ziółkowska[1, 2], N. Romanyuk[3], P. Jendelová[3], D. Jirák[2]
[1]Charles University, First Faculty of Medicine, Institute of Biophysics and Informatics, Prague, CZECH REPUBLIC, [2]Institute for Clinical and Experimental Medicine, Department of Computed Tomography, Magnetic Resonance and Clinical Experimental Spectroscopy, Prague, CZECH REPUBLIC, [3]Institute of Experimental Medicine, Czech Academy of Sciences, Department of Neuroregeneration, Prague, CZECH REPUBLIC

Purpose/Introduction: Potential of induced pluripotent stem cell-derived neural precursor (iPSC-NP) transplantation represents an intriguing therapeutic approach to neural regeneration [1]. In this study, we transplanted human iPSC-NPs in ischemic stroke model in rats and monitored their effect on neuroregeneration using magnetic resonance imaging (MRI) (lesion volume changes) and spectroscopy (MRS) (metabolite concentration changes: Inositol-Ins, Taurine-Tau, Glycerophosphocholine + Phosphocholine-GPC + PCh, N-acetyl-aspartate + N-acetyl-aspartyl-glutamate -NAA + NAAG, Creatine + Phosphocreatine-Cr + PCr and Glutamate +Glutamine-Glu + Gln) [2].

Subjects and Methods: Focal cerebral ischemia was induced by intraluminal right middle cerebral artery occlusion (MCAO). Cell-treated animals were transplanted 7 days after MCAO. Both grafted and control animals were divided into groups based on initial lesion size assessed from T_2-weighted MR images acquired at 4.7T: small control lesion-SCL, small treated lesion-STL, big control lesion-BCL, big treated lesion-BTL. The effect of transplanted iPSC-NPs on metabolic changes was determined by ^{1}H-MRS (single-voxel PRESS sequence with water suppression) of both hemispheres 1 month and 4 months after MCAO. Spectra were evaluated using the LC Model.

Results: Typical MR images with visible lesion volume are presented in the figure 1A. Volume analysis revealed that after 1 month significant lesion increase was found in BTL and BCL groups (Fig. 1B) and after 4 months lesion volume decrease in SCL and BTL groups. Metabolite concentrations changes between both hemispheres are summarized in Fig. 2. The biggest differences were observed in BTL group (4 metabolites with $p < 0.01$ in both time points) in which the lesion volume decrease after 4 months. Metabolites achieve lower concentrations on the lesion side in all groups. Spectroscopic results correlated with volumetric measurements, the highest correlation was observed for NAA + NAAG (Fig. 3).

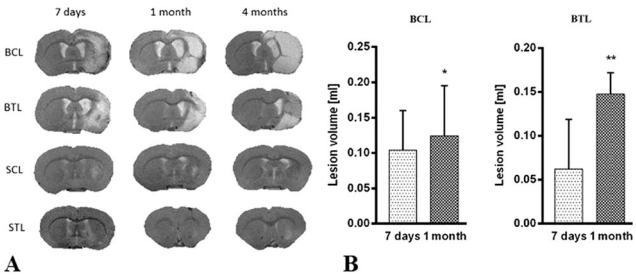

Fig. 1 (A) T2-weighted MR images of lesions at three time points in all groups. (B) Lesion volume change [ml] between 7 days and 1 month: BCL and BTL groups.

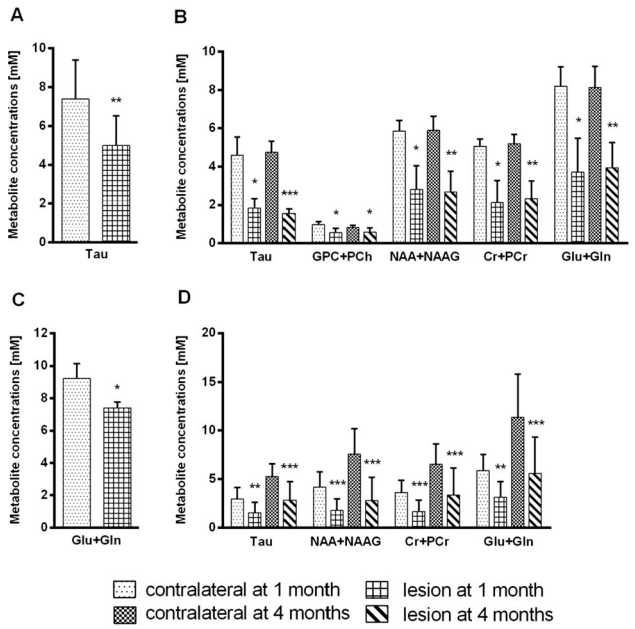

Fig. 2 Metabolite concentrations compared from both hemispheres 1 and 4 months after MCAO. (A) SCL 1 month. (B) BCL 1 and 4 months. (C) STL 1 month. (D) BTL 1 and 4 months.

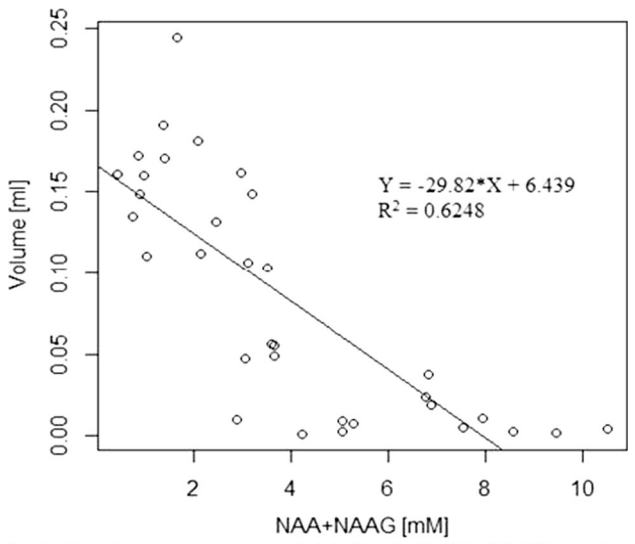

Fig. 3 Correlation of volumetry to spectroscopy results from the lesion side. Lesion volume [ml] and NAA+NAAG concentrations.

Discussion/Conclusion: Our data indicates that iPSC-NP transplantation may be an interesting tool for post-ischemic tissue repair and that metabolite concentrations increase in the contralateral hemisphere can indicate neuronal changes, especially in animals with big lesions. Further research into the ability of iPSC-NPs to differentiate into tissue-specific neurons and its effect on the long-term restoration of lesioned tissue is necessary.

References:
1. Baker et al. (2017). Sci Rep 7(1), 10075.
2. Saunders, D.E. (2000). Br Med Bull 56(2), 334-345.

Acknowledgement: Institute for Clinical and Experimental Medicine IKEM, IN00023001; Charles University, First Faculty of Medicine.

L01.29

Gadolinium Deposition in the brain following intravenous injection of GBCAs: Did we focus on the wrong locations?

H. Richter[1], A. Jeibmann[2], S. Fingerhut[3], A. Radbruch[4], M. Sperling[5], U. Karst[5]
[1]Clinic for Diagostic Imaging, Vetsuisse faculty, Diagnostic Imaging Research Unit, ZÜrich, SWITZERLAND, [2]University hospital Münster, Institute of Neuropathology, Münster, GERMANY, [3]University Münster, Münster, GERMANY, [4]University Clinic Essen, Essen, GERMANY, [5]University Münster, Institute of Inorganic and Analytical Chemistry, Münster, GERMANY

Purpose/Introduction: Recent studies reporting gadolinium deposition in the deep cerebellar nuclei (DCN) following the injection of gadolinium based contrast agents have forstered intensive research into potential neurological consequences. While current research mostly focusses on potential side efects in the brain, other organs exhibiting higher amounts of gadolinium might be at higher risk to develop pathologies. In the current study we compared the amount of gadolinium deposited in the cerebellum and in the skin after a single injection at a dose comparable to a human patient´s in a large animal model.

Subjects and Methods: Eighteen sheep were randomly assigned in six groups of three animals which received a single injection of 0.1 mmol/kg bodyweight of either the macrocyclic GBCAs gadobutrol, gadoteridol or gadoterate meglumine, the linear GBCAs gadobenate dimeglumine or gadodiamide, or saline. Animals were euthanized ten weeks after injection. Concentration of gadolinium in the cerebellum and the skin were assessed by acid digestion followed by inductively coupled plasma-mass spectrometry (ICP-MS).

Results: Average gadolinium concentration for the macrocyclic GBCAs and the saline group was below the limit of quantification (1.9 ng/g tissue) for the brain. In contrast average concentration in the skin was up to eight times higher for macrocyclic GBCAs and hence above the limit of quantification. For linear GBCAs Gd concentration in the brain was up to 15 ng/g (for gadobenate) and up to 32 ng/g (for gadodiamide) while the conenctrations in the skin were eight times higher (124 ng/g for gadobenate and 282 ng/g for gadodiamide).

Discussion/Conclusion: Our results support the hypothesis that the average amount after a single injection of GBCAs is approximately eight times higher in the skin than in the cerebellum.

Moreover the results support the hypothesis that the amount of gadolinium deposited in the cerebellum might be an indicator for gadolinium stored in other organs. Clinical relevance of the gadolinium in the brain or the skin remain unknown.

References: Gadolinium retention in the dentate nucleus and globus pallidus is dependent on the class of contrast agent.

Radbruch A, Weberling LD, Kieslich PJ, Eidel O, Burth S, Kickingereder P, Heiland S, Wick W, Schlemmer HP, Bendszus M. Radiology. 2015 Jun;275(3):783-91.

L01.30

MRI characterization of long-term cerebral alterations in a NHEJ deficient mouse model following low dose irradiation at the juvenile stage

L. Mouton[1, 2], O. Etienne[3], D. A. Barrière[4], E. Pérès[5], J.-P. de Villartay[6], F. Boumezbeur[4], F. Boussin[7], D. Le Bihan[4]
[1]CEA/NeuroSpin, Gif sur Yvette, FRANCE, [2]CEA/NeuroSpin/ Frédéric Joliot Institutes, Gif sur Yvette, FRANCE, [3]Stem Cells and Radiation, CEA, INSERM, Université Paris Sud, Université de Paris, LRP, UMR Genetic Stability, Fontenay-aux-Roses, FRANCE, [4]CEA/ NeuroSpin/Frédéric Joliot Institute, Gif sur Yvette, FRANCE, [5]Normandie Univ, UNICAEN, CEA, CNRS, ISTCT/CERVOxy group, UMR6030 GIP CYCERON, Cean, FRANCE, [6]Institut Imagine, INSERM, Université Paris Descartes Sorbonne Paris Cité, Laboratory "Genome Dynamics in the Immune System", UMR1163, Paris, FRANCE, [7]Stem Cells and Radiation, CEA, INSERM, Université Paris Sud, Université de Paris, LRP, UMR Genetic Stability,, Fontenay-aux-Roses, FRANCE

Purpose/Introduction: In mammals, brain development extends beyond birth and well into childhood. As a consequence, post-natal radiation exposure is likely to impair neurogenesis [1]. While the effects of high doses of radiation on the brain have been studied and are reasonably well understood, the effects and mechanisms of the brain's responses to low doses of radiation remain rather obscure, especially in juveniles. Moreover the individual radiosensitivity is dependent on DNA repair mechanisms. In this context, it is relevant to evaluate the low dose radio-induced effects on the brain on models with different expressions of DNA repair systems. This study aims at characterizing, by anatomical and diffusion MRI, cerebral damages following postnatal low dose irradiation in wild-type (WT) and knock-out mice in double-stranded DNA repair (Xlf-/-) [2].

Subjects and Methods: WT and Xlf–/– C57BL/6 N male mice were irradiated on the postnatal day 10 (PN 10) with a dose of 100 mGy from a ^{137}Cs source using a medical irradiator. At 3 months after exposure to low dose radiation, irradiated ($N_{WT,IRR}$ = 23, $N_{Xlf\text{-}/\text{-},IRR}$ = 16) and non-irradiated ($N_{WT,Sham}$ = 21, $N_{Xlf\text{-}/\text{-},Sham}$ = 25) mice were imaged with 11.7 T MR scanner. The MRI protocol consisted in the acquisition of: (i) a whole-brain 3D T_2*-weighted anatomical images and (ii) a diffusion MRI (20 b-values: 0-3000 s/mm^2 along 6 directions). The ROIs-based pipeline analysis was performed on: (i) the anatomical images and (ii) the diffusion parametric maps (ADC, K, MD, FA, S-index [3]) to evaluate respectively volumetric and microstructural changes [4]. Statistical significance between irradiated and sham cohorts were assessed using a Student's *t* test.

Results: No significant changes were observed in total brain, grey matter or white matter volumes neither in WT nor Xlf–/– exposed mice. As shown in Figure 1, the diffusion parameters variations observed across cohorts in selected ROIs such as the Cc, SVZ or Hip. Contrary to WT mice, Xlf–/– irradiated mice exhibit a significant MD increase combined to a decreased FA and S-index values.

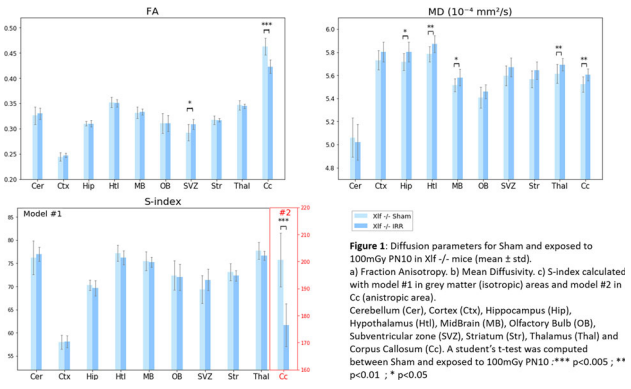

Figure 1: Diffusion parameters for Sham and exposed to 100mGy PN10 in Xlf -/- mice (mean ± std).
a) Fraction Anisotropy. b) Mean Diffusivity. c) S-index calculated with model #1 in grey matter (isotropic) areas and model #2 in Cc (anistropic area).
Cerebellum (Cer), Cortex (Ctx), Hippocampus (Hip), Hypothalamus (Htl), MidBrain (MB), Olfactory Bulb (OB), Subventricular zone (SVZ), Striatum (Str), Thalamus (Thal) and Corpus Callosum (Cc). A student's t-test was computed between Sham and exposed to 100mGy PN10 :*** p<0.005 ; ** p<0.01 ; * p<0.05

Discussion/Conclusion: Considering the low dose irradiation (100 mGy), no significant volumetric nor microstructural changes were expected in WT [5]. However in Xlf-/- mice, their increased radio-sensitivity manifests in subtle microstructural variations particularly visible in the Cc. As shown previously [4], S-index is the most sensitive diffusion metric to detect radiation-induced brain damages. In the future, diffusion MRI and genotyping could be combined to explore heterogeneity in radio-sensitivity across exposed human populations.

References:

[1] Nieman B.J et al. Int J Radiat Oncol Biol Phys 2015.
[2] Abramowski V et al. Cell Death Differ. 2018.
[3] Iima M, Le Bihan D. Radiology. 2016.
[4] Pérès E et al., Int J Radiat Oncol Biol Phys 2018.
[5] Verreet T et al., Front Behav Neurosci 2016.
[6] Ashburner J. and Friston K.J, NeuroImage 2000.

I07 Teaching Session

15:00–16:00 *Room 1 - Willem Burger Zaal*

The Role of Efficient MRI in Animal Imaging

I07.01
Scanning Without Anaesthesia

O. Gröhn
University of Eastern Finland, A. I. Virtanen Institute, Kuopio, FINLAND

Learning Objectives: To understand potential influence of anesthesia to functional and metabolic MRI.
To learn different approaches for awake fMRI, and understand the benefits and limitations.
Body: Anesthesia is commonly used during MRI to prevent movement and to decrease stress in the animals. However, anesthesia has also significant undesirable effects. This is most clearly seen on fMRI responses to stimuli or drugs and resting state activity [1,2] as anesthesia interferes with normal brain function and neurovascular coupling. Also, metabolic studies with C13 labeled compounds are influenced by anesthesia [3]. Furthermore, there is increasing awareness that effects of anesthetics can extend beyond the duration of anesthesia [4, 5].
To avoid the disrupting effects of anesthetics, several groups have implemented awake animal fMRI imaging protocols [6-9]. Awake animals are likely to move and experience stress during fMRI, which raises the demand for carefully optimized restraint and habituation protocols. Several studies have demonstrated, that rats are able to adapt to the level of restraint required for fMRI [6,8,9].
In this lecture, overview of the existing approaches for awake fMRI will be given, including an approach with 3D printed restraint kit developed in our group [9]. The importance of proper habituation and monitoring of stress level indicators is emphasized. Examples will show the feasibility of obtaining high quality fMRI, functional connectivity, and hyperpolarized MRI data from awake animals [3,9]. In addition, a novel approach for awake fMRI using zero echo time multi- band SWIFT (MB-SWIFT) approach will be introduced [10, 11]. This approach turned out to be optimal for awake fMRI studies as it is quiet and has high tolerability to movement artefacts due to high excitation and read bandwidths.
Existing studies show that awake metabolic and fMRI studies are feasible and new approaches will make them more commonly available and increase the reliability and translatability of the results. While the use of anesthetized animals remains to be the most sensible option for anatomical and (micro) structural imaging, scanning without anesthesia can provide an exciting alternative for fMRI and metabolic studies.
Acknowledgements NIH U01-NS103569-01, Academy of Finland, Erkko foundation
References:
[1] Paasonen. Eur. Neuropsychopharm. 26, 518–531, 2016
[2] Paasonen. Neuroimage 172, 9–20, 2018
[3] Hyppönen. Proc. ISMRM, 0722, 2019
[4] Stenroos. Proc. ISMRM, 3754, 2019
[5] Colon. Prog. in neurobiol. https://doi.org/10.1016/j.pneurobio.2017.01.005., 2017
[6] King. J. Neurosci. Methods 148, 154–160, 2005
[7] Febo. Front. Psychiatry 2:43., 2011
[8] Chang. J. Neurophysiol. 116, 61–80. 10.1152, 2016
[9] Stenroos. Front Neurosci. 2018, 20;12:548. 2018
[10] Lehto. Neuroimage. 159:443-448, 2019
[11] Paasonen. Proc. ISMRM, 3753, 2019

I07.02
Fast Imaging

S. Miraux
CNRS, RMSB UMR5536, Bordeaux, FRANCE

Learning Objectives: Rodent models, rats and mice especially, remain very widespread in basic and pre-clinical research. These models are developed for surgical purposes, or to obtain more informations on pathologies (transgenic), or to obtain pharmacological properties of new drugs They allow a better understanding of organ functioning, pathologies and enable the evaluation of new therapeutic strategies.
However, the size of these animals makes them difficult to explore by MRI. It is indeed necessary to achieve much higher spatial resolutions than in humans. While a millimeter resolution can be sufficient in humans, it should reach approximately 200 µm in rats and even higher in mice. This, of course, has an important consequence on the signal-to-noise ratio, which is a priori much lower.
Although specific equipments are being developed for rodent MRI (intense magnetic fields, high intensity gradient systems, surface probes), the most used method to increase the signal-to-noise ratio is to accumulate the signal over multiple averages. Operators must therefore choose the type of image or information they need to obtain. However, to better explore animal models, research teams are increasingly seeking for multi-contrast, multi-parametric and, if possible, quantitative information.
It is therefore important to limit the time necessary to acquire images in order to collect as much information as possible either from the same animal or from cohorts of animals.
We will therefore review the different recent acceleration strategies implemented by research teams to acquire images more and more resolved in space and time.
These strategies may involve instrumental (cryoprobe, multi-mouse system) or methodological (image acquisition, reconstruction) developments.
Body: Examples based on non-cartesian imaging, Compressed Sensing, parallel imaging will be shown and illustrated with applications in the field of NeuroImaging, cardiovascular imaging or whole body imaging.
References: -

S04 Scientific Session

15:00–16:00 *Room 2 - Van Weelde Zaal*

Gadolinium-free Imaging: Perfusion MRI

S04.02

Measurement of microstructural compartment blood flow based on partial volume correction of ASL MRI using neurite orientation dispersion and density imaging (NODDI)

I. Asllani[1], L. Petitclerc[2], M. Bozzali[1], M. van Osch[2], M. Cercignani[1]
[1]University of Sussex, Brighton, UNITED KINGDOM, [2]Leiden University Medical Center, Leiden, NETHERLANDS

Purpose/Introduction: To measure perfusion in intra- and extra-neurite compartments within the gray matter (GM) tissue by combining ASL with neurite orientation dispersion and density imaging (NODDI).

Background: In ASL MRI, labeling of the arterial water is followed by a delay (PLD) that needs to be sufficiently long to allow for the tagged water to cross the vasculature and perfuse into the tissue[1]. Because of the T1-relaxation, rapid readout sequences are employed, resulting in a typical voxel volume of $\sim$ 60 mm^3. As such, the ASL signal in a voxel is a weighted sum of flows from different tissue and arterial compartments within the voxel, known as partial voluming effect. A partial volume correction (PVC) method has been developed for use in ASL based on the assumption of local homogeneity in flow for each tissue[2]. The method makes no distinction between different compartments within the same tissue. We investigated the potential of the method to further differentiate GM flow into extra-neurite compartment, (e.g., soma, glial cells) and intra-neurite, (comprised of axons, etc.)[3] contributions by obtaining information about these compartments from a diffusion weighted imaging (DWI) model, referred to as NODDI[3]. We tested the hypothesis that as PLD increases, the intra-neurite GM CBF also increases.

Subjects and Methods: *Theory*: The blood flow (f) at each voxel is modeled as:

$$Eq.1: f_T = VF_{In} \cdot f_{In} + VF_{En} \cdot f_{En} + VF_{Iso} \cdot f_{Iso}$$

where, VF_{In}, VF_{En}, VF_{Iso} represent respectively the intra-neurite, extra-neurite, and non-tissue compartmental volume fractions[3]. The VF images are obtained from the NODDI data[3]. By assuming that for each compartment, f_j is constant over a 'kernel', Eq.1 can be re-written to reflect the flow at the voxel positioned at r_j in the center of the kernel[2:]

$$Eq.2: fj = \left[VF^T \cdot VF\right]^{-1} \cdot VF^T \cdot f_T$$

Imaging: T1w (MPRAGE), NODDI, and ASL images were obtained on 7 participants (age = 34.5 $\pm$ 7.4 y, 4 men) on a Siemens 3T. To test the hypothesis that the intra-neurite flow would increase with increasing PLD, ASL images were acquired with PLDs: 500 ms, 800 ms, 2200 ms. Only results from voxels with GM content > 80% are presented.

Results: Fig. 1 shows images used by the PVC algorithm to extract flow from each microstructural compartment, which are shown in Fig. 2.

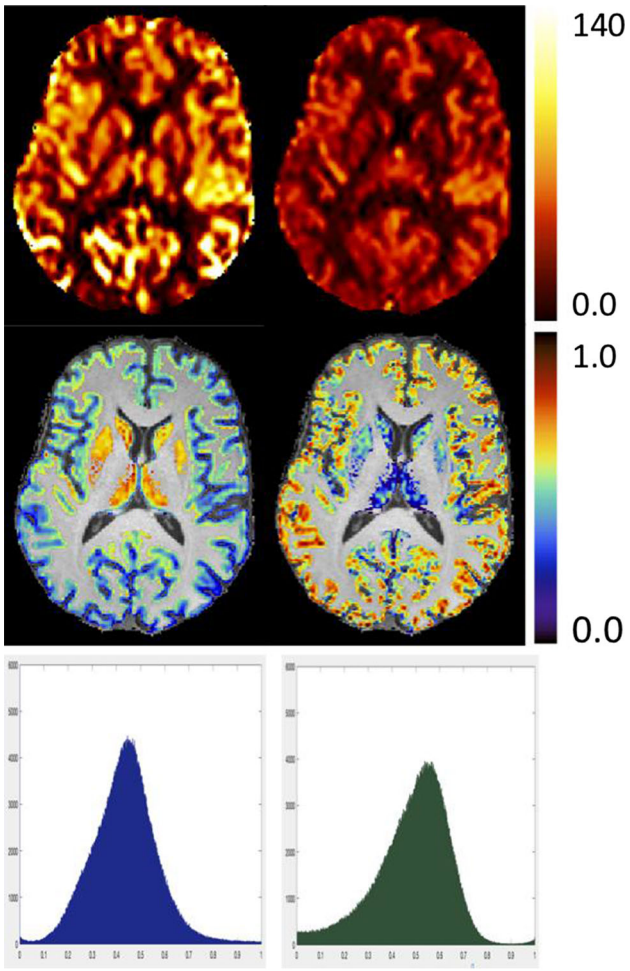

Fig1: 1st row: CBF images for PLD800 (left) and PLD2200 (right); 2nd row: Intra-neurite (left) and Extra-neurite compartments; 3rd row: Distribution of Intra-neurite (left) and Extra-neurite (right) volumewithin GM>0.8 mask.

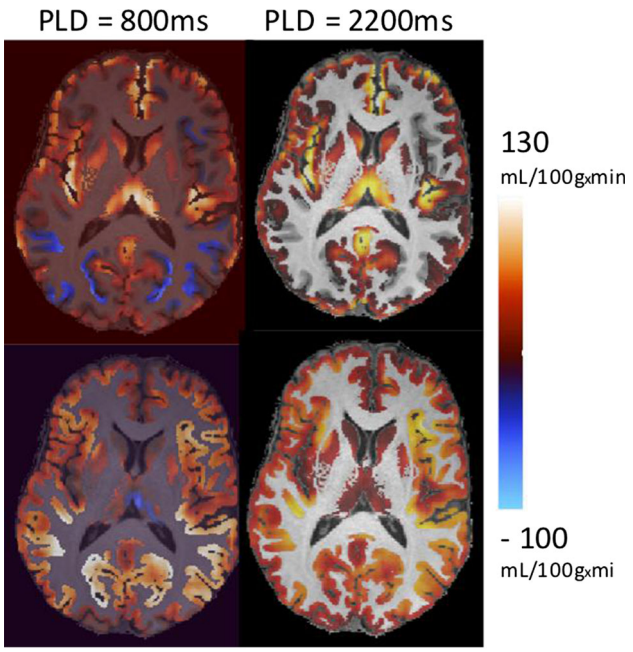

Fig.2: Intra-neurite (top) and Extra-neurite (bottom) CBF images from a single participant for PLD=800ms and 2200ms. Note the negative flow in the Intra-neurite CBF for PLD=800ms.

For PLD_{2200}, CBF in the extra- and intra-neurite compartment was 66 ± 10 and 59 ± 8 mL/100 g·min, respectively. As hypothesized, for PLD_{800}, the CBF signal was contained primarily in the extra-neurite compartment, 94 ± 17 *vs.* 38 ± 11 mL/100 g·min. For PLD_{500}, the intra-neurite CBF iwas essentially zero (– 0.9 ± 0.6 mL/100 g·min).

Discussion/Conclusion: We combined NODDI with ASL MRI to distinguish between CBF in the intra- and extra-neurite compartments in GM. While results look promising, more work is needed to validate the method and test its clinical feasibility.

References:

1. Alsop DC et al. MRM, 2016.
2. Asllani I et al. MRM, 2009.
3. Zhang H et al. NeuroImage, 2012.

S04.03

Examination of optimised PLD protocols for pCASL accounting for dispersion and macrovascular contamination over a prolonged ATT range

X. Zhang, F. Kennedy McConnell, J. G. Woods, T. W. Okell, M. A. Chappell
University of Oxford, Institute of Biomedical Engineering & Wellcome Centre for Integrative Neuroimaging, Oxford, UNITED KINGDOM

Purpose/Introduction: In pCASL, one or multiple post-labelling delays (PLD) are used before image readout to allow inverted spins to perfuse into the target tissue. Recently, a general framework was proposed for optimising PLD sampling protocols for pCASL under an ideal kinetic model.[1] This work examines the two optimised protocols: CBF-ATT_{opt} and CBF_{opt}, along with a reference multi-PLD protocol and single-PLD protocol, under the effects of dispersion and macrovascular contamination.[2,3] These protocols were optimised for a normal ATT range of 0.5 s < ATT < 1.8 s, but here we will examine them over a prolonged range of 0.5 s < ATT < 3.0 s.

Subjects and Methods: For each protocol, pCASL signals were simulated using MATLAB from the standard kinetic model with/without a Gamma dispersion kernel and macrovascular component (MVC). Gaussian white noise was added to ensure an SNR of 10.[4] Noisy signals were then fitted with the standard model to obtain perfusion and ATT estimates and associated errors.

Results: Figure 1 shows that all protocols underestimated CBF at prolonged ATT. CBF_{opt} had the least sensitivity to prolonged ATT and macrovascular contamination. When aBV % was increased, CBF was found to be overestimated whilst ATT underestimated (Figure 2). CBF_{opt} had the smallest slope against aBV %, with greater variability (standard deviation) when aBV % was very high. Reference multi-PLD and CBF-ATT_{opt} displayed much lower variability than CBF_{opt} for ATT estimation when the MVC effect was strong. Figure 3 shows that the three multi-PLD protocols gave similar ATT estimation at shorter ATT under each model, but CBF-ATT_{opt} had consistently lower variability than CBF_{opt}. However, at prolonged ATT, CBF_{opt} performed better than CBF-ATT_{opt} in ATT estimation with a similar level of variability.

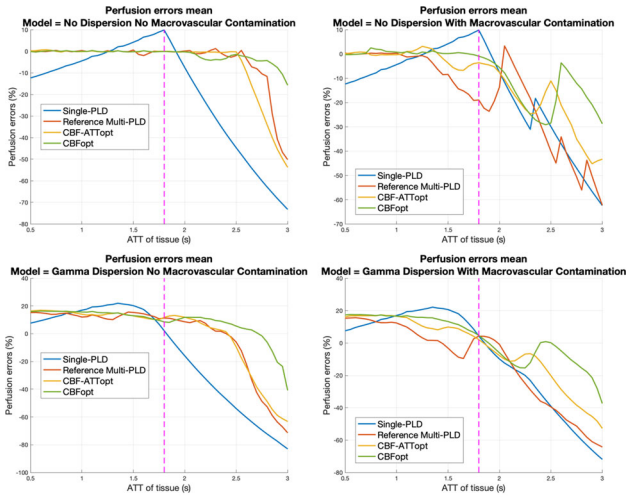

Figure 1. Mean of perfusion estimation errors over 2000 simulations for the different protocols under different models, assuming fixed aBV = 0.2%. The dashed magenta line indicates the maximum ATT used in Woods et al. (1.8s).

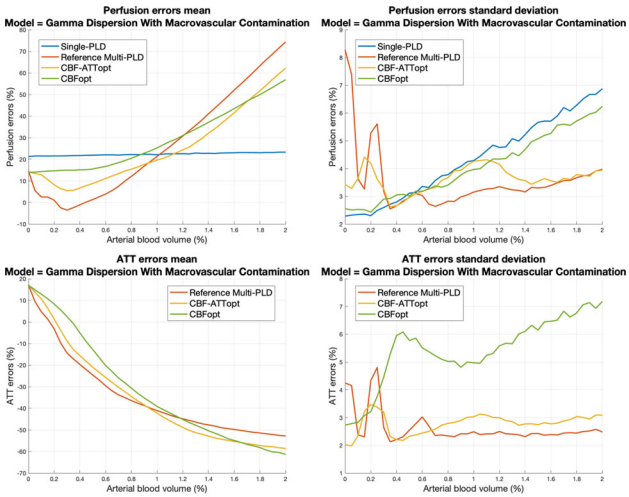

Figure 2. Mean and standard deviation of perfusion and ATT estimation for Gamma Dispersion with Macrovascular contamination (GDWM), assuming fixed ATT = 1.4s.

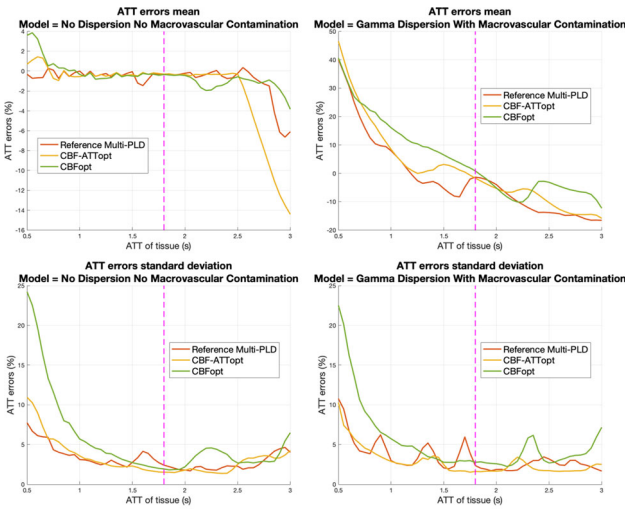

Figure 3. Mean and standard deviation of ATT estimation errors for different protocols under NDNM and GDWM models, assuming fixed aBV = 0.2%. The dashed magenta line indicates the maximum ATT used in Woods et al. (1.8s).

Discussion/Conclusion: In conclusion, CBF_{opt} was found to be the least sensitive to macrovascular contamination and prolonged ATT for perfusion estimation. Whilst CBF-ATT_{opt} was, by design, optimal for combined CBF and ATT estimation for a normal range of ATT, CBF_{opt} still performed reasonably well in ATT estimation if there were unanticipated delays to arrival time beyond the normal range.

References:

Woods, Joseph G., et al. "A general framework for optimizing arterial spin labelling MRI experiments." Magnetic resonance in medicine81.4 (2019): 2474-2488.

Chappell, Michael A., et al. "Modeling dispersion in arterial spin labelling: validation using dynamic angiographic measurements." Magnetic resonance in medicine 69.2 (2013): 563-570.

Chappell, Michael A., et al. "Separation of macrovascular signal in multi-inversion time arterial spin labelling MRI." Magnetic resonance in medicine 63.5 (2010): 1357-1365.

Mehta, Rutej R., et al. "Quantification of errors in cerebral blood flow measurements due to dispersion in arterial spin labelling." 2015 37th Annual International Conference of the IEEE Engineering in Medicine and Biology Society (EMBC). IEEE, 2015.

S04.04

Kinetics of Arterial Blood Transport in the Lung Assessed by PCASL True-FISP Imaging

P. Martirosian[1], F. Seith[2], R. Pohmann[3], M. Schwartz[1], T. Küstner[1], K. Scheffler[3], K. Nikolaou[2], F. Schick[1]

[1]*University Hospital of Tübingen, Section on Experimental Radiology, Tübingen, GERMANY,* [2]*University Hospital of Tübingen, Department of Diagnostic and Interventional Radiology, Tübingen, GERMANY,* [3]*Max Planck Institute for Biological Cybernetics, Tübingen, GERMANY*

Purpose/Introduction: The evaluation of the regional blood flow in pulmonary vessels and in lung parenchyma along the cardiac cycle can be of importance for the clinical diagnosis of lung diseases. Pulsed arterial spin labeling (ASL) techniques have been used for evaluation of the blood bolus delivery curve in the lung by a variation of the delay time between blood preparation and image recording.[1] However, acquiring only few number of label/control scans in a single breat hold, the sensitivity of this technique was not high enough to clearly reveal homogenous signal changes of the lung parenchyma. The goal of this work was to assess the potential of an ECG-triggered pseudo-continuous ASL (PCASL) technique with imaging by True-FISP sequence[2] to measure the temporal and spatial characteristics of pulmonary blood flow at 1.5T.

Subjects and Methods: Ten healthy volunteers were examined on a 1.5T MR scanner using a PCASL sequence[3] with a True-FISP imaging module. Eight measurements with different post labeling delays (PLDs) 100-1500 ms were performed. The labeling pulse was placed nearly perpendicular to the pulmonary trunk (Fig. 1a) and applied during the systolic period by ECG-triggering. True-FISP sequence parameters for coronal imaging (Fig. 1b) were adapted to achieve short TE/TR. PCASL images were acquired by employing a timed breathing protocol. The overall scan time for eight measurements was 17:25 min. All images were registered before further evaluation in order to reduce motion effects using open-source toolbox elastix[4] in a self-written MATLAB® script. To provide an accurate perfusion signal evaluation of the lung parenchyma, the lung was segmented using a Gaussian mixture model clustering three components (large vessels, small vessels, and parenchyma)[5] based on data with shortest PLD.

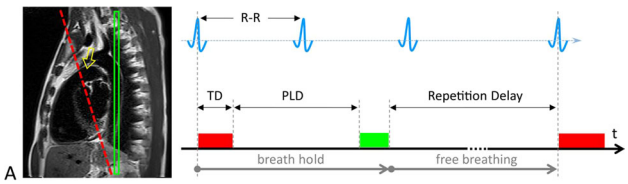

Sequence parameters		Labeling parameters	
TR/TE	2.1/0.9 ms	PLDs	100:300:1500 ms
Flip angle	70°	Tag duration (TD)	300 ms
Bandwidth	1260 Hz/Pixel	Labeling flip angle	25°
Matrix size	144x192	Gradient strength	7 mT/m
In-plane resolution	2.5x2.5 mm^2	Label/Control scans	10/10
B Slice thickness	10 mm	Repetition delay	5000 ms

Figure 1: (A) Labeling plane was positioned perpendicular to pulmonary trunk (red line) and coronal images (green slice) were acquired. Schema of ECG-triggered PCASL sequence: TD was 300ms; imaging was performed at diff. PLDs. (B) Sequence parameters

Results: Temporal perfusion-related signal development in large and small pulmonary arteries and in lung parenchyma (was computed using corresponding tissue masks (Fig. 2b, c). In perfusion images of a healthy volunteer (Fig. 2a), large and small pulmonary arteries are visible at short PLDs, whereas the signal from lung parenchyma gets mainly increased for longer PLD > 900 ms. Perfusion images of lung parenchyma of three healthy volunteers at different PLDs are shown in Fig. 3A. Temporal development of perfusion-related signal in lung parenchyma (Fig. 3b) is clearly delayed compared to the earlier signal changes in larger vessels in all cases.

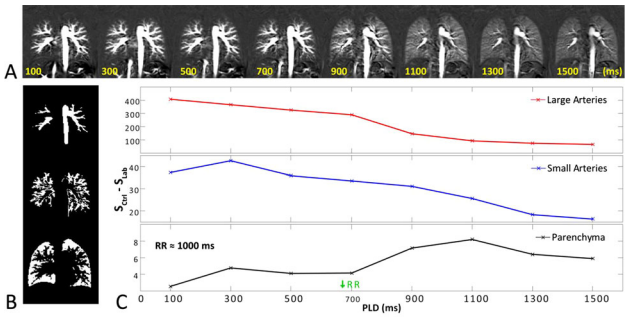

Figure 2: (A) Perfusion images of a volunteer acquired at PLDs from 100 ms to 1500 ms. (C) Time course of perfusion signal in large

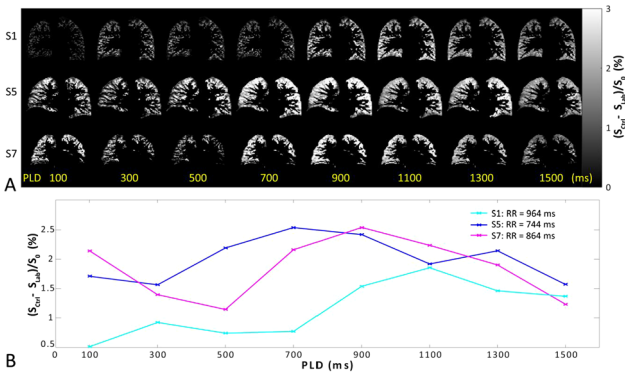

Figure 3: (A) Perfusion images of healthy volunteers (Subject 1, 5, and 7) acquired at different PLDs. (B) Temporal developments of perfusion signal of segmented lung parenchyma show a good accordance with the cardiac cycle of corresponding subjects.

Discussion/Conclusion: We could demonstrate that ECG-triggered PCASL-True-FISP imaging at 1.5T has the potential to assess the course of labeled blood through pulmonary arteries and lung parenchyma. The sequence provides perfusion images of the lung with high spatial resolution and with high signal intensity without application of contrast media.

References:

[1] Bolar DS, MRM 2006;55.
[2] Martirosian P, ISMRM 2017;p1889.
[3] Pohmann R, MRM 2010;63.
[4] Klein S, IEEE TMI 2010;29.
[5] Walker SC, NMR Biomed 2015;28.

S04.05

Unchanged location of watershed areas after revascularization therapy in patients with asymptomatic internal carotid-artery stenosis

L. Schmitzer, S. Kaczmarz, N. Sollmann, C. Zimmer, C. Preibisch, J. Göttler
Technical University of Munich, School of Medicine, Klinikum rechts der Isar, Department of Neuroradiology, Munich, GERMANY

Purpose/Introduction: Internal carotid artery stenosis (ICAS) accounts for approx. 10% of all strokes .[1,2] Watershed areas (WSAs) are particularly vulnerable to hypoperfusion and ischemia due to their location between vascular territories .[3] Yet, perfusion territories vary in health[4] and even more in stenosis patients[5], an observation we confirmed in a previous study, using a WSA segmentation procedure based on time-to-peak (TTP) maps.[6] While revascularization treatment is known to significantly alter cerebral hemodynamics,[7] it is unclear whether WSAs localization changes. To answer this, we conducted a follow up study in patients after stenosis treatment and healthy controls.

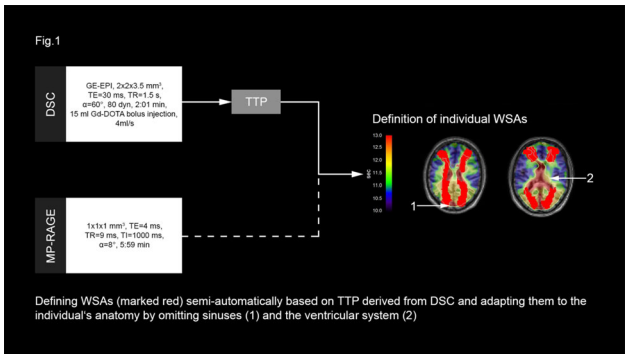

Subjects and Methods: Sixteen patients (age 73.0 ± 6.1y, five females) and 17 healthy elderly (age 72.3 ± 5.5y, eleven females) were examined twice with the same MRI protocol on a clinical 3T Philips Ingenia (mean follow-up time: 14.6 ± 4.6 months) including dynamic susceptibility contrast (DSC) MRI (Fig. 1). Patients had undergone successful carotid endarterectomy or carotid artery stenting; controls did not have any interventions.

As described previously, [6] WSAs were defined semi-automatically based on TTP-maps (Fig. 1).

Every subject's WSAs mask was normalized to MNI-space and voxelwise probability maps were calculated for each group. Probability maps depict the likelihood for every voxel to belong to WSAs across subjects. Spatial overlap of each subject's watershed mask of both scans was assessed by the Dice coefficient (DC, ranging from 0 (no overlap) to 1 (complete congruence)).DCs were compared between groups.

TTP values were normalized by the mean individual white matter TTP, extracted within each individual WSAs, and compared between hemispheres.

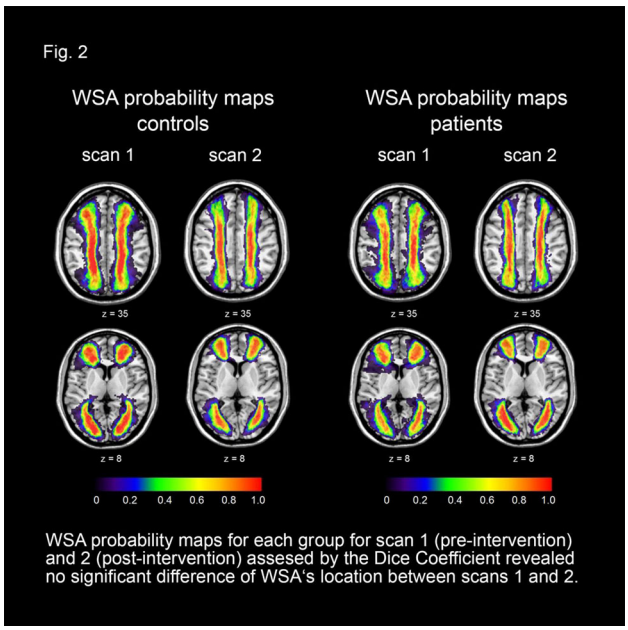

Results: WSAs could be reliably segmented in both groups (Fig. 2). The mean DC for the WSA comparison between scans 1 and 2 was similar (≈ 0.6) in controls and patients (non-significant difference,

two-sample t-test, p = 0.287). In patients and within WSAs, relative TTP (rTTP) differed significantly between hemispheres pre-interventionally ($p < 0.001$) but not post-interventionally (p = 0.446, Fig. 3).

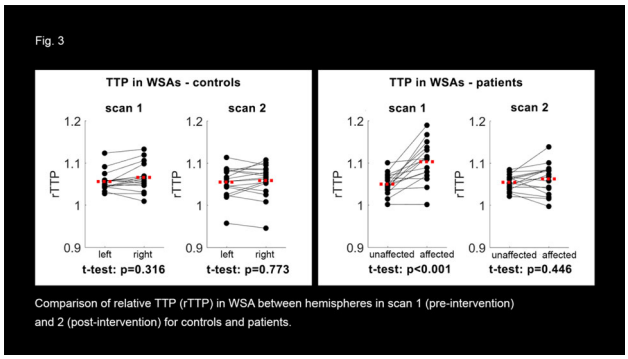

Discussion/Conclusion: Similar DCs in patients and controls (» 0.6) suggest that WSAs did not show significant spatial changes (Fig. 2) after therapy while normalized post-interventional rTTP-values in patients indicates altered cerebral hemodynamics(Fig. 3). As shifts of vascular territories have been reported after treatment of symptomatic ICAS patients, [5] our finding demonstrates that the watershed areas - as brain tissue at higher risk for ischemia - remain unchanged.
Despite changing cerebral hemodynamics, revascularization therapy does not change the spatial extent of WSAs in patients with asymptomatic ICAS.

References:

1. D'Amore, Front Neurol Neurosci, 2012
2. Jorgensen, Neurol Sci, 1969
3. Momjian-Mayor, Stroke, 2005
4. Richter, Am J Neurorad, 2017
5. VanLaar, Vasc Surg, 2007
6. Kaczmarz, Neuroradiology, 2018
7. Kawai, J Stroke CVDiesease, 2014

S04.06

Introduction of Venous Velocity Selective Inversion to measure venous blood T_2

S. Schmid, S. L. Franklin, M. C. van der Plas, M. J. van Osch
C.J. Gorter Center, LUMC, Radiology, Leiden, NETHERLANDS

Purpose/Introduction: The oxygen extraction fraction (OEF) can be measured by exploiting T_2-measurements of the venous blood to infer venous oxygen saturation (Yv), from which OEF can be approximated by assuming full oxygenation of arterial blood. When additional cerebral blood flow and hematocrit measurements are available, cerebral metabolic rate of oxygen ($CMRO_2$) can be determined. Current OEF-methods, such as TRUST[1], QUIXOTIC[2], VSEAN[3] and T_2-TRIR[4] based on pulsed and VS-ASL, suffer from low SNR and limited coverage. In this study a new method, dubbed venous velocity selective inversion (vVSI), is introduced to spatially non-selectively label the venous blood and measure the T_2. This method benefits from the improved SNR of Velocity Selective Inversion[5] (VSI) and could be used to measure OEF in the venous and arterial blood with a single scan.

Subjects and Methods: The vVSI-method employs a pulsed ASL (PASL) module $T_{1,blood}$*ln(2) sec before VSI-labeling to null the arterial pool and cycles through 4 different labeling combinations, followed by a T_2-preparation module before a multi-slice readout (Figure 1). When using the pulsed ASL label condition (Pl) in the post-processing arterial signal will be nulled and thus eliminated. Subtraction of VSI label (Vl) and control (Vc) images will then provide a venous signal map. Similarly, when using the control condition of VSI and subtracting PASL control (Pc) and Pl, only arterial signal is obtained.

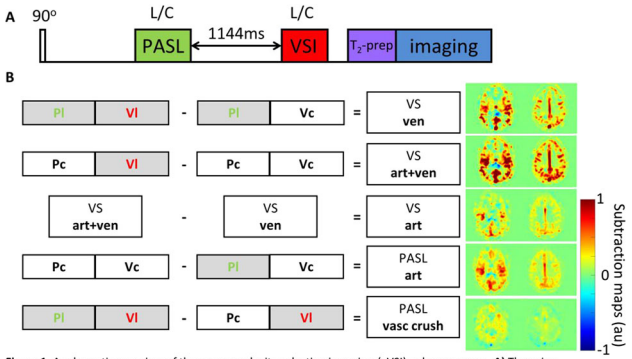

Figure 1. A schematic overview of the venous velocity selective inversion (vVSI) pulse sequence. **A)** The spins were inverted by the pulsed ASL labeling module (STAR, 150mm label thickness) 856ms after the pre-saturation pulse, followed by a delay of 1144ms before the VSI-labeling module (v_c=2.8cm/s), assuming $T_{1,blood}$=1664ms. Read out was performed by GE-EPI acquisition of 11 slices of 7mm thickness, 450ms after VSI. A multi-echo MLEV T_2-preparation module (TE=0, 40, 80, 160ms) was added before imaging to estimate the T_2-signal to determine the OEF. **B)** Subtraction scheme to obtain the 5 different images (only 2 slices shown) from the 4 labeling conditions.

Four healthy volunteers (20–45 years, 2f/2 m) were scanned using a multi-slice EPI-readout and 32ch-head coil at 3T. All volunteers provided written informed consent and the study was approved by local IRB. A single slice TRUST-scan[1] was acquired for T_2-comparison in 2 subjects. In each slice the voxel with the highest venous VSI signal in the posterior region was selected to locate the sagittal sinus and the signal at the 4 echo times was fitted with a mono-exponential to measure the T_2.

Results: In figure 1 the 5 different spin labeling subtraction maps are shown. The venous VSI-maps at multiple effective echo times (eTE) are shown in figure 2. Table 1 contains the average T_2–values in the sagittal sinus for each volunteer.

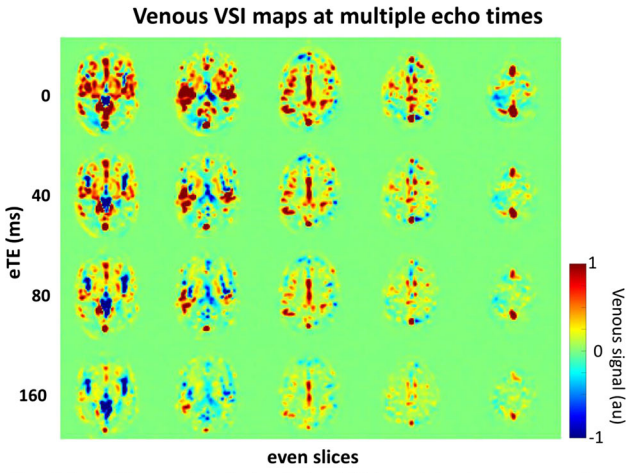

Figure 2. Venous VSI maps at the 4 effective echo times (eTE) from a single volunteer, only even slices are shown. Venous signal can not only be measured in the largest veins, but is also present closer to the tissue. In the lower slices negative signal from fresh arterial inflow is visible.

volunteer	T2 vVSI (ms)	T2 TRUST (ms)
1	72.9 ± 4.4	60.2
2	61.4 ± 4.4	55.3
3	63.6 ± 3.9	-
4	58.2 ± 3.0	-

Table 1. T2 in the sagittal sinus of 11 slices for venous VSI (mean ± stdev) and T2 of a single voxel for TRUST

Discussion/Conclusion: By using different combinations of PASL and VSI it is possible to either selectively label the venous blood pool by nulling the arterial signal during labeling with VSI, or acquire signal from only the arterial blood pool without acquisition of an additional scan. In this study it was demonstrated that the venous T_2 could be measured in the sagittal sinus. The T_2-values from vVSI were slightly higher than TRUST. In future work a QUIPSS-module will be incorporated in the sequence to suppress the fresh inflow of arterial signal and the T_2-preparation will be included in a 3D-readout to reduce the scan time.

References:

1. Liu, et al. MRM, 2016.
2. Bolar, et al. MRM, 2011.
3. Guo & Wong. MRM, 2012.
4. Petersen, et al. ISMRM, 2012.
5. Qin & Van Zijl. MRM, 2016.

S05 Scientific Session

15:00–16:00 *Room 3 - Ruys & van Rijckevorsel Zaal*

UHF Acquisition & Artefact Corrections

S05.02

Improving 7T brain scans for anatomical and functional modalities by reducing B1 + inhomogeneity; Pads or Universal Pulses?

T. Roos, T. Knapen, W. van der Zwaag
Spinoza Centre for Neuroimaging, Amsterdam, NETHERLANDS

Purpose/Introduction: At 7T the B1 + field is not homogenous, even in smaller volumes like the brain. For anatomical scans this causes spatially varying contrast and reduced SNR. Functional scans are impaired by a reduction in BOLD sensitivity and reduced SNR. High permittivity dielectric pads can improve the B1 + field by creating a local B1 + field that can improve the overall homogeneity (1). Parallel transmit (MultiX) systems offer more control over the B1 + field and smart pulse design can also be used to improve homogeneity (2,3). Proper utilisation of these systems can be complex, but calibration-free Universal Pulses (4) lower this barrier. In this study the performance of dielectric pads is compared to a UP in both anatomical and functional brain scans.

Subjects and Methods: Nine healthy volunteers were scanned with a Philips Achieva 7T system. Three sets of identical scans were acquired with either the classic Nova Medical 32Rx2Tx coil with a barium titanate pad (1) or a Nova Medical 32Rx8Tx coil with both Universal Pulse excitation and CP quadrature. The Universal Pulse is a 1 ms long Kt-points based pulse with 5 subpulses and calculated on 16 other volunteers with interleaved gready-local optimization (3).

A T1w MP-RAGE was acquired with α/Te/TR/TI: 8°/3 ms/3 s/1 s, 0.8 mm3 resolution and 288*286*232 matrix size. For the functional runs, the volunteers performed a visually cued motor task with a 13 s block design and 10 repetitions during an 3D-EPI acquisition with 1.8mm3 resolution, a 112*112*98 matrix size and α/TE/TRvol: 8°/16 ms/1.3 s. For Susceptibility Distortion Correction Topups were collected for every run. The standard excitation pulses were replaced with UPs in both MPRAGE and EPI.

All data was preprocessed using the fMRIPrep pipeline. Quantitative metrics were obtained with MRIQC and GLM analysis was performed using Nistats and other Python software from the NiPy suite.

Results:

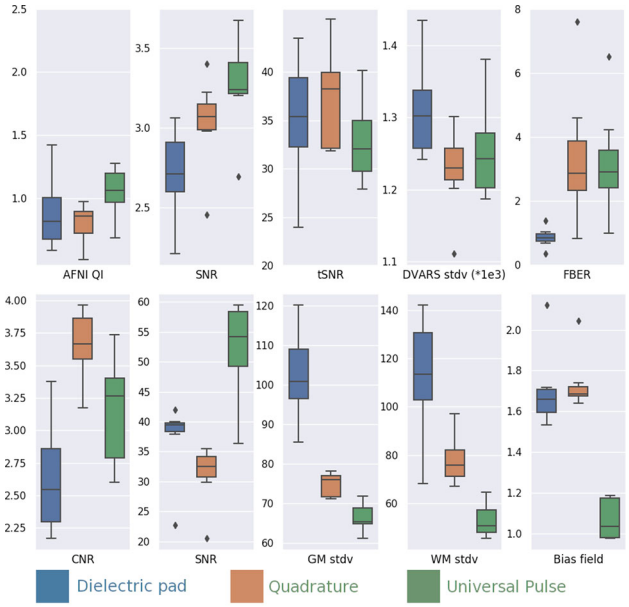

Figure 1. MRIQC quality measures for 3D-EPIs (top row) and MPRAGE data (bottom row). Generally, UP data has lower bias field and signal variations, resulting in higher QI scores.

Both functional and anatomical data improved in terms of homogeneity by changing to the 8ch system and using a UP (Fig. 1). Although the SNR improved in the EPI, overall tSNR did not.

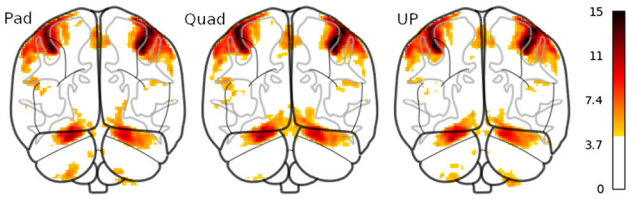

Figure 2. Functional group-level results. The motor task induced activation in the primary motor areas, secondary somatosensory areas, anterior and posterior cerebellum. Differences are most notable in the posterior cerebellum (most inferior)

Nevertheless, more bilateral activation is found in the cerebellum (Fig. 2), indicating increased image quality and BOLD sensitivity.

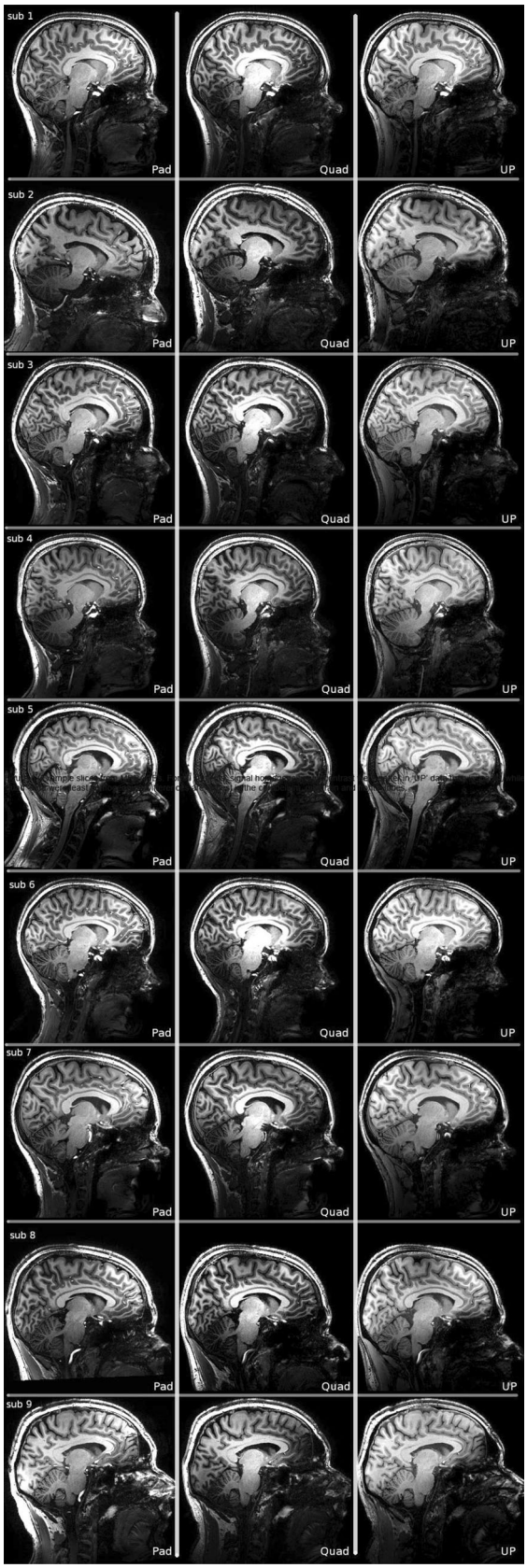

Figure 3. Example slices from MPRAGEs. For all subjects, signal homogeneity and contrast were better in 'UP' data than in 'pads', while 'quad' data were least homogenous. Differences are largest in the cerebellum, midbrain and frontal lobes.

Signal strength and contrast in the MPRAGE improved markedly in areas of low B1 + in the quadrature mode (Fig. 3).

Discussion/Conclusion: Dielectric pads improve B1 + signal homogeneity in the standard setup, but the 8 channel system performs significantly better still. The use of UPs allows a wide audience to profit from this increased performance without the need for complex and slow pulse calculations and B1 + field mapping.

Future work could look into combining dielectric pads with Universal Pulses.

References:

1. Vaidya MV, JMRI. 2018.
2. Cloos MA, MRM. 2012.
3. Grissom WA, MRM. 2012.
4. Gras V, MRM 2017.

S05.03

High-resolution 3-point Dixon liver imaging at 7T with B1 + homogenization using 8-channel phase shimming in parallel transmission

B. Runderkamp[1], G. Strijkers[2], M. Caan[2], W. van der Zwaag[3], A. Nederveen[1]

[1]*Amsterdam UMC, location AMC, Radiology & Nuclear Medicine, Amsterdam, NETHERLANDS,* [2]*Amsterdam UMC, location AMC, Biomedical Engineering & Physics, Amsterdam, NETHERLANDS,* [3]*Spinoza Centre for Neuroimaging, Amsterdam, NETHERLANDS*

Purpose/Introduction: The gain in signal facilitated by 7T MRI may be exploited to improve abdominal image quality. However, at this high field strength the B1 + wavelength reduces to below abdominal dimensions, which causes B1 + inhomogeneities that cannot be corrected for with traditional quadrature transmission.

The aim of this work was to use multi-channel parallel transmission with phase shimming to address B1 + inhomogeneities in the abdomen, enabling high-resolution 7T liver MRI with water-fat separation.

Subjects and Methods: Five healthy volunteers were scanned with a 7T MRI scanner (Philips) using an 8-channel Tx/Rx body coil [1] (MRCoils). A 3-echo 3D FFE (Dixon) was used with the following parameters: FOV: 450x300x95 mm^3, voxel size: $2 \times 2 \times 2$ mm^3, SENSE factor: 1.5(AP), water-fat shift: 0.7 pixels(RL), TE/dTE/TR = 1.06/1.00/4.43 ms, flip angle = 8̊, breath-hold duration (BHD): 20.8 s.

A second scan was performed with equal FOV and SENSE factor but anisotropic voxel size: $1 \times 1 \times 5$ mm^3, TE/dTE/TR = 1.45/1.40/5.73 ms, water-fat shift: 1 pixel, flip angle = 10̊, BHD: 21.2 s.

In both scans, two volumes of interest (VOIs) were drawn in two consecutive scans in the liver for transmit phase shimming (Figure 3a). RF shimming was performed with a toolbox (MRCodeTool), minimizing the standard-deviation/(mean)^3 in the VOI. B1 maps from a DREAM acquisition served as input [2]. Additionally, the two scans were combined by a maximum intensity projection (MIP). For water-fat separation, the 'Hernando graphcut' algorithm [3] was used from the FW Toolbox [4]. For comparison, a 3-point Dixon abdominal scan was also acquired at 3T, with similar parameters except TE/dTE/TR = 3.38/3.27/12.0 ms and BHD: 25.6 s.

Results: Figure 1 shows the resulting 7T MRI scans (echo 2) of all 5 volunteers.

Water and fat images at 3T and 7T are compared in Figure 2. Image quality at 7T was good, but visually slightly inferior to 3T. The RF shimming at 7T was largely successful but some signal dropout could still be observed in and around the liver and spleen.

Figure 3 shows the reduction of local B1 + inhomogeneity through phase shimming in combination with MIP reconstruction of the 2 scans with different shim VOI.

Also, a higher level of detail is seen for the protocol with higher in-plane resolution, with no apparent SNR loss.

Discussion/Conclusion: We have shown high-resolution 3D liver MRI at 7T with B1 + homogenization through phase shimming in parallel transmission.

The concept of combining 2 shims to improve homogeneity was explored, and could be extended to a time-interleaved approach [5] to improve co-registration.

Further resolution improvement, compared to current clinical 3T protocols, can likely be achieved in combination with acceleration techniques like Compressed Sensing [6], to facilitate acquisitions within a single breath-hold.

References:

[1] Raaijmakers, 2016.
[2] Nehrke, 2012.
[3] Hernando, 2010.
[4] FW Toolbox ISMRM, 2012/Gleich, MatlabBGL, 2006.
[5] Orzada, 2010.
[6] Lustig, 2007.

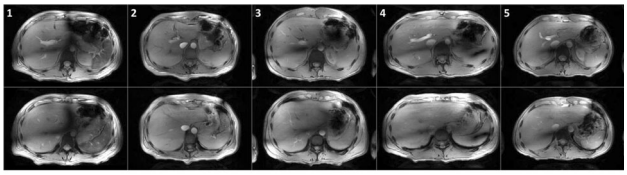

Figure 1: 3-echo 3D FFE (echo 2) abdominal scans at 7T of the 5 volunteers. For each volunteer, two transversal slices are shown of the scan with voxel size 1x1x5mm3 and shim VOI II. In FH-direction, both VOIs cover approx. two-thirds of the FOV.

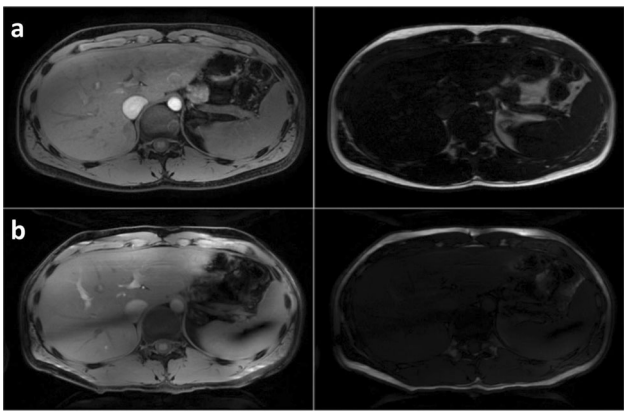

Figure 2: Water (left) and fat (right) images from 3-echo 3D FFE (Dixon) abdominal scans at a) 3T and b) 7T of a representative volunteer. In b), the scan with voxel size 1x1x5mm3 and shim VOI II is shown.

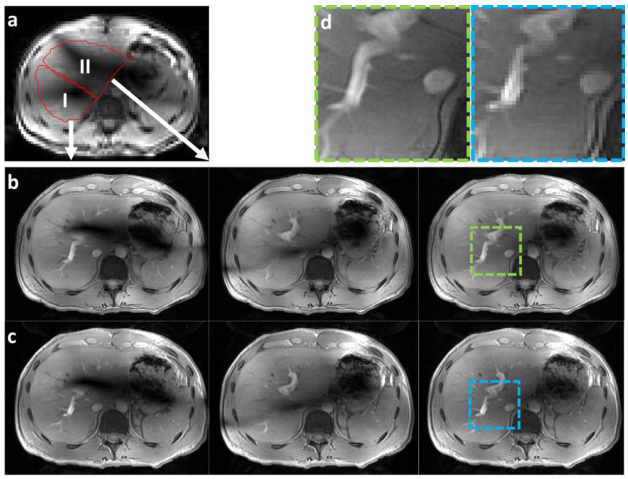

Figure 3: a) The two shim VOIs used. 3-echo 3D FFE (echo 2) scans at 7T with b) voxel size 1x1x5mm3 and c) 2x2x2mm3, using VOI I (left), II (middle) and MIP-reconstructed (right). d) Resolution comparison in the area indicated by the squares in b,c.

S05.04

Correction of temporal B0-fluctuations in ultra high resolution quantitative multi-parametric mapping (MPM) at 7T

L. Vaculciakova, K. Podranski, L. J. Edwards, K. J. Pine, N. Weiskopf

Max Planck Institute for Human Cognitive & Brain Sciences, Neurophysics, Leipzig, GERMANY

Purpose/Introduction: Multi-parametric quantitative MRI enables simultaneous measurement of MR parameters and offers the potential to characterise human brain microstructure. An efficient implementation of this concept, the multi-parameter mapping (MPM) protocol, uses 3 multi-echo 3D FLASH volumes to simultaneously quantify R1, R2*, PD and MT[4]. Ultra high spatial resolution is needed to resolve small structures playing an important role in brain function, e.g. cortical laminae, but means low SNR and high sensitivity to respiration-related variation of the B0 field, particularly at 7T[1]. We addressed B0 field fluctuations by implementing free induction decay (FID) navigators[2,3] into the MPM protocol, and tested their performance for 500 μm quantitative parameter mapping.

Subjects and Methods: We scanned 3 healthy volunteers on a 7T Siemens Magnetom MRI scanner (32-channel receive coil; gradient/RF-spoiled multi-echo 3D gradient echo[4]; 500 μm isotropic; TR 27.5 ms; 6 equispaced TEs [2.8,…,16.1] ms; 434/496/352 (phase/read/slice); 2 × 2 accelerated SENSE). We added one FID navigator per TR after the imaging echoes, measured at k-space centre. Subjects 1,2: T1-, PD- and MT-weighted (excitation flip angles $\alpha = 25°, 5°, 5°$ plus MT saturation pulse) volumes were acquired (20 min/contrast). Subject 3: 2 T1- and PD-weighted ($\alpha = 25°, 5°$) volumes were acquired in one session to assess reproducibility. We collected

respiratory traces using a BIOPAC breathing belt for frequency variation estimate validation.

We applied TR-, TE- and channel-specific B0-fluctuation phase correction correction to each acquired k-space line before a custom 2D SENSE reconstruction. Maps were created using the hMRI toolbox (http://hMRI.info).

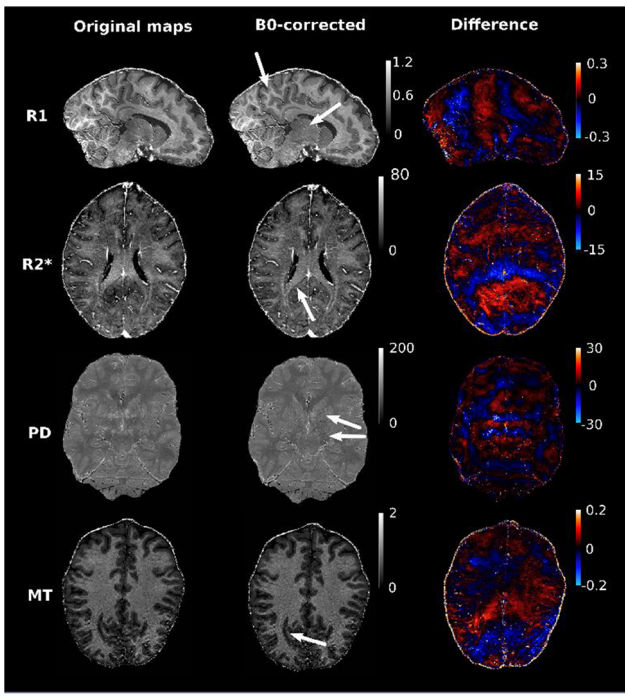

Fig.1- Reduction of artifacts in quantitative multi-parameter mapping (MPM) due to navigator based B0-fluctuation correction. Reconstruction of the same data without (left column) and with (middle column) navigator correction. Difference maps between corrected and uncorrected reconstruction (right column) highlights the effects of the correction.

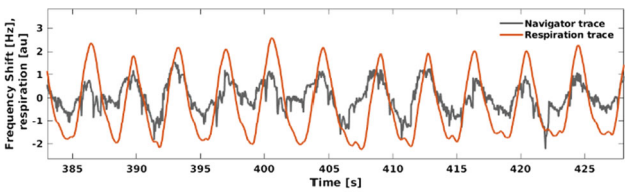

Fig.2 - Frequency shifts estimated from the navigator signal (gray; from a single channel) and respiration traces measured with the breathing belt (orange) are highly correlated.

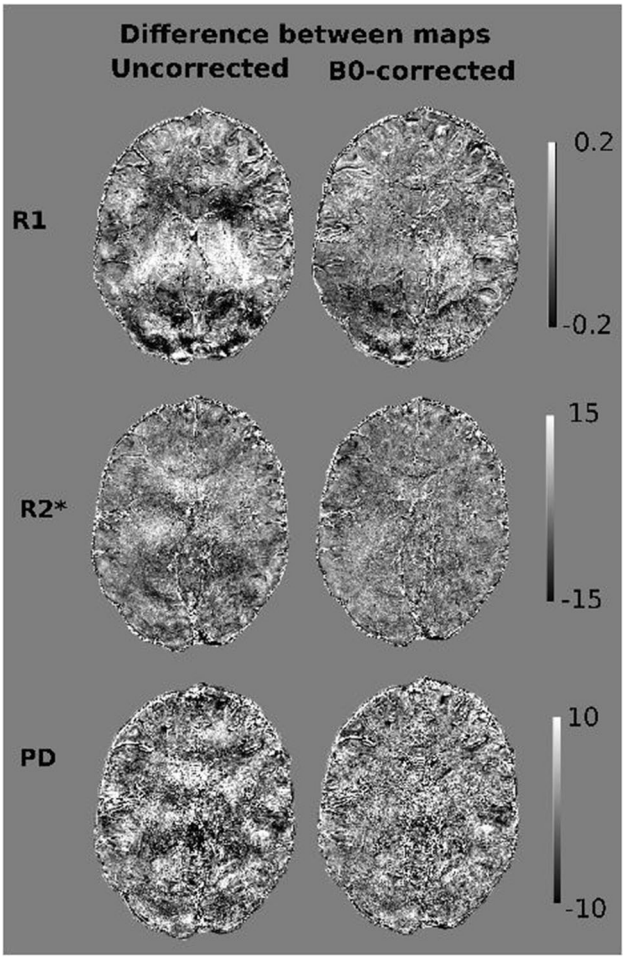

Fig.3 - Scan-rescan reproducibility assessment shows improvement of stability due to navigator based B0-fluctuation correction. Maps show differences between two consecutive MPM acquisitions in a single scan session without (left column) or with (right column) navigator correction. Note that the identical k-space raw data were used but only reconstructed differently.

Results: Fig. 1 shows the typical improvements in quality of the MPM maps when correcting for B0 variations over time. Navigator-derived frequency fluctuations correlated strongly with breathing belt measurements of respiratory motion (Fig. 2). Differences between repeat measurements were reduced by navigator correction (Fig. 3). This suggests high reproducibility of quantitative MR parameters even at 500 μm resolution.

Discussion/Conclusion: High resolution 7T quantitative MPM acquisitions show promise for characterizing cortical microstructure. The increased impact of physiological noise was addressed by introducing FID navigators into the sequence. We corrected for temporal B0 fluctuations without needing additional hardware modifications[5,6], at the small cost of prolonging TR by 2.5 ms. The combination of navigators with high resolution MPM is currently being optimized. However preliminary results indicate correction improved the quality of all parameter maps (R1, R2*, PD, MT).

References:

1. Van de Moortele et al. MRM 2002.
2. Hu and Kim. MRM 1994.
3. Ehman and Felmlee, Radiology 1989.

4. Weiskopf et al. Front Neurosci 2013.
5. van Gelderen et al. MRM 2007.
6. Vannesjo et al. MRM 2012.

S05.05
Isotropic High-Resolution DIADEM-VAT at UHF

Y.-H. Tung[1], M.-H. In[2], S. Ahn[3], A. Sciarra[4], O. Speck[1]
[1]Otto von Guericke University Magdeburg, Department of Biomedical Magnetic Resonance, Magdeburg, GERMANY, [2]Mayo Clinic, Department of Radiology, Rochester, UNITED STATES, [3]Siemens Healthcare, San Francisco, UNITED STATES, [4]Otto von Guericke University Magdeburg, Medicine and Digitalization, University Department of Neurology, Magdeburg, GERMANY

Purpose/Introduction: As multi-shot echo-planar imaging (EPI), DIADEM[1,2] was suggested for distortion-free imaging and combined with view-angle-tilting (VAT)[3] to further accelerate the scan time without any image blurring caused by the applied VAT gradient (G_{VAT}) in the reconstructed distortion-free image[4]. However, the mechanism of signal-to-noise ratio (SNR) degradation in DIADEM data with VAT gradients and the application of thin slices, which demand high G_{VAT}[3], were not investigated yet. In this study, we performed high-resolution DIADEM-VAT scans with different slice thicknesses (i) to investigate how the G_{VAT} attenuates the signal in the DIADEM-VAT acquisitions and (ii) to optimize the SNR for a thin slice acquisition.

Subjects and Methods: Fully-sampled DIADEM-VAT phantom scans were performed on a 7T scanner (Siemens Healthineers, Erlangen, Germany) using a 32 channel head coil (Nova Medical, Wilmington MA, USA) to evaluate the effect of signal modulation with VAT gradients. *In-vivo* scans were performed with an acceleration factor (rFoV) of 10. The experimental parameters were in phantom: FoV/resolution = 224 × 224/1.4 × 1.4 mm^2, slice thickness = 1.4 and 0.7 mm, 10 slices, VAT (G_{VAT}/G_{PE}) ratio = 0, 6.8, and 13.6. TR/TE = 2000/80 ms, GRAPPA = 3, no partial Fourier, and the effective echo-spacing = 333 µs; and in in vivo: FoV/resolution = 224 × 224/0.7 × 0.7 mm^2, slice thickness = 0.7, 1.4, and 2.8 mm, 40 slices, VAT ratio = 12.0, 6.0, and 3.0. TR/TE1/TE2 = 7000/69/89 ms, GRAPPA = 4, no partial Fourier, the effective echo-spacing = 262 µs, and the reduced resolution (rR) factor = 6.7.

Results: Signal modulation with G_{VAT} appeared as image blurring and signal attenuation, respectively on the distorted image (or EPI) I(y,x) and the distortion-free image I(s,x) calculated from DIADEM data and the effect increased linearly with the VAT ratio (Fig. 1). Since the signal modulation profile of VAT was decoded in DIADEM-VAT acquisition, these profiles could be seen directly in DIADEM-VAT data I(x,y,ks) along the ks dimension after 2D iFFT in kx and ky (Fig. 2a). Interestingly, since the modulation profile became wider in a given VAT ratio for a thinner slice acquisition, there would be no signal penalty for a thinner slice acquisition requiring a higher VAT ratio (Fig. 2b). In addition, the signal attenuation could be minimized with a higher rR factor by avoiding the acquisition of the low signal profile areas, which improved the SNR of the DIADEM images by a factor of 2 (Fig. 2c). These effects were also shown in in vivo data (Fig. 3).

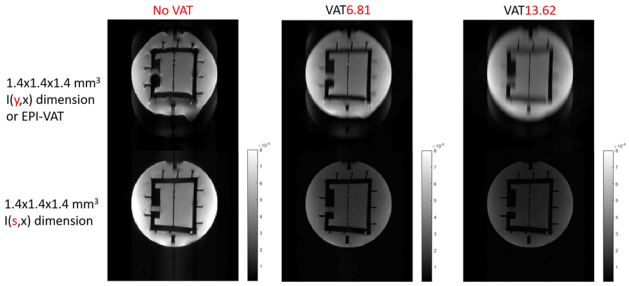

Fig.1 Full-sampled DIADEM-VAT.

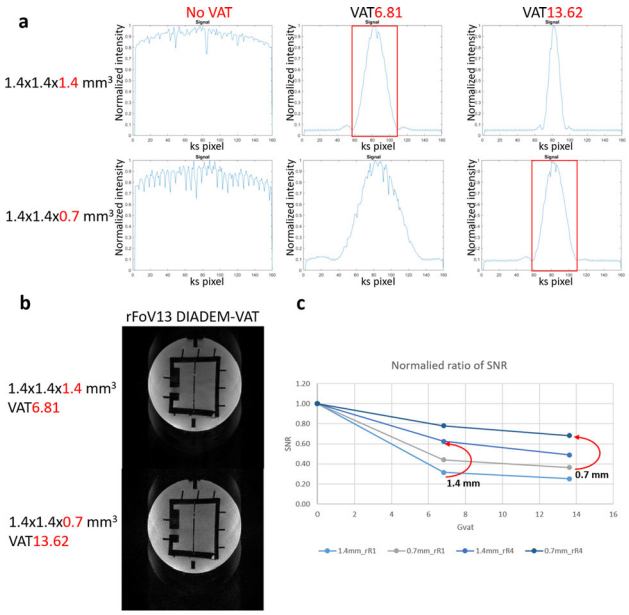

Fig.2 a: Signal modulation profile of VAT b: Accelerated DIADEM-VAT images c: SNR optimization by rR.

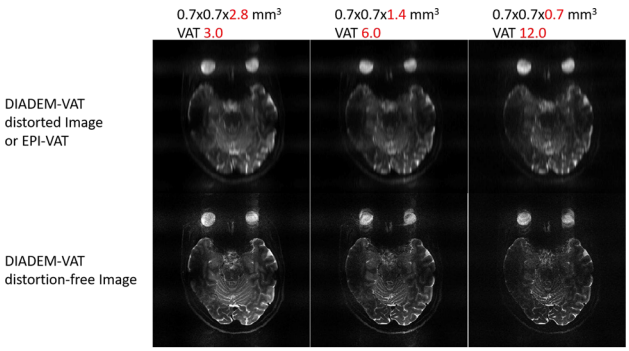

Fig.3 High resolution in vivo images with different slice thickness.

Discussion/Conclusion: Since the signal modulation effects with VAT can be directly measured in DIADEM-VAT data, we were successfully able to improve the SNR with a higher rR factor and to demonstrate no or negligible SNR penalty even for a thinner slice acquisition.

References:

1. In MH, et al., NeuroImage. 2017; 148:20-30.

2. In MH, et al., ISMRM 2018, p.1203.
3. Ahn S and Hu XP, MRM. 2012; 68(4):1211-9.
4. Tung YH et al., ISMRM 2018,p.6042.

S05.06

Development of a dedicated flexible ^{1}H-^{31}P RF coil for cardiac MR spectroscopy at 7 T

S. Roat[1], M. Vít[2], A. I. Schmid[1], **E. Laistler**[1]
[1]*Medical University of Vienna, Division MR Physics, Center for Medical Physics and Biomedical Engineering, Vienna, AUSTRIA,*
[2]*Technical University of Liberec, Liberec, CZECH REPUBLIC*

Purpose/Introduction: Phosphorus-31 magnetic resonance spectroscopy (^{31}P-MRS) is a noninvasive technique to investigate dynamic aspects of cardiac metabolism in vivo. ^{31}P MRS is inherently limited by low SNR, which can be mitigated by increasing B_0. Cardiac MR experiments at ultra-high fields are highly challenging due to increased magnetic field inhomogeneities, RF non-uniformities and power deposition constraints. In order to fully exploit the SNR gain, elaborate RF coil development is necessary. RF coils built upon rigid housings may not account for the large interpatient variability that is observed in cardiac MR. Conforming the resonator to the shape of the body increases electromagnetic coupling and therefore achievable SNR. In this study we show first results of a dedicated flexible RF coil array for cardiac ^{31}P metabolic examinations.

Subjects and Methods: A flexible 12-channel transmission line resonator (TLR) array for torso MRI was accomplished prior to this work (1). Suitable RF coil designs for the ^{31}P array were investigated via 3D electromagnetic simulation in a comprehensive simulation study (2), resulting in a theoretical superiority of a 3 element array design with an element size of 9.4 × 14.1 cm^2 positioned centered over the heart (Fig. 1a). To maintain the flexibility of the TLR design, the ^{31}P array was constructed out of flexible wire (∅ = 2 mm) and a fixed overlap for nearest neighbor decoupling. To prevent coil cross talk between ^{1}H and ^{31}P elements, every second capacitor in series was replaced with an LCC trap (3), three traps per element (Fig. 1b). Performance of the ^{31}P array was tested on the bench measuring S-parameters for 4 human volunteers (2 m/2f) using a network analyzer (E5071C, Agilent, Santa Clara, CA, USA). LCC trap performance was validated within the scanner, by acquiring flip angle maps in a saline phantom (σ = 0.5 S/m, ε = 80) with and without the ^{31}P array present. Measurement sequence: saturated Turbo FLASH (satTFL) sequence, rectangular slice-selective saturation pulse: 700 ms duration, 300 V amplitude, 10 mm thick slices.

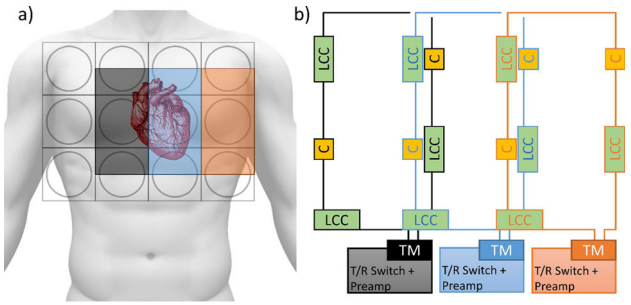

Fig 1 ^{31}P coil schematics. a) *depicts the position of the 3 element ^{31}P array (gray, blue and orange rectangles) in contrast to the location of the heart and the underlying ^{1}H array (12 circular TLR elements). The ^{31}P array is positioned to yield a maximum B_1^+ distribution in the left ventricle (2).* ***b)*** *shows a detailed schematic view of the 3 element ^{31}P array, indicated are the locations of the LCC traps (LCC, green) and the fixed capacitors (C, yellow). The corresponding T/R switch boards and preamps are located directly after the tuning and matching network.*

Results: Bench measurements show sufficient matching and isolation for both nearest neighbor interaction ($S_{ii} \leq -17.5$ dB and $S_{ij} \leq -14.5$ dB). Coronal B_1^+ maps with a distance of 0–5 cm in 1 cm steps from the phantom surface with (S1) and without (S2) the ^{31}P array present can be seen in Fig. 2 (top/middle row). A difference map (Fig. 2 bottom row) of those 5 slices shows well working LCC trap performance.

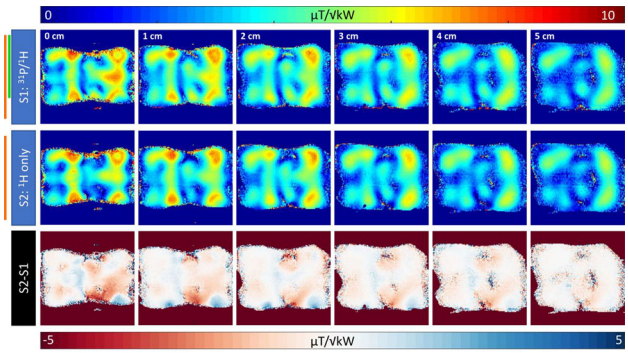

Fig 2 ^{1}H B_1^+ maps with (S1) and without (S2) ^{31}P array. *Top row shows 10 mm coronal B_1^+ slices (distance from surface is denoted in the left corner of each map, 0 cm – 5 cm) with the ^{31}P array positioned below the proton array, whereas in the middle row the same slices are shown without the ^{31}P array present. Bottom row shows the resulting difference of the B_1^+ maps above.*

Discussion/Conclusion: In this work we present preliminary first results of the implementation of a dedicated flexible ^{1}H-^{31}P RF coil for cardiac MR spectroscopy at 7T. Bench measurements and first scanner tests indicate a well working ensemble of differently designed (TLR and wire) RF coil.

Funding: Austrian Science Fund (FWF) grants P28059-N36 and P28867-B30

References:

(1) Hosseinnezhadian, S et al. JMR 2018.
(2) Goluch-Roat, S et al. ISMRM 2019.
(3) Meyerspeer, M et al. MRM 2013.

S06 Scientific Session

15:00–16:00 Room 4 - Plate & Van der Vorm Zaal

Breast Imaging

S06.02
WITHDRAWN

S06.03
Q-space imaging is more sensitive to breast tumour heterogeneity than conventional diffusion MRI

N. Senn[1], Y. Masannat[2], E. Husain[3], B. Siow[4], S. Heys[2], J. He[1]
[1]University of Aberdeen, Aberdeen, UNITED KINGDOM, [2]Aberdeen Royal Infirmary, Breast Unit, Aberdeen, UNITED KINGDOM, [3]Aberdeen Royal Infirmary, Pathology, Aberdeen, UNITED KINGDOM, [4]The Francis Crick Institute, MRI Unit, Aberdeen, UNITED KINGDOM

Purpose/Introduction: Neoadjuvant chemotherapy is increasingly prescribed in patients with breast cancer to improve surgical outcome. However, patients with locally advanced breast cancers not responding to treatment are exposed to unnecessary drug toxicity and delays to surgical intervention [1]. Although a reduction in tumour heterogeneity is a principle manifestation of early treatment response, existing radiological methods lack the adequate sensitivity required to identify non-responding patients [2]. Q-space imaging (QSI), an advanced diffusion-weighted MRI method, provides unique profiling of tissue microstructure [3]. We therefore hypothesise that QSI provides significantly greater sensitivity to tumour heterogeneity than existing diffusion imaging methods, and shows a strong fidelity with the underlying cellularity heterogeneity from histology.

Subjects and Methods: Diffusion weighted images were acquired with multi-shot PGSE sequence on a 3T MRI clinical scanner (Philips Healthcare, Netherlands), using a 32-channel receiver coil. QSI (32 q-values, qmax 655 cm^{-1}) and conventional diffusion-weighted imaging (16 b-values, bmax 2400 s mm^{-1}) sequences were performed on twenty whole invasive carcinoma tumours (diameter range of 18–39 mm) freshly excised from patients (age range of 35–78 years). Images were processed voxel wise to obtain maps of full width at half maximum displacement from QSI [4], and diffusivity from monoexponential model (MONO), diffusion kurtosis imaging (DKI) [5], and stretched exponential model (SEM) [6]. Tumour heterogeneity was evaluated as the skewness in histogram distributions [7]. The sensitivity to tumour skewness from QSI was compared against the skewness from other diffusion methods using paired t-tests and the relative effect gradient obtained from the linear regression of skewness values. The correlation to the skewness of underlying cellularity from histology was examined using Spearman's correlation.

Results: The skewness obtained from QSI (1.34 ± 0.77) was significantly higher than the skewness obtained from MONO (1.09 ± 0.67, P = 0.015), SEM (1.07 ± 0.70, P = 0.014), and DKI (0.97 ± 0.63, P = 0.004), (Figure 1, Table 1). QSI yielded a higher effect gradient to tumour skewness (percentage increase) compared to MONO (35.1%), SEM (35.1%), and DKI (58.7%), (Figure 2). The skewness from QSI was significantly correlated with the cellularity skewness from histology ($\rho = -0.468$, P = 0.038).

Discussion/Conclusion: QSI was found to be more sensitive to tumour skewness than existing diffusion imaging methods, and to correlate with the underlying cellularity from histology. Our findings show QSI provides a sensitive non-invasive marker of tumour heterogeneity that is immediately applicable for monitoring early treatment response at a personalised care level.

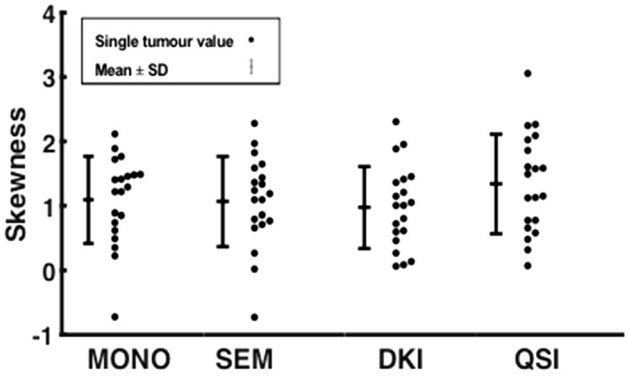

Figure 1. Dot plot distributions of skewness for MONO, SEM, DKI and QSI. The error bar represents the cohort mean ± standard deviation and each dot represents a single tumour value.

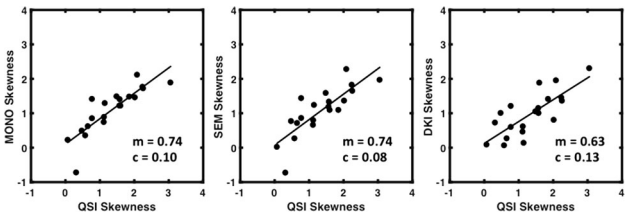

Figure 2. Skewness values from MONO, SEM, and DKI, correlated against the skewness values from QSI. Each dot represents a single tumour value. The gradient of the line of best fit represents the relative effect gradient.

	Skewness		Skewness QSI correlation		Skewness Cellularity correlation
	Mean ± SD	t-score P-value	R, P-value	Gradient, Intercept	ρ, P-Value
QSI	1.34 ± 0.77				ρ = -0.468 P = 0.038
MONO	1.09 ± 0.67	t = -2.686 P = 0.015	R = 0.846 P < 0.0005	0.74, 0.10	ρ = -0.433 P = 0.056
SEM	1.07 ± 0.70	t = -2.711 P = 0.014	R = 0.817 P < 0.0005	0.74, 0.08	ρ = -0.389 P = 0.090
DKI	0.97 ± 0.63	t = -3.314 P = 0.004	R = 0.771 P < 0.0005	0.63, 0.13	ρ = -0.541 P = 0.014

Table 1. Mean ± SD skewness values and the paired T-test comparison to QSI. Pearson's correlation, gradient and intercept of linear regression between the skewness values from each method and QSI. Correlation to cellularity skewness from histology.

References:

1. Karakatsanis (2018). BJS.
2. Kim (2016). JJR.
3. Cohen (2002). NMR Biomed.
4. Yamada (2015). MRM.
5. Jensen (2005). MRM.
6. Bennett (2003). MRM.
7. King (2013). Radiology.

S06.04

Lipid composition of whole breast tumour is associated with lymphovascular invasion (LVI)

S. M. Cheung[1], Y. Masannat[2], E. Husain[3], V. Mallikourti[1], S. D. Heys[2], J. He[1]

[1]*University of Aberdeen, Aberdeen, UNITED KINGDOM,* [2]*Aberdeen Royal Infirmary, Breast Unit, Aberdeen, UNITED KINGDOM,* [3]*Aberdeen Royal Infirmary, Pathology Department, Aberdeen, UNITED KINGDOM*

Purpose/Introduction: The 10-year survival of breast cancer has improved with advanced systemic and endocrine therapy (1). However, recurrence and metastasis after initial successful treatment, caused by lymphovascular invasion (LVI), remains a challenge (2). Currently LVI is assessed provisionally using the biopsy sample, while definitive LVI can only be determined after surgery (3). LVI amplifies the impact of genetic mutations on fatty acids (FA) regulation, leading to the deregulation of lipid composition (4). Double quantum filtered (DQF) correlation spectroscopy (COSY) is a novel method capable of non-invasive lipid composition measurement (5). We hypothesised that DQF-COSY can differentiate LVI positive from LVI negative breast tumours through the observation of lipid composition.

Subjects and Methods: In this cross sectional study, 13 LVI negative and 17 LVI positive female patients (age 39 – 78 years) with invasive ductal carcinoma were enrolled (Table 1). Freshly excised tissue with tumour were scanned on a 3T whole body clinical MRI scanner (Achieva TX, Philips Healthcare, Best, Netherlands) using a 32-channel receiver coil for high sensitivity detection and body coil for uniform transmission. Lipid composition was acquired from a single voxel encompassing the tumour using DQF-COSY sequence (5), with TR of 582 ms, initial TE of 25 ms, a t1 increment of 1 ms, 256 increments. Saturated FA (SFA) ((1.3, 1.3) ppm), monounsaturated FA (MUFA) ((2.1, 5.3) ppm), polyunsaturated FA (PUFA) ((2.8, 5.3) ppm) and glycerides ((4.2,4.2) ppm) were quantified as ratios to methyl fat ((0.9, 0.9) ppm). All 2D spectral data were quantified in Felix software (v2007 m Accelrys Inc., San Diego, USA) (6). Histopathological analysis was performed to derive Ki-67 expression.

Demographics	All (n=30)	Lymphovascular invasion (LVI)		*p*-value
		Negative (n = 13)	Positive (n = 17)	
Age (years)	61.1 ± 11.5	59.2 ± 12.6	62.6 ± 10.6	0.4375
Body Mass Index (BMI)	30.4 ± 6.4	31.2 ± 7.5	29.5 ± 5.4	0.5451
Tumour Size (cm)	2.5 ± 0.8	2.4 ± 0.7	2.5 ± 0.8	0.6070
Tumour features				
Histology grade				
II	15	6	9	-
III	15	7	8	
Oestrogen Receptor (ER+)	22	8	14	-
Human Epidermal growth factor Receptor 2 (HER2+)	6	2	4	-
Triple-Negative Breast Cancer (TNBC)	7	5	2	-

Table 1. Patient demographics. Descriptive statistics of breast cancer patients with histopathological findings are shown for each group

Results: There was a significant difference in MUFA (p = 0.0189) between LVI negative (median: 0.63, IQR: 0.49–0.96) and LVI positive (median: 0.37, IQR: 0.25–0.64) (Fig 1). There was a significant difference in glycerides (p = 0.0226) between LVI negative (median: 2.5, IQR: 1.92–4.15) and LVI positive (median: 1.32, IQR: 0.95–2.43). There was a significant difference in SFA (p = 0.0491) between LVI negative (median: 1.22, IQR: 1.13–1.26) and LVI positive (median: 0.95, IQR: 0.88–1.26). There was no significant difference in PUFA between LVI negative (median: 0.28, IQR: 0.21–0.32) and LVI positive (median: 0.23, IQR: 0.10–0.28). There were no significant correlations between lipid components and Ki-67 expression (Fig 2).

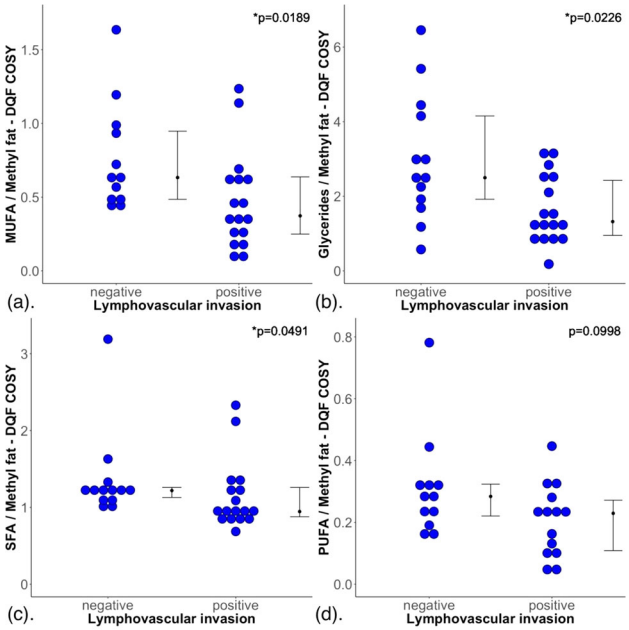

Figure 1. The group difference in (a) monounsaturated fatty acids (MUFA), (b) glycerides, (c) saturated FA (SFA) and (d) polyunsaturated FA (PUFA), are shown in dot plots. Statistically significant p values are marked by '*'.

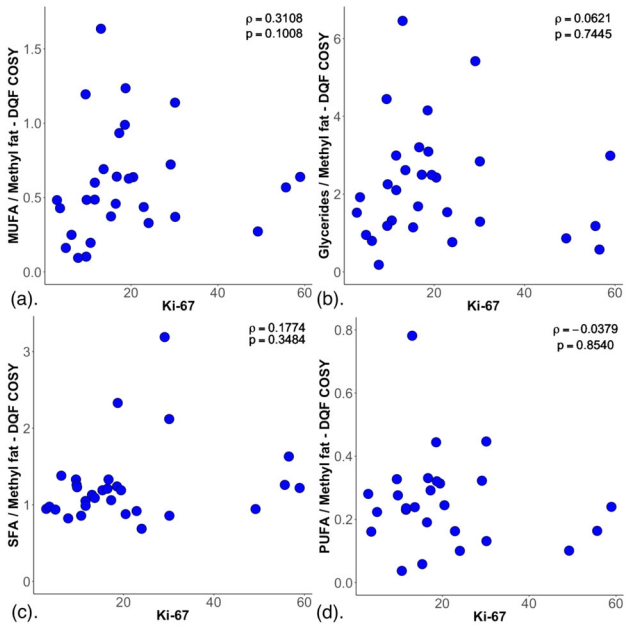

Figure 2. (a) Monounsaturated fatty acids (MUFA), (b) glycerides, (c) saturated FA (SFA) and (d) polyunsaturated FA (PUFA) were correlated with Ki-67 within the entire cohort, and shown as scatter plots. There were no significant correlations.

Discussion/Conclusion: DQF-COSY is a sensitive marker of LVI through the associated lipid composition deregulation, in turn

providing a potential prognostic tool for identifying patients with high risk of recurrence.

References:

1. Quaresma M, et al. *The Lancet* (2015).
2. Mamounas EP, et al. *JCO* (2012).
3. Sharifi S, et al. *Mod Path* (1999).
4. Klahan S, et al. *Tumour Biol* (2017).
5. Prescot AP, et al. *JMRI* (2005).
6. Ramadan S, et al. *Radiology* (2015).

S06.05

Accelerating Acquisition of RESOLVE-DWI with Simultaneous Multi-slice (SMS) Technique in Diagnosing Breast Lesions

H. Yiqi[1], A. Tao[1], Z. Chenao[1], Z. Xiaoyong[2], Y. Xu[3], L. Wei[4], X. Liming[1]

[1]Tongji Hospital, Tongji Medical College, Huazhong University of Science and Technology, Radiology, Wuhan, CHINA, [2]Siemens Healthcare, MR Collaborations, Shenzhen, CHINA, [3]Siemens Healthcare, MR Scientific Marketing, Shenzhen, CHINA, [4]Siemens Shenzhen Magnetic Resonance, Shenzhen, CHINA

Purpose/Introduction: To investigate the feasibility and effectiveness of diffusion weighted imaging (DWI) using Simultaneous Multi-slice readout-segmented echo planar imaging (rs-EPI) to diagnose breast lesions.

Subjects and Methods: The IRB approved study was performed on a 3T scanner with a dedicated 16-channel phased-array breast coil (MAGNETOM Skyra, Siemens Healthcare, Erlangen, Germany). 46 female patients (average age of 42.3 years; range of 26-57 years) with 48 lesions (41 malignant and 7 benign) were enrolled in this study. Patients underwent bilateral breast MRI using a prototypical SMS rs-EPI sequence and a conventional rs-EPI sequence. T1-weighted MRI, T2-weighted MRI, and dynamic contrast-enhanced (DCE-MRI) were also conducted as references. The details of imaging parameters of both DWI sequences were listed in Figure 1. ADC, MK, MD values were quantitatively calculated for each lesion on both sequences. In addition, all images were qualitatively analyzed by a blinded read using a 5-point scale (1 = poor, 5 = excellent). The difference and correlation of both quantitative and qualitative parameters between conventional rs-EPI and SMS rs-EPI data were statistically analyzed.

Results: Compared to conventional rs-EPI, The acquisition time of SMS rs-EPI was markedly reduced (2:17 vs 4:27 min). The Pearson's correlation showed a excellent linear relationship for each parameter between SMS rs-EPI and conventional rs-EPI (r = 0.935, 0.914 and 0.965 for MK, MD and ADC respectively; $P < 0.01$ for all, Fig. 2). Furthermore, the ROC analysis demonstrated SMS rs-EPI had better diagnostic performance than conventional rs-EPI, however the values didn't differ significantly (Fig. 3). In blinded read, SMS rs-EPI showed comparable imaging quality with conventional rs-EPI (Fig. 4 and 5), with moderate to good inter-rater reliability (ICC = 0.63–0.83).

Figure 1

Imaging parameters of the conventional and SMS rs-EPI sequences.

Parameter	conventional rs-EPI	SMS rs-EPI
TR(ms)	5000	2340
TE(ms)	70	71
time acquisition	4:27	2:17
FOV(mm)	280*170	
Acquisition Matrix	115*188	
Flip Angle	180	
slice thickness(mm)	5	
Spacing Between Slices(mm)	1	
Band-Width(Hz/Px)	887	
b-value(s/mm2)	0,50,1000,2000	

SMS, simultaneous multi-slice; rs-EPI, readout-segmented echo planar imaging; TR, repetition time; TE, echo time; FOV, field of view.

Figure 2

The correlation of parameters between conventional and SMS rs-EPI for breast lesions.

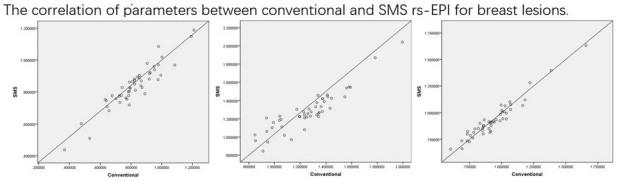

MK r=0.935,P=0.000 MD r=0.914,P=0.000 ADC r=0.965,P=0.000

Figure 3

AUC of conventional and SMS rs-EPI parameters for the differential diagnosis of the breast lesions.

	MK	MD	ADC
Conventional rs-EPI	0.734(95%CI 0.587-0.851)	0.859(95%CI 0.728-0.943)	0.823(95%CI 0.686-0.918)
SMS rs-EPI	0.747(95%CI 0.601-0.861)	0.904(95%CI 0.783-0.970)	0.874(95%CI 0.747-0.952)
P-value	0.675	0.351	0.237

AUC, Area under Curve; MK, Mean kurtosis; MD, Mean diffusion.

Figure 4

Qualitative Comparison of Image Quality conventional and SMS sequences

Parameter	Score Range	Conventional rs-EPI	SMS rs-EPI	P
Image sharpness	1-5	4.47±0.57	4.35±0.64	0.965
Anatomic distortion	1-5	4.07±0.57	4.13±0.50	0.588
Image contrast	1-5	4.26±0.58	4.35±0.57	0.471
Lesion conspicuity	1-5	4.20±0.54	4.04±0.70	0.288
Detailed structure	1-5	4.37±0.53	4.24±0.71	0.463
Overall image quality	1-5	4.48±0.55	4.34±0.66	0.234

Figure 5

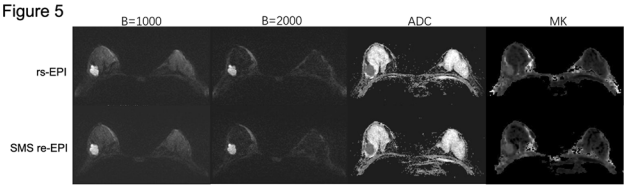

Coventional and SMS rs-EPI images for patient with invasive breast cancer respectively.

Discussion/Conclusion: Compared to conventional rs-EPI technique, SMS rs-EPI can markedly reduce the acquisition time and yield similar diagnostic accuracy and comparable image quality, which may be useful to expand the scope of its clinical application in breast imaging, and increase the patient throughout. SMS RESOLVE allows for rapid realization of breast MR imaging, which may serve as a superior alternative for the diagnosis of breast lesions.

References:

1. W. Bogner et al. Readout-segmented echo-planar imaging improves the diagnostic performance of diffusion-weighted MR breast examinations at 3.0T. Radiology 263 (2012) 64–76.
2. R. Frost et al. Scan timereduction for readout-segmented EPI using simultaneous multi slice acceleration: diffusion-weighted imaging at 3 and 7 Tesla. Magn. Reson. Med.74 (2014) 136–149.

S06.06

Impact of respiration-induced B_0-fluctuations on image blurring in diffusion breast imaging

T. Palm[1], M. Pistel[1], S. Ohlmeyer[1], E. Wenkel[1], R. Janka[1], B. Hensel[2], M. Uder[1], F. B. Laun[1]
[1]*University Hospital Erlangen, Friedrich-Alexander-Universität Erlangen-Nürnberg (FAU), Institute of Radiology, Erlangen, GERMANY,* [2]*Friedrich-Alexander-Universität Erlangen-Nürnberg, Max-Schaldach-Stiftungsprofessur, Center for Medical Physics and Engineering, Erlangen, GERMANY*

Purpose/Introduction: It has been shown that breathing influences the B_0 field in the female breast (1) and thereby causes image distortions/displacements (2-4). Here, it is investigated if ADC maps of the breast are blurred when acquired in free breathing and if the effect can be mitigated by breath hold acquisitions.

Subjects and Methods: 4 healthy female volunteers (age 23 - 27 years) were examined on a 3 T MR scanner (Magnetom Skyra, Siemens Healthcare, Germany) using a dedicated 16-ch breast coil. The volunteers were placed in prone position. Phase maps of one central slice in the breast were acquired using a gradient-echo sequence (TR = 14 ms, TE = 2.46, 4.92 ms, Voxel size = 1.7 × 1.7 × 5 mm^3, BW = 800 Hz/Px, 100 repetitions). They were converted into field fluctuation maps by $\Delta B = (\Phi_{TE1}-\Phi_{TE2})/(\Upsilon\cdot\Delta TE)$. For 2 of the volunteers, a spin echo sequence with echo planar read-out was used for diffusion-weighted imaging (TR = 1800 ms, TE = 100 ms, Voxel size = 2.5 × 2.5 × 5 mm^3, BW = 1110 Hz/Px, b = 50, 800 s/mm^2, 24 averages, fatsat), once with free breathing and once in breath hold. Apparent diffusion coefficient (ADC) maps were calculated. Image blurring of the ADC maps was quantified by the Blanchet sharpness index (5).

Results: Fig. 1 shows ΔB_{max} as measured in the breast with free breathing. ΔB_{max} is largest near the anterior chest wall. The spatial distribution was similar for all 4 volunteers. In Fig. 2, two echo planar images acquired in different stages of the breathing cycle are displayed. They are shifted by several voxels. In Fig. 3, representative ADC maps are shown, which were acquired with and without breath hold. The ADC maps acquired in breath hold have increased image sharpness. Mean Blanchet sharpness index over 2 volunteers: 20.2 ± 3.3 (breath hold), 12.8 ± 0.9 (free breathing).

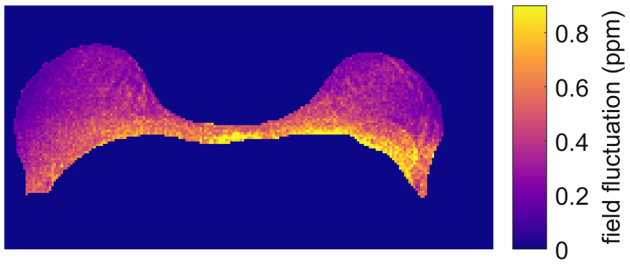

Fig. 1: Representative map of the max. field fluctuations within the breast of one healthy volunteer. Field fluctuations are highest towards the chest wall, specifically in the left breast

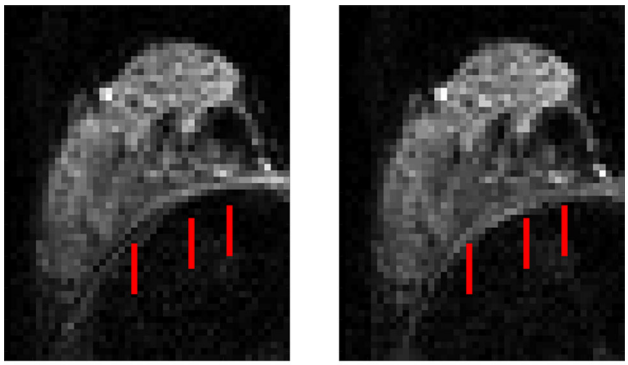

Fig. 2: Echo planar image shift due to field variation in the right breast. Images were acquired with same parameters (TE = 74 ms, b = 50 s/mm², BW = 1116 Hz/Px) in different stages of the breathing cycle. Red vertical lines are guides to the eye

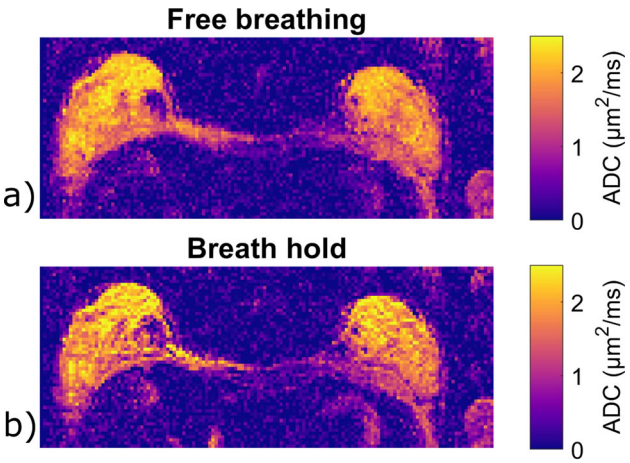

Fig. 3: ADC maps with a) free breathing and b) breath hold acquisition. The image displayed in a) appears to be more blurred than the image in b). Blanchet sharpness index : a) 13.4 (free breathing), b) 17.9 (breath hold).

Discussion/Conclusion: The field fluctuations result in considerable image shifts when using echo planar imaging. They appear non-negligible for echo planar DWI of the female breast. For demonstration purposes, the used bandwidth was chosen smaller than that usually employed in clinical practice (∼ 2000 Hz/Px), but the effect appears to be relevant even at doubled bandwidth. Thus, it is recommendable to either use breath hold acquisitions or distortion-free DWI approaches (6). Possibly, image registration might help

minimize the blurring (7), although high b-value images that possess little image information might represent a challenge for registration algorithms.

In conclusion, respiration-induced field fluctuations result in non-negligible image shifts in echo planar DWI of the female breast and should be addressed, in particular for an optimal assessment of small lesions.

References:

1. Peters NH, *JMRI*. 2009;29(3):731-5.
2. Raj D, *PhysMedBiol*. 2001;46(12):3331.
3. Jezzard P, *FunctMRI*. 2000:1173-81.
4. Raj D, *PhysMedBiol*. 2000;45(12):3809.
5. Blanchet G, *ICASSP*. 2012.
6. Merrem A, *InvestRadiol*. 2017;52(7):428-33.
7. Takatsu Y, *MagnResonImaging*. 2019;57:277-84.

L02 Lightning Talks

15:00–15:30 The Stage

From Low to High Field MRI: Hardware, Safety, QA

L02.01
Low magnetic field MR imaging

N. Salameh, M. Sarracanie
University of Basel/Laboratory for Adaptable MRI Technology, Department of Biomedical Engineering, Allschwil, SWITZERLAND

Purpose/Introduction: Over the last 30 years, the MR community has put tremendous efforts in developing hardware and software for high field to ultra-high field MRI, enabling today's impressive 7 T images in humans. The first developments in that direction have been initially driven by the need of higher nuclear spin polarization in order to achieve high spatial resolutions in acquisition times acceptable in clinical settings. With today's needs of reducing health costs and dealing with long waiting-lists and space shortage in hospitals, we propose to use low magnetic field MRI as a cost-effective and site-friendly solution for patient triage, of particular interest in remote areas where access to conventional scanners is extremely limited.
Subjects and Methods: While transitioning to higher field strengths in the late 80 s early 90 s, endogenous tissue contrasts have been overlooked although it is a known fact that the dispersion in relaxation rates is higher at lower field strengths (see Figure 1, modified from [1]). We propose to benefit from low-field native contrast available at 0.1 T as well as its higher flexibility in term of siting requirement and compensate for lower NMR sensitivity by using high performance sequences and RF detectors similar to what was described in [2].

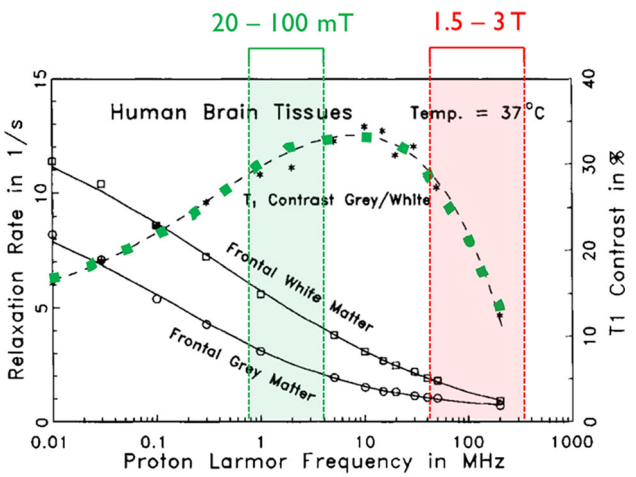

T1 relaxation rate with respect to Larmor frequency. The T1 dispersion in brain tissue samples (plain lines) as well as their relative contrast (dotted line) is more important in the low to moderate field regime. (modified from [1])

Results: We installed and fully equipped a low-field imaging platform comprising three resistive MRI systems (non-commercial) of different scales: a small one for tube-like phantoms, an intermediate one ideal for extremities or preclinical studies, and a whole-body scanner for human studies, all of them sited in one single room of about 110 m^2. The very first images using SSFP-based sequences obtained on those scanners are shown in Fig. 2 (acquisition times ranging from 30 s to a few minutes).

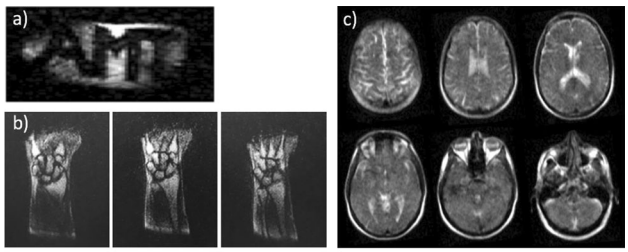

Samples of 3D images acquired at 0.1 T on our a) smallest magnet in a vial filled with water, b) on our intermediate scanner in a human wrist, and c) on our whole-body scanner in a human head. In c) 30 slices have been acquired in 30 seconds.

Discussion/Conclusion: We were able to acquire good SNR 3D sets of images in a reasonable acquisition time at 0.1 T. We also proved that low-field technologies are less demanding regarding siting requirements and that we can operate three scanners in the same room without impacting our image quality. This latter point has a strong advantage compared to higher-field scanners when it comes to optimizing space in hospitals. Future work includes in priority the development of advanced sequences enabling better contrast between tissue species.
References:
[1] Fischer et al., MRM 1990;
[2] Sarracanie et al., Sci. Rep. 2015

L02.02
Characterization of poly(sodium acrylate)/sodium silicate hydrogels with Low Field NMR Relaxometry

I. Habina[1], A. T. Krzyżak[1], J. Mastalska-Popławska[2], A. Stempkowska[3]
[1]AGH University of Science and Technology, Faculty of Geology, Geophysics and Environmental Protection, Cracow, POLAND, [2]AGH University of Science and Technology, Faculty of Materials Science and Ceramics, Cracow, POLAND, [3]AGH University of Science and Technology, Faculty of Mining and Geoengineering, Cracow, POLAND

Purpose/Introduction: Among numerous materials used to construct MRI phantoms, gels are of great importance [1]. The addition of paramagnetic ions helps to get a material with a desired relaxation properties, however in more complex systems relaxivities of the obtained samples depend not only on its concentration but also e.g. on gel concentration and structure [2]. Here we present Low Field NMR relaxometry characterization of the silicate-polymer hydrogel samples with the increasing Na^+ ions concentration as an example of such an intricate dependency. The obtained materials are studied in order to develop phantoms for calibration of diffusion tensor imaging sequences [3].
Subjects and Methods: Hydrogels samples were prepared as mixtures of sodium water glass R-145 (WG) and poly(sodium acrylate) (pANa) for which monomer was aqueous solution of sodium acrylate (ANa, 20 wt %). Samples were prepared with WG:pANa mass ratio from 1:10 to 7:1. As a reference pure pANa samples were also synthetised from 20 to 37 wt % aqueous solutions of sodium acrylate.
NMR measurements were conducted on an NMR Rock Core Analyzer system at magnetic field of 0.05 T. Carr-Purcell-Meiboom-Gill sequence was used to register T_2 decay with echo time of 200 µs and repetition time of 5 s. Inverse Laplace Transform was used to obtain T_2 distributions.

Results: In Fig. 1 transverse relaxivity ($R_2 = 1/T_2$) in relation to Na + concentration is presented. An increase from 1.3 s^{-1} for sample 1:10 (5.4 wt % of Na^+) to 15.5 s^{-1} for sample 7:1 (10.2 wt % of Na^+) is observed. The nature of the observed changes is best reflected by the cubic polynomial in opposite to linear relations observed for pure solutions of paramagnetic ions [4]. Relaxivities measured for pure polymer samples are also increasing but in much lower range: from 0.9 s^{-1} (for 4.9 wt % of Na^+) to 1.9 s^{-1} (for 9.1 wt % of Na^+) and their changes can be described by quadratic function satisfactorily.

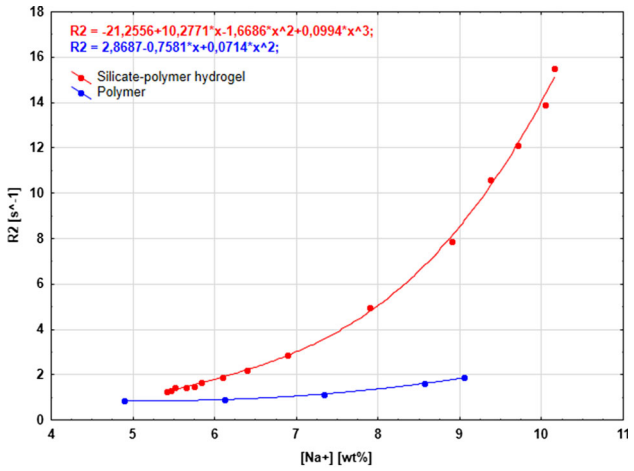

Fig.1. Relaxivities R2 for samples of SW-pANa mixtures and pure polymer, pANa in relation to Na+ concentration.

Discussion/Conclusion: Observed cubic polynomial relation of R_2 relaxivities on Na^+ ions concentration for polymer-silicate hydrogels samples in comparison to quadratic relation for pure polymer samples reveals the existence of more complex dependency between components of the studied system. NMR studies of other characteristics, such as diffusion, may give more comprehensive insight into these materials.

Acknowledgements The work was financed by the National Centre of Research and Development (contract no. Strategmed2/265761/10/NCBR/2015).

References:

[1] Hellerbach A., Schuster V., Jansen A. Sommer J, PLoS One (2013)8(8):e70343.
[2] Yoshimura K. et al., Magn Reson Med (2003) 50:1011-1017.
[3] Kłodowski K., Krzyzak A. T., Magn Reson Imaging (2016) 34(4):404–409.
[4] Thangavel K., Saritas E. U., Turk J Elec Eng@Comp Sci (2017)25:2108-2121.

L02.03

B_0 Mapping and Image Reconstruction in Low Field Permanent Magnet MRI Systems

K. Koolstra[1], T. O'Reilly[1], P. Börnert[2], A. Webb[1]
[1]*Leiden University Medical Center, Radiology, Leiden, NETHERLANDS,* [2]*Philips Research Hamburg, Hamburg, GERMANY*

Purpose/Introduction: Low field permanent magnet MRI systems have relatively large B_0 inhomogeneities, which lead to image distortions when using fast Fourier transform (FFT)-based reconstructions. It is possible to correct for those distortions in model-based (MB) image reconstruction, but existing techniques rely on having an accurate B_0 map, which is challenging to acquire and can also change if the magnet temperature drifts. Therefore, image-based B_0 mapping would provide an attractive solution. Standard techniques assume that the phase in a pixel of the image is given by the phase of the sampled signal at the echo-top. However, for very strong inhomogeneities this assumption does not hold, and leads to inaccurate B_0 maps. This work presents an iterative B_0 mapping approach in which B_0-induced phase changes during sampling are corrected for by MB image reconstruction.

Subjects and Methods: The studied low-field system is a k = 1 Halbach magnet [1], producing a 0.05T magnetic field at the center of the bore (Fig. 1). The B_0 field was measured in a 10 × 10 cm^2 FOV at 5 × 5 mm^2 resolution using a gaussmeter connected to a robot. This was used as the input for the simulations.

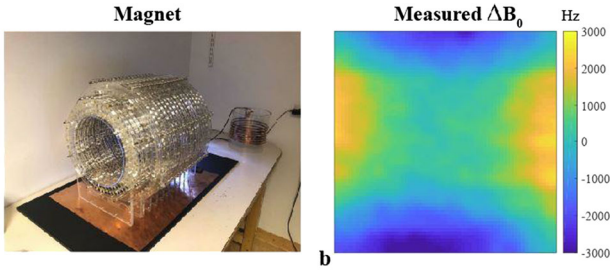

Figure 1. Magnet setup. (a) The Halbach magnet, producing a 0.05T magnetic field at the center. (b) The ΔB0 field in Hz was measured on a 10×10 cm2 with a gaussmeter connected to a robot.

Two spin echo k-space data sets with an unshifted and shifted (T =150 µs) readout gradient were simulated for a Shepp Logan phantom from the signal models$(k(t)) = \int \rho(x) e^{-2\pi \Delta B_0^{(x)i(t+T)}} e^{-k \cdot x} dx$ (ρ the spin density, ΔB_0 the measured field in Hz), using a gradient strength of 11.7 mT/m, a sampling dwell time of 20 µs and 164 complex sampling points.

From the two k-space data sets ΔB_0 maps were reconstructed using three different approaches.

(1) Image reconstruction using FFT and standard B_0 mapping based on the phase difference map.
(2) Set $\Delta B_0(\mathbf{x}) = 0$ as the initial guess. Iterate: Image reconstruction using FFT and conjugate phase reconstruction (CPR) to correct for B_0-induced phase changes during the readout process [2], B_0 mapping as in 1).
(3) Set $\Delta B_0(\mathbf{x}) = 0$ as the initial guess. Iterate: MB image reconstruction taking into account the B_0 field in the encoding matrix [3], B_0 mapping as in 1).

Results: Figure 2 shows the ΔB_0 map within the phantom used to generate the simulated data, the estimated ΔB_0 maps and corresponding error maps using approaches 1–3, running 3 iterations in approaches 2–3. Figure 3 shows the corresponding reconstructed images.

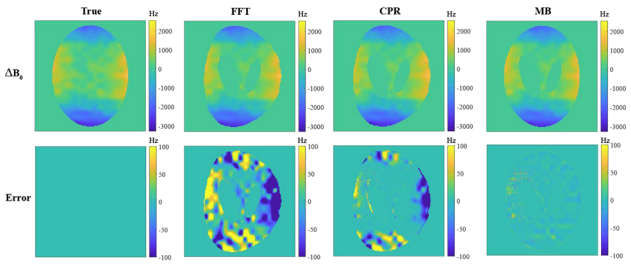

Figure 2. B0 mapping using approaches 1-3. The standard technique (FFT) shows large errors in inhomogeneous regions. Combining B0 mapping with CPR reduces the errors, but not sufficiently. Reconstruction via MB results in the lowest error map.

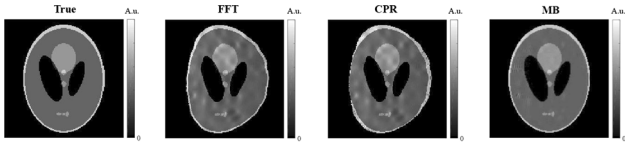

Figure 3. Image reconstructions using approaches 1-3. The FFT reconstruction results in large deformations of the object. CPR slightly reduces the deformations. The quality of the MB reconstruction is closest to the true image.

Discussion/Conclusion: Large errors (> 300 Hz) are observed when performing standard B_0 mapping. Iteratively applying CPR reduces these errors, but in regions where the inhomogeneities are large compared to the gradient strength there are still strong artifacts. Iteratively applying MB image reconstruction results in a much smaller ΔB_0 error, and the corresponding image is of higher quality. This approach can help to improve the accuracy of B_0 mapping at low field, and to correct for related image distortions.

References:

1. O'Reilly T et al. ISMRM. 2019;0272.
2. Man L et al. MRM. 1997;37:785-792.
3. Koolstra K et al. ISMRM. 2019;2445.

L02.04

Fast Field-Cycling MRI for molecular dynamics imaging

L. Broche[1], J. Ross[1], G. Davies[1], M. J. Macleod[2], D. Lurie[1]
[1]University of Aberdeen, Aberdeen Biomedical Imaging Centre, Aberdeen, UNITED KINGDOM, [2]NHS Grampian, Aberdeen, UNITED KINGDOM

Purpose/Introduction: Fast Field-Cycling (FFC) MRI is a new non-invasive technology[1] that allows measuring quantitative information on molecular dynamics time scales, from tens of nanoseconds to a few milliseconds, by varying the magnetic field during a pulse sequence to generate T_1-based contrast. In the body T_1 is closely linked to the autocorrelation function of water and fatty molecules so its field-dependant spectrum, also called the T_1 dispersion curve, provides a direct view of molecular motions over a range of time scales that is determined by the strength of the magnetic field, via the Larmor frequency of the spin system observed. The T_1 dispersion curve has been used for decades to study materials and various models exist that predict the dispersion profiles in particular microscopic environments[2–6]. Our efforts over the last years have focused on developing a system able to measure T_1 dispersion curves in vivo to exploit this source of information in medicine and to provide unique insights of tissue architectures.

Subjects and Methods: The FFC-MRI scanner can reach any field from 0.2 T to 20 μT within 12.5 ms and T1-weigthed images are produced at five field strengths to complete the scan within 30 min. We have measured T_1 dispersion curve and contrast in vivo and non-invasively in volunteers, including patients from stroke and cancer, and compard with images from standard modalities, including CT and 3T MRI, and patient diagnostic.

Results: Image contrast derived on T_1 was found to be larger at lower field in general, with good correlation with clinical images and in particular with diffusion weighted imaging. Interestingly, T_1 contrast at 0.2 T was usually found to be less informative than at fields below 20 mT, at least in the pathologies investigated to date. Early results from T_1 dispersion curve measured in vivo show good agreement with ex vivo data, opening the way to in vivo molecular dynamics biomarkers and characterisation of molecular motions.

Discussion/Conclusion: The device we constructed is an excellent research tool to investigate T_1 contrast over a large range of magnetic fields that are difficult to reach using conventional imaging methods. Early results show promising applications in stroke and cancer and other studies using cell models of breast cancer lines have already showed links with cellular activity[2,3]. Several studies are under way to exploit this new source of information.

References:

1. Lurie DJ, et al. *Comptes Rendus Phys*. 2010.
2. Kimmich R, Anoardo E. *Progr Nucl Magn Res Spect* 2004.
3. Korb J-P, Bryant RG. *Comptes Rendus Phys*. 2004.
4. Koenig SH, Brown RD. *Magn Reson Med*. 1993.
5. Kruk D, Herrmann A, Rössler EA. *Progr Nucl Magn Reson Spect*. 2012.
6. Fries PH, Belorizky E. *Journ Chem Phys*. 2015.
7. Ruggiero MR, et al. *Angew Chem Int Ed*. 2018.
8. Baroni S, et al. *Magn Reson Chem*. 2019.

L02.05

Flexible multi-turn multi-gap coaxial coils: investigation of size- and shape-adaptation for different anatomical targets at 1.5, 3 and 7 Tesla

L. Nohava[1], R. Czerny[2], M. Obermann[2], M. Pichler[2], J. Felblinger[3], R. Frass-Kriegl[2], J.-C. Ginefri[1], E. Laistler[2]
[1]Université Paris-Sud/CNRS, Université Paris-Saclay, IR4 M (Imagerie par Résonance Magnétique et Multi-Modalités), UMR 8081, Orsay, FRANCE, [2]Medical University of Vienna, Division MR Physics, Center for Medical Physics and Biomedical Engineering, Vienna, AUSTRIA, [3]Université de Lorraine, Inserm, IADI, Nancy, FRANCE

Purpose/Introduction: Flexible radio frequency coils form-fitted to the region of interest and size-adapted for the anatomical target provide an SNR-optimal setup for MR signal reception[1,2]. In this work, we investigate light-weight coaxial coils (CCs)[2] employing the multi-turn multi-gap (MTMG) principle[3,4,5] that are made from commercially available coaxial cables and designed for ^{1}H imaging at 1.5, 3 and 7T targeting different anatomical sites.

Subjects and Methods: 3 coil diameters were investigated with respect to anatomical targets: 4 cm (skin, hand, wrist), 7 cm (elbow, ankle, head), 10 cm (head, knee, breast).

Resonance frequencies (f_0) were numerically calculated to determine suitable CC geometries and cable parameters (Fig. 1a) to fabricate CCs tuned to 63.9, 123.2 or 297.2 MHz. Thereby, configurations with proper calculated f_0 and with lowest number of gaps n_g and turns n_t were selected for further investigation. Moreover, standard loop coils (SLCs) with the same diameters and target f_0 as the CCs were fabricated.Coils were characterized on the bench by measuring f_0 and Q-factors in unloaded and loaded condition using a single pick-up probe. CCs and SLCs were compared in flat configuration. Additionally, CCs were tested in bent configuration with two bending radii representing curvatures of different anatomical sites (Fig. 1b). A container (24.5 l) and 4 balloons (0.5, 1, 3 or 5 l) with 3 mm coil-sample spacing were used as phantom load (σ = 0.2S/m), respectively (Fig. 1c).

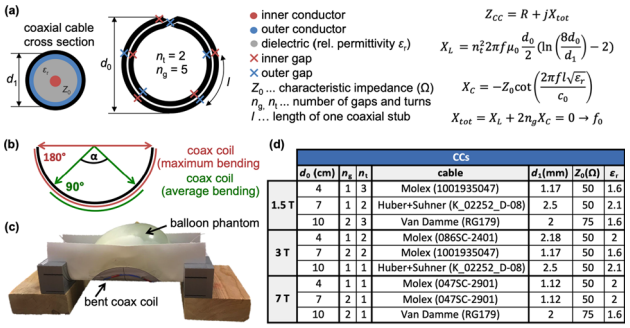

(d)

	CCs						
	d_0 (cm)	n_g	n_t	cable	d_1(mm)	Z_0(Ω)	ε_r
1.5 T	4	1	3	Molex (1001935047)	1.17	50	1.6
	7	1	2	Huber+Suhner (K_02252_D-08)	2.5	50	2.1
	10	2	3	Van Damme (RG179)	2	75	1.6
3 T	4	1	2	Molex (086SC-2401)	2.18	50	2
	7	2	2	Molex (1001935047)	1.17	50	1.6
	10	1	1	Huber+Suhner (K_02252_D-08)	2.5	50	2.1
7 T	4	1	1	Molex (047SC-2901)	1.12	50	2
	7	2	1	Molex (047SC-2901)	1.12	50	2
	10	2	1	Van Damme (RG179)	2	75	1.6

Fig. 1: (a) Cable and coil parameters determining f0, equations for f0 calculations, (b) bending configurations for CC bench tests, (c) measurement set-up, (d) CC configuration and cable type per coil diameter and B0 field strength

Results: For each diameter and B_0 field strength, CCs with a suitable n_g/n_t configuration and cable type were found (Fig. 1d). Calculated CC frequencies and bench measurement results are summarized in Fig. 2. Similar Q_{loaded} for CCs and SLCs were observed.

		CCs (flat)					SLCs (flat)					CCs (avg. bending)					CCs (max. bending)				
	d_0 (cm)	fcalc (MHz)	fu (MHz)	Qu	fl (MHz)	Ql	fu (MHz)	Qu	fl (MHz)	Ql		fu (MHz)	Qu	fl (MHz)	Ql		fu (MHz)	Qu	fl (MHz)	Ql	
1.5 T	4	62,6	60,5	276	57,6	138	63,9	340	63,8	169		59,2	242	59,4	189		59,5	248	59,4	201	
	7	62,3	58,1	239	57,7	69	63,9	370	63,7	85		57,9	250	57,5	106		58,1	248	57,7	142	
	10	57,8	54,9	122	52,5	35	63,9	420	63,6	47		54,0	103	53,5	51		54,9	101	53,9	56	
3 T	4	119,0	111,0	303	112,3	83	123,3	348	123,0	86		112,8	301	112,7	192		114,0	295	113,6	218	
	7	123,5	126,8	280	126,1	31	124,0	431	123,4	29		129,2	281	126,6	56		131,0	285	128,3	100	
	10	115,6	108,5	238	107,1	20	123,2	429	122,6	18		109,6	245	107,1	33		111,9	246	108,1	48	
7 T	4	308,9	293,4	240	292,7	26	297,4	254	296,6	23		297,2	216	293,3	45		297,9	200	293,4	79	
	7	334,0	298,8	205	301,6	9	297,3	281	295,5	9		301,9	163	292,2	9		307,1	158	301,8	17	
	10	299,0	271,8	135	274,0	7	297,3	206	300,1	5		275,5	126	271,3	7		279,8	117	266,9	10	

Fig. 2: Calculated frequencies (fcalc) for CCs and bench measurement results in loaded (l) and unloaded (u) condition for CCs and SLCs in flat configuration and CCs in bent configurations

The average deviation between calculated and measured f_0 is 6.6%, the maximum deviation (10.5%) occurs for a high n_g/n_t ratio (Fig. 3a). Loading in flat configuration affects f_0 stronger for CCs than for SLCs (Fig. 3b). On average, bending shifts f_0 by ± 1.4% (slight bending) or ± 2.0% (strong bending), as shown in Fig. 3c. Loading the CCs in bent condition results in an average Δf_0 of 1.6% (Fig. 3d), the maxima were observed for large coils and high f_0.

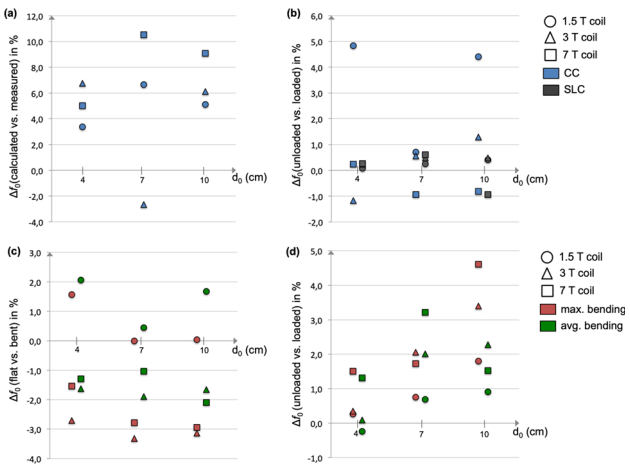

Fig. 3: Frequency shift in % (a) between calculated and measured f0 (unloaded, flat) for all CCs (b) due to loading for CCs and SLCs (flat) (c) due to bending (maximum, average) for all CCs (unloaded) (d) due to loading in bent configurations

Discussion/Conclusion: Applying the MTMG principle, the parameter space of achievable coil sizes and f_0 can be enlarged for CCs. Here, we demonstrate the feasibility of light-weight and flexible CCs with 3 different diameters at 3 common B_0 field strengths using commercially available cable types. The comparison of flat and bent measurements demonstrates the CCs' robustness regarding deformation. Bench tests with coil interfaces as well as MR measurements are part of an on-going study.

References:

1. Kumar, MRM 61 (2009)1201–1209.
2. Zhang, Nat Biomed Eng 2 (2018) 570–577.
3. Frass-Kriegl, JMR 273 (2016) 65–72.
4. Nohava, ISMRM (2019) 0565.
5. Czerny, ISMRM (2019) 1550.

Acknowledgement FWF/ANR grant Nr. I-3618, OeAD/WTZ grant FR 03/2018.

L02.06

A highly flexible array with high intrinsic inter-element decoupling at 7T

I. Zivkovic, T. Ruytenberg, A. Webb
Leiden University Medical Center, Radiology Department, Leiden, NETHERLANDS

Purpose/Introduction: Surface loop coils are common array elements and one major challenge is to overcome the coupling between elements[1]. Different methods exist to decouple neighbouring coils such as geometrical overlapping and pre-amplifier decoupling, decoupling via transformers, decoupling based on capacitive/inductive networks or decoupling with passive resonators.
In this paper, we propose a modified high impedance coil design[2], adapted from the principles based on ham radio antennas[3] with a loop diameter of ∼ 100 mm at 7T. The proposed coil geometry provides high decoupling between adjacent and non-adjacent elements without overlapping or preamplifier decoupling. The performance of transceive elements was assessed using a five-channel array for hand imaging.

Subjects and Methods: *Transceive loops (Fig. 1) were created of coaxial cable (K_02252_D-08, Huber + Suhner, Switzerland).*

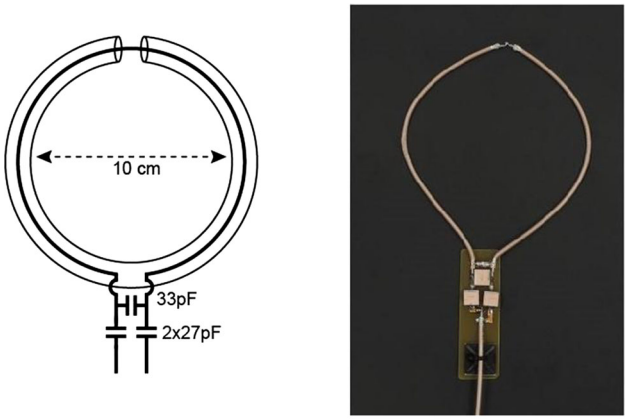

Figure 1. Schematics and photo of the fabricated coaxial coil.

Two high voltage rated capacitors of 27 pF (300 V, Dalicap Co.,Ltd., China) were connected in series and one high voltage rated 33 pF capacitor was connected in parallel. Transceiver array constructed for hand imaging consists of five coil elements attached to a glove: each coil has been attached to the individual finger. The hand images were obtained using a 3D T1-weighted gradient-echo sequence with the following parameters: TR/TE = 25/4.9 ms, FA = 25°, voxel size = 0.5 × 0.5 × 4.0 mm^3, NSA (whole hand) = 3, NSA (finger) = 5.
Results: Figure 2 shows the five-channel glove coil transceiver array and measured noise correlation matrix. The lowest inter-element coupling was between elements 4 and 5 (− 11 dB) which we attribute

to the not suitable positioning in the process of fitting the individual elements on the glove.

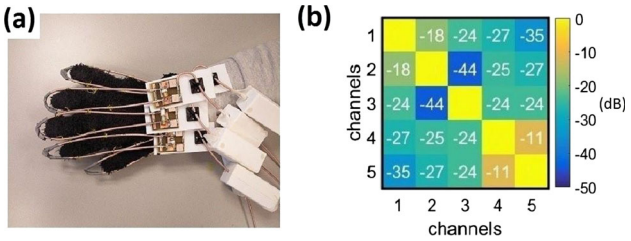

Figure 2. (a) Photo of the glove array and (b) measured noise correlation matrix.

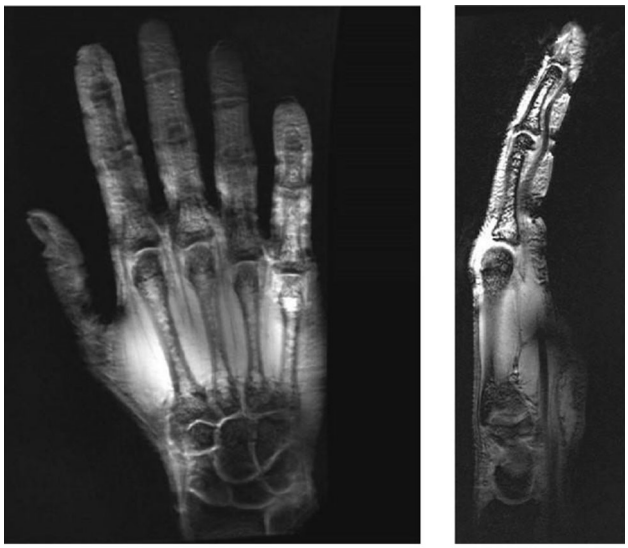

Figure 3. GRE images of the whole hand (left) and finger (right).

Figure 3 shows an image of the hand with fine bone structure visible on a single finger image.

Discussion/Conclusion: Five element array attached to the glove for hand imaging is presented. The proposed geometry also has parallels in recently-described high impedance coils[2], with the difference being that in our design capacitor is connected in parallel to the loop (instead of inductor connected in parallel) and that configuration eliminates using of pre-amplifiers for decoupling so the coil can be used for both transmit and receive.

We demonstrated that proposed coaxial coil can be used as transceive element in hand imaging application. It is possible to expand the application of the proposed coil concept for imaging of different body parts for which rigid coil design is not suitable, such as larynx. The proposed coil is also convenient as array element in size-adjustable tight fitting head arrays.

Acknowledgments This work was made possible by NWO domain TTW under grant #13783 and European Research Council Advanced Grant (670629 NOMA MRI).

References:

1. Roemer PB et al. MRM. 1990;16(2):192-225.
2. Zhang B et al. Nat Biomed Eng. 2018;2(8):570-7.
3. Demaw D. QST. 1988;4:30-2.

L02.07

Fast and unconditionally safe in vivo MR head protocol for home-made coil prototype assessment at 7T

A. Vignaud[1], F. Mauconduit[1], V. Gras[1], O. Girard[2], F. Kober[2], L. Hertz-Pannier[1], A. Raaijmakers[3], N. Boulant[4], R. Abdeddaim[5]
[1]CEA\NeuroSpin & Université Paris-Saclay, Gif-Sur-Yvette, FRANCE, [2]Aix-Marseille Université, CNRS, CRMBM, Marseille, FRANCE, [3]University Medical Center, Department of Radiology & Eindhoven University of Technology, Department of Biomedical Engineering, Utretch & Eindoven, NETHERLANDS, [4]CEA, NeuroSpin & Université Paris-Saclay, Gif-Sur-Yvette, FRANCE, [5]Aix Marseille Université, CNRS, Centrale Marseille, Institut Fresnel, Marseille, FRANCE

Purpose/Introduction: Ultra-High-Field (UHF) Magnetic Resonance Imaging (MRI) scanners hold great promises for clinical and neuroscientific research. State of the art RF single transmitter channel coil technologies eventually run into inevitable RF field inhomogeneity problems making full exploitation of UHF scanners difficult. Parallel Transmission (pTx) is the dominant strategy to solve the issue [1,2], but other attempts to mitigate the B1 + field have been made by using high dielectric constant materials [3] or metamaterial [4,5] patches inside standard birdcage coils. Regardless of the chosen strategy, for efficiency iterating between coil designs, a quick yet safe evaluation of the global and local SAR evaluation [6] is required to make sure temperature remains within acceptable limits, while too drastic constraints can compromise the range of tests that can be performed in vivo [7].

In this work, we propose an MR protocol allowing the safe use of home-made coils in vivo at any step of the RF coil development securing valuable information for the developer and making sure that neither local nor global SAR limits will be ever reached.

Subjects and Methods: The constraint set here relies simply on energy conservation to guarantee the respect of the IEC SAR guidelines: even if, hypothetically, the total input RF power were focused in a single 10 g-piece of biological tissue, regulatory SAR limits would not be exceeded. Hence, in the following (Table), we describe a set of MR sequences that respect this rule and still deliver valuable MR images at reasonable acquisition time (TA). The sequences are compiled into a special version to lock critical parameters and ensuring safe use based on this strategy.

For demonstration of feasibility, we carried out experiments on a 7T MRI scanner with a transceiver birdcage. In vivo acquisitions were performed on healthy volunteers.

Table: *Parameters of the identified "restricted SAR mode" sequences. The protocol includes a localizer (proton density weighted), a B0 and a B1+ mapping sequences. They have been validated on phantom and in vivo using a transceiver birdcage coil to minimize SNR available. SAR values are presented with the maximum reference voltage and with all power hypothetically focusing into a single 10g-piece of biological tissue.*

Goal	Localizer	B0 map	B1+ map
Sequence type	2D TFL	2D GRE	2D XFL [8]
Exc RF pulse type	Sinc	Sinc	Sinc
Duration (us)	1000	1000	1000
FA (°)	3	5	3
RF saturation	-	-	RECT
Sat duration (us)	-	-	1000
Sat FA (°)	-	-	60
REF Voltage (V)	470	470	470
TR (ms)	20000	400	20000
Ny	128	64	64
Multislice mode	Sequential	Sequential	Sequential
Spatial resolution (mm^3)	2x2x4	4x4x4	4x4x4
Slice number	3	5	3
TA	2min	2min	2min
Max SAR_{local} (W/kg) - 6min (10s)	6 (12)	6.6 (6.6)	3.6 (8.3)
"Normal" mode IEC SAR_{local} limits (W/kg) 6min (10s)	10 (20)		
SAR_{global} (W/kg) - 6min (10s)	0.012 (0.024)	0.013 (0.013)	0.007 (0.016)
"Normal" mode IEC SAR_{global} limits (W/kg) 6min (10s)	3.2 (6.4)		

Results: In the Table, the MR sequence parameters are provided with an estimation of the worst global and local SAR possible while using the highest reference voltage possible with the used coil. As an example, the Figure provides preliminary results on an volunteer with selected sequences.

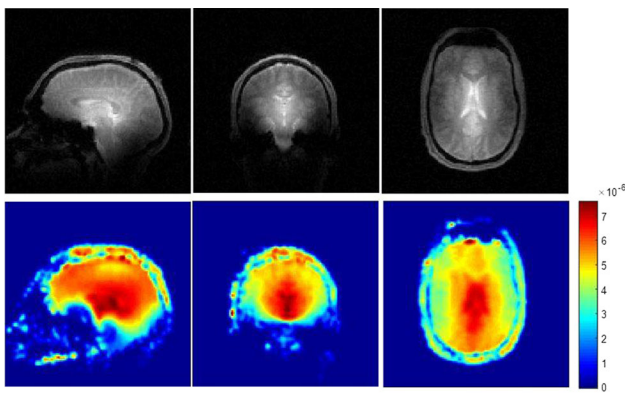

Figure: *On top row, the three orthogonal slices from a 2min proton density weighted localizer and on the bottom row 2min XFL B1+ maps (in μT for 1ms 90° rectangular pulse) acquired under "restricted SAR mode" rules, with a transceiver birdcage on a healthy volunteer at 7T. While using optimal reference voltage for this coil and volunteer, with parameters described in Table, 10s local SAR would never exceed 5W/kg for any of the sequences, even if all the power was focusing in a single 10g-piece of biological tissue.*

Discussion/Conclusion: With so-called "Restricted SAR mode" protocol, it becomes possible to acquire an MR image of reasonable quality in vivo, including in pTx at the price of longer B1 + mapping, without any prior coil or implant safety validations besides the usual electrical and mechanical tests.

References:

[1] Katscher U. et al. NMR Biomed 2006; 19: 393–400
[2] Grissom W. et al. Magn Reson Med 2006; 56: 620–629
[3] Webb A.G. Concept Magn Reson A 2011; 38: 148-184
[4] Slobozhanyuk A.P. et al. Adv Mater 2016; 28:1832-8
[5] Dubois M. et al. Physical Review X 2018; 8:31083
[6] IEC 2010- 2–33: 601
[7] Cloos M.A. et al. Proc Intl Soc Mag Reson Med 2013; 21
[8] Klose U. Med Phys 1992; 19: 1099–1104

Authors would like to acknowledge EU H2020 FET-OPEN M-CUBE project No 736937

L02.08

Suitability analysis of different phantom fluids for MR image artifact measurements with a 7 T MR system

T. Spronk[1], O. Kraff[1], J. Kreutner[2], G. Schaefers[3], H. Quick[1]
[1]Erwin L. Hahn Institute for MR Imaging, University of Duisburg-Essen, Essen, GERMANY, [2]MR: comp GmbH, Testing Services for MR Safety & Compatibility, Gelsenkirchen, GERMANY, [3]MRI-STaR-Magnetic Resonance Institute for Safety, Technology and Research GmbH, Gelsenkirchen, GERMANY

Purpose/Introduction: With the recent clinical application of 7 Tesla MRI in brain and joint imaging, evaluation of MR artifacts of medical implants in high field MR environments gains importance[1]. The testing procedure for artifacts requires a phantom containing a liquid, which provides homogeneous signal intensity over the whole phantom. The aim of this investigation was to compare four different phantom materials in terms of their suitability for artifact size testing in 7 T MR Systems.

Subjects and Methods: Measurements were performed with a 7T whole-body MRI research system (MAGNETOM 7T, Siemens Healthcare, Germany) in combination with a cross-vendor established and clinically used 1-channel transmit/32-channel receive radiofrequency (RF) head coil (Nova Medical, Wilmington, MA). Phantom materials were a copper-sulfate-solution ($CuSO_4$) according to ASTM F2119[1], a sodium chloride solution (NaCl), rapeseed oil and Polyvinylpyrrolidon (PVP), filled into a polyethylene phantom. Signal uniformity U was calculated according to IEC 62464[2]. A titanium rod (length: 100 mm, diameter: 3.1 mm) was inserted perpendicular to the static magnetic field direction in the phantom. According to ASTM F2119, spin (SE) and gradient echo (GRE) images with transversal slice orientation and phase-encoding direction in both anterior–posterior (AP) and right-left (RL) direction were acquired.

Results: Comparing the uniformity of SE and GRE in Fig. 1, oil is the only liquid that produces an adequate uniformity (uniformity > 70) over the whole phantom in both sequences. PVP and NaCl would also be suitable materials for the GRE, but they show very poor uniformity in the SE sequence (< 30). $CuSO_4$ shows strong B1 artifacts (SE) and an over-exposure of the image (GRE). This requires a correction of the FFT factors in the image reconstruction which complicates the test procedure and shows that the 7T MRI system and RF coil are not adjusted for this type of liquid. Due to the inhomogeneities in the SE, only the artifact size of the GRE over the different liquids are compared and shown in Fig. 2 and listed in Tab 1. A maximum difference in the artifact size of 1 mm was observed.

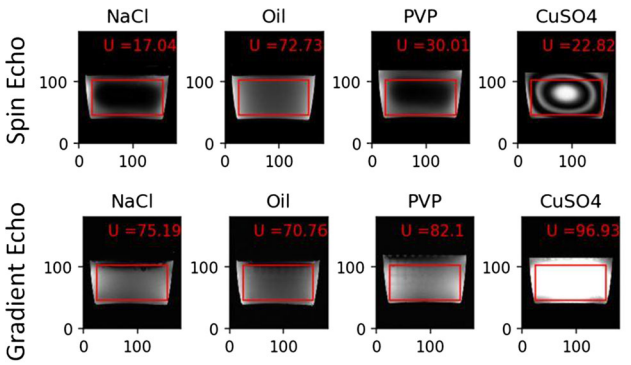

Fig. 1: Reference images with the different filler materials during different scanning sequences. The red rectangle shows the ROI, where the uniformity was evaluated.

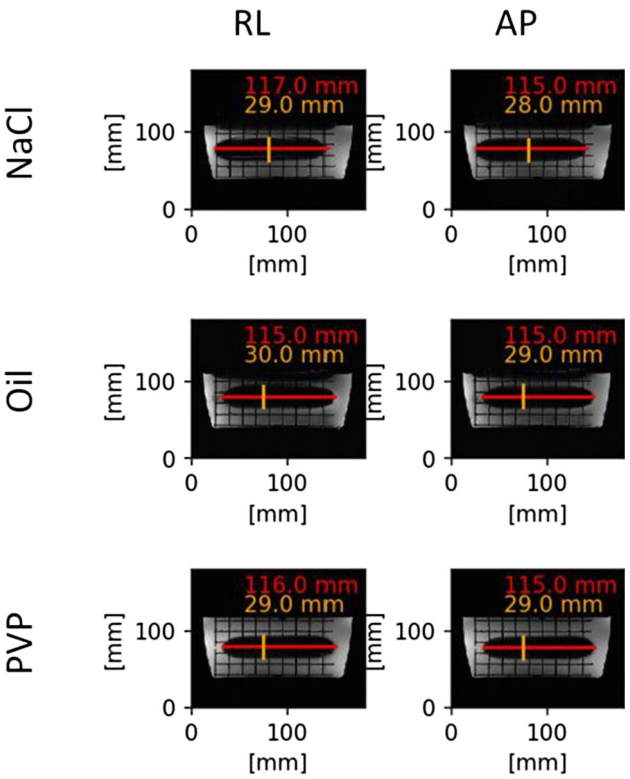

Fig. 2: Vertical and horizontal artifact extensions related to the filler material and the phase-encoding direction.

	Horizontal artifact size [mm]	Vertical artifact size [mm]
NaCl - RL	8.5	13.0
NaCl - AP	7.5	12.5
Oil - RL	7.5	13.5
Oil - AP	7.5	13.0
PVP - RL	8	13.0
PVP - AP	7.5	13.0

Tab. 1: Vertical and horizontal artifact sizes related to the filler material and the phase-encoding direction. "RL" = right-left, "AP" = anterior-posterior; Artifact size = (artifact extension – test object size)/2

Discussion/Conclusion: This study shows that $CuSO_4$, which is proposed in the ASTM standard, is not a practical liquid for the evaluation of MR imaging artifacts at 7T. Also, alternative solutions such as PVP and NaCl are not suitable for this evaluation. In our case only rapeseed oil provided sufficient uniformity for artifact testing. In addition, it could be shown that the artifact size is not influenced by the used fluid. This clearly shows that oil can be used as a potential substitute for $CuSO_4$ and that these measurements can be easily compared with previous artefact tests which utilized $CuSO_4$.

References:

[1] ASTM F2119-07 : Standard Test Method for Evaluation of MR Image Artifacts from Passive Implants. 2013.

[2] IEC 62464-1: Magnetic resonance equipment for medical imaging. 2007.

L02.09

Theoretical *CNR* of PERES coil array for neural current UHF MRI

S. Solis[1], R. Martin[1], F. Vazquez[1], O. Marrufo[2], **A. Rodriguez**[3]

[1]Universidad Nacional Autonoma de Mexico, Facultad de Ciencias, Departamento de Fisica, Mexico City, MEXICO, [2]National Institute of Neurology and Neurosurgery MVS, Department of Neuroimaging, Mexico City, MEXICO, [3]Universidad Autonoma Metropolitana Iztapalapa, Department of Electrical Engineering, Mexico City, MEXICO

Purpose/Introduction: The most important positive aspect with ultra high field (UHF) MRI that is also most widely named when justifying the expense and effort of pursuing higher magnetic fields is *SNR* [1]. The *SNR* of coil or coil array is also a vital parameter to investigate the neuronal electrical activity in MRI. The contrast-to-noise ratio (*CNR*) particularly depends on the *SNR* to optimally detect signal changes due to the electrical activity of neurons as reported in [2]. We theoretically studied the *CNR* of a PERES coil array for parallel magnetic resonance imaging (*p*MRI), using its baseline *SNR* [3] at UHF MRI.

Subjects and Methods: We used the baseline *SNR* expression for the circular coil array derived in [3], and the theory developed by Mansfield [4], and the experimental results in [5], to obtain the corresponding $CNR_{\text{PERES-SENSE}}$ for a coil array with 4 coil elements:

$$CNR_{PERES} = SNR_{PERES-SENSE}(1 - \gamma B_z(r)TE - \pi/2)) \quad (1)$$

and $SNR_{\text{PERES-SENSE}} = 1.25(SNR_{\text{cir-SENSE}}/\sqrt{2}\ g)$, where $SNR_{\text{cir-SENSE}}$ is the circular coil *SNR*, and $R = 4$ and g are defined in [3]. Eq. (1) was used to theoretical compute the $CNR_{\text{PERES-SENSE}}$ as a function of position and along the green line as shown in Fig. 1b)

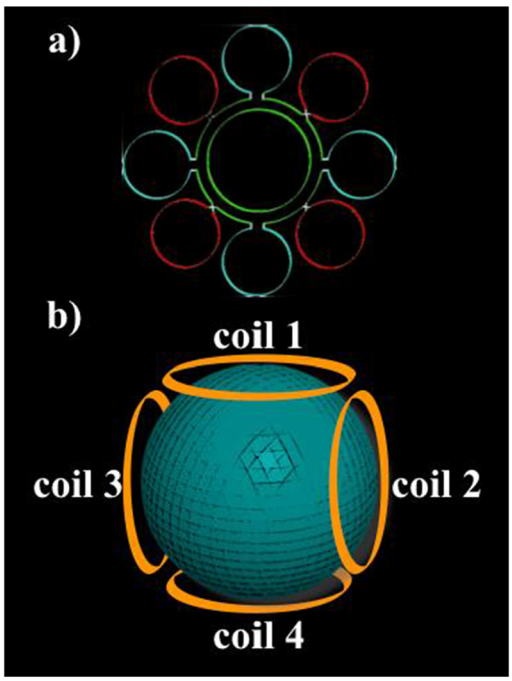

Figure 1. a) Illustration of an 8-petal PERES coil and, b) Setup for the theoretical computations of CNRPERES.

This computation was done for each and every coil in the same fashion. *CNR* calculations were calculated for those resonant frequencies of proton corresponding to current MR imagers already available to run imaging experiments of humans. We took TE values

varying from 1 to 10 ms at 10 ms step. Similarly, $CNR_{\text{cir-SENSE}}$ calculations were done for comparison purposes.

Results: We derived an analytical expression to theoretically calculate the *CNR* of the PERES coil array for SENSE MRI at UHF MRI. With this general mathematical formula (eq. (1)), we calculated the CNR_{PERES} for both coil arrays. Fig. 2 shows a comparison of the roll-offs for the two coil arrays at 500 MHz and TE = 50 ms.

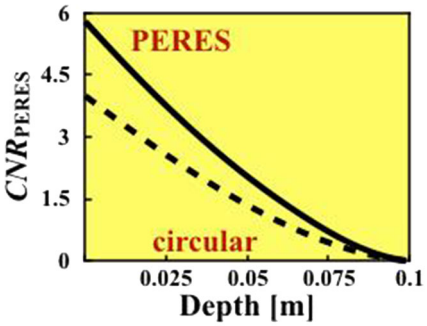

Figure 2. Comparison plot of theoretical roll-offs for the circular and PERES coil arrays.

An important theoretical improvement of *CNR* can be appreciate for the PERES coil array over the circular array one. A greater improvement can be appreciated for points in the vicinity of the coil plane, and as for points away, *CNR* rapidly decreases similarly as a standard surface RF coil does. We also computed roll-offs varying the TE as shown in Fig. 3. There is hardly an important variation for the theoretical CNR_{PERES}, This is particularly important because it is possible to use any TE value in this time interval.

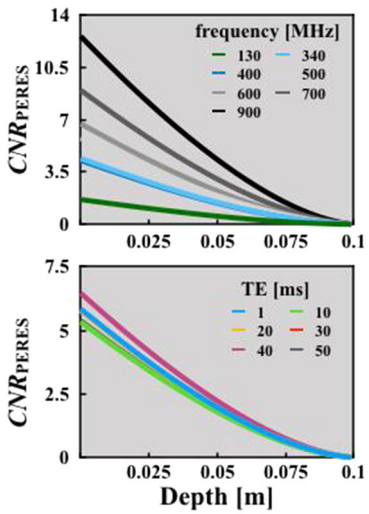

Figure 3. CNRPERES profiles for different resonant frequencies (upper) and and TE values (lower).

Discussion/Conclusion: The PERES coil array outperformed the conventional coil array for points in the coil plane vicinity. From these theoretical results, the PERES coil array is a good candidate for neural current UHF MRI experiments involving brain activation near the coil plane.

References

1. Ladd, ME. *et. al*. Prog Nucl Magn Reson Spectrosc. 2018:109:1.
2. Konn, D. *et. al.* MRM 2003:50:40.
3. Solis, S. *et. al.* Ann Meet ESMRMB. 2017:Abstract #615, S576.
4. Mansfield, P. J Phys D Appl Phys. 1988:21:1643.
5. Rodriguez, A. *et. al*. MRI 2005:10:1027.

L02.10

Development of the First Dual-Function Head & Neck Hyperthermia Applicator: The MRcollar

G. G. Bellizzi[1], K. Sumser[1], R. Forner[2], T. Drizdal[3], G. C. van Rhoon[1], J. A. Hernandez Tamames[4], D. T. Yeo[5], M. M. Paulides[6]
[1]*Erasmus MC Cancer Institute, Department of Radiation Oncology, Rotterdam, NETHERLANDS,* [2]*UMC Utrecht, Dept. Radiology, Utrecht, NETHERLANDS,* [3]*Czech Technical University in Prague, Department of Biomedical Technology, Prague, CZECH REPUBLIC,* [4]*Erasmus MC Cancer Institute, Department of Radiology, Rotterdam, NETHERLANDS,* [5]*GE Global Research, Niskayuna (NY), UNITED STATES,* [6]*Eindhoven University of Technology, Department of Electrical Engineering, Eindhoven, NETHERLANDS*

Purpose/Introduction: Accurate temperature monitoring in hyperthermia (HT) is needed in head and neck (H&N) because of the unpredictable and heterogeneous thermoregulation [1]. MR thermometry (MRT) has shown potentials for non-invasive 3D temperature monitoring as replacement for currently used interstitial thermometry probes which is invasive and has a sparse spatial sampling. Volunteers pilot studies showed that high SNR are required for precise MRT. This is possible by using the MR system for heating (with as important limitation a suboptimum heating distribution) or by a dedicated close-body Rx coil array inserted inside the HT device. Such integration enables an independent choice of the HT and MR operating frequencies and achieve both target conformal heating and temperature monitoring by widely available MR scanners. Along this line we developed the MRcollar: an integrated H&N applicator that combines MR and radiofrequency (RF) HT systems for heating and imaging (Fig. 1). In this communication, we present the MRcollar development and the feasibility of inserting a tailored Rx coil array.

Subjects and Methods: The MRcollar is a 12-element applicator enabling optimal contact with the surface of H&N patients. A novel planar Yagi-Uda antenna design [2] was used for maximum applicator MR transparency: by alignment of metallic surfaces to the B0 and B1 + fields, a minimal footprint in the transverse plane was achieved and an intrinsic geometrical decoupling with the integrated Rx coil elements. Antennas are encased in dielectric parabolic reflectors to enabling minimum cross-talk. Applicator performance was assessed with respect to antenna matching characteristics, heating and MR compatibility using phantom experiments. A first Rx coil prototype was been designed. To accommodate placement and minimize systems interaction (Fig. 1), we designed a specific one-sided tuning circuit, a balanced matching circuit and one active detuning diode.

Results: Experiments validating the MRcollar design showed a good antenna match ($S_{11} < -15$ dB) and low cross-coupling ($S_{ij} < -30$ dB). Satisfactory heating capability was demonstrated (+ 7 °C in 3 min, 180 W). Minimal effect of the MRcollar system on MR image quality was observed. Experiments showed that the water-bolus, used for skin cooling and matching purposes, affects image quality more than metallic parts of the device, but B1 + field homogeneity in the ROI was shown to be unaffected. Bench testes proved a good coupling of the prototyped Rx coil with the load ($Q_{\text{loaded}}/Q_{\text{unloaded}} = 3.3$), good tuning ($S_{11} \simeq -14$ dB) and detuning features ($\Delta S21 \simeq -25$ dB compared between diode detuning activated vs. un-activated on a single receive loop).

Discussion/Conclusion: The MRcollars was shown to provide good heating capabilities and MR compatibility. Efforts are devoted to the experimental validation of the integrated MR Rx coil array.

(left) MRcollar system, (right) MRcollar system inside 1.5T MRI scanner bore.

References:
[1] Verhaart, Int J Hyp, 2015.
[2] Paulides, Phys Med Biol, 2017.

L02.11

'Model of Categories/Areas for Items' introduced for a unifying assignment of MR safety and compatibility test methods

G. Schaefers, H. Engels
MRI-STaR - Magnetic Resonance Institute for Safety, Technology and Research GmbH/MR:comp GmbH, Gelsenkirchen, GERMANY

Purpose/Introduction: A schematic 'Model of Categories/Areas for Items' used inside the MR environment (outside and inside the RF shielded magnet room) is suggested for assigning MR testing methods more precisely based on MR interactions potentionally taking place when deciding on MR testing of items/devices.

Subjects and Methods: Items/devices should be classified into categories/areas of items/devices dependent on their magnetic and electromagnetic interaction. Local borderlines in FIG. 1 of those areas for $B_{x,y,z}$, B_0 and dB/dt as well as RF (B_1/E) electromagnetic fields are of course individual per MR system. The borderlines are defined based on significance of exposure level and as used in this example they need to be dimensioned realistically for real MR environments. On each side of those borderlines, on the one hand side we find a 'negligible' exposure level and interaction, whereas on the other hand side we find a 'significant' exposure level and interaction related to the three field sources.

Example: RF and dB/dt borderlines are close to each (RF or gradient) coil, respectively, due to a high decay of those fields. A high exposure level exists towards the coils vs. a low exposure level towards the rest of the area of the shielded room (three dimensional fringe fields) in which RF and dB/dt interactions such as induction of voltage will theoretically take place, but are however 'negligible' in absolute dimension dependent on the relevance for the individual item/device. On the other direction into the (RF or gradient) coil, however, we detect a high RF or dB/dt interaction, if an item/device is placed inside the coil

(a) outside the patient with skin contact or,
(b) introduced as instrument partially into a patient or,
(c) be fully implanted inside a patient.

The further consideration for this item/device is the property of interacting with magnetic and electromagnetic fields; also interacting with static magnetic fields and it's provided spatial gradient fields, $dB_{x,y,z}/d_{x,y,z}$. Especially for the electromagnetic field, the question is: 'Is this item an electrical conductor or is it an electrical insulator'. Both properties do support interaction within the electromagnetic field. The relevant impact is necessary to be described in dimension of its dependency of frequency.

Results: The results are show in the following figure and table:

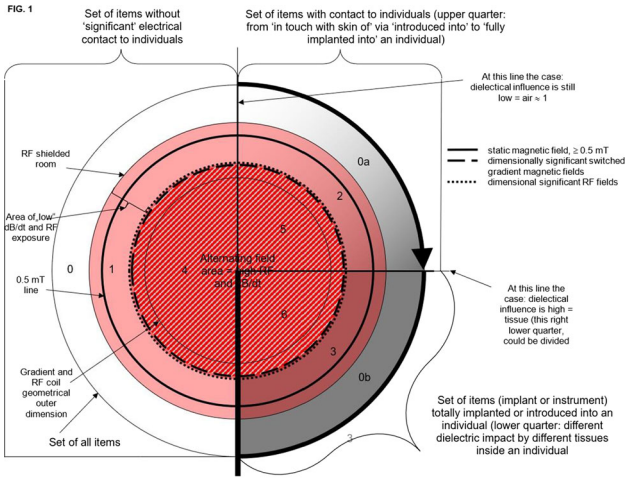

Model of Categorisation of Items/Devices inside the MR Environment

Table modified and extended from ASTM F2503/ IEC 62570

				„Categories/Areas No.1-6"					
			Device examples for the 6 initial categories suggested:	Accessories like a shelf, tray, display, fire extinguisher, etc.	Wheel chair, trolley, cannula (patient contact)	Active implant or device outside the bore, inside the MR room	Active instrument or device inside the bore (no galvanic contact)	ECG monitoring cable with electrode, invasive measurement catheter	Non-active and active implants
Issues	General hazards	Testing and/or analysis requirement	Test method	1	2	3	4	5	6
MR safety	Force	Static magnetic field-induced displacement force	ASTM F2052	x	x	x	x	x	x
	Torque	Static magnetic field-induced torque	ASTM F2213	(x)	x	x	x	x	x
	Heat	RF field-induced heating	ASTM F2182, ISO/TS 10974	-	(x)	x	(x)	x	x
		Gradient field-induced heating	ISO/TS 10974	-	(x)	x	x	x	x
	Vibration	Gradient field-induced vibration	ISO/TS 10974	-	(x)	x	x	x	x
	Extrinsic electric potential	Gradient field-induced (lead) voltage	ISO/TS 10974	-	(x)	x	x	x	x
	Rectification	RF field-induced rectified (lead) voltage	ISO/TS 10974	-	(x)	(x)	(x)	(x)	(x)
	Malfunction	Static magnetic field-induced malfunction	ISO/TS 10974	x	x	x	x	x	x
		H^+ field-induced device malfunction	ISO/TS 10974	(x)	(x)	x	x	x	x
		Gradient field-induced malfunction	ISO/TS 10974	-	(x)	x	x	x	x
MR compatibility	Misinterpretation of image (Image quality issues)	Susceptibility and RF artifacts, size of distortion	ASTM F2119	-	-	(x)	x	x	x
		Signal-to-noise (due to RF emission)	Individual MR system manufacturer test method	x	x	x	x	x	x
		B_0-field distortion (due to magnetic materials)	Individual MR system manufacturer test method	(x)	(x)	(x)	x	x	x
		Eddy currents (due to conductive materials)	Individual MR system manufacturer test method	-	-	-	x	x	x
		MR signal silence (due to protons in plastics)	Individual MR system manufacturer test method	-	-	-	x	x	x
		....further MR image quality interactions to be clarified with MR system manufacturers	Individual MR system manufacturer test methods	?	?	?	?	?	?

TAB. 1: MR interactions and MR test methods that have been identified by different committees. The model is summarized in this table and is assigned to the MR environmental location (category/area) of an item/device and the magnetically and electromagnetically interaction of an item/device inside the MR environment. x = tests mandatory, (x) = tests could be relevant dependent on significance of MR interaction and use/intention of the item/device, - = no test necessary due to materials or limited area/intention of use.

„Categories/Areas No.1-6"					
Accessories like a shelf, tray, display, fire extinguisher, etc.	Wheel chair, trolley, cannula (patient contact)	Active implant or device outside the bore, inside the MR room	Active instrument or device inside the bore (no galvanic contact)	ECG monitoring cable with electrode, invasive measurement catheter	Non-active and active implants
1	2	3	4	5	6

Item/device examples for example categories/areas 1-6 inside the MR environment

Discussion/Conclusion: A schematic called 'Model of Categories/Areas for Items' has been introduced for dividing the MR environment into different areas being helpful categories for assignment of methods for MR safety and compatibility testing of items (accessories, instruments, implants, devices, etc.) dependent on their location of use and intended use inside the MR environment.

References: ASTM F2503, IEC 62570.

Acknowledgement to Hans Engels and various colleagues from ASTM/ISO/IEC standardisation committes for reviewing and commenting

L02.12

Construction and Characterization of an Automatized Measurement System for Low Friction Surface Method according to ASTM F2213-17

D. Malik[1], **J. Kreutner**[1], W. Görtz[1], G. Schaefers[2]
[1]MR COMP GmbH, Gelsenkirchen, GERMANY, [2]MRI-STaR - Magnetic Resonance Research Institute for Safety, Technology and Research GmbH, Gelsenkirchen, GERMANY

Purpose/Introduction: The recent version of ASTM F2213-17 for evaluation of magnetically induced torque on medical implants proposes different methods with increasing precision. One method is based on assessing an upper limit of torque by comparing it to a friction force. Our goal was to develop an automated setup for evaluation of low friction force and characterize the precision of this method.

Subjects and Methods: A motorized mechanism was developed to lift a low friction surface at constant speed. The low friction surface was placed in a frame, such that the surface itself can be removed and safely be used in the MRI scanner or exchanged by other surfaces. The movement of the test object was observed using a light barrier, which immediately stopped the lifting of the surface when movement was detected. Stopping angle θ was measured using a digital goniometer. The coefficient of friction μ is calculated as $\mu = \tan\theta$.

A reference object was used to evaluate the suitability of different materials (Teflon (PTFE), acryl (PMMA), POM and glass) as low friction surface and measurements with each surface were repeated 100 times.Furthermore, the impact on device position on μ was evaluated by intentionally varying the position on the surface between each run.

Finally the surface of PTFE and POM was manually modified to evaluate the impact of different wear levels (new, slight/strong scratches, polished).

Results:

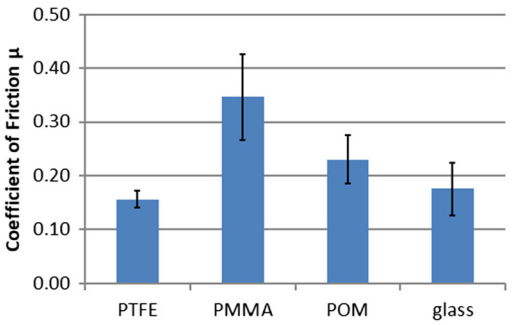

FIG. 1: Average measured coefficient of friction for different materials. Error bars indicate standard deviation for each surface. A larger variation for POM can be seen, while PTFE provides reproducible results.

Results for different surfaces using the reference object are shown in Fig. 1. μ varies between surfaces from 0.15 (PTFE) to 0.35 (PMMA). While PTFE shows only small variation of μ, much larger variations for other surfaces are observed as indicated by larger error bars representing the standard deviation.

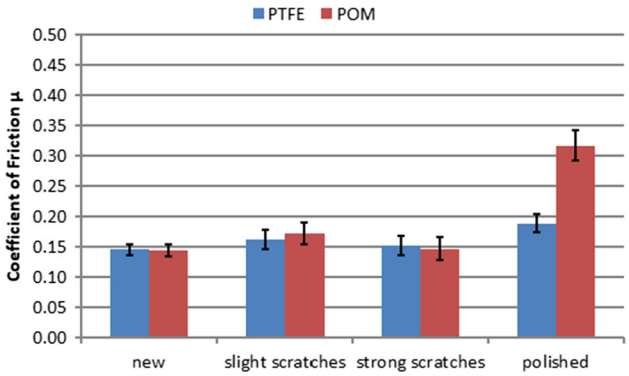

FIG. 2: Impact of wear levels on two surface materials. A polished surface leads to an increased coefficient of friction.

Results for different wear levels are summarized in Fig. 2. In general an increase of μ can be observed for polished surfaces, while scratches showed only little impact.

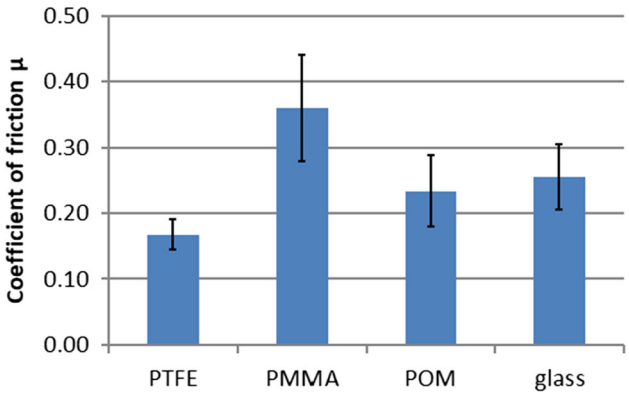

FIG. 3: Average coefficient of friction for different surface materials, while intentionally varying the test object position. Compared to FIG. 1 an increased coefficient of friction is observed for glass.

Data from variable position of the device on the surface is shown in Fig. 3 with an almost identical variation in results as in Fig. 1. Only for glass a slight increase from 0.18 to 0.26 was observed.

Discussion/Conclusion: Our results show that repeatability of the method strongly depends on the materials involved. In this case only PTFE showed highly reproducible results, while PMMA (acryl, as suggested in F2213) provided the highest variation. The impact on device position was negligible except for glass, indicating that positioning of the test object is of less importance for repeatability, while the surface condition has significant influence on the outcome. However, the observed behavior depends also on the material and shape of the test object and effects might differ for other objects. Therefore, careful selection of low friction materials is required for this method. Precision and repeatability depend on many parameters and an additional safety factor should be considered for labelling.

References: [1] ASTM F2213-17.

L02.13

Experimental approach to evaluate currents on an AIMD-Lead using Rogowski coils

V. Hammersen[1], S. Scholz[2], W. Goertz[2], U. Stoeber[3], J. Kreutner[1], G. Schaefer[2]

[1]*MRI-STaR GmbH, Gelsenkirchen, GERMANY,* [2]*MR:comp GmbH, Gelsenkirchen, GERMANY,* [3]*Fachhochschule Muenster, Physikalische Technik, Burgsteinfurt, GERMANY*

Purpose/Introduction: Active implantable medical devices (AIMDs) with at least one electrode lead can pick up RF-energy during an MRI scan. This energy is transferred as current or voltage to the AIMD port and cause malfunction of the device, which can be tested according to ISO/TS10974 [1]. To quantify these currents, modified AIMDs are used with current or voltage sensors attached to their entry points. This alteration affects the measurement integrity. To overcome this problem we evaluated the use of Rogowski coils [2] for a contactless current determination on AIMD leads.

Subjects and Methods: The characteristic Rogowski coil design was obtained by manufacturing a hook shaped holder with a slightly larger inner diameter than the electrode lead and evenly winding a wire in a helical manner across this hook (8 windings), before returning it through the helix centre (Fig. 1). In the next step a calibration unit was designed by attaching a resistance of 50Ω to the inner conductor of a coaxial cable and connecting its opposite side multiple times with the outer conductor (see Fig. 2). This setup was used to calculate the current, respectively the calibration constant, with the monitored net power input and the defined resistance. Prior to the actual measurements the calibration unit was exchanged with the electrode lead.

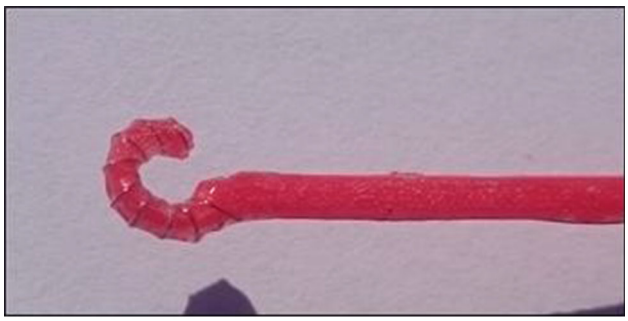

Rogowski coil

All measurements were performed within a NaCl-Solution (electrical conductivity 0.47S/m, relative electric permittivity of 78) to simulate the electric properties of muscle tissue [1]. An RF-generator (AFG3152C, Tektronix) provided the power input (– 22dBm to + 23dBm) at 64 MHz. Net input power was determined with a bidirectional coupler (ZFBDC20-62HP + , Mini-Circuits). The voltage output by the Rogowski probe and the coupler were measured by a digital storage oscilloscope (DSO9064A, Keysight).

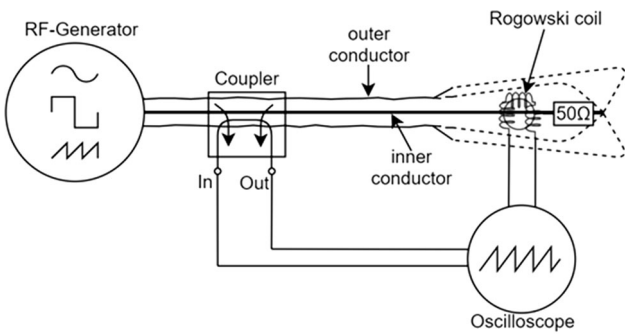

Calibration circuit

Results: The calibration (Fig. 3) shows excellent linearity between current in the calibration unit and the voltage measured by the Rogowski coil. A calibration constant representing the correlation between those two variables with 0.114 mA/mVpp was determined with an R^2 of 0.9998. Distortions are insignificant and can be neglected. The same effects can be observed while performing the actual measurement (Fig. 3). The currents are highly linked to the input power and can be evaluated in a broad range reaching from 22µA up to 2.58 mA. Noticeable distortions are limited to very low input power levels. Care should be taken regarding the alignment of the sensor relative to the lead trajectory as even small angular deviations can distort the measurement result.

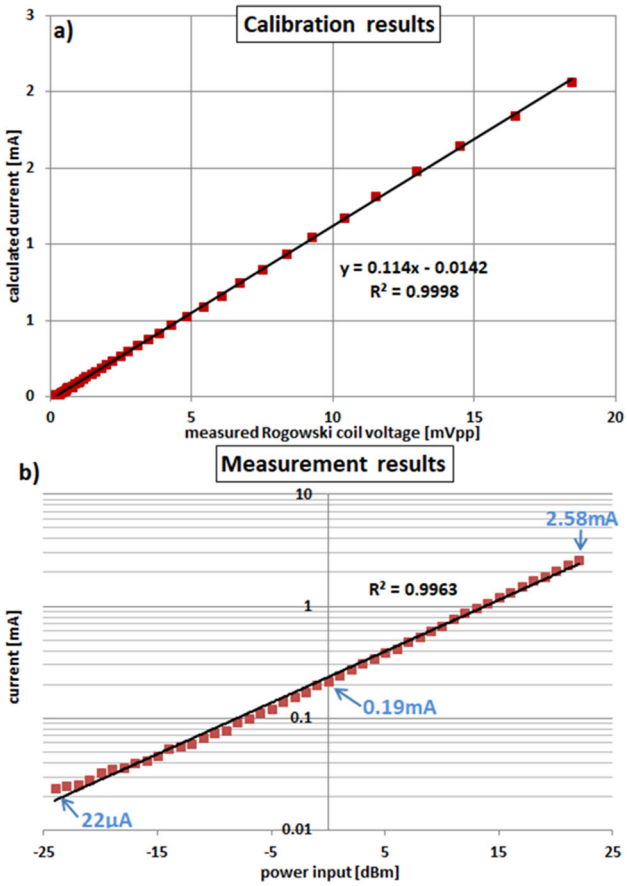

a) Calibration results, currents were calculated with monitored power input in the calibration unit and the resistance of 50Ω b) Measurement results, currents were calculated with measured voltage of the Rogowski coil and the calibration constant

Discussion/Conclusion: Our results indicate that Rogowski coils can be considered as a suitable approach for measuring RF-induced currents. The high sensitivity enables the detection of very small currents in the AIMD leads.

References:

1) ISO/TS 10974:2018.
2) Using Rogowski coils for transient current measurements. D.Ward, J.Exon. Engineering Science and Education Journal Vol:2(3), 1993.

L02.14

Effect of the BSD-2000 3D/MR hyperthermia applicator on MR Image Quality

K. Sumser[1], G. Bellizzi[1], J. Hernandez Tamames[1], G. van Rhoon[1], M. Paulides[2], S. Curto[1]
[1]*Erasmus University Medical Center, Rotterdam, NETHERLANDS,* [2]*Eindhoven University of Technology, Eindhoven, NETHERLANDS*

Purpose/Introduction: Medical devices operating within the MR environment are thoroughly tested and quantified for MR safety. This forms the basis of MR compatibility. While the effect on imaging doesn't affect the safety aspect, it can influence the diagnostic capabilities, therefore it also requires quantitative evaluation. Hyperthermia treatment exploits MR capabilities in non-invasive 3D temperature imaging by inserting MR compatible devices within the bore. In this study, we quantitatively evaluated the impact of the Pyrexar BSD-2000 3D/MR compatible hyperthermia applicator (referred as Sigma Eye) and its 100 MHz heating signal on MR imaging by B1 + (flip angle (FA) maps) and Signal-to-Noise Ratio (SNR) measurements.

Subjects and Methods: The Sigma Eye consists of 12 dipole antenna pairs which are equally distributed over three rings. A dedicated water bolus provides coupling between antennas and the human body, and also cools the patient skin during heating. To evaluate the impact on image quality, a cylindrical phantom filled with perfax has been imaged in three different setups: (1) a scan of the phantom only (indicated as reference scenario), (2) a scan with the applicator around the phantom in treatment position (heating off), (3) a scan when the applicator is turned on with 600 W input power (heating on). FA maps were evaluated using Bloch-Siegert sequence and SNR was evaluated on clinically used MR thermometry sequence, i.e. double echo gradient echo. 37 ROIs (each 45 pixel^2) for every slice (5 in total) were chosen inside the phantom (Fig. 1b) to evaluate FA variation and the SNR inside the phantom.

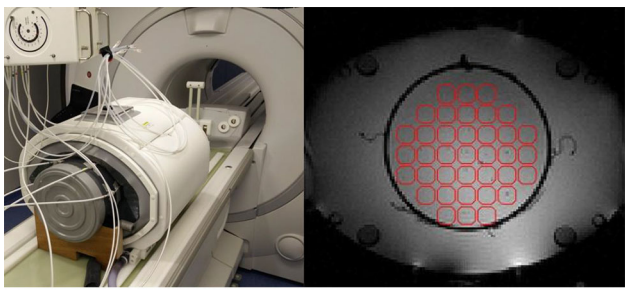

Figure 1. Experimental Setup and Post Processing ROIs (a) Sigma Eye – MR compatible hyperthermia applicator with cylindrical phantom placed inside (b) Example Magnitude Image and ROIs used for SNR and FA homogeneity analysis.

Results: The reference FA maps showed a homogeneous distribution intra-slice (std: 1.8°) as well as along the phantom (std: 1.4°). The measured mean FA was slightly lower than the prescribed value (27.6° vs 30°). A small impact of the applicator (both on and off) was seen on the FA distributions intra-slice (std: 2.4°). However, the inter-slice variation became higher (max ΔFA = 8.5°). Furthermore, the measured mean FA (21.6°) was 28% lower than the prescribed value. Adding the RF-heating signal caused a negligible reduction on FA maps.

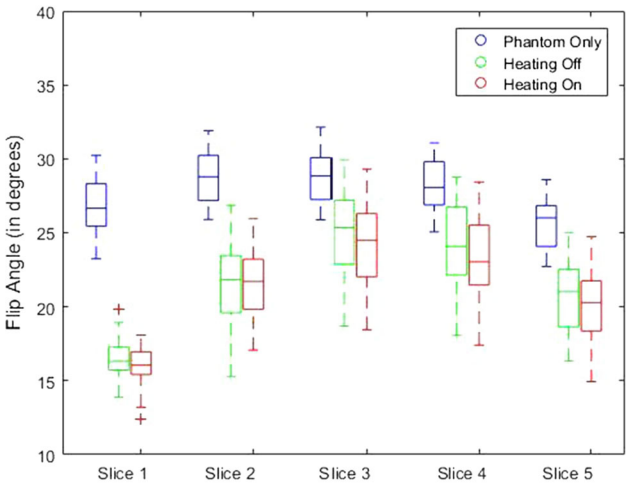

Figure 2. Change in Flip angle for three different experimental settings; prescribed FA is 30°.

Results shown homogeneous values of the reference SNR intra-slice (0.5 dB) and inter-slice (1.5 dB) with a mean SNR values of 48 dB. This value dropped by 20% in measurement configuration 2. Also, an increase in intra-slice (1.5 dB) and inter-slice (2.2 dB) variation was observed. Note, there are no significant differences to mention between the echo times or when the RF-heating signal was on.

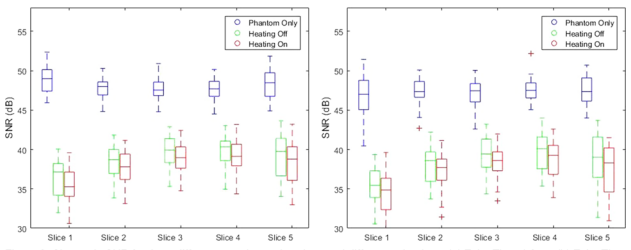

Figure 3. Change in SNR for three different experimental settings and different echo times (a) Echo Time 4.6 ms (b) Echo Time 18.4 ms.

Discussion/Conclusion: The FA efficiency is greatly affected when the applicator is included. This reduction in efficiency reduces the signal intensity. On the other hand, 100 MHz heating signal has a low impact on both FA and SNR maps. In the light of these quantitative measurements, modifications in sequence parameters should be made to achieve required SNR for the aimed applications.

References: -

I08 Teaching Session

16:10–17:40 *Room 1 - Willem Burger Zaal*

Clinical Impacts and Needs of Machine Learning

I08.01
Towards developing clinically applicable learning-based methods for disease detection

E. Konukoglu
ETH, Information Technology and Electrical Engineering, Zurich, SWITZERLAND

Learning Objectives: Attendees will be able to

1. Describe the underlying concepts in machine learning based approaches for analyzing images.
2. Draw a time line of the developments in machine learning based approaches.
3. Explain the current state of approaches for detecting diseases, both supervised and unsupervised.
4. Describe the remaining challenges that needs to be overcome to create clinically applicable and reliable technologies.

Body: Machine learning holds great potential to increase efficiency, repeatability and accuracy of using medical imaging in clinical practice by taking over manually demanding tasks, such as taking measurements, and aiding in detecting diseases. Despite substantial progress, a number of technical challenges remain for realizing the potential. In this talk, I will first provide a very basic description of machine learning-based approach towards disease detection without assuming background on the topic. Then I will describe some recent algorithmic advances, focusing on lesion detection and subject-specific mapping of disease effects. The last part of the talk will focus on the remaining major technical challenges that needs collaborative effort between engineering, clinical sciences and practice to overcome.
References: No previous knowledge of machine learning will be assumed.
Familiarity with regression based models would be useful.

I08.02
Time after time. Application of machine learning techniques for primary and adaptive radiotherapy treatment planning

R. Jena
University of Cambridge, Department of Oncology, Cambridge, UNITED KINGDOM

Learning Objectives: Understanding role of image segmentation in radiation therapyUnderstanding of 3 distinct machine learning architectures (Random Forests, CNNs and GANs)
Body: Segmentation of tumour targets and normal tissue structures is a vital initial step in the workflow for precision radiation therapy. It is time consuming, and errors in this early step of treatment preparation propagate all the way through the radiotherapy pathway. I present two distinct areas of work. The first is the development of two machine learning techniques (random forests and autofocus convolutional neural networks) for segmentation of tumour and normal tissues for primary and adaptive treatment planning, and the second is the use of a novel machine learning algorithm (generative adversarial network) to generate synthetic CT images from MRI scans, to facilitate the recalculation of dose in adaptive radiotherapy treatment planning.
References:
Autosegmentation of prostate anatomy for radiation treatment planning using deep decision forests of radiomic features.
Macomber MW, Phillips M, Tarapov I, **Jena** R, Nori A, Carter D, Folgoc LL, **Criminisi** A, Nyflot MJ.Phys Med Biol. 2018 Nov 22;63(23):235002.

I08.03
Radiomics for lesion characterisation

L. Fournier
Hopital Europeen Georges Pompidou - Université de Paris, Radiology, Paris, FRANCE

Learning Objectives:

- To learn the definition of radiomics and radiomics tools available.
- To understand what information radiomics can provide on lesion characterisation.
- To understand how the radiomics process may lead to discovery of new imaging biomarkers.

Body: Radiomics is a new 'data-driven' approach for extracting large sets of complex descriptors from routine (or not) clinical images. Advanced methods of image processing are applied to images to extract a large number of descriptors, such as texture analysis from histograms, co-occurrence matrices, fractal analysis, etc.… This large set of data can be analysed using bio-informatics and bio-statistics methods to mine images for information on underlying biology, such as gene expression profiles (called radiogenomics), molecular profiles, expression of receptors, microenvironment such as immune cell infiltration or angiogenesis. Texture parameters more specifically are considered to reflect tumour heterogeneity.
A large number of studies has shown correlations between single or combined features ('radiomics 'signature') in diverse settings, mainly oncology, to differentiate bening vs malignant lesions, to predict biological factors or prognosis.
The discovery of possibly predictive or prognostic radiomics signature should however be validated in an independent population to demonstrate its performance in clinical settings, and its potential to impact clinical management.
References:
1. Sanduleanu S, Woodruff HC, de Jong EEC, van Timmeren JE, Jochems A, Dubois L, Lambin P. Tracking tumor biology with radiomics: A systematic review utilizing a radiomics quality score. Radiother Oncol. 2018 Jun;127(3):349-360.
2. Grossmann P, Stringfield O, El-Hachem N, Bui MM, Rios Velazquez E, Parmar C, Leijenaar RT, Haibe-Kains B, Lambin P, Gillies RJ, Aerts HJ. Defining the biological basis of radiomic phenotypes in lung cancer. Elife. 2017 Jul 21;6.
3. Larue RT, Defraene G, De Ruysscher D, Lambin P, van Elmpt W. Quantitative radiomics studies for tissue characterization: a review of technology and methodological procedures. Br J Radiol. 2017 Feb;90(1070):20160665.
4. Yip SS, Aerts HJ. Applications and limitations of radiomics. Phys Med Biol. 2016 Jul 7;61(13):R150-66.

S07 Scientific Session

16:10–17:40 Room 2 - Van Weelde Zaal

Acquisition & Reconstruction

S07.02
Radial Simultaneous Multi Slice Imaging for Passive Marker Needle Guide Tracking

A. Reichert, A. J. Krafft, M. Bock
Dept.of Radiology, Medical Physics, Medical Center University of Freiburg, Faculty of Medicine, University of Freiburg, Freiburg, GERMANY

Purpose/Introduction: MR-guided percutaneous interventions benefit from robust and fast localization of MR-safe passive marker needle guides via a phase-only cross correlation (POCC) algorithm[1-3]. With the POCC method 2 parallel tracking images are acquired orthogonal to a cylindrical marker, and the position information in the tracking images is used to align a targeting image with the instrument trajectory. Thus, during targeting the images automatically follow the marker movement.
The detection of the marker, i.e. the acquisition of the tracking images, should be as short as possible[4] to allow real-time instrument tracking without latencies. Here, we propose radially undersampled simultaneous multi-slice (SMS) imaging[5] in combination with POCC detection that considers the projection-dependent PSF for marker tracking[6].
Subjects and Methods: Radial SMS acquisition of the marker is performed with a phase-cycled dualband pulse[4,5] where the RF phase of the second slice is alternated between projections (Fig. 1). Radial k-space reconstruction of the original data shows the first slice and suppresses the second parallel slice due destructive interference at the k-space center. Recovery of the second slice is achieved by multiplication of the reversed phase pattern in k-space before reconstruction, i.e. multiplication of the phase $e^{i\pi} = -1$ to every other radial spoke.

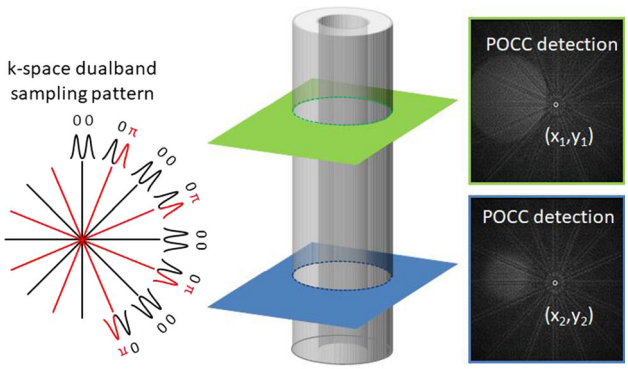

Fig. 1: Even spokes (black) have same phase for both slices, whereas odd spokes (red) have an opposite sign. Reconstruction leads to the upper slice of the marker (green). Multiplication of odd spokes with e^(iπ) reconstructs the lower slices (blue).

POCC tracking accuracy in the radially undersampled SMS marker images was assessed in a phantom experiment in a 1.5T whole body MR system (MAGNETOM Symphony, Siemens Healthcare) using the body array and the spine coil for reception. Images were collected perpendicular to the symmetry axis of a commercially available passive marker (Invivo GmbH, Schwerin) with different numbers of evenly spaced projections (N_p = 64, 32, 16, 8, 4, 2) and for each projection number, 200 images were obtained (TR/TE = 5.64/2.20 ms, $\alpha = 30°$, FOV = 300 × 300 mm, matrix = 256 × 256). Additionally, single band excitations were performed for comparison (Fig. 2).

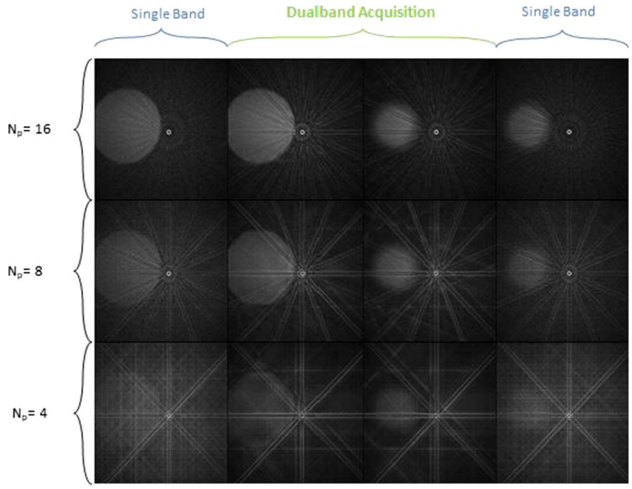

Fig. 2: The first and fourth column represents both slices acquired separately with decreasing radial projections. The second and third columns show both slices acquired simultaneously and are separated during reconstruction.

Reconstruction and POCC detection of the marker position was performed online with subpixel precision. The root-mean-square error RMS = $\sqrt{(s_x^2 + s_y^2)}$ with standard deviations s_x and s_y was calculated over each set of 200 images (Fig. 3).

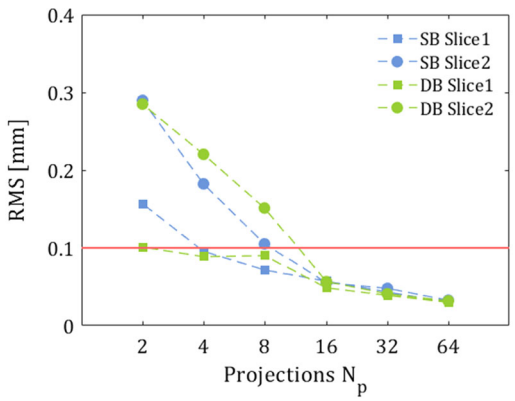

Fig. 3: Evaluation of the accuracy in a phantom experiment. The root mean square increases with decreasing radial projections. RMS values below 0.1 (indicated by red line) indicate a reasonable tracking accuracy.

Results: Using radial SMS imaging for POCC marker detection, the marker was detected in all images for $N_p \geq 16$ with comparable detection accuracy as in sequentially acquired images.
Discussion/Conclusion: Our results demonstrate that it is possible to implement simultaneously acquired radial projections for marker detection while maintaining a reasonable POCC targeting accuracy. This technique allows for a twofold shorter acquisition time compared to conventional radial acquisitions of the marker.

References:

[1]de Oliveira A, et al. MRM 2008;59:1043–50.
[2]Krafft AJ,et al. PhysMed 2013;29:607–14.
[3]Zamecnik P, et al. Radiology 2014;273:879–86.
[4]Reichert A, et al. MAGMA 2018;31:781–8.
[5]Yutzy SR, et al. MRM 2011;65:1630–7.
[6]Reichert A, et al. ISMRM, 2018.

S07.03
Silent Multi-Contrast Neuroimaging

E. Ljungberg[1], T. Wood[1], A. B. Solana[2], S. Williams[1], F. Wiesinger[2], G. Barker[1]
[1]King's College London, Neuroimaging, London, UNITED KINGDOM, [2]General Electric Healthcare, ASL Europe, Munich, GERMANY

Purpose/Introduction: Acoustic noise is a significant issue for MR sequences that use cartesian acquisition schemes. The Rotating Ultra-Fast Imaging Sequence (RUFIS) is a 3D-radial sequence which makes almost no acoustic noise[1,2]. It is equivalent to a rapid gradient-echo sequence with a modified gradient scheme, with either proton density or minimal T_1-weighting. To allow clinical adoption of RUFIS, a full range of contrasts must be available. Here we show that appropriate magnetisation preparation modules can easily produce T_1-, T_2- and MT-weighted RUFIS images.

Subjects and Methods: Similar to contrast-prepared FLASH[3], preparation modules were added between RUFIS segments (figure 1). The scheme was adjusted for each contrast, as shown in table 1. All data was acquired on a 3T scanner (GE MR 750) with either a 12- (GE) or 32-channel (Nova Medical) head coil.

T_1-weighting was achieved with an MP2-RAGE structure (inversion pulse and two inversion times at 700/2300 ms). This produces two images that can be combined to remove receive coil bias and calculate a T_1-map[4].

T_2-weighting was encoded in the longitudinal magnetisation with an mBIR-4 T_2-preparation pulse before the RUFIS segment[5]. Multiple echo times were obtained by repeating the T_2-preparation and acquiring the same segment before a relaxation delay to allow for signal recovery.

MT-weighting was produced with ten 1 ms Hanning pulses, separated by a 1 ms gap, followed by the RUFIS segment, with an initial 1 s of dummy segments to ensure steady-state saturation. The saturation frequencies were alternated to create an inhomogeneous-MT mode[6].

	T1	T2	MT
Spokes per segment	384	128	64
Flip-angle [deg]	2 & 3	2	2
TR [ms]	2	2.4	1.16
Receive bandwidth [kHz]	20	15.6	31.25
Voxel size [mm3]	0.9x0.9x0.9	1.5x1.5x1.5	2x2x2
Recovery time [ms]	1330	1500	N/A
Scan time [min]	10	11	2

Acquisition parameters

Results: Excellent contrast with image quality comparable to conventional cartesian acquisition schemes was observed for all contrasts (figure 2). In all cases, the sequence was just audible inside the scanner, as an example the MT-prepared sequence measured 72 dB, compared to 109 dB for the cartesian equivalent.

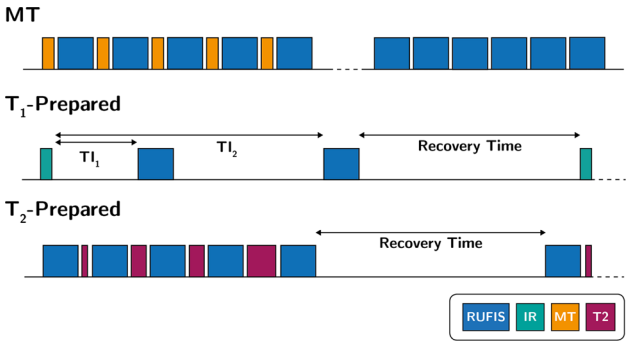

Figure 1: Overview of the pulse sequence designs for contrast prepared RUFIS imaging.

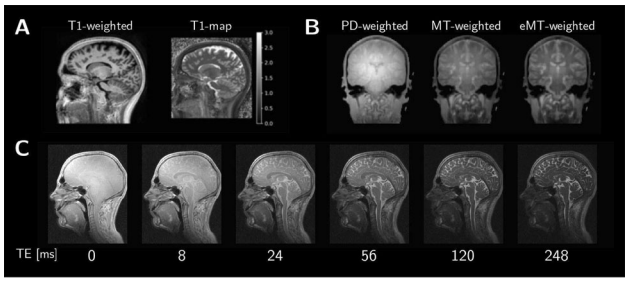

Figure 2: (A) T1-weighted and T1-map from MP2RAGE acquisition, (B) PD, MT and enhanced MT (eMT) from MT preparation, and (C) T2-weighted images from T2-preparation.

Discussion/Conclusion: We have shown that preparation modules can be used with RUFIS to produce high quality, full brain images with standard clinical contrasts (T_1, T_2, MT) and minimal acoustic noise. Diffusion weighting was not demonstrated but could be included by adding additional gradients to the T_2-preparation module[5].

A fully silent clinical protocol would be transformative for MR, as hearing protection would no longer be required in the scanner, leading to easier communication and increased patient comfort.

References:

1. Madio DP, Lowe IJ. Magn Reson Med. 1995;34(4):525–9.
2. Costagli M., et al. Eur Radiol. 2016;26(6):1879–88.
3. Haase A., Magn Reson Med. 1990;13(1):77–89.
4. O'Brien KR, et al., PLoS One. 2014;9(6): 1-7.
5. Cao P, et al., Magn Reson Med. 2018;79(1):62–70.
6. Mchinda S, et al., Magn Reson Med. 2018;79(5):2607–19.

S07.04
Golden angle spiral arterial spin labeling

M. van der Plas[1], P. Börnert[2], T. van Osch[1]
[1]Leiden University Medical Center, C.J. Gorter Center for High Field MRI, Department of Radiology, Leiden, NETHERLANDS, [2]Philips GmbH Innovative Technologies, Research Laboratories Hamburg, Hamburg, GERMANY

Purpose/Introduction: Previously, golden angle radial sampling was used in combination with arterial spin labeling (ASL) to reconstruct angiographic and perfusion images from the same dataset[1,2]. A non-cartesian golden angle based sampling scheme in k-space allows for an extremely flexible approach to obtain multiple reconstructions from a single dataset, since k-space is uniformly sampled for any arbitrary temporal window[3]. However, radial trajectories require a large amount of spokes to sufficiently cover k-space and therefore a

large number of excitation pulses making it a rather in-efficient sampling scheme[4]. Moreover, the many excitation pulses will lead to increased SAR values and signal attenuation. Spiral trajectories, on the other hand, are more efficient regarding k-space coverage and are even more flexible, since the sampling density can be varied. The goal of the current pilot study is to combine a golden angle spiral sampling scheme with ASL, to achieve high temporal resolution angiographic images and high-quality perfusion images from one data set.

Subjects and Methods: Two volunteers (27–29 years, 2f) were scanned using a 32-channel head coil on a 3T (Ingenia, Philips). A pulsed STAR labeling scheme[5] with a label thickness/gap of 150/20 mm was used with a post-label delay of 100 ms and a Look-Locker, TFE-spiral readout. Angiographic signal was reconstructed at a temporal resolution of 50 ms, and the perfusion images were reconstructed with a temporal window of 200 ms and smoothed post hoc. In a scan time of 3:57 min per slice, 40 averages were acquired for two slices separately, one 30 mm slice at the circle of Willis and one 6 mm slice more superior (Fig. 1).

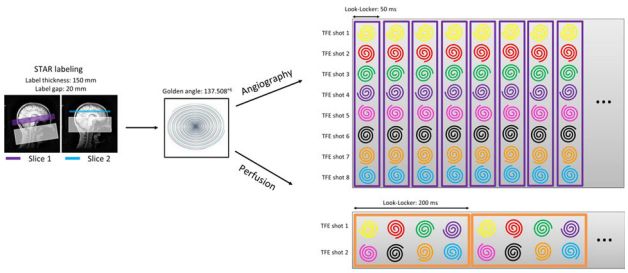

Figure 1. Overview of the STAR labeling scheme with a golden angle Look-Locker TFE-spiral readout for the angiographic and perfusion signal.

Results: Figure 2 shows the angiographic data at a temporal resolution of 50 ms and MIPs for both of the volunteers. With this temporal resolution, the in- and outflow of the labeled blood in the arteries can be imaged. At the later time points, the perfusion data is reconstructed with a temporal window of 200 ms, see Figure 2. Figure 3 shows the angiographic and perfusion images for the more superior slice showing a more conventional perfusion map.

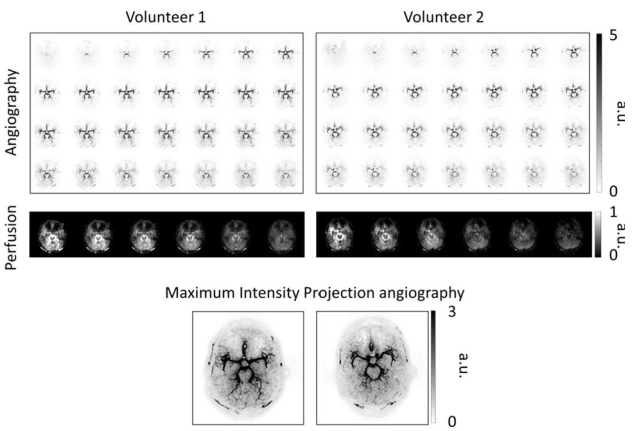

Figure 2. Angiographic images at a temporal resolution of 50ms with a PLD range of 100-1450ms for the 30mm slice at the circle of Willis and MIPs. The perfusion phase is reconstructed with a temporal window of 200ms with a PLD range of 1500–2500ms.

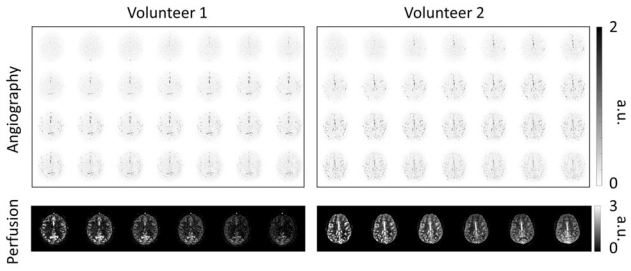

Figure 3. Angiographic images at a temporal resolution of 50ms with a PLD range of 100-1450ms for the more superior slice. The perfusion phase is reconstructed with a temporal window of 200ms with a PLD range of 1500–2500ms.

Discussion/Conclusion: By combining the golden angle spiral read-out with a STAR labeling scheme, single slice high temporal resolution angiography and good quality perfusion images were reconstructed. The signal in the later timepoints during the perfusion phase is attenuated due to the many excitation pulses. This could be solved by using a time-encoded labeling scheme as a second method for obtaining temporal information[2]. Due to difficulties with the reconstruction on the scanner, it was decided to acquire the dataset twice (same acquisition settings), but with different reconstruction settings for reconstructing the angiographic and perfusion images at different temporal resolutions.

References:

1. Okell T, MRM, 2018.
2. Van der Plas MCE, ISMRM #306.
3. Winkelmann S, IEEE, 2007.
4. Jackson J, MRM, 1992.
5. Edelmann R, MRM, 1998.
6. Tolouee A, JMR, 2015.

S07.05

Long Short Term Memory Recurrent Neural Network for MR Fingerprinting parameter estimation

N. Andriamanga[1], C. M. Pirkl[1], A. Sekuboyina[1], G. Buonincontri[2], M. I. Menzel[3], P. A. Gómez[1], M. Piraud[1], B. H. Menze[1]
[1]Technische Universität München, Department of Informatics, Munich, GERMANY, [2]IRCCS Fundazione Stella Maris, Pisa, ITALY, [3]GE Healthcare Global Research, Munich, GERMANY

Purpose/Introduction: Recent deep learning approaches[1,2] demonstrated their ability to successfully circumvent computationally and memory expensive dictionary matching (DM) in MR Fingerprinting (MRF). However, none of them takes advantage of the temporal correlations of the MRF signals. Here, we rely on Long Short-Term Memory (LSTM) recurrent neural networks (RNN) aiming for:

1. Reliable T1 and T2 predictions.
2. Insights into the parameter encoding along the signal train.

Subjects and Methods: The proposed cell architecture (Fig. 1) builds on the initial designs by [3,4]. At each time step, it processes 100 consecutive time-points of the MRF signal magnitude, updating its hidden memory state, to eventually output T1 and T2 estimates (target repetition).

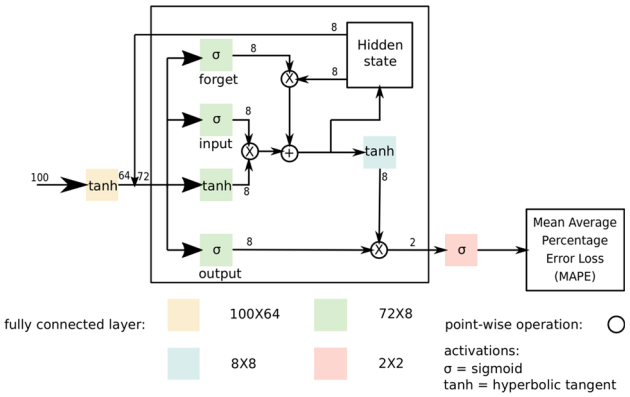

Figure 1. LSTM cell architecture. The hidden state is initialized with zeros and updated with 100 MRF signal magnitude time points at each time step (forget, input gates) and then used to compute the output (output gate).

To train our model, we created a dataset of synthetic MRF signals[5] for combinations of T1 = [100:20:4000]ms and T2 = [20:4:600]ms, discarding atoms with T2 > T1. The training was done with mean average percentage error loss for 2000 epochs adding Gaussian noise (5% standard deviation) to the training data for robustness. The clean dataset was also used to obtain a DM reference.

We evaluated our method on an MRF scan of a healthy volunteer (m, 24y), after obtaining informed consent in compliance with the German Act on Medical Devices.

The MRF acquisition (3T MR750w system, GE Healthcare, 8-channel receive-only head RF coil) is based on the FISP scheme[6]: After an initial inversion (TI = 18 ms), flip angles follow a sinusoidal variation (1000 repetitions) with TR/TE = 10 ms/1.908 ms, spiral sampling (377 interleaves), 22.5x22.5 cm^2 FOV, 1.3 mm^2 in-plane resolution and 5 mm slice-thickness. To accelerate MRF image reconstruction, a singular-value-decomposition was applied to the k-space data. The first 10 singular-values were backprojected to yield the full image time-series

Results: Overall, LSTM predictions agree well with the DM reference (Fig. 2). We observe that T1 estimates at early time steps are already in good agreement with the DM results, while a reliable T2 prediction requires more time steps. This demonstrates that the recovery from the inversion pulse is dominated by T1 relaxation, while T2 relevant information is encoded throughout the acquisition (Fig. 3).

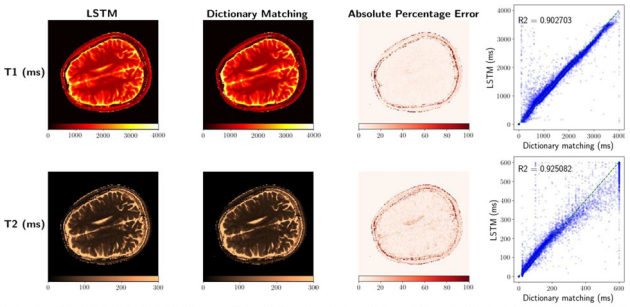

Figure 2. T1 and T2 LSTM prediction vs DM estimates with percentage error maps and scatter plots. The predictions agree well with the reference with a slightly lower accuracy for T2>400ms.

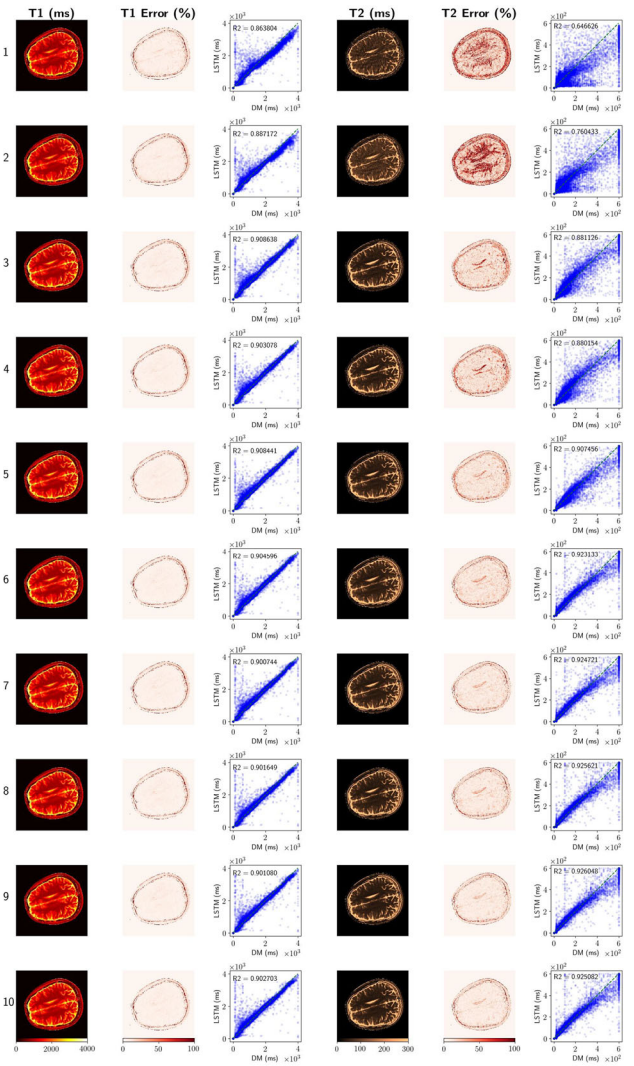

Figure 3. T1 and T2 LSTM predictions for each time step compared to DM estimates. Accurate T1 predictions are obtained pretty quickly from the inversion pulse recovery while T2 predictions improve more gradually.

Discussion/Conclusion: The proposed LSTM model achieves a prediction quality comparable with conventional DM whilst significantly reducing reconstruction time as well as computational requirements. Capturing the temporal features of the MRF signal, our approach reveals insights regarding how T1 and T2 relevant information is encoded and thereby provides new opportunities for MRF sequence optimization.

References:

1. Cohen O et al. *Mag. Res. Med.* 2018;80(3):885–94.
2. Golbabaee M et al. arXiv:1809.01749.
3. Hochreiter S, Schmidhuber J. *Neural Comput.* 1997;9(8):1735–1780.
4. Gers FA et al. *Neural Comput.* 2000;12(10):2451–2471.
5. Weigel M. *J. Magn. Reson. Imaging JMRI.* 2015;41(2):266–295.
6. Jiang Yet al. *Magn. Reson. Med.* 2015;74(6):1621–1631.

S07.06

Reconstruction of Dynamic Perfusion and Angiography Images from Sub-sampled Hadamard Time-encoded ASL Data using Deep Convolutional Neural Networks

S. Yousefi, H. Sokooti, L. Hirschler, M. van der Plas, L. Petitclerc, M. Staring, M. J.P. van Osch
Leiden University Medical Center, Radiology, Leiden, NETHERLANDS

Purpose/Introduction: Arterial spin labeling (ASL) is a non-invasive technique for acquiring quantitative measures of cerebral blood flow (CBF)[1]. Hadamard time-encoded(te) pCASL allows time-efficient acquisition of dynamic ASL-data and when done with and without flow-crushing, 4D MRA and arterial input function measurements can be obtained[2]. While improving quantification, this approach is also a factor two slower. In this study, we propose an end-to-end 3D convolutional neural network (CNN) in order to accelerate CBF quantification from sparse sampling (50%) of te-pCASL with and without flow crushers. For training and evaluation of the CNN, we propose a framework to simulate the te-PCASL signal.

Subjects and Methods: Fig. 1a shows the proposed framework for generating the training and validation data. The ASL signal is simulated by a tracer kinetic model of te-pCASL. This model is a function of arterial arrival time, tissue arrival time and blood flow, which were extracted from in vivo data and registered to BrainWeb[3] scans. This study contains 1676 simulated subjects, each including crushed and non-crushed input data at 8 timepoints, and angiographic and perfusion output data at 7 timepoints. The proposed CNN, Fig. 1b, leverages design elements from DenseNet4 with loop connectivity patterns in a typical U-shape ($\sim$ 400 K parameters). We leverage a Huber loss function for training the network, with weights based on the gradient magnitudes from Fig. 2a. In order to manage memory usage, we utilize patch-based training. The simulated dataset was divided into 1174 subjects for training, 167 for validation, and 335 for testing. For augmenting the training data, noise, flipping and $\pm$ 13° rotation have been applied randomly. The network was trained for 30 k iterations.

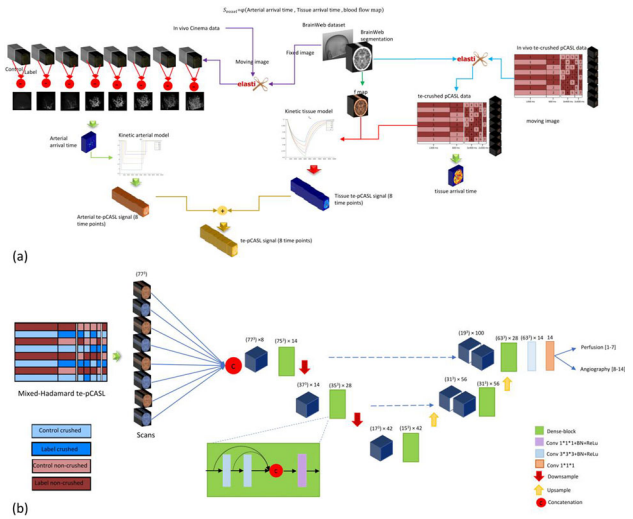

Fig. 1- a) Simulated data generator framework; b) the proposed CNN

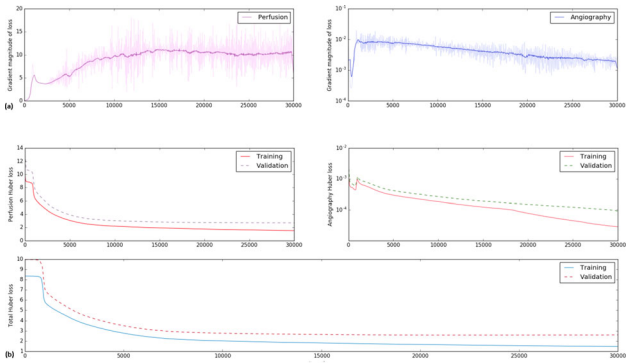

Fig. 2- a) Gradient magnitude b) loss functions for angiography/perfusion during training

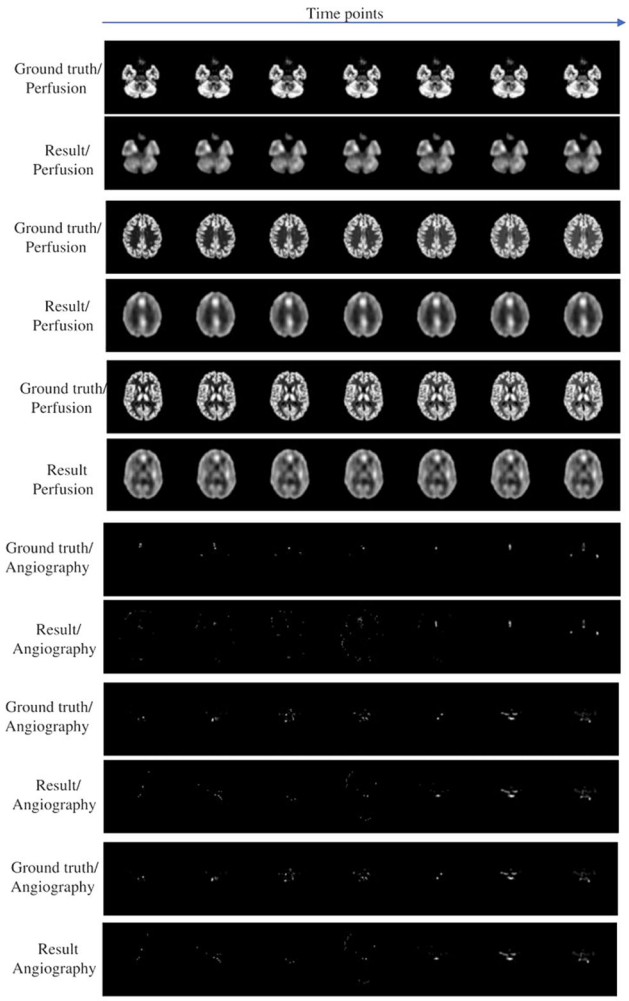

Fig. 3- Example results

Results: Fig. 2b, shows the network's training loss for the perfusion and angiography separately and their combination. The average MSE for the perfusion and the angiography is 5.30 $\pm$ 0.22 and 5.02 $\pm$ 0.17. Fig. 3 shows the outputs of the network for some slices of perfusion/angiography at different timepoints. Due to the averaging property in the Huber loss function, the results suffer from over-smoothing. It takes an average of

0.12 ± 0.18 s to reconstruct all perfusion and angiography scans from the sparsely-sampled crushed/non-crushed data (size 101^3).

Discussion/Conclusion: This study demonstrates that CNNs are promising to reconstruct angiographic and perfusion images from sparsely sampled Hadamard ASL-data. A next step is the use of perceptual losses to improve sharpness of the results, as well as validation on in vivo data.

References:

1. Teeuwisse et al. MRM, 1712-1722, 2014.
2. Petersen et al. MRM, 219-232, 2006.
3. Cocosco et al. NeuroImage. 1997.
4. Huang et al. IEEE CVPR, 4700, 2017.

S07.07

Recent Developments in Electrical Properties Tomography with the 3D Contrast Source Inversion Approach

R. Leijsen[1], W. Brink[1], R. Remis[2], A. Webb[1]
[1]*Leiden University Medical Center, Leiden, NETHERLANDS,* [2]*Delft University of Technology, Delft, NETHERLANDS*

Purpose/Introduction: Accurate mapping of tissue electrical properties (EPs; conductivity and permittivity) is of great interest for accurate SAR predictions[1]. EPs are also used for patient-specific electromagnetic modeling in hyperthermia treatment planning[2]. In addition, EPs can be used as biomarkers to aid the discrimination of cancerous from benign tissue[3].

In Electrical Properties Tomography (EPT), EPs are retrieved in a non-invasive manner by using estimates of the transmit magnetic (B_1^+) field. The most frequently used method is the Helmholtz-based method[4]. However, this assumes homogeneous media, making it unable to accurately reconstruct tissue boundaries and, due to differentiation operators acting on the data, very sensitive to noise.

Contrast Source Inversion (CSI) is an iterative reconstruction approach that solves the inverse problem in a global manner, exploiting the noise-robustness of its integral operators[5,6]. In this iterative procedure, a cost functional is minimized which measures the discrepancy between measured and modeled data as well as the discrepancy in satisfying Maxwell's equations.

Here, we show our recent developments of the 3D CSI-EPT implementation, showing its potential for accurate reconstructions of EPs.

Subjects and Methods: The Nova Medical circularly polarized birdcage transmit head coil was simulated at 7T in XFdtd[7] and the Ella model[8] with voxels of 2.5 × 2.5 × 3.5 mm was inserted. Incident EM fields were simulated, and based on knowledge of this data, reconstructions were obtained using a Helmholtz-based EPT method with a 7v7 × 5 FD kernel[4] as well as a 3D CSI-EPT method which includes multiplicative total variation regularization[9]. The reconstructions were obtained using both noiseless and noisy data with an SNR of 70 and 50, to assess their noise sensitivity.

Results: The Helmholtz-based method is unable to reconstruct tissue boundaries, even for noiseless cases, while 3D CSI-EPT is much better in this respect. Presence of noise degrades the reconstruction of smaller tissue structures, however the main structures are properly reconstructed. The Helmholtz-based method is unable to acquire accurate reconstructions at these SNR levels.

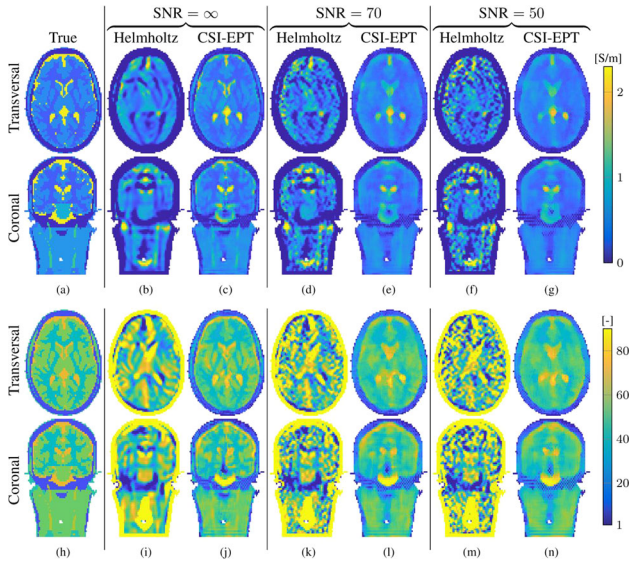

True model and reconstructions obtained with the Helmholtz-based and regularized CSI-EPT methods, at different SNR levels. Noiseless CSI reconstructions are shown at 10000 iterations, noisy at 1000. Conductivity (a-g) and relative permittivity (h-n).

Discussion/Conclusion: CSI-EPT is able to reconstruct tissue boundaries, and is more noise robust due to its integral approach. Additionally, the multiplicative regularization parameter makes the implementation insensitive to overfitting of noise, showing potential to be used for clinical implementations. To implement the method in practice, several aspects remain to be addressed, primarily the assumption of the possibility to measure B_1^+ phase.

References:

[1]Gandhi, Magn Reson Med 1999.
[2]Balidemaj, Int J Hyperther 2016.
[3]Tha, Eur Radiol 2018.
[4]Mandija, Magn Reson Med 2018.
[5]Balidemaj, IEEE TMI 2015.
[6]Leijsen, IEEE TMI 2018.
[7]Remcom State College.
[8]IT'IS Foundation.
[9]Haffinger, PhD Dissertation, 2013.

This work was supported in part by the ERC Advanced Grant 670629 NOMA MRI.

S07.08

Mapping whole brain cardiac and respiratory induced tissue motion using a single-shot multi-slice acquisition with at 7T MRI

J. J. Sloots[1], P. Luijten[1], G. J. Biessels[2], J. Zwanenburg[1]
[1]*University Medical Center Utrecht, Radiology, Utrecht, NETHERLANDS,* [2]*University Medical Center Utrecht, Neurology, Utrecht, NETHERLANDS*

Purpose/Introduction: Brain tissue deformation induced by the cardiac and respiration cycles could be a valuable source of information on the brains tissue properties including waste clearance[1]. We have shown that displacement encoding with stimulated echoes (DENSE) allows for separate assessment of cardiac and respiration induced tissue strain[2]. However, our method required a single-shot 'snapshot' approach that was limited a single slice acquisition. Here,

we present a multi-slice approach with whole brain coverage and provide a proof of principle in a single subject.

Subjects and Methods: The cardiac triggered, single-shot multi-slice (MS) DENSE sequence was implemented based on our previous developed DENSE sequence[2]. The slice acquisition order was permuted for every successive dynamic scan so that each slice was acquired at multiple time points within the cardiac cycle (Fig. 1).

To provide proof of principle, a volunteer was scanned at 7T (Philips; 32ch Nova head coil) after obtaining written informed consent. DENSE measurements (60 slices, resolution: 3 mm^3, SENSE: 2.5 AP, multi-band factor: 3) repeated over 160 dynamics: 20 permutations * 2 motion encoding strengths (0.6 mm/2π, 0.4 mm/2π) * 2 opposite encoding directions (to distinguish between motion induced phase and phase confounders) * 2 averages. Physiological data was recorded by using a vector cardiogram (VCG) for triggering and a respiration belt to trace abdominal breathing.

Motion encoded snapshot images in the Feet-to-Head direction were unwrapped and fitted voxelwise by using the physiological data in a linear model[2] to isolate the confounders, respiration and four heart phases at 20, 40, 80 and 100% of the cardiac interval.

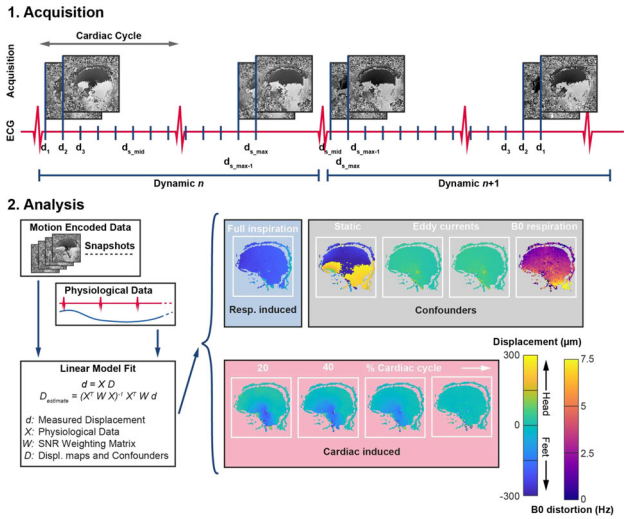

Fig. 1. Data acquisition and analysis. (1) The DENSE MRI sequence was used to obtain motion encoded images. (2) The motion encoded image and physiological data were used in a linear model to isolate various displacement components from confounders.

Results: The linear fit resulted in smooth displacement maps over the complete brain (Fig. 2). For a full inspiration, we observed a slight rotation of the complete head, where the back of the head moves in de Head direction and the front of the head moves in the Feet direction. Associated strain maps at peak systole showed predominantly expansion of about $3{\cdot}10^{-3}$ in the deep brain (Fig. 3).

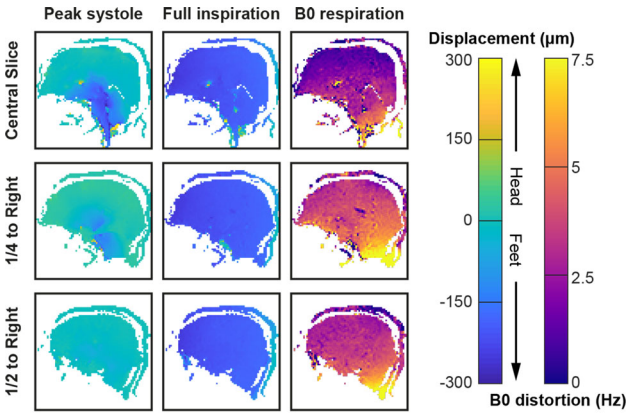

Fig. 2. Displacement maps obtained using the linear model for sagittal slices at different locations (rows). Columns show peak systolic displacement, displacement for a full inspiration and B0 distortion for a full inspiration, respectively.

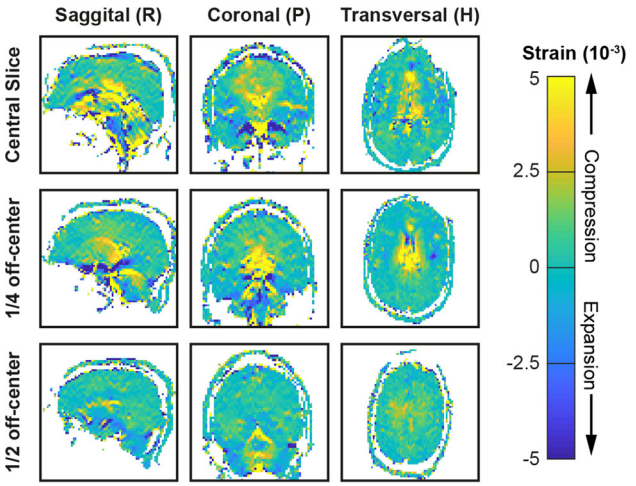

Fig. 3. Whole brain FH strain field computed as the spatial derivative along FH motion encoding direction of the FH motion field. Sagittal, coronal and transverse cross-sections (columns) show the FH strain field at different locations (rows).

Discussion/Conclusion: Single-shot MS DENSE yields whole brain cardiac- and respiratory induced tissue motion and strain in approx. 5 min. The respiration induced B_0 offset fluctuations (typical range: 0-10 Hz) compare well to the literature[3]. In contrast to the strain maps, displacement maps showed striping artifacts reflecting inter-slice differences that require further attention and improvement. Despite the amplified noise induced by the use of spatial derivatives, we still obtained strain maps with sufficient SNR to assess the strain in small ROIs. This novel approach may serve as a physiological marker on physiological blood volume dynamics in the brain.

References:

1. Mestre, H, et al. *Clin Sci* **131**:2257-2274 (2017).
2. Sloots, J J, et al. *ISMRM Proc* #368 (2018).
3. Van Gelderen, P, et al. *Magn Reson Med* **57**:362-368 (2007).

S08 Scientific Session

16:10–17:40 *Room 3 - Ruys & van Rijckevorsel Zaal*

New Findings in Neuroradiology

S08.02

Are physical activity and sedentary time associated with measures of structural brain connectivity? - Novel insights from The Maastricht Study

L. Vergoossen[1], J. Jansen[1], C. Stehouwer[2], N. Schaper[2], R. Henry[2], C. van der Kallen[2], A. Koster[3], M. Schram[2], W. Backes[1]
[1]Maastricht University Medical Center, Radiology and Nuclear Medicine; School for Mental Health and Neuroscience, Maastricht, NETHERLANDS, [2]Maastricht University Medical Center, Internal Medicine; School for Cardiovascular Disease, Maastricht, NETHERLANDS, [3]Maastricht University, Social Medicine; School for Public Health and Primary Care, Maastricht, NETHERLANDS

Purpose/Introduction: Less physical activity (PA) and more sedentary time (ST) are thought to reduce the risk on CVD.[1] We aim to obtain better insight into the association of objectively measured PA and ST (instead of using questionaires[2]) with brain tissue alterations and hypothesize that low PA and high ST are associated with lower white matter connectivity in brain regions involved in PA and specifically motor function.

Subjects and Methods: *Subjects*: In The Maastricht Study[3], a T2DM-enriched population-based study (n = 1715, 52% men, mean age 60 ± 8 years), we performed 3T brain MRI (MAGNETOM Prisma fit, Siemens Healthcare, Erlangen, Germany).

MRI: A 3D T1-weighted MPRAGE sequence (TR/TI/TE 2300/900/2.98 ms, 176 slices, 1 mm^3 voxel) was acquired for anatomic reference. Diffusion tensor MRI (dMRI) data were acquired using a Spin Echo EPI sequence (TR/TE 6100/57 ms, 65 slices, 64 gradient directions (b = 1200 s/mm^2) and three b_0).

Quantitation: Atlas-based (AAL2) volumes of interest (120 regions) were transformed to dMRI space for each individual. The main processing steps were eddy current and head motion correction, calculation of the diffusion tensor, estimation of FOD using CSD, and whole brain deterministic tractography. Brain connectivity was expressed as node degree, and calculated in the networks for the strongest connections (thresholded at sparsity 0.8) in the whole cerebrum. Furthermore, local node degree (Fig. 1) was calculated for the deep gray matter structures (DGM) (i.e., caudate nucleus, putamen, pallidum, and thalamus) and the primary motor cortex (PMC), which are specifically involved in motor function.[4]

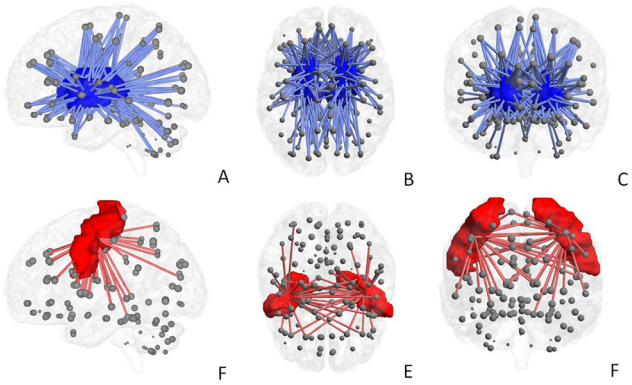

Fig. 1: Local connectivity of DGM and PMC in three orthogonal views. Gray dots: 120 atlas regions. Blue and red volumes: DGM (A-C) and PMC (D-F) regions, respectively. Lines: connections between regions (number of lines = node degree).

Physical behaviour: PA and ST were measured with a (activPAL3, 24 h, 8 days) PA monitor, and expressed as mean time stepping and sitting, respectively, during wake time per day. For this study higher intensity physical activity (HPA), i.e., the number of minutes with a high step frequency (> 110 steps/min)[5], was used as PA measure.

Statistics: Multivariable linear regression was used to investigate the association of HPA and ST with connectivity measures, adjusted for relevant confounders (Table 1).

Results: After full adjustment, lower HPA was associated with lower node degree of DGM (Table 1, Fig. 2A-B). The association between low HPA and lower node degree of PMC was statistically significant in model 1, but attenuated after adjustment for cardiovascular risk factors (model 2). ST was associated with global lower node degree after full adjustments (Fig. 2C-D).

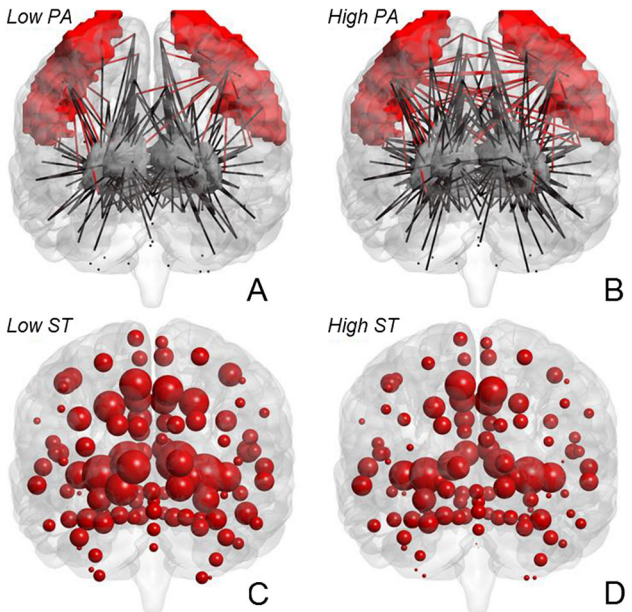

Fig. 2: Node degree for low (A) and high (B) ST. Larger spheres = higher node degree. Local connectivity of DGM (gray volumes) and PMC (red volumes) for low (C) and high (D) HPA. Lines: connections between regions (number of lines = node degree).

	Average Node Degree	P	Degree Deep gray matter	P	Degree Primary motor cortex	P
HPA Time, β (95% CI)						
Model 1	-0.006 (-0.057, 0.045)	0.812	**0.084 (0.035, 0.132)**	**0.001**	**0.051 (0.003, 0.099)**	**0.038**
Model 2	-0.001 (-0.055, 0.053)	0.974	**0.068 (0.017, 0.119)**	**0.009**	0.037 (-0.013, 0.087)	0.147
Sed. Time, β (95% CI)						
Model 1	**-0.067 (-0.120, -0.014)**	**0.013**	-0.050 (-0.101, 0.001)	0.053	-0.035 (-0.085, 0.016)	0.176
Model 2	**-0.076 (-0.131, -0.020)**	**0.007**	-0.029 (-0.081, 0.024)	0.290	-0.013 (-0.065, 0.039)	0.629

Associations between physical activity measures with node degree. Regression coefficients and 95% CI indicate the mean difference in node degree per SD increase in HPA and sedentary time.
Model 1: Adjusted for wake time, age, sex, education level, MRI date. Model 2: Model 1 + additionally adjusted for BMI, systolic blood pressure, antihypertensive medication, total-to-HDL-cholesterol-ratio, lipid-modifying medication, smoking status, alcohol use, history of cardiovascular disease, diabetes status, WML volume and ICV.

Table 1: Associations of HPA and ST with node degree of the whole brain, deep gray matter structures and the primary motor cortex.

Discussion/Conclusion: We found that lower HPA was associated with fewer connections to DGM and PMC, and that more ST was associated with lower node degree. It is concluded that low PA and high ST seem to mitigate the white matter innervation of the human brain.

References:

1. Hayes, et al. Front Aging Neurosci 2013.
2. Gons, et al. Neurology 2013.
3. Schram, et al. Eur J Epidemiol 2014.
4. Brooks. J Neurol Sci 1995.
5. Tudor-Locke, et al. Sports Med 2012.

S08.03

Evaluation of thalamo-cortical connectivity using diffusion-weighted MRI in infants with epilepsy associated with thalamic lesions

A. R. Oliveira[1], P. Figueiredo[1], A. Leal[2], R. G. Nunes[1]
[1]*ISR-Lisboa/LARSyS and Department of Bioengineering, Instituto Superior Técnico, Universidade de Lisboa, Lisbon, PORTUGAL,*
[2]*Department of Neurophysiology, Centro Hospitalar Psiquiátrico de Lisboa, Lisbon, PORTUGAL*

Purpose/Introduction: Thalamic lesions are commonly associated with Continuous Spike-Wave of Sleep (CSWS); a model for the genesis of this epilepsy syndrome has been proposed[1], which states that thalamo-cortical disruptions are at the origin of the continuous spiking in CSWS. To further investigate this hypothesis, we have previously used diffusion-weighted MRI (DWI) to parcellate the thalamus into its subnuclei, in a group of CSWS patients[2]. Here, we test for asymmetries between the healthy and lesioned hemispheres in the thalamic nuclei parcellated in [2] based on their volume and connection strengths.

Subjects and Methods: Four CSWS patients with unilateral thalamic lesions were studied using a 1 mm^3 T1-weighted image and a 2.3 or 2.5 mm isotropic DWI with b = 1000 s/mm^2; 65 or 35 directions and 1 non-DWI volume. 5 cortical areas were defined: temporal, prefrontal, motor and somatic, posterior parietal and occipital areas. For each patient, a thalamic mask was drawn and used as seed in probabilistic tractography[3], with the cortical masks used as targets. The thalamus was parcellated considering, for each voxel, the cortical region with highest probability of connection[3]. The volume of each nucleus was quantified and normalized to the total volume of the ipsilateral thalamus. The probability of connection between each nucleus and the corresponding cortical area was calculated and normalized by the total number of connections of the ipsilateral thalamus and by the number of voxels in the respective target.

Results: An example of the thalamic parcellation is shown in Fig. 1 and an example of the volume and connection strength measurements of the thalamic nuclei is in Fig. 2. We found that the most commonly affected thalamo-cortical connections were those involving the temporal cortex, followed by the posterior parietal and occipital ones, which is consistent with the periventricular localization of the lesions. The analysis of connection strength evidenced connectivity changes in thalamic nuclei in the lesioned hemisphere that were not necessarily the ones with highest volumetric asymmetries. Results are consistent with the spikes' localization based on EEG studies; similar results were obtained for the other patients - Fig. 3.

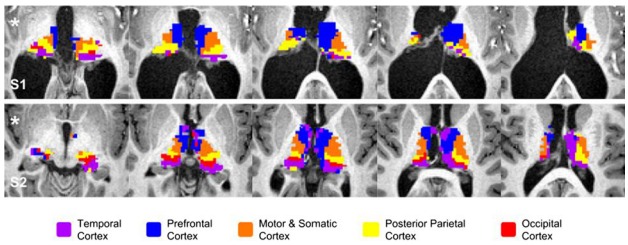

Fig.1: Thalamic parcellation for patients 1 and 2. Slices are shown 4 mm apart from each other, along the vertical axis of the reference system. * symbol identifies the AC-PC plane in each subject.

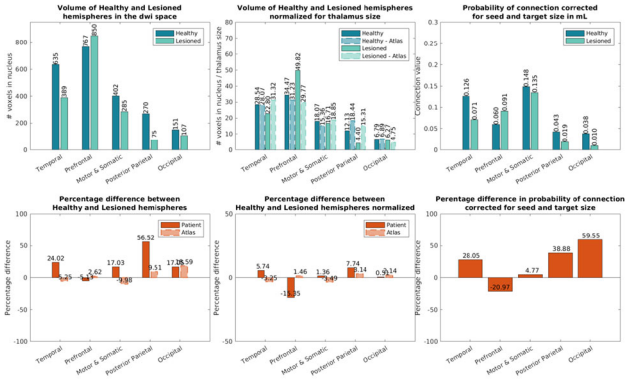

Fig.2: Illustrative results for patient 4. Left: absolute volume; Middle: normalized volume; Right: normalized connection strength; for each thalamic nucleus in each hemisphere (top) and respective difference between hemispheres (bottom).

Subject	Hemisphere of thalamic lesion	Epileptic activity distribution	Larger differences in thalamic nucleus volumes between healthy and lesioned hemispheres	Larger differences in thalamic nucleus connection strength between healthy and lesioned hemispheres
1	Right	Temporal lobe ipsilateral to lesion	Prefrontal; Motor & Somatic	Motor & Somatic; Occipital; Prefrontal
2	Right	Occipital near Posterior Parietal lobe, near mid sagital plane; and Prefrontal lobe ipsilateral to lesion	Posterior Parietal; Parietal	Posterior Parietal; Parietal
3	Left	Occipital lobe with propagation to Prefrontal cortex; Prefrontal lobe. Both ipsilateral to lesion	Temporal; Occipital; Prefrontal	Prefrontal; Occipital; Temporal
4	Right	Occipital lobe with a slight propagation towards anterior direction, ipsilateral to lesion	Posterior Parietal; Temporal	Occipital; Posterior Parietal; Temporal

Fig.3: Summary of results for each patient, regarding the distribution of epileptic activity (from EEG data) and the thalamo-cortical dysconnectivity pattern found with DWI.

Discussion/Conclusion: The joint assessment of volumetric and connectivity changes provides a more complete evaluation of thalamo-cortical asymmetries. The thalamo-cortical connectivity metrics used here were more consistent with the distribution of epileptic events observed on the EEG, than in [2]. The results are consistent with the hypothesis that a partial disruption of thalamic inputs to the cortex could be responsible for the genesis of epileptic activity in CSWS.

Acknowledgements: Portuguese Science Foundation for support through PTDC/SAUENB/112294/2009 and UID/EEA/50009/2019.

References:

1. Leal, A et al. *Epilepsy Behav.*,78:243, 2018.
2. Oliveira, A et al. *OHBM* 2019.
3. Behrens, T. E. et al. *Nat Neurosci.*, 6:750, 2003.

S08.04

Diffusion-weighted imaging reveals structural brain changes in cosmonauts after long-duration spaceflight

S. Jillings[1], A. Van Ombergen[2], E. Tomilovskaya[3], S. Laureys[4], P. zu Eulenburg[5], S. Sunaert[6], J. Sijbers[7], F. Wuyts[1], B. Jeurissen[7]
[1]University of Antwerp, Dept. of Physics, Lab for Equilibrium Investigations and Aerospace, Antwerp, BELGIUM, [2]University of Antwerp, Dept. ENT, Translational Neurosciences, Antwerp, BELGIUM, [3]Russian Academy of Sciences, Institute of Biomedical Problems, Moscow, RUSSIAN FEDERATION, [4]University of Liège, Dept. of Neurology, GIGA Consciousness, Liège, BELGIUM, [5]Ludwig-Maximillian's University, Dept. of Neurology, Deutsches Schwindel- und Gleichgewichtszentrum, Munich, GERMANY, [6]University of Leuven, Dept. of Imaging and Pathology, Translational MRI, Leuven, BELGIUM, [7]University of Antwerp, Dept. of Physics, imec-Vision Lab, Antwerp, BELGIUM

Purpose/Introduction: Human space travel causes changes in several physiological systems of the body. Given the limited knowledge on the effect of space travel on the brain [1], this prospective study aimed to investigate structural brain changes as a result of spaceflight using diffusion magnetic resonance imaging (dMRI).

Subjects and Methods: Eleven cosmonauts who spent 6 months aboard the International Space Station were scanned with a multi-shell dMRI protocol (b values of 0, 700, 1200 and 2800 s/mm^2) before launch (pre-flight) and upon return to Earth (post-flight). Seven cosmonauts were scanned again 7 months later (follow-up). From the dMRI data, apparent densities of cerebrospinal fluid (CSF), gray matter (GM), and white matter (WM) were obtained using multi-tissue spherical deconvolution [2]. Tissue densities were warped nonlinearly to an unbiased study-specific group template, taking into account the longitudinal nature of the data, and modulated to account for local volume changes introduced by the nonlinear warps [3]. Modulated densities were compared voxel-wise between launch and return using nonparametric two-sample paired t-tests (significance threshold $p < 0.05$, family-wise error corrected). Voxels with significant differences between launch and return were used as regions-of-interest (ROIs) for ROI-based statistical comparisons between return and follow-up and launch and follow-up.

Results: CSF increased between launch and return in inferior areas along the temporal and frontal lobes, the ventricles, and in the Sylvian fissure (+41%), while GM and WM decreased adjacent to these structures (GM: -20%, WM: -7%). CSF decreased in superior areas, such as the longitudinal fissure and the (para)central sulci (-23%), while GM increased in the adjacent cortical gyri (+15%) (see Fig. 1).

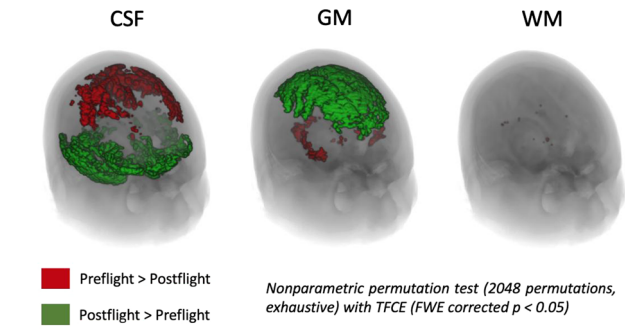

Paired voxel-wise whole-brain analyses of CSF, GM and WM densities between preflight and post-flight scans of cosmonauts.

At follow-up, CSF, GM and WM normalized to a large extent but CSF remained decreased in superior areas compared to pre-flight (-5%; $p = 0.046$). GM remained decreased compared to pre-flight in inferior areas (GM: -8%; $p = 0.016$) (see Fig. 2).

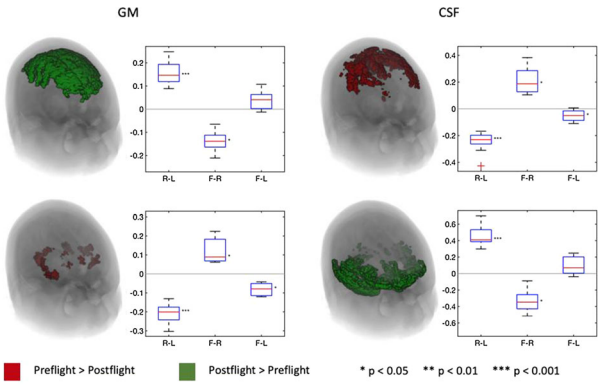

ROI-based paired differences in CSF and GM densities between preflight (L), post-flight (R) and follow-up (F) scans of cosmonauts. ROIs are shown left to the corresponding boxplots using volume rendering.

Discussion/Conclusion: The fluid redistribution occurring in microgravity likely accounts for our results, causing local morphological changes in the brain tissue. This would explain the complementary GM increases with CSF decreases and vice versa, as well as their reversibility. The incomplete recovery at follow-up points towards a persisting physiological disturbance of fluid homeostasis throughout the body in addition to the established acute physical consequences of space travel. In conclusion, dMRI robustly depicts post-spaceflight changes in the brain related to fluid redistribution, which appear to be partly reversible over time.

References:

1. Van Ombergen et al. NPJ Microgravity. 2017;3: 2.
2. Jeurissen et al. Neuroimage. 2014;103: 411–426.
3. Raffelt et al. Neuroimage. 2011;56: 1171–1180.

S08.05

The added value of radiomics to a clinical prognostic model in patients with low-grade glioma

M. van Riel[1], F. Incekara[1], S. van der Voort[1], M. Wijnenga[2], S. Klein[1], M. van den Bent[3], M. Smits[1]
[1]Erasmus MC, Radiology, Rotterdam, NETHERLANDS, [2]Erasmus MC, Neurology, Rotterdam, NETHERLANDS, [3]Erasmus MC, Neuro-Oncology, Rotterdam, NETHERLANDS

Purpose/Introduction: In recent years, radiomics has become of increasing interest in studies of patients with low-grade glioma (LGG). Imaging features extracted from Magnetic Resonance Imaging (MRI) have shown to have the potential to predict genotype and overall survival in patients with LGG.[1,2] However, until now, the potential of radiomics to add prognostic value to clinical prognostic models has hardly been investigated.

The purpose of this study is to investigate the added prognostic value of quantitative magnetic resonance imaging features to a clinical prognostic model for patients with LGG.

Subjects and Methods: This retrospective cohort study included adult patients with newly diagnosed LGG who underwent tumor resection or biopsy between October 2002 and March 2017 at the Erasmus MC, University Medical Center Rotterdam (EMC). A set of 77 imaging features were extracted from preoperative T1w and T2w magnetic resonance sequences. These included first order histogram, texture, shape and location features of the volume of interest. The primary outcome of our study was overall survival (OS) and the secondary outcome was progression-free survival (PFS).

Results: A total of 259 patients were included. The median follow-up was 5.3 years (interquartile range, 3.4-8.2). The median OS was 9.08 years (95% CI: 6.70-11.5). Four imaging features increased the

fit of our clinical prognostic model for OS significantly: T1 local binary pattern peak (hazard ratio (HR) 1.028, p = 0.041), T2 histogram energy (HR 1.000, p < 0.001), T2 histogram peak (HR 1.000, p = 0.002) and standard deviation of radial distance (HR 1.412, p < 0.001). The median PFS was 4.14 years (95% CI: 3.49-4.79). Only one imaging feature increased the fit of our clinical prognostic model for PFS significantly: standard deviation of radial distance (HR 1.278, p = 0.006).

Discussion/Conclusion: This study demonstrates that several radiomics features have the potential to help predict OS and PFS in patients with LGG more accurately than models constituted only by clinical features. In our study, four quantitative MRI features were found to be of added prognostic value. However, future studies should validate our results.

References:

[1]Lu CF, Hsu FT, Hsieh KL, Kao YJ, Cheng SJ, Hsu JB, et al. Machine Learning-Based Radiomics for Molecular Subtyping of Gliomas. Clin Cancer Res. 2018;24(18):4429-36.

[2]Qian Z, Li Y, Sun Z, Fan X, Xu K, Wang K, et al. Radiogenomics of lower-grade gliomas: a radiomic signature as a biological surrogate for survival prediction. Aging (Albany NY). 2018;10(10):2884-99.

Figure 1

Multivariate Cox regression of clinical and imaging features (overall survival)

		B	SE	Wald	df	Sig.	Exp(B)
Molecular diagnosis	IDH wildtype 1p19q- intact	*	*	101,443	2	,000	*
	IDH mutation 1p19q-intact	-2,879	,365	62,210	1	,000	,056
	IDH mutation 1p19q-codeletion	-4,347	,434	100,253	1	,000	,013
Mild enhancement		,952	,310	9,402	1	,002	2,590
Extent of resection		-1,029	,278	13,674	1	,000	,357
Postoperative tumor volume		,005	,003	2,159	1	,142	1,005
T1w LBP peak		,027	,013	4,176	1	,041	1,028
STRD**		,345	,072	22,718	1	,000	1,412
T2w histogram energy		,000	,000	15,024	1	,000	1,000
T2w histogram peak		,000	,000	9,435	1	,002	1,000

*reference variable
**standard deviation of radial distance

Figure 2

Multivariate Cox regression of clinical and imaging features (progression free survival)

	B	SE	Wald	df	Sig.	Exp(B)
Age at surgery	-,031	,008	13,780	1	,000	,969
IDH mutation	-1,837	,294	39,117	1	,000	,159
Extent of resection	-,005	,002	6,545	1	,011	,995
SDRD*	,144	,052	7,683	1	,006	1,155

*standard deviation of radial distance

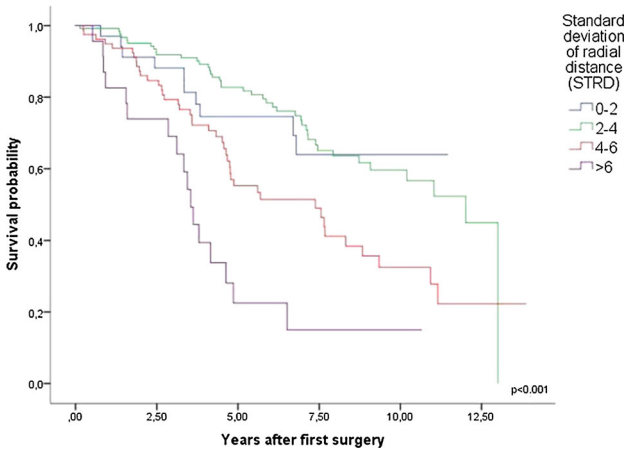

S08.06

Implementation and validation of ASL perfusion measurements for population-based imaging

E. A. H. Warnert[1], R. Steketee[1], M. Vernooij[2], J. A. Hernandez-Tamames[1], M. Vogel[3], G. Kotek[1]

[1]*Erasmus MC, Radiology & Nuclear Medicine, Rotterdam, NETHERLANDS,* [2]*Erasmus MC, Epidemiology, Rotterdam, NETHERLANDS,* [3]*GE Global Research, Munich, GERMANY*

Purpose/Introduction: Measurement of cerebral blood flow (CBF) with pseudocontinuous arterial spin labelling (pCASL) is a cost-effective and safe option for repeated assessment of cerebral perfusion, especially attractive for large population-based studies in which healthy participants undergo longitudinal MRI scans. The Rotterdam Study[1] started in 2005 with a designated scanner and in view of longitudinal follow-up of the same healthy participants the MRI setup has not changed since. We have extended the MRI protocol of the Rotterdam Study with pCASL, for which we needed to implement a pCASL sequence on an MRI system from 2005 and validate the quantification of this in-house implementation.

Subjects and Methods: Imaging was performed on two 1.5T MRI systems (GE Healthcare, USA); (I) the population imaging scanner; Signa EXCITE, software version 11; (II) Optima MR450w, software version DV26, including the GE-product version of pCASL[2]. The product pCASL (DV26) was converted in-house to scanner I.

Acquisition parameters for both pCASL implementations; 3D spiral gradient echo read-out with background suppression, 512 points per arm, 8 arms, reconstruction diameter = 200 mm and matrix 128x128x30, slice thickness 4 mm, post label delay 1.525 s, label duration 1.45 s, NEX = 3,TE/TR 0.011 s/4.6 s. Each pCASL acquisition included a proton density weighted image for normalisation[3].

A perfusion phantom (QASPER, Gold Standard Phantoms, London, UK) and 3 young healthy volunteers (all female, < 27 years) underwent pCASL scanning on both MR systems, for comparison of sequences.

Thirty elderly participants (19 females, aged 86 ± 4 years) of the Rotterdam Study underwent scanning on scanner I only, which included pCASL scans and single slice phase contrast measurements through the major brain feeding arteries.

All volunteer CBF maps were quantified with *oxford_asl* (FSL, UK)[4]. Whole brain grey matter CBF was calculated using segmentations from T_1–weighted structural scans, linearly registered to the CBF maps (*flirt* in FSL).

Results: The scaling factor between the two pCASL implementations calculated from the flow phantom was 30.9 for flow velocities > 30 cm/s (Figure 1). After outlier removal, whole brain grey matter CBF values were 62.7 ± 6.4 ml/100 g/min and not correlated with phase contrast blood flow measurements (Figures 2 & 3).

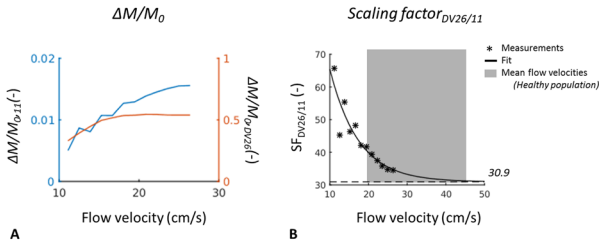

Figure 1A. ΔM/M0 plotted against the flow velocity set for the flow phantom for the pCASL implementations (Scanner I blue, Scanner II orange. B. Scaling factor (SF) plotted against flow velocity, with a fitted asymptote of 30.9.

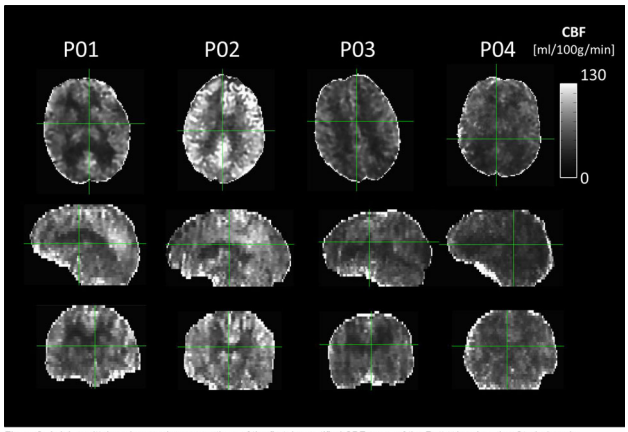

Figure 2. Axial, sagittal, and coronal cross-sections of the first 4 quantified CBF maps of the Rotterdam Imaging Study (aged > 80 years), implemented on the population scanner (software version 11).

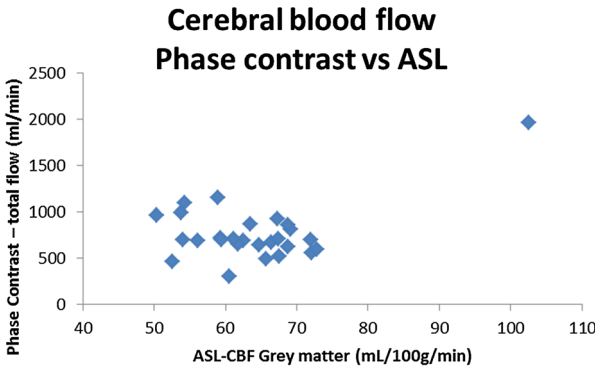

Figure 3. ASL GM CBF plotted against total PC flow (in ml/min). Data shown here for 27 elderly participants. Excluding the outlier (CBF GM > 100 ml/100g/min), there is no significant correlation between GM CBF and total PC flow.

Discussion/Conclusion: An in-house implementation of 3D pCASL on a population MRI system allowed for the application of pCASL in the Rotterdam Study. Future work includes further investigation of the relationship between ASL CBF and phase contrast blood flow measurements, including the effect of blood flow velocity on quantification of ASL CBF in (elderly) participants with slow blood flow (< 30 cm/s).

References:

1. Ikram MA et al. Eur J Epid. 2017.
2. Maleki N et al. MRMPBM. 2012.
3. Dai W et al. MRM. 2013.
4. Alsop DC et al. MRM 2015.
5. Albayrak R et al. J Clin Ultras. 2007.

S08.07

In-vivo functional and structural MRI of the sensory thalamic nucleus

R. Sanchez Panchuelo, M. Ali, K. Aphiwatthanasumet, P. Gowland, R. Bowtell
University of Nottingham, Sir Peter Mansfield Imaging Centre, Nottingham, UNITED KINGDOM

Purpose/Introduction: Maladaptive reorganization of the somatosensory system may originate at the level of the thalamic nuclei in the pathway to the cerebral cortex, however, the reliable localization thalamic nuclei with MRI has been difcult. Using 7T MRI we have previously identied the thalamic nuclei in post mortem images and some of the structures in vivo [1]. Here, we use structural and functional MRI at 7T to independently localized the sensory ventro-posterior lateral (VPL) nuclei of the thalamus in vivo.

Subjects and Methods: One subject underwent fMRI on 4 separate occasions. fMRI data was collected during thermonoxious skin stimulation to the palm below the thumb on the right hand using an MRI-compatible Peltier thermode (Medoc Pathway). The fMRI paradigm was a block design with 5 s periods of stimulation at the subject pain threshold (46-46.5^{o}C) interleaved with baseline periods (40^{o}C) of varying (25-30 s) duration. Two fMRI runs were performed using GE-EPI (TE = 25 ms, TR = 2 s, MB = 3, 54 slices, 1.5 mm isotropic resolution). High spatial resolution (0.3 × 0.3 × 1.2 mm^3) cardiac-gated FLASH (TE = 25 ms) and TSE (TSEfactor = 10, RA = 90^{o}, TE = 87 ms) data were acquired in a separate anatomical scan session. The phase of the FLASH image data was used to obtain a quantitative susceptibility map (QSM), which was used together with the FLASH magnitude and TSE data for k-means clustering to identify various thalamic nuclei. The thermonoxious fMRI time series were analyzed using a GLM. The location of activations in the thalamus were spatially compared with the subject's structural boundaries and with the Talairach atlas probabilistic VPL region [2].

Results: Thermonoxious stimulation evoked BOLD responses within the thalamus in all 4 fMRI sessions. Figure 1B shows contralateral (top) and ipsilateral (bottom) clusters compared to the probabilistic VPL region (blue line), and corresponding time series (Fig. 1C).

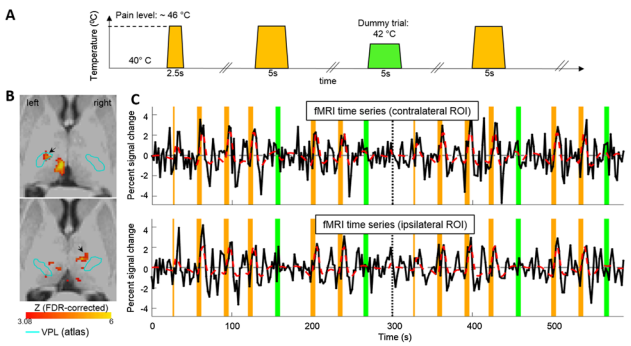

Figure 1: (A) Stimulation paradigm showing pain (yellow) and dummy (heat at 42ºC, green) trials. (B) Activation map (z>3.08, FDR corrected) for session 1 overlaid onto anatomical space. The blue line denotes the outline of the probabilistic (Tailarach) VPL region. (C) Time series for clusters indicated by the arrows in panel B.

Figure 2 compares the subject's anatomical boundaries (white line) to probabilistic VPL and functional maps across 4 sessions. The probabilistic VPL expands the subject specific anatomically defined VPL (anteriorly) and LP (posteriorly) regions in both hemispheres (Fig. 2B). In contralateral thalamus, a region was found active across 3 sessions which falls within the anterior part of the probabilistic VPL and the medially within the subject specific anatomically defined VPL (Fig. 2C). This seems to be consistent with the medial to lateral organization within the VPL for digit digits-arm-leg described from direct electric stimulation in humans [3].

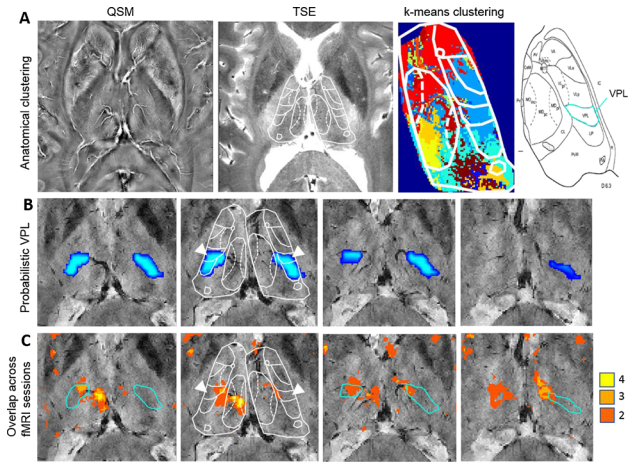

Figure 2: (A) Anatomical delineation of thalamic nuclei (white line) from the k-means clustering based on QSM, FLASH magnitude and TSE images. VPL location shown by blue outline on sketch. (B) Probabilistic VPL (Tailarach) overlaid onto magnitude FLASH images for a set of contiguous slices, White arrowheads indicate the subject specific VPL regions. (C) Conjunction map of active areas across scanning sessions (shown where at least 2 sessions overlap) formed based on responses where z>3.08 (FDR-corrected). Blue line: boundary of probabilistic VPL.

Discussion/Conclusion: fMRI responses to thermonoxious hand stimulation at 7T revealed robust contralateral thalamic activation (overlap across 3 sessions for $z > 3.08$ after FDR correction) which overlap with VPL anatomical and probabilistic delineations.

References:

[1] Ali et al. (2016). ISMRM, 54.
[2] Lancaster et al. (2007). HBM, 28:1194–1205.
[3] Lenz et al. (1988). J Nuerophys, 59:299-316.

S08.08
WITHDRAWN

S08.09
Diffusion kurtosis imaging in assessment of interhemispheric and associative pathways of patients with severe traumatic brain injury

E. Pogosbekian[1], E. Sharova[2], M. Chelyapina-Postnikova[2], L. Fadeeva[1], N. Zakharova[1], I. Pronin[1]
[1]*Federal State Autonomous Institution « N.N. Burdenko National Scientific and Practical Center for Neurosurgery » of the Ministry of Healthcare of the Russian Federation, Neuroimaging, Moscow, RUSSIAN FEDERATION,* [2]*Institute of Higher Nervous Activity and Neurophysiology of RAS, Laboratory of General and Clinical Neurophysiology, Moscow, RUSSIAN FEDERATION*

Purpose/Introduction: Earlier we found high correlation between diffusion tensor imaging (DTI) values in corpus callosum (CC) and consciousness state in patients with severe traumatic brain injury (STBI) [1]. Later we supposed that patient's consciousness state also is related with interior fronto-occipital (IFOF) tract integrity [2,3]. Diffusion kurtosis imaging (DKI) is extension of DTI and it is more sensitive to white matter changes [4]. DKI yields many metrics and we've discovered which ones can be helpful in STBI diagnostics. In this work we measured correlation between DKI values and clinical state of STBI patients, and compared patients group with healthy controls one.

Subjects and Methods: In the study 9 STBI patients with diffuse axonal injury were participated (6 men, 3 woman; age from 18 to 40, av. 26) and 13 healthy volunteers (8 men, 5 women; age from 21 to 55, av. 34). They were scanned on 3.0T MRI, voxel size $3 \times 3 \times 3$ mm with interpolation to $1 \times 1 \times 1$ mm, FOV 240 mm, b-values were 1000 and 2500 s/mm2, 60 diffusion directions for each b-value. Two raters manually placed 7 CC regions of interest (ROIs) on middle sagittal slices by Witelson's scheme [5] and 3 ROIs for each IFOF tract on frontal slices (Fig. 1).

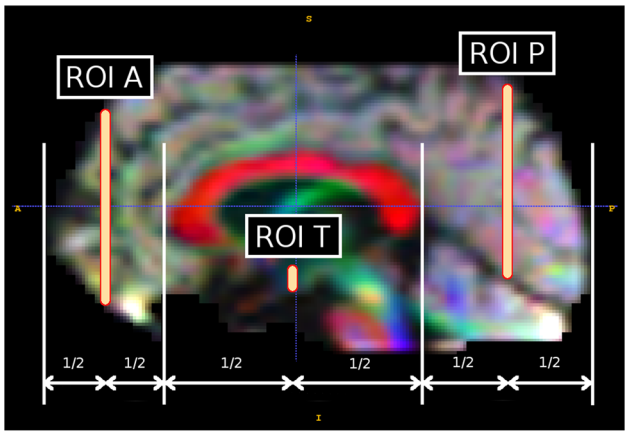

Figure 1: IFOF ROIs location scheme.

The raters calculated IFOF tracts using HARDI CSD approach [6]. In posterior and anterior ROIs were persisted areas of intersection with the tracts (Fig. 2).

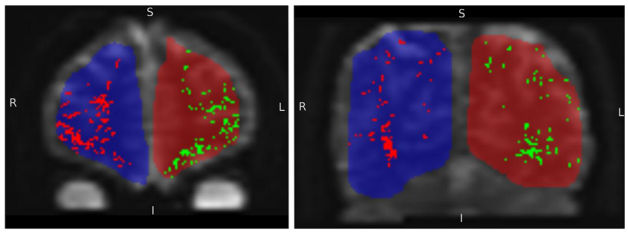

Figure 2: Areas of intersection between IFOF tracts and manually drawn ROIs. ROIs A are on left picture and ROIs P are on right picture.

Voxels where mean kurtosis is negative or greater than 3 were excluded. Consciousness state was evaluated by Glasgow coma scale, Dobrokhotova's scale [7] and Glasgow outcome scale. Motor function was assessed by hemiparesis. Spearman correlation coefficients (SCC) were calculated between clinical values and DKI metrics. Healthy controls group and patients one were compared by Mann–Whitney test.

Results: We've got high (0.7-0.9) and significant ($p < 0.001$) SCC for all the clinical data in some areas (marked by " + "), the results are presented in Table 1.

	CC Splenium	CC Isthmus	CC Posterior midbody	CC Anterior midbody	CC Rostral body	CC Genu	ROI A right
AK	+	+	+	+	+		
AWF					+		+
AxEAD	+	+					
AxIAD	+	+	+				
FA	+	+		+	+		+
KA	+	+		+	+	+	
RadEAD	+	+					
RK	+	+		+	+		+

Table 1: ROIs where SCC>0.7. Abbreviations: AK—axial kurtosis, AWF—axonal water fraction, AxEAD—axial extra-axonal diffusivity, AxIAD—axial intra-axonal diffusivity, KA—kurtosis anisotropy, RadEAD—radial extra-axonal diffusivity, RK—radial kurtosis.

DKI values in the same ROIs differed significantly ($p < 0.001$) between groups. Inter-rater correlations were from 0.74 to 0.89.

Discussion/Conclusion: Some DKI parameters in our research had high correlation with clinical data of patients with STBI. These ones can be helpful in studies of white matter diseases. Almost all measurements in IFOF ROIs didn't correlate with consciousness state. That doesn't match our theory and we suppose that poor correlation is result of low statistical sampling, which can be improved in future studies.

Supp. by grant: RHSF 18-013-00355

References:

1. E. Pogosbekian et. al. ESMRMB 2015 Congress Book of Abstracts 3 s308.
2. E. Sharova et. al. J Neurol Stroke 8.4 (2018): 245-253.
3. J. Leon-Carrion et. al. Brain Res. 2012 Oct 2;1476:22-30.
4. E. Fieremans et. al. American Journal of Neuroradiology, 34(11), 2105-2112.
5. S. Witelson. Brain 112.3 (1989): 799–835.
6. C. Tax et. al. NeuroImage, 2014, 86, 67-80.
7. T. Dobrokhotova, et al. Sotsial'naya i klinicheskaya psikhiatriya, 1996; 6 (2):26–36. (In Russ.).